Network Fault Analysis with Increased Distributed Generation Penetration and Evaluation of Solutions to Issues Caused by Distributed Generation

By

Han Qin

A Thesis Submitted for the Degree of

Doctor of Philosophy

School of Engineering

The University of Warwick

October 2017

Contents

List of Figures

List of Tables

Declaration

This thesis submitted to the University of Warwick in support of the application for the degree of Doctor of Philosophy. Not any parts or in whole has been send to other degree or qualifications at any other university. The work presented in Chapter 3 and Chapter 4 has been written in the deliverables and reported to the Project of FlexDGrid, WPD. Parts of the work in Chapter 3 and Chapter 6 are published by the author in peer reviewed research papers listed. The work described in this thesis is carried out by the author in the School of Engineering of the University of Warwick, unless is commonly understood or referenced in the text.

Han Qin

October 2017

Acknowledgement

I would like to give my sincerely thank to all people and organisations who offered help and supports to me during my PhD study. Among them, there are some persons I would like to present my thankfulness individually.

First and foremost, I would like to present my most gratefully and sincerely thanks to my supervisor, Professor Li Ran, for all his help, encouragement, guidance and care during my whole PhD study in the University of Warwick. During this time, he played lots of important roles to me. Firstly, he is a wise and patient supervisor in my academic experience. From the very beginning when I applied the PhD study to the final stage of my thesis writing, Li has always been patient and kind to offer his professional supervision to my work. He is also very strict to my works with high standard. Though I know it is still a long way for me to reach his requirement, I have seen my improvements thanks to Li's effort. Secondly, he is like a guide in my life. He shares his life experience with me and lead me to the right direction when I feel confused in my life. Finally, he is also a kind elder for all his students. He always cares about all his students' personal life and treats us like his own children. I would like to thank Li for helping me to overcome the difficulties and challenges in the study.

Secondly, I would like to thank the School of Engineering, University of Warwick to offer me the opportunity to have my PhD study here with all the software and hardware supports in my study. I would also like to send my appreciation to the Western Power Distribution (WPD) for offering me the opportunity to attend the FlexDGrid project and the scholarship for my PhD study.

Also, I would like to thank my second supervisor Dr. Olayiwola Alatise for his help in the FleDGrid project. I would like to thank my colleagues, Dr. Mohamed Abdel Motalab Ali Soli Ahmad and Dr. Qian Zhou for their supports and help in the FlexDGrid project and I really enjoyed working with them. Here I would like to deeply mourn Qian who has passed away due to cancer in 2016.

In addition, I would like to thank my friends and colleagues: Yuan Tang, Tianqu Hao, Ruizhu Wu, Ji Hu, Fan Li, Tianxiang Dai, Chenyao Bai, Xuan Guo, Roozbeh Bonyadi, Saeed, Erfan Bashar, the whole PEATER Group and a much longer list that cannot fit here, for their supports in my life in the UK and all the happy memories they have left to me.

Finally, and most importantly, I would like to thank my beloved family and devote this work to them. I would like to send my grateful and sincerely thanks to my mother Xiangdong Han and my father Chaoyun Qin for all the supports, understanding and love to me during my whole study period abroad. They devote all their love to me without anything in return. I am proud to have them and will try to be the proud of them. I wish them to know that I do and will always love them. I would also like to thank my grandparents, uncles, aunts and cousins. Thank them for loving me. Last but not the least, I would like to give my thank to my lovely and beautiful friend, Manyuan Li. Thanks for accompanying and supporting me during the time, and all the happiness and tears we had together.

Han Qin

October 2017

Abstract

Due to concerns of climate change, an increasing number of distributed generation (DG) units have been installed globally in the last two decades. This lead to issues on many aspects in the distribution network operation and management, in which the two most concerned issues are the voltage violation and fault level increase. To regulate the voltage profile and control power flow in the network, power electronic devices based soft open point (SOP) has been developed and trailed in the distribution network according to recent research. These studies mainly focused on the functions and control strategies of the power electronic compensator. However, the protection strategy and power loss of the power electronic device used in the SOP have been rarely investigated. In addition, conventional fault analysis neglects the fault current contributed from domestic load, which is hindering, and the increase DG penetration. In this work, the short-circuit behaviour of small sized induction machines in domestic load has been studied. A method for the estimation of fault current by load with higher accuracy is developed. Furthermore, the short-circuit behaviour of small and medium sized synchronous machine based DG has been investigated. A recommendation on the first symmetrical short-circuit current for synchronous machine based DG has been proposed for the situation when detailed information of the DG is unavailable. A study on the fault level change due to changes in both generation and load in the UK distribution network has been conducted and the results are presented. Regarding the SOP protection strategy, two topologies using thyristor crowbars in the protection of static synchronous series compensator (SSSC) based SOP are proposed. For these two protection topologies, the feasibility of the strategy has been thoroughly analysed in several aspects. The results indicate that with proper selection in the thyristor crowbar and coupling transformer, these protection topologies are feasible and effective. To investigate the power loss for the power electronic devices, several cases have been studied based on 11kV distribution network model with back to back voltage source converter (B2B VSC) based SOP. The results show that in most cases, the utilisation of B2B VSC based SOP can reduce the total network loss. Nevertheless, when the DG penetration level or the imbalanced loading level between two feeders is low, the B2B VSC will further increase the total network loss. Finally, one of the solutions to the fault level issue due to the DG installation is to employ fault current limiter (FCL) into the distribution network. The power loss of saturated iron core FCL has been analysed. The results show that the power loss of a saturated iron core FCL can be 1% or even less of the transferred power. It is more efficient compared to the power semiconductor type for the fault current mitigation.

Nomenclature

ac	alternative current
ANSI	American National Standards Institute
ASHP	air source heat pump
B2B VSC	back to back voltage source converter
BJT	bipolar juction transistor
CFL	comact fluorescent light
CHP	combined heat and power
CIGRE	Conference on Large High Voltage Electric System
CIRED	Conference on Electricity Distribution Networks
dc	direct current
DFIG	double fed induction generator
DG	distributed generation
DNO	distribution network operator
ER G74	Engineering Recommendation G74
ESQCR	Electricity Safety, Quality and Continuity Regulations
EU	Europe Union
EV	electrical vehicle
FCC	fault current contribution
FCL	fault current limiter
FES	Future Energy Scenarios
FL	fault level
FLC	fault level contribution
GDHP	ground source heat pump
GTO	gate turn-off thyristor
HTSFCL	high temperature superconducting fault current limiter
HV	high voltage
HVAC	high voltage alternative current
HVDC	high voltage direct current
IEC	International Electrotecnical Commission
IGBT	insulated gate bipolar thyristor
IGCT	integrated gate communicated thyristor
LED	light-emitting diode
LV	low voltage
MPPT	maximum power point tracking
MV	medium voltage
n	hatmonic order
NGC	National Grid Code
NGS	National Grid System
O/f	over frequency
O/V	over voltage
pf	power factor
PI	proportional and integral feedback
PL	penetration level
PV	photovoltaic
PWM	pulse width modulation

RMS root mean square
SP Scottish Power
SPWM sinusoidal pulse width modulation
SSSC static series sychronous compensator
STATCOM static synchronous compensator
SVC static Var compensator
TOUT Time of Use Tariffs
U/f under frequency
U/V under voltage
VSC vlotage source converter

[xabc] matrix expression of quantities in abc coordinates
[xdq] matrix expression of quantities in dq0 coordinates
ΔI difference between results from different methods
ΔV21 voltage rise at load busbar in per unit system
As swept area of rotor disk
As initial value of aperiodic
C capacitance of a capacitor
c voltage factor
Cp power efficient
D stator bore diametre
E energy stored in a capacitor
Ed.c. energy stored in the d.c. bus
eoff turn off loss
eon turn on loss
erec diode reverse recovery energy
Etotal total energy loss
f frequency
F(s) square of the d.c. bus voltage
FCCref referemce fault current contribution
FLbreak break fault level contribution of sychronous machine
FLC normalised fault level contribution
FLC'break normalised fault level cotrinution of sychronous machine through transformer
FLCbreak normalised break fault level contribution of sychronous machine
Fref(s) reference voltage input for the d.c. bus voltage control loop
g acceleration due to gravity
Gd.c.(s) gains of the PI controller for the d.c. bus voltage control loop
GPLL(s) gains of the PI controller for the phase-locked loop
H effective head
I phase current at rated output power
Ib symmetrical current
Ibreak break fault current
ic collector current
id d-axis current
Idc dc component of short circuit current
If fault current
if diode foreard current
IfDG fault current contributed by distributed generation

Ifi	fault current component
IfM	fault current contributed by rotating load
Ifup	fault current contributed by upstream network
Ik"	initial symmetrical short circuit current
Im	magnetising current
Imake	make fault current
Ip	peak short circuit current
Ip'	simulated value of peak short circuit current
Ip"	measured value of peak short circuit current
iq	q-axis current
Ir	rated current of small scale induction machine
Isc_break	break short circuit current of synchronous machine
Isc_subtransient	subtransient short circuit of sychronous machine
K1	adjacent coeffiecient
K2	adjacent coeffiecient
KId.c.	integation gain factor for the d.c. bus voltage control loop
KIG	integation gain factor for the phase-locked loop
KPd.c.	propotional gain factor for the d.c. bus voltage control loop
KPG	propotional gain factor for the phase-locked loop
L	stator length
Lf	inductance of the filter
P	power output
P	real power flowing into the d.c. bus
P(s)	power flowing into the d.c. bus
p.u.	per unit system
PDG	real power output of DG
pf	load power factor
PL2	real power comsumed by load
Pn	rated power capacity
Q	flow rate
Q	reactive power flowing into the d.c. bus
QDG	reactive power input/output of DG
QL2	reactive power consumed by load
R	cable resistence
R'	transient resistance
R1	resistance of the primary winding
R2	resistance of the secondary winding
Rc	core loss resistance
Rf	resistance of the filter
Rf	Thevenin equivalent resistance of the fault
RL	Thevenin equivalent resistance of the transmission line
Rm	magnitizing resistance
Rr'	induction machine per phase rotor winding resistance with respect to the stator winding
Rs	Thevenin equivalent resistance of the source
Rs	induction machine per phase stator winding resistance
RT	Thevenin equivalent resistance of the transformer
s	rotor slip
Sn	rated capacity

Sr	rated capacity of sychronous machine
t	time
T(θ)	transformation matrix of θ
tf	turn off time
tr	turn on time
trr	reverse recovery time
ud	d-axis voltage
Un	norminal phase to phase voltage at fault location
uq	q-axis voltage
Ur	rated voltage of sychronous machine
v	wind velocity
V	voltage over the capacitor
V1	primary busbar voltage
V2	load busbar voltage
vabc	grid voltage
vce	on-state voltage
vd.c.	d.c. bus voltage
vfabc	voltage of the filter
vfabc	diode formward voltage
vgd	d-axis voltage of vabc
vgq	q-axis voltage of vabc
VL	norminal line voltage
Vm	peak amplitude of the norminal voltage of the grid
Vn	norminal voltage
vq	q-axis component
Vφ-n	phase to netural voltage
Vφ-φ	phase to phase voltage
X	cable reactance
X'	transient reactance
X/R	reactance/resistance ratio
X1	reactance of the primary winding
X2	reactance of the secondary winding
Xd"	d-axis subtrainsient reactance of sychronous machine
xd"	per-unit d-axis subtransient reactance of sychronous machine
xe	error of the reference and feedback
Xf	Thevenin equivalent reactance of the fault
Xkl"	initial positive sequence reactance
XL	Thevenin equivalent reactance of the transmission line
xL	per-unit leakage reactance of the windings
XL	leakage reactance
xL	per-unit leakage reactance
Xm	magnetiszing reactance
Xm	magnetising reactance
xmd	per-unit d-axis magnetising reactance
Xr'	induction machine per phase rotor winding reactance with respect to the stator winding
Xs	Thevenin equivalent reactance of the source
Xs	induction machine per phase stator winding reactance
XT	Thevenin equivalent reactance of the transformer

Z'	transient impedance
ZDG	Thevenin equivalent impedance of DG
Zf	Thevenin equivalent impedance of the fault
Zload	Thevenin equivalent impedance of load
Zs	Thevenin equivalent impedance of source
Zt	equivalent transformer impedance
δ	ration of a load to the total load
η	overall efficiency
θ	time dependent angle between d-axis and α-axis
$\theta 0$	angular velocity of Park Trasformation
$\theta ref(s)$	reference angular velocity inputed for the phase-locked loop
κ	calculation factor
ξ	damping factor for the phase-locked loop
$\xi d.c.$	damping factor for the d.c. bus voltage control loop
ρ	density of certain material
$\tau a.c.$	a.c. time constant of ac component in short-circuit current by sychronous machine
$\varphi 0$	assummed initial angle between d-axis and α-axis
ω	angular frequency of the grid
$\omega d.c.$	natural angular velocity

Chapter

1 Introduction

1.1 History of Electrical Power System

The world's first power station was built at Cragside, England, designed by Lord Armstrong in 1868. It supplied power to the daily usage for private farm buildings using water powered Siemens dynamos. In January 1882, the first public power station, Holborn Viaduct Generating Station, started to operate at London. It was a project of Thomas Edison and the station supplied power at 100 V driven by a steam engine [1]. The first central generating station was later built in Pearl Street in New York, also by Thomas Edison in 1882. It supplied power at 110V using a steam powered generator [2]. All these three stations supplied direct current (dc) to the customer.

The first full alternating current (ac) power system in the world was built by William Stanley in Great Barrington, Massachusetts in 1886 [3]. The first ac station in Great Britain was opened at Deptford and transmitted at 10kV to customers in London in 1891 [4]. In the same year, the first three-phase ac transmission system from Lauffen to Frankfurt was built in Germany by Oskar von Miller. The transmission system was at 40Hz and 15kV, covering a distance of 109 miles (175km) [5]. Thereafter, centralized generation and three-phase ac power system have gradually developed into the structure today and been used for electrical power supply in the world.

In the recent decades, the high voltage dc (HVDC) technology has been studied and developed by many researchers and engineers. This was driven by [6]:

1) The need to transmit large amount of electricity over a very long distance due to the energy resources far from the load centres;
2) More cost-effective of long distance HVDC compared to HVAC transmission; and
3) The increasing amount of offshore wind power generation is to be transmitted back to the in-land load centres.

The development of HVDC accelerates the utilisation of power electronic devices in the power system. Additionally, the number of distributed generation (DG) is increasing with a decrease in the total capacity of traditional centralised generation.

1.2 Brief Introduction to Distribution Network

An electric power system consists of three major components: generation system (large central power plants), transmission system and distribution system. Each component has its typical voltage level and is connected to another component through step up/down power transformers, the structure is indicated in Figure 1.1.

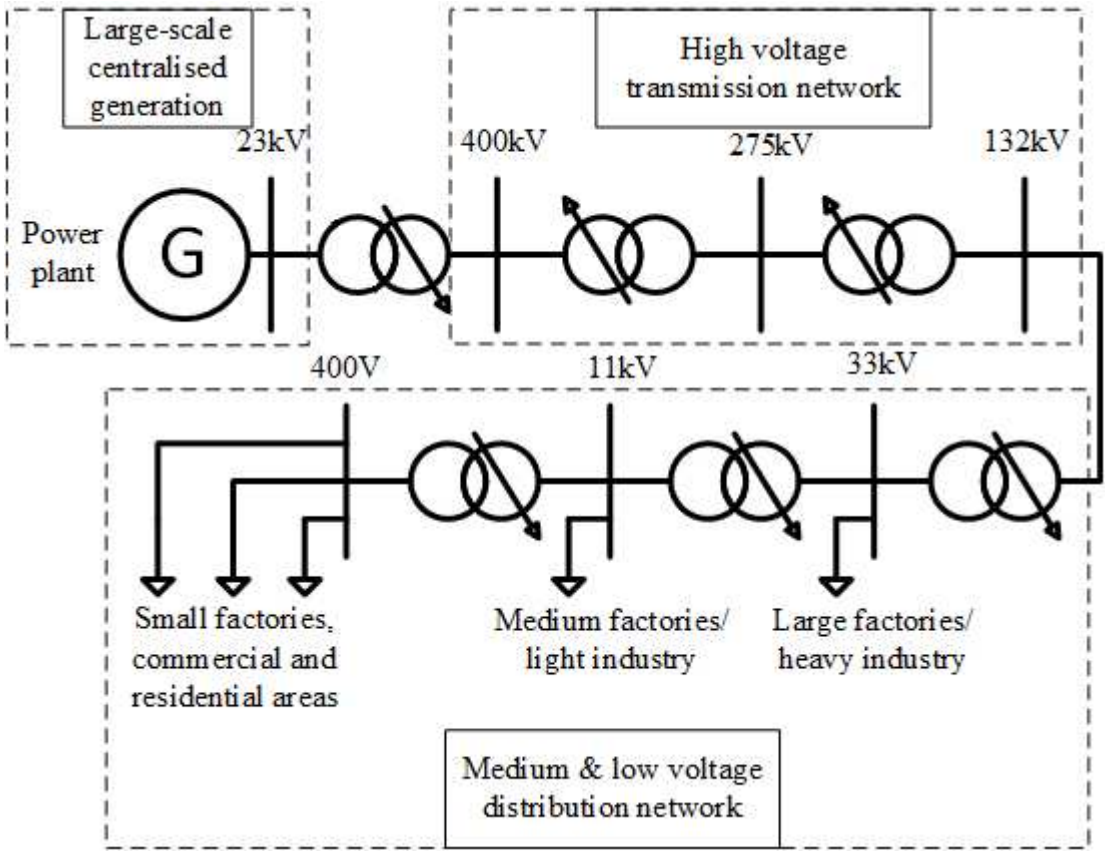

Figure 1. 1 Power system structure

Typically, a distribution network (400V to 33kV phase to phase nominal voltage) starts from the distribution substation fed by several transmission lines from the transmission system [7]. The typical primary distribution substation at the bulk supply point uses two to four 50MVA 132/11kV step-down transformers, depending on the supplied peak load, to supply an area of 3-6 square miles in the UK [8]. The topology of a distribution network is typically designed in radial (open ring) structure, as indicated in Figure 1.2.

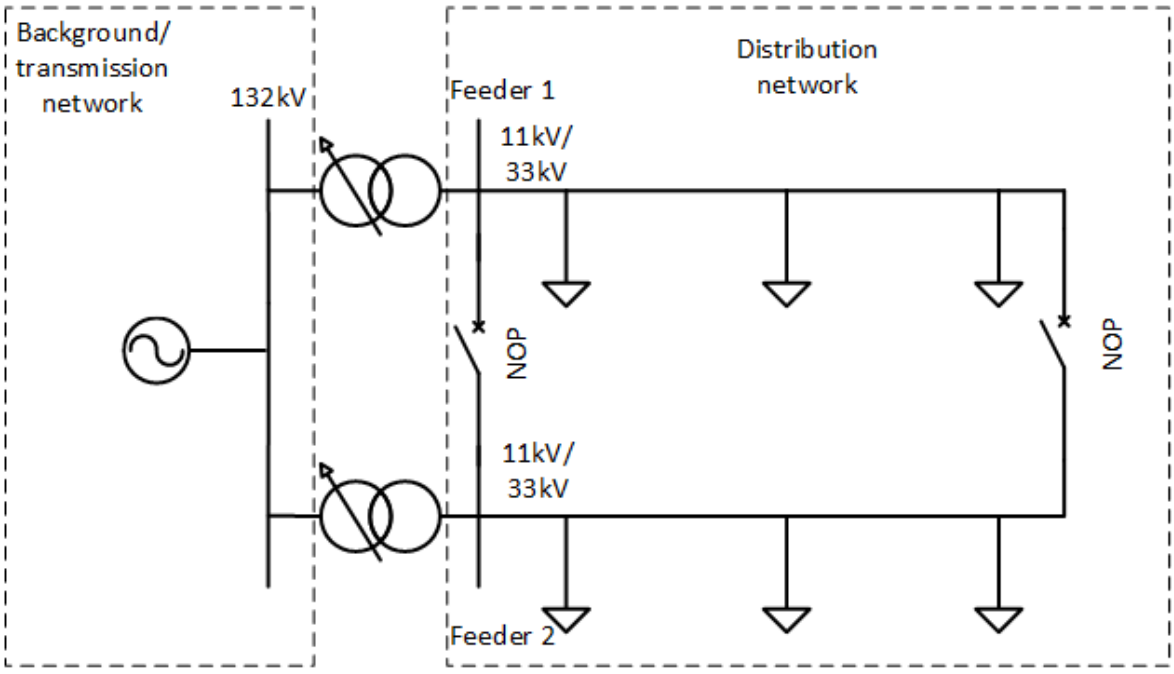

Figure 1. 2 Diagram of a typical distribution network in radial (open ring) structure

Circuit breakers are used to connect branches that when the circuit breaker closes, the radial structure can be transformed into a loop structure to improve the reliability in delivering power to the customers. Fuses and circuit breakers are connected in series in the network to provide protection against the occurrence of short circuits (faults). The ratings of the protection equipment are originally designed to withstand short circuit current from both upstream and downstream dynamic loads without DG in the past. However, with the increasing energy demand and global climate change, the distribution network nowadays is adopting more DGs installed by the electrical energy customers. These changes have brought about a number of issues in network operation and management for the distribution network operators (DNOs).

1.3 Brief Introduction to Distributed Generation

The arrangement using centralised generation and high voltage transmission has been adopted in the modern electrical power system development over the past 90 years [9]. This arrangement has a number of advantages. The centralised large generating units can be made efficient in the electricity generation with relatively small number of staff in the operation. The high voltage transmission network allows the generating plants to be dispatched at any time and limits the electrical losses over long distance transmission. The distribution network can be designed simply for unidirectional power flow and sized to accommodate customer loads only [10].

Since the early 1990s, a revival of interests in connecting generation to the distribution network has been raised in response to the increasing load demand and global warming. This type of generation has been named, from different aspects, as [11]:

- Dispersed generation to distinguish it from centralised generation;
- Distributed generation since the generation units are connected in the distribution network; or
- Embedded generation from the concept of generation embedded in the distribution network.

These three terms can be considered synonymous and interchangeable. The use of these terms is mainly regional.

Investigations on DG have been conducted by working groups of both the International Conference on Large High Voltage Electric System (CIGRE) on 1997 and the International Conference on Electricity Distribution Networks (CIRED) on 1998 and 1999 [12-14]. The reports of both working groups pointed out that there is no universally accepted definition of DG but some common attributes may be listed as:

- Not centrally planned or despatched,
- Sizing between 50kW to 100MW, and
- Connected to the distribution network.

The review of technologies of DG and the impacts of DG on the network is made in the literature review in Chapter 2, Section 2.1.

1.4 Research Objectives and Contributions

Due to increasing DG penetration, voltage and fault level issues are caused by DG in the distribution network. Aiming at eliminating these issues, more accurate estimations of the network fault level, at present and in the future, are required. Furthermore, solutions are proposed by employing fault current limiter (FCL) and soft open point (SOP) into the distribution network. Evaluations to these solutions are also required regarding the operation loss. Regarding the former issues, the main research objectives are listed as following:

- Investigating the fault level contribution from dynamic load consisting of small induction machines in the distribution network, which has a considerable effect on the network fault level;
- Investigating the fault level contribution from small and medium size synchronous machines;
- Clarifying the effect of DG to the network voltage profile and fault level considering different DG locations;
- Investigating the potential effect of synchronous machine based DG on the missing zero-crossing of the total fault current in the distribution network;
- Investigating the distribution network loading conditions due to the increase in the number of customers and the utilisation of low-carbon technology electrical appliances;

- Analysing the feasibility of using thyristor crowbar in the protection of series compensator based SOP which can be used to mitigate the network issues; and
- Evaluating the operational power loss of back-to-back voltage source converter (B2B VSC) based SOP and saturated iron core FCL in the distribution network.

The original contributions of the thesis to the wider research topics are:

- The short circuit behaviour of small induction machines used in domestic load has been studied. Regarding to the analysis, improvements have been made to the calculation methods for the short-circuit current contribution of small induction machines. With the improvement, load models of domestic and commercial customers with dynamic load modelled as induction machine are altered accordingly. With the altered load model, the normalised fault level contributions of domestic, commercial and industrial loads are obtained for more accurate estimation in DG connection design studies. These fault level contributions can be used for the fault level analysis when detailed load composition is not available. A method for substation specific system fault level estimation is then provided based on the normalised fault level contribution. This method can be used as a reference for DNOs in the network operation.
- The short circuit behaviour of small scale synchronous generators has been studied and the normalised fault level contribution of the small scale synchronous generators is obtained. Based on the normalised fault level contribution, the effects of increasing DG penetration to the network voltage profile and fault level increase are clarified with the consideration of DG locations.

- Furthermore, the effects of small and medium size synchronous machines to the missing zero-crossing phenomenon of fault current in the distribution are analysed. The results can be used in the management of DG connection in the distribution network for DNOs.
- The fault level changes due to the displacement of centralised fire powered plants and increasing downstream distributed generation have been studied using practical substation data. The results can be used as reference for DNOs in the fault level management in network operation.
- The load composition estimation due to the changes in the customer behaviour in the UK power system has been made for the next two decades. And the further changes in the load fault level contribution is also estimated based on the changing load composition for the next twenty years, which can be beneficial in the DNOs' network management.
- The feasibility of using shunt thyristor crowbars in the protection of series compensator based SOP is analysed. Further suggestion in the selection of thyristors for this application is given, making use of the short-term surge current capability of the devices.
- The effects of using B2B VSC for the SOP in the distribution network are analysed. Further analysis on the power loss of this application is conducted and different scenarios are analysed to determine the conditions which can bring benefit to the DNOs regarding to the total system loss.

- A power loss study has been conducted on the saturated iron core FCL. This provides a reference for the utilisation of this type of FCL in the network operation for DNOs.

1.5 Outlines of the Thesis

The thesis is outlined as follows:

Following this introduction chapter, a literature review of distributed generation, power electronic compensators and FCLs is presented in Chapter 2. The short-circuit study of dynamic load is conducted in Chapter 3. Also in Chapter 3, the study on fault current contribution of small and medium size synchronous machine based DGs during a network fault is presented, together with a clarification of the effects of distributed generation on the network voltage profile and fault level. In Chapter 4, the possible scenarios of the electrical network changes in the UK are analysed. The analysis is conducted separately regarding the generation changes in the upstream network and the load changes in the downstream network. Chapter 5 presents a feasibility study on the protection to series compensator based SOP using shunt thyristor crowbars. In Chapter 6, the benefit of using B2B VSC as the SOP is analysed. Furthermore, the loss study on the B2B VSC based SOP is presented in Chapter 6. Chapter 7 is the loss study of the saturated iron core FCL. The conclusion and future work are presented in the Chapter 8.

Chapter

2 Literature Review

2.1 Review of Distributed Generation

The revival of DG in the early 1990s is in response to the global warming issue. The rapid development of DG over the last decade is mainly motivated by the finical mechanisms of governments in response to the climate change. In order to reduce the carbon emission, many governments have set targets to increase the use of renewable energy. For example, the UK government has developed the 2050 Pathway to achieve the target to reduce the carbon emission by 20% by 2020 and 80% by 2050 relative to the 1990 level.

This is achieved by replacing current fossil fuels power plants and installing new generations using renewable energy and other means [15]. Compared to the fossil fuels, a renewable energy source has much lower energy density, which means that the generation plants will be smaller and geographically widely spread. Hence the renewable generation plants developed by entrepreneurs and large electrical customers are dispatched according to the energy source or customer location. In general, the benefits of effective DG integration are [16-18]:

- Reducing central generation capacity;
- Increasing the utilisation of transmission and distribution network capacity;
- Enhancing system security; and
- Reducing overall costs and CO_2 emission

2.1.1 Technical Impacts of Distributed Generation on the Distribution Network

Traditionally, the distribution network has been designed to accept power from the transmission network and to distribute it to customers. The power flow in the distribution network is unidirectional. However, with significant penetration of DG, the power flow may become reversed. The power distribution is no longer a passive circuit but an active system with the power flow and the voltage determined by both generation units and loads [19].

The changes in power flow will cause increase or reduction of network power loss.

Due to changes in power flow, the penetration of DG can also cause voltage variations, increase the network fault levels and affect the power quality.

2.1.1.1 Network Voltage Changes

DNOs have an obligation to supply their customers at a voltage within specified limits, typically around ±5%. In the UK, the voltage regulation for distribution network is between +10% and -6% and DNOs typically adopt ±6% in the practice to avoid confusion in network operation [20, 21]. The voltage profile of a radial distribution feeder is shown in Figure 2.1.

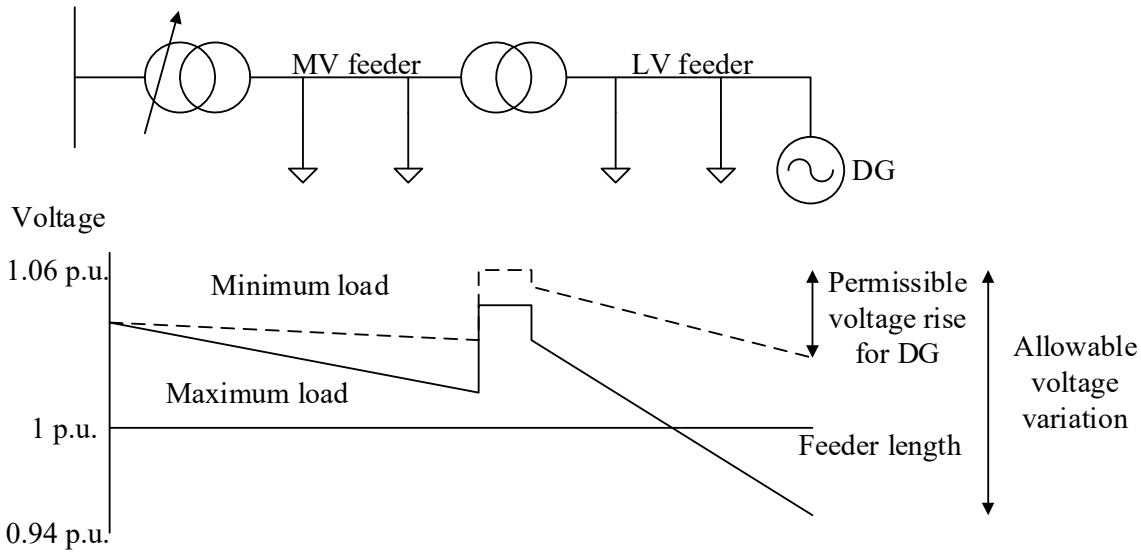

Figure 2. 1 Voltage variation down a radial feeder

As indicated in Figure 2.1, the voltage at the starting point of the MV feeder is held constant by a tap-changing transformer. The voltage drops along the distribution network due to line impedance and the load on the feeder. The voltage boost in the middle of the feeder is due to taps of the MV/LV transformer and the voltage drop on the LV feeder is due to the low voltage loads [22, 23].

When DG is installed by the customer, it is regarded as being directly connected to the MV network through a step-up transformer. The output power of DG changes the power flow in the network and causes voltage variation [24]. An example is given for a simple two-bus radial distribution network as shown in Figure 2.2.

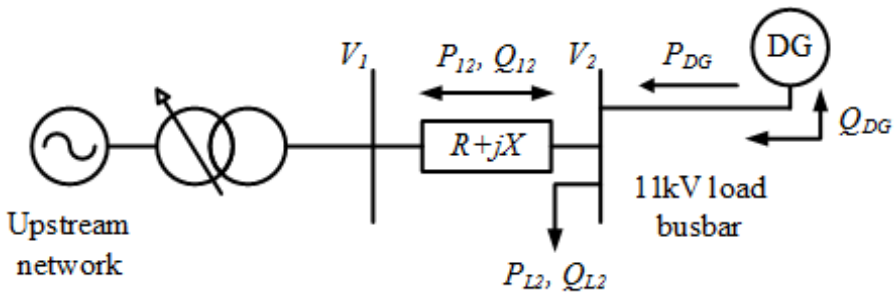

Figure 2. 2 Simple two-bus radial distribution network

The voltage rises at the load busbar caused by DG in per unit (p.u.) can be approximately calculated by:

$$\Delta V_{21} = V_2 - V_1 \approx \frac{R(P_{DG} - P_{L2}) + X(Q_{DG} - Q_{L2})}{V} \tag{2.1}$$

where V_1 and V_2 are the voltages of the primary and load busbars; V is the nominal voltage; R and X are the circuit resistance and impedance; and P_{DG}-P_{L2} and Q_{DG}-Q_{L2} are the active and reactive power flowing through the branch. The voltage rise can be controlled by importing or exporting reactive power from or to the DG. However, in the current practice of network management by the DNOs, the power factor of DG using rotating generators is usually required to be set as unity, which means the DG export active power only. This is due to that it will be difficult for DNO's to predict the voltage change in the network if DGs are not operated at unity power factor. This operation strategy may cause significant voltage violation when the load level changes from high to low.

2.1.1.2 Increase in Network Fault Level

Many types of distribution generation plants use directly connected rotating machines and these will contribute to the network fault levels. Both induction and synchronous generators will increase the fault level although their behaviour under sustained fault condition differs.

The rise of fault level depends on the DG capacity and DG location. In urban areas, the fault level at many of the existing networks is approaching 70% of the switchgear ratings caused by the additional contribution from dynamic loads [25]. Hence the increase in fault level by DG connection can cause serious safety issues to the network operation. This can significantly limit DG deployment an in urban distribution network.

Furthermore, to increase the short circuit rating of distribution network by upgrading the switchgear and cables can be extremely expensive and difficult particularly in congested city substations and cable routes. Current practice to increase the DG penetration without causing serious fault level rise is to introduce a high impedance, such as high impedance transformer or reactor between the generator and the network. But this solution is at the expense of increased power loss and voltage variations at the generator. In recent years, researchers have been applying fault current limiters (FCLs) and power electronic devices in the protection with DG penetration [26, 27].

2.1.1.3 Power Quality

Two aspects of power quality are usually considered to be important with DG: 1) transient voltage variations and 2) harmonic distortion of the network voltage [28]. Depending on the network circumstance, the installation of DG can either increase or decrease the quality of the voltage received by other users in the network.

The transient voltage variation is caused during the connection and disconnection of relatively large DG to the network. The transient voltage variation can be limited by careful design of DG plant. But for directly connected induction generators on weak networks, the transient voltage rise can be the limitation on increasing DG penetration rather than steady-state voltage rise. For synchronous generators, the starting inrush current can be negligible disturbance to the network if soft-start unit is used.

However, the disconnection of DG at full output may also lead to significant voltage drops. Incorrectly designed DG plant with power electronic interface to the network may inject harmonic currents which can lead to unacceptable network voltage distortions.

2.1.2 Technologies Used in Distributed Generation

The technology available for DG varies widely. It generally has the following characteristics. Firstly, many of the technologies utilise renewable energy resources. The availability of the different resources varies significantly in areas and efficiency. Secondly, many of the technologies have been modularized. For instance, technologies like micro-hydro units, photovoltaic (PV) arrays, wind turbines and fuel cells consist of a number of small modules. These modules are manufactured in factories and can be installed at the required location in a very short time comparing to large centralised power stations. Furthermore, each module unit can function independently despite the status of the other modules, which means the failure in one module does not affect the other modules. The effect of module failures on the total available power output is relatively small as compared to a unit failures in large centralised power stations. Finally, the adding on or relocation of modules is allowed by the technologies. An important type is the combined heat and power (CHP) generation. This technology uses various heat generation technologies to supply heat demand and drive synchronous or induction generators for electricity. Detailed description of several technologies used in DG is introduced in the following sub-sections.

2.1.2.1 Combined Heat and Power Plants

Combined heat and power is, at present the most significant type of distributed generations. Generally, the generated electrical power is consumed inside the host premises or industrial plant of the CHP facility. The heat is either used for the industrial process and/or for space heating inside the premises or transported for the district heating. The typical overall efficiency of CHP can be 67% with electrical efficiency of 23% and heat efficiency of 44% [29]. This would lead to a 35% reduction in the primary energy use compared to electrical and heat generation from separate power stations and boilers. This further leads to a reduction in total CO_2 emission by over 30%.

The prime movers of CHP units at present predominantly include: gas engine, gas turbine, fuel cell and domestic boiler system. In the last case, the hot gas firstly drives the generator to generate electricity through the steam turbine. Afterwards, the gas is passed to the industrial process or through a heat exchanger for the space heating. The generator, commonly a synchronous or induction generator, is directly connected to the grid through a step-up transformer. Due to the capability of reactive power control, synchronous machines are more preferred than induction machines in the electricity generation of CHP [30, 31].

The grid interface of a fuel cell type of CHP unit is through a power electronic stage [32]. The fuel cell directly converts fuel energy into heat and electricity without using kinetic energy as in the gas engine or steam/gas turbine.

Some small scale domestic CHP units use fuel cell or an external combustion engine such as Stirling engine to drive a rotary or linear permeant magnet generator. These small-scale CHP units is connected to the single-phase grid through power electronic interfaces.

The basic configuration of a CHP units with gas turbine is illustrated in Figure 2.3. At present, most of the CHP units in the distribution network operate in the mode of producing heat as the main output and electricity as by-product by the current power.

For fuel cell CHP units, the connection to the gird is through a power electronic interface, as shown in Figure 2.4. This can limit the current contribution to a grid fault [32].

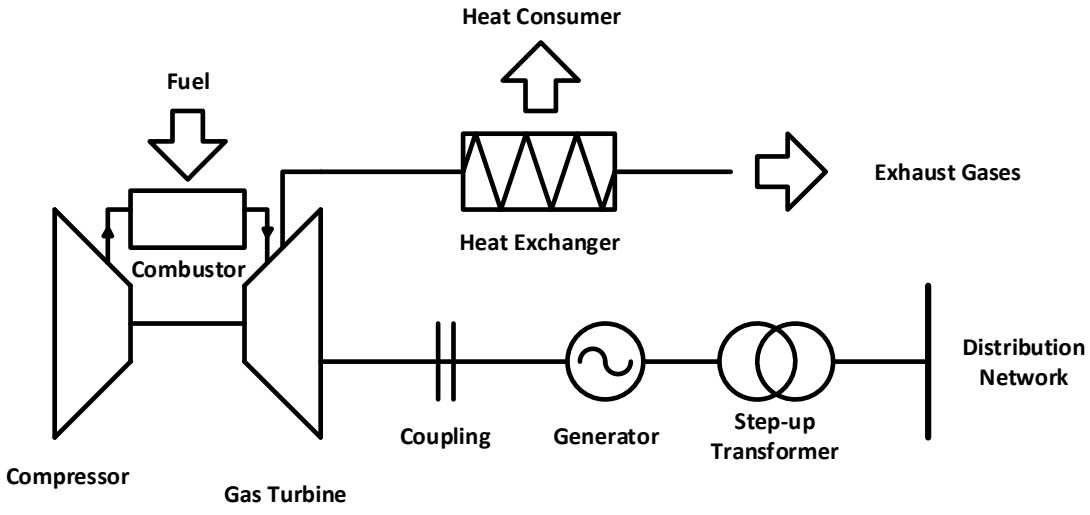

Figure 2. 3 Configuration of a gas turbine CHP [33]

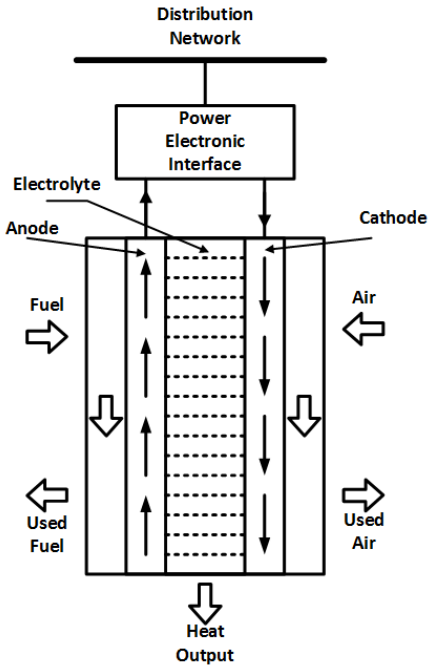

Figure 2. 4 Configuration of fuel cell CHP [34]

2.1.2.2 Renewable Energy Generation

At present, the distribution of DGs using CHP is mainly determined by the local load and the operation of CHP is generally controlled in response to the energy demands of the heating scheme. Similarly, the siting of electricity generation using renewable energy source is determined by the location of the renewable energy source and their output varies with the availability of the source [35]. For small DGs using renewable energy resources, it is not cost-effective to provide large energy storage. This is an important difference compared with DGs using fossil fuel, which has high energy density and can be stored economically.

2.1.2.2.1 Small-scale Hydro Generation

Hydro generation is a relatively mature technology and the operation of small and medium sized hydro generating units in parallel with distribution system is well understood [36, 37]. The hydro schemes experience large variation according to availability of the water flow if significant water storage capacity is not available. This variation is largely affected by the rainfall, particularly if the catchment is on rocky or shallow soil which lacks vegetation cover and steep, short streams [38]. Uneven rainfall will lead to a variable hydro resource and it is interesting to note that the capacity factor for hydro generation in the United Kingdom for 2008 was only some 35%. (Capacity factor is the ratio of annual energy generated to that which would be generated with the plant operating at the rated output all year).

The power output of a hydro-turbine is given by:

$$P = Q H \eta \rho g \tag{2.2}$$

where P is the output power (W), Q is the flow rate (m^3/s), H is the effective head (m), η is the overall efficiency, ρ is the density of water ($1000g/m^3$) and g is the acceleration due to gravity ($\sim 9.8m/s^2$). Various forms of turbine are used for differing combinations of flow rate and head. For small hydro units (<100kW), a cross-flow impulse turbine, where the water strikes the runner as a sheet rather than a jet, may be used. The typical reasonable efficiencies can be achieved with impulse turbine down to 1/6 of the rated flow [10].

Generators commonly used in small-scale hydro scheme are induction or synchronous machines. Considering the safety of turbine-generator when over-speeding due to the loss of loads, the squirrel-cage induction generator is more preferred than wound rotor synchronous machine. Due to the operating characteristic of the turbine to the variable flow rates, the number of variable speed hydro-generator sets in use is increasing. This requires the use of power electronic interface for the connection to the distribution network.

2.1.2.2.2 Wind Power Plants

The power developed by a wind turbine extracted from the kinetic energy of the passing wind is:

$$P = \frac{1}{2} C_p \rho_a v^3 A_s \tag{2.3}$$

where C_p is the power efficiency (a measurement of the effectiveness of the aerodynamic rotor), P is the output power (W), v is the wind velocity (m/s), A_s is the swept area of rotor disk (m^2) and ρ_a is the density of air ($1250 g/m^3$).

As the developed power is proportional to the cube of wind speed, it is very important to locate the generation in the area of high mean annual wind speed and the availability of the resource is an important factor in the determination of the site of wind farm [39].

Typically, a 2MW wind turbine has a rotor diameter of 60 to 80 m mounted on a 60 to 90 m high tower. The wind turbine must be designed to withstand large forces during high winds as the force exerted on the rotor is proportional to the square of the wind speed. The three-bladed horizontal-axis rotor design gives a good value of power efficiency, which varies with the relative speed of the rotor and the wind (the tip speed ratio). The maximum value of C_p in practice is approximately 0.4 to 0.45 [40].

The wind turbine can be operated, in response to the variation of the wind speed, in fixed or variable speed [41, 42]. For a fixed speed wind turbine, the induction generator is commonly in use. The schematic representation of a fixed speed wind turbine is shown in Figure 2.5. The aerodynamic rotor is coupled to the induction generator via a speed increasing gearbox. The cage rotor induction generator is typically for 690V, 1000 or 1500 rpm. Pedant cables within the tower connect the generator to power factor correction capacitors and an anti-parallel soft-start unit located in the tower base. The wind turbine is typically connected into the 11kV or 33kV network in UK through a step-up transformer.

For a variable speed wind turbine, the generator can be either induction or synchronous generator. The schematics of variable speed wind turbine using induction and synchronous generators are shown in Figures 2.6 and 2.7. The double fed induction generator (DFIG) uses a back to back voltage source convertor (B2B VSC) in the rotor circuit. It controls the power flows when the generator operates above the synchronous speed. If the required speed operation is in a wide range, the arrangement in Figure 2.7 can be used. The B2B VSC is used to interface the wind turbine drive train to the network.

The generator can be either induction or synchronous generator and the pulse width modulation (PWM) control is used on the converter bridges. The variable speed operation gives two main advantages: 1) reducing the mechanical loads and 2) smoothing output power.

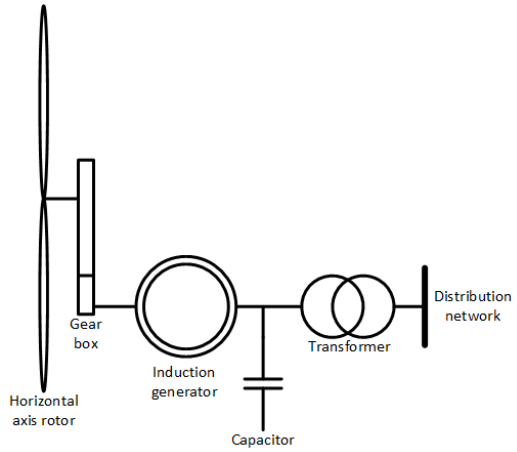

Figure 2. 5 Fixed speed induction generator wind turbine [43]

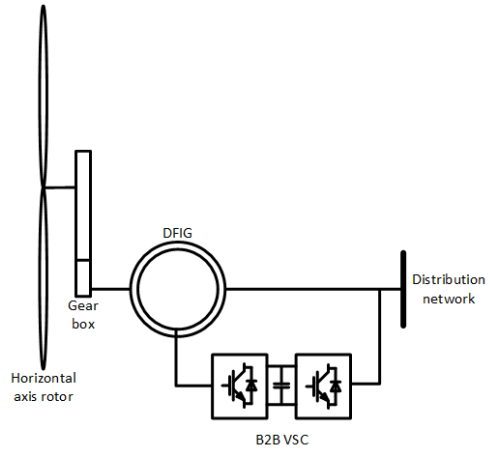

Figure 2. 6 Figure 2.6 DIFIG wind turbine [43]

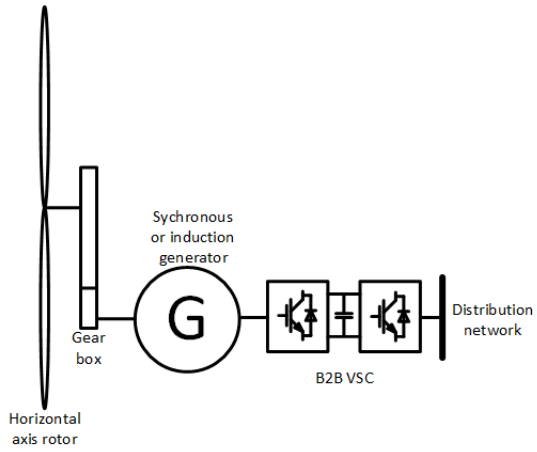

Figure 2. 7 Figure 2.7 Full power converter wind turbine [43]

2.1.2.2.3 Solar Photovoltaic Generation

Photovoltaic generation is a well-established technology with a number of major manufactures producing related equipment. The physics of photovoltaic energy conversion has been described by a number of authors [44-46]. Its main application was off-grid for high value and small electrical load that were far from the nearest distribution network for many years in the past. In the recent years, stimulated by support through feed-in tariffs its use as grid-connected distributed generation has increases rapidly particularly in Germany and Spain [47, 48]. The interests of PV generation in Europe is focused on smaller installations, which is typically 1 to 50kW roof mounted PV modules.

These small PV installations are connected directly at customers' premises and so to the low voltage distribution network. This form of generation is distributed largely in residential and commercial customers. The schematic representation of a small PV generation connected to the grid is shown in Figure 2.8. The inverter typically consists of :1) a maximum power point tracking (MPPT) circuit, 2) an energy storage element, 3) a dc to dc converter to increase the voltage, 4) a dc-ac convert stage, 5) an isolation transformer and 6) an output filter. Usually PV inverters operate at unit power factor and have a very limited effect on the network voltage [49, 50].

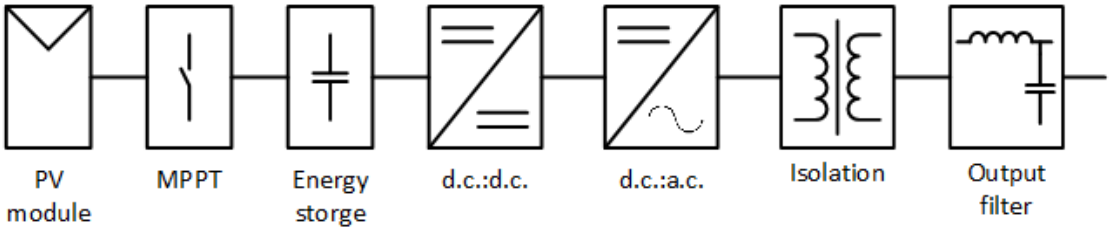

Figure 2. 8 Figure 2.8 Grid-connected small PV inverter [51]

2.1.3 Grid Regulation and Standards Regarding DG Installation

Embedded generators above 11kVA in MV or LV networks are governed by Engineering Recommendation G59 (Issue 3, 2013) [52, 53]. The main schemes used in the UK regarding the aspects mentioned in Section 2.1.1 are as follows.

Voltage limits

Where the generating plant is remote from a network voltage control point, a voltage range of ±10% of the declared voltage is applied at the connection point. The step voltage change caused by the connection and disconnection of generating plant from the distribution system is subject to a typical limit of ±3% for infrequent planned switching events and ±10% for unplanned outages.

Power quality

The connection and operation of generating plant may cause a distortion of the distribution system voltage waveform resulting in voltage fluctuations, harmonics or phase voltage unbalance. The limits on the low order harmonic distortion are set as shown in Table 2.1.

Table 2. 1 Limits for harmonic emission [53]

Harmonic order	Maximum permissible harmonic current
n	A
Odd harmonics	
3	2.3
5	1.4
7	0.77
9	0.4
11	0.33
13	0.21
15≤n≤39	0.15x8/n
Even harmonics	
2	1.08
4	0.43
6	0.3
8≤n≤40	0.23x8/n

Protection setting

In order to avoid unnecessary disconnection of generating plant during distribution network faults or switching events and the consequent disruption to generators and customers, appropriate sensitive settings are indicated in the Tables 2.2 and 2.3.

Table 2. 2 Settings for long-term parallel operation [53]

Protection Function	Small Power Plant①				Medium Power Plant②	
	LV③ Protection		HV④ Protection			
	Trip Setting	Trip Delay Time (s)	Trip Setting	Trip Delay Time (s)	Trip Setting	Trip Delay Time (s)
U/V stage 1	$V_{\phi\text{-}n}$⑤ -13%	2.5	$V_{\phi\text{-}\phi}$⑥ -13%	2.5	$V_{\phi\text{-}\phi}$⑥ -13%	2.5
U/V stage 2	$V_{\phi\text{-}n}$⑤ -20%	0.5	$V_{\phi\text{-}\phi}$⑥ -20%	0.5		
O/V stage 1	$V_{\phi\text{-}n}$⑤ +14%	1	$V_{\phi\text{-}\phi}$⑥ +10%	1	$V_{\phi\text{-}\phi}$⑥ -13%	1
O/V stage 2	$V_{\phi\text{-}n}$⑤ +19%	0.5	$V_{\phi\text{-}\phi}$⑥ +13%	0.5		
U/f stage 1	47.5Hz	20	47.5Hz	20	47.5Hz	20
U/f stage 2	47Hz	0.5	47Hz	0.5	47Hz	0.5
O/f stage 1	51.5Hz	90	51.5Hz	90	51.5Hz	0.5
O/f stage 2	52Hz	0.5	52Hz	0.5		
Loss of Mains (Vector Shift)	$K_1$⑦ x 6 degrees		$K_1$⑦ x 6 degrees		Inter-tripping expected	
Loss of Mains (Rate of Change of Frequency)	$K_2$⑧ x 0.125 Hz/s		$K_2$⑧ x 0.125 Hz/s		Inter-tripping expected	

Table 2. 3 Settings for infrequent short-term parallel operation [53]

Protection Function	Small Power Plant①			
	LV③ Protection		HV④ Protection	
	Trip Setting	Time (s)	Trip Setting	Time (s)
U/V stage 1	$V_{\phi\text{-}n}$⑤ -10%	0.5	$V_{\phi\text{-}\phi}$⑥ -6%	0.5
O/V stage 1	$V_{\phi\text{-}n}$⑤ +14%	0.5	$V_{\phi\text{-}\phi}$⑥ +6%	0.5
U/f stage 1	49.5Hz	0.5	49.5Hz	0.5
O/f stage 1	50.5Hz	0.5	50.5Hz	0.5

① **Small Power Plant:** A Power Plant which is connected to a System notionally connected to a Grid Supply Point in:

NGC's Transmission Area with a Registered Capacity of less than 50MW;

SP Transmission Limited's Transmission Area with a Registered Capacity of less than 30MW;

Scottish Hydro-Electric Transmission Limited's Transmission Area with a Registered Capacity of less than 10 MW.

② **Medium Power Plant:** A Power Plant which is connected to a System notionally connected to a Grid Supply Point in NGC's Transmission Area with a Registered Capacity of 50 MW or more but less than 100 MW.

③ **Low Voltage (LV)** A voltage normally exceeding extra low voltage (50V) but not exceeding 1000V ac or 1500V dc between conductors, or 600V ac or 900V dc between conductor and earth.

④ **High Voltage (HV)** A voltage exceeding 1000V ac or 1500V dc between conductors, or 600V ac or 900V dc between conductor and earth.

⑤ $\mathbf{V_{\phi\text{-}n}}$ is a value of 230V of the phase to neutral voltage of the LV system connection point in all cases

⑥ $\mathbf{V_{\phi\text{-}\phi}}$ is a value to suit the nominal phase to phase voltage of the HV system connection point

⑦ $\mathbf{K_1}$ = 1.0 (for low impedance networks) or 1.66 – 2.0 (for high impedance networks)

⑧ $\mathbf{K_2}$ = 1.0 (for low impedance networks) or 1.6 (for high impedance networks)

Fault-ride through

For medium and large power plants, the grid code calls for fault-ride through capability. In this case a single stage with a permitted time delay of 2.5 s and setting of -20% should be applied. Another detailed description is given by Grid Code CC6.3 in the UK: each generating unit or power park module shall be designed such that upon both clearance of the fault on the onshore transmission system and within 0.5 seconds of restoration of the voltage at the user system point to 90% of nominal or greater if embedded, active power output shall be restored to at least 90% of the level available before the fault. The diagram of the fault-ride through is shown in Figure 2.9.

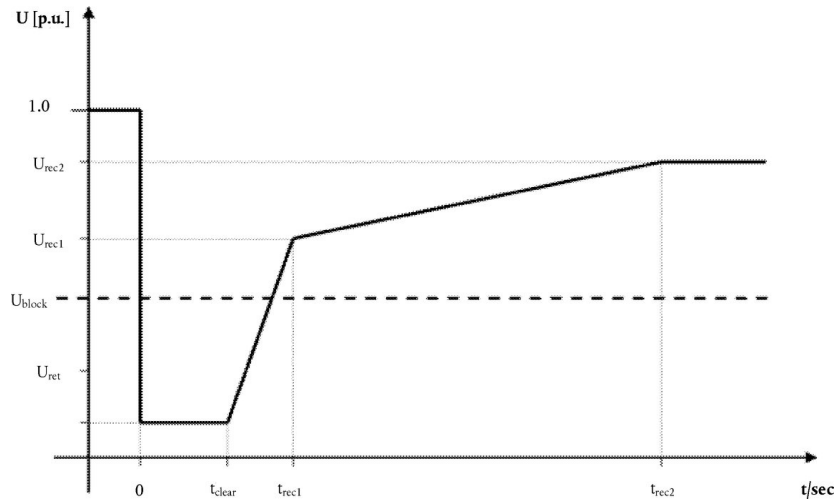

Figure 2. 9 Diagram of a fault-ride through

Short circuit current contribution

Directly Coupled Generation: the installer should provide the parameters shown in Table 2.4 of the generating units to the DNO when connecting the generating units to the distribution system. These parameters are important for DNOs in the management of the network fault level.

Table 2. 4 Short circuit parameters [53]

Parameter	Symbol
Peak short circuit current	I_p
Initial value of aperiodic current	A
Initial symmetrical short circuit current	I''_k
dc component of short circuit current	I_{dc}
Reactance/Resistance ratio of source	X/R

Inverter Connected Generation: Inverter connected generating units generally have small short circuit fault contributions. However, DNOs need to understand the contribution that they do make to system fault levels in order to determine that they can continue to safely operate without exceeding design fault levels for switchgear and other circuit components. Therefore, a test which ensures that at least 10% of nominal voltage remains and which allows the generating units to feed into a load with an X to R ratio of 2.5 is specified as details in 13.8.4.6A (A 1.4.6) of G59 for common Inverter requirements [53].

2.2 Review of Power Electronic Compensators

As aforementioned in 2.1.1.1, the voltage drop along the feeder is affected by both the active and reactive power transferred. Hence, by appropriate reactive shunt compensation, the steady-state transmittable power can be increased and the voltage profile along the line can be properly controlled [54]. Conventionally in a power system, shunt connected fixed or mechanically switched reactors and capacitors are applied to regulate the voltage profile under different conditions [55]. Theoretically, when applied reactive shunt compensation at sufficiently close intervals along the line, it is possible to transmit power up to the thermal limit of the line [56]. However, shunt compensation is ineffective in controlling the actual transmitted power, which is ultimately determined by the series line impedance and the angle between the voltages across line. Practical experience has demonstrated that by using variable series compensation, it is more effective to control power flow in the line and increase network stability [57]. With the development of power converters, flexible alternating current transmission system (FACTS) devices are becoming available in the power system. Compared to conventional passive compensators, FACTS devices, using voltage source converter (VSC), can realise network management with more flexibility through various VSC control strategies.

2.2.1 Voltage Source Converter

Voltage source converters (VSCs) convert dc voltage to ac voltage, and vice versa. The dc voltage source is required to be stiff, which is usually achieved by using large capacitors [58-60].

The simplest topology of a VSC is shown in Figure 2.10, which is a two-level ac/dc converter (with IGBT/diode modules). The power semiconductor switch in a VSC is always forward-biased due to the dc bus voltage. Therefore, self-controlled forward or asymmetric blocking switches, such as IGBT, GTO, BJT and IGCT can be used in VSC. A diode is connected across the device for reversed current flow, ensuring the four-quadrant operation of the converter. Typically, pulse width modulation techniques are used in the control of VSCs, and the most common one adopted in industrial converter is the sinusoidal PWM (SPWM), for simplicity in use [61].

A VSC can control the power flow, voltage and current at the ac side. These functions can be very useful in the network operation to:

- Regulating bus voltage and control the network power flow;
- Support critical loads during loss of mains; and
- Blocking short circuit current during fault in the network.

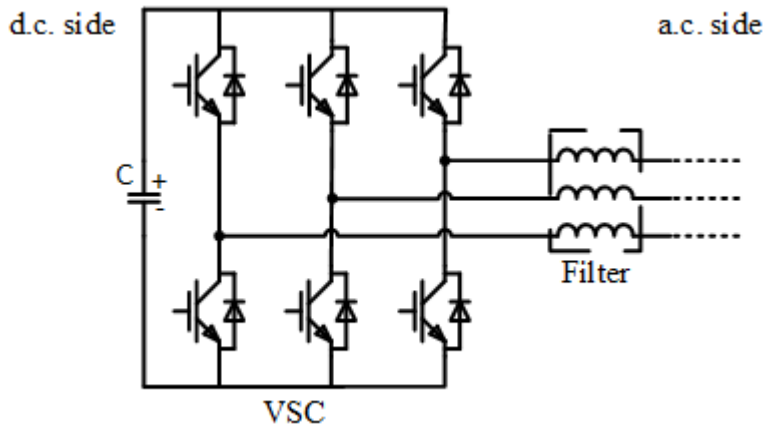

Figure 2. 10 Topology of a two-level VSC

2.2.2 Static Shunt Compensators

The static shunt compensator is connected in parallel with the power system at the primary busbar, midpoint or end of a power feeder, as shown in Figure 2.11. The commonly used technologies in the static Var compensation are: static Var compensator (SVC) and static synchronous compensator (STATCOM).

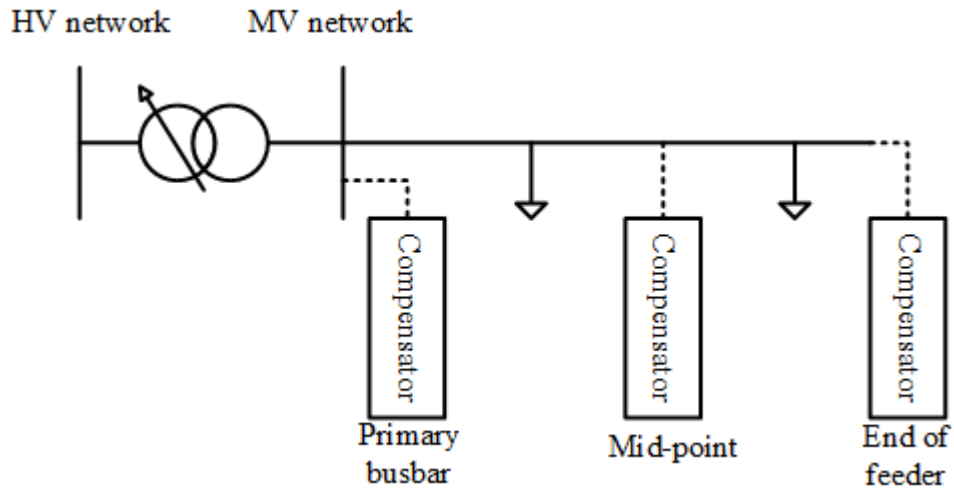

Figure 2. 11 Installation locations of shunt compensator in a power system

2.2.2.1 Static Var Compensator

The static Var compensator (SVC) includes thyristor switched capacitor (TSC) and thyristor controlled reactor (TCR). It consists of a capacitor or a reactor connected in series with a thyristor crowbar as the controlled switch. It is mainly connected in parallel to the primary busbar of a power system and use the measured grid voltage to control the thyristor switch. It's grid interface is shown in Figure 2.12 and a real product is shown in Figure 2.13. Compared to mechanical switches, power thyristors have the advantages of high reaction speed, insignificant contribution to short-circuit fault and low maintenance [54].

Depending on the power systems, applications of SVC are different. In transmission system, the SVC can [62]:

- Stabilise the voltages in weak power systems;
- Reduce power losses in transmission lines;
- Increase the transmission capacity to reduce, defer, or eliminate the need for new lines;
- Contribute to power and voltage oscillations damping; and
- Enhance voltage and stability control.

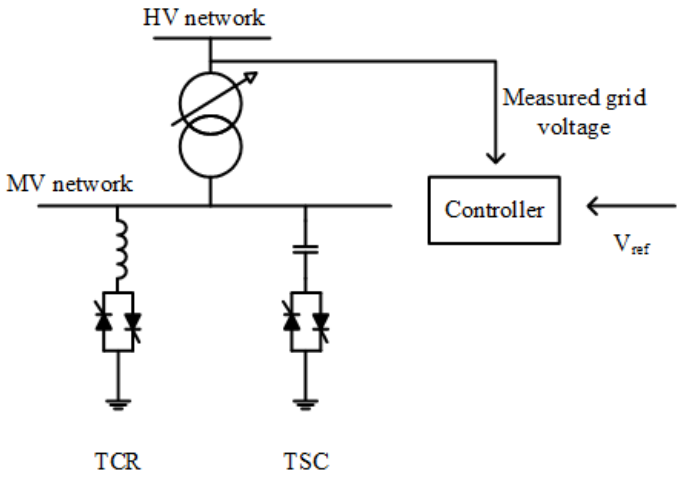

Figure 2. 12 Diagram of SVC in a power system

Figure 2. 13 Site View, Barnstable SVC [63]

And in distribution system, the of SVC can [62]:

- Stabilise the voltage at the receiving end of long distribution lines;
- Reduce the reactive power absorbed from the main grid, which leads to lower losses and improved tariffs;
- Balance the asymmetrical loads; and
- Reduce the voltage fluctuations and light flicker.

2.2.2.2 Static Synchronous Compensator

A static synchronous compensator (STATCOM) is connected in parallel to the power system though a step-up transformer. The term "synchronous" denotes that the device is equivalent to an ideal synchronous machine, which can provide compensation to the power system by producing a set of three-phase fundamental frequency sinusoidal voltages. The diagram of a STATCOM and real product by ABB are shown in Figures 2.14 and 2.15. The VSC in the STATCOM can control the magnitude, phase angle and frequency of the ac side voltage. Therefore, the STATCOM can exchange variable reactive power, at the point of compensation, with the power system according to the operation requirements [64].

Applications of STATCOM in a power system include:

- Fast voltage control and maintaining voltage levels of a busbar or an area;
- Flicker compensation;
- Improvement of the network transmission capability;
- Improvement of static and transient stability reserve; and
- System oscillation damping.

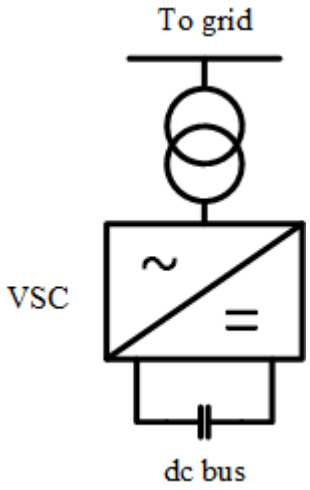

Figure 2. 14 Diagram of a STATCOM

Figure 2. 15 ABB PCS 6000 6-16MVA STACTOM [65]

2.2.3 Series Compensators

Conventional technologies for static series compensator include: gate turn-off thyristor-controlled series compensator (GCSC), thyristor-switched series capacitor (TSSC), thyristor-controlled series capacitor (TCSC) and static synchronous series compensator (SSSC). The interface of a back-to-back voltage (B2B VSC) source converter in the power system is to connect two ac lines with a dc link by two converters. If the two ac lines are of the same feeder, this is equivalent to connect the B2B VSC in series with the feeder.

The series compensator is connected in series with the power system at the mid-point of the transmission or in the interconnection between the ends of feeders, as shown in Figure 2.16. Regarding high flexibility in the compensation, only the SSSC and B2B VSC are further reviewed in the following sections. GCSC, TSSC and TCSC are shown in Figure 2.17

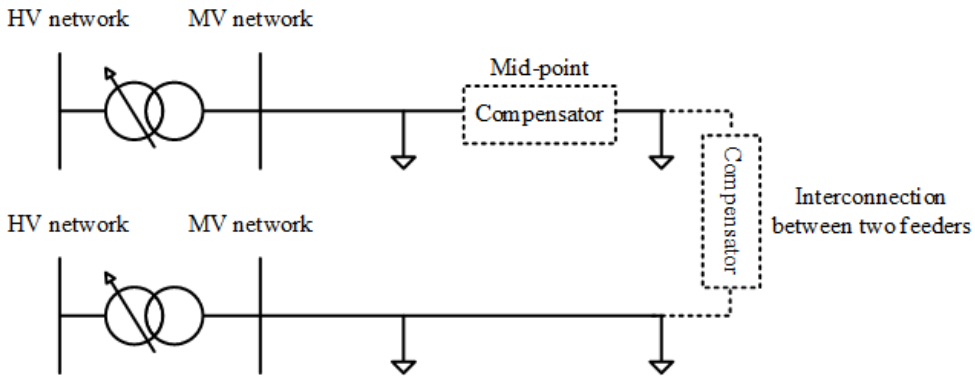

Figure 2. 16 Installation locations of series compensator in a power system

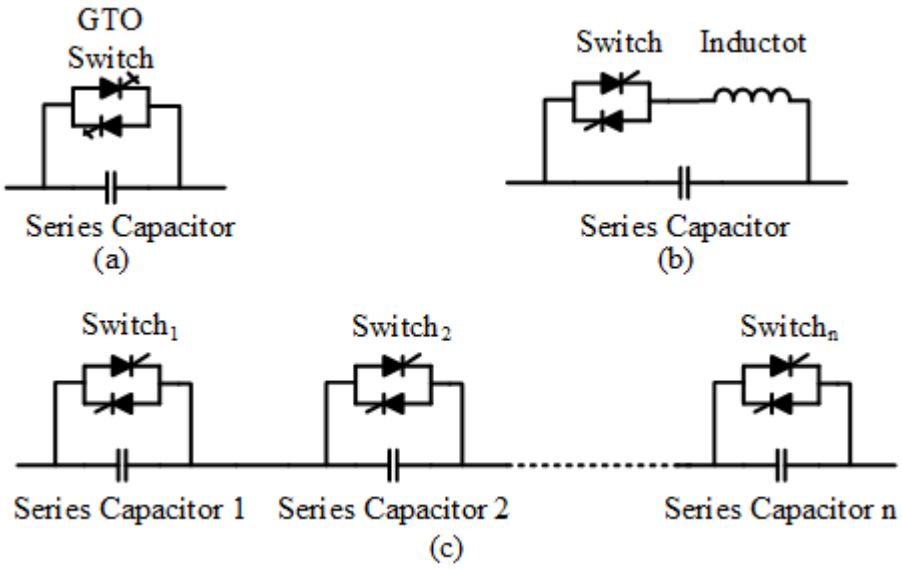

Figure 2. 17 (a) GTSC, (b) TCSC and (c) TSSC

2.2.3.1 Static Synchronous Series Compensator

A static synchronous series compensator (SSSC) is a series compensator using VSC as the synchronous voltage source [66]. Similar to the STATCOM, the VSC in the SSSC can also generate controllable voltage with desired magnitude and phase angle in the fundamental frequency. The VSC is connected in series with the ac power system through a coupling transformer, the most recent coupling technology between SSSC and ac power system can be through filters only, as in a transformerless SSSC [67]).

By exchanging power between the ac power system and the dc voltage source, both the active and reactive power flows in the ac power system can be affected, if the dc voltage source is supplied by an adequate energy source [68]. The diagram of a SSSC is shown in Figure 2.18. In addition to the STATCOM functionalities, the applications of SSSC also include: power flow control and sub-synchronous resonance mitigation [69].

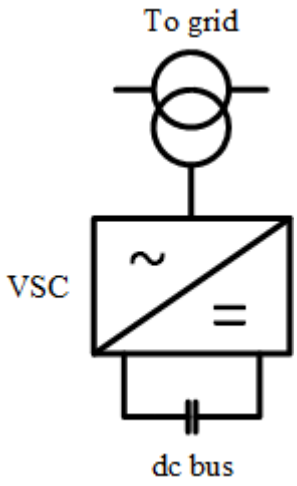

Figure 2. 18 Diagram of a SSSC

2.2.3.2 Back-to-back Voltage Source Converter

The term back-to-back (B2B), coventionally refers to 1) back-to-back converter, applied in the control of DIFIG in wind turbine [70] and 2) the structure of HVDC transmission where two ac networks are connected by two converter stations [71, 72]. In recent years, researches on the application of B2B VSC in the MV distribution network have become popular.

By connceting energy storage device to the dc bus of the B2B VSC, it can inject active and reactive power into the ac network. This makes it capable in various applications for the opeartion of distributin network. The diagram of a B2B VSC is shown in Figure 2.19.

Applications of a B2B VSC in the distribution network include [73]:

- Regulating the voltage profile of the ac network of each side independently;
- Realising the active power exchange between two distribution feeders;
- Backing up the power supply of a micro grid during loss of mains;
- Increasing the DG penetration; and
- Improving the transferred power quality.

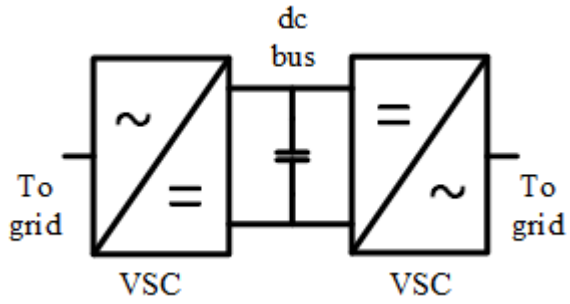

Figure 2. 19 Diagram of a B2B VSC

2.3 Review of Fault Current Limiter

Conventionally, the fault current limiting devices installed in the electrical power gird are fuse and inductor. As for other equipment in the network, high-impedance transformer can also limit the fault current. However, as the impedance of the inductor or transformer is fixed in normal operation and fault, the equipment will increase the impedance of the line and inherently limit the power transfer during normal operation. For the fuse, it requires manual replacing after fault is cleared, which will supply. For the series inductor, it impedes the quick recovery of a system from fault and increases the line X/R ratio, which will further affect the transient recovery voltage (TRV) ratings of circuit breakers [74]. Hence a device that has fast reaction to fault and can reset itself after fault with minimal impact on normal operation of is required in the protection of a power system. This defines the characteristics of a fault current limiter (FCL).

A fault current limiter, also known as fault current controller (FCC), is a device installed in the power system, which can effectively limit system fault current with limited impact on normal operation of the power system. A FCL is required to have low insertion impedance, voltage drop and power loss in normal operation. During fault, the FCL is required to have quickly transit from normal to the fault state, limiting the fault current and withstanding the fault condition for sufficient time [75]. Generally, the FCL can be divided into three types: resistive superconductor FCL [76], saturated iron core (transformer type) FCL [77]and solid-state FCL [78]. The first two types are review in detail in the following sections. The main installation positions of a FCL are shown in Figures 2.20, 2.21 and 2.22 [79].

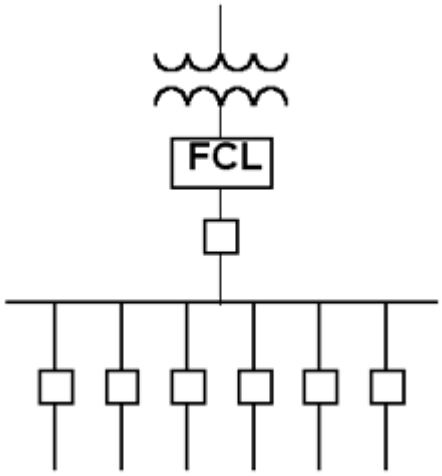

Figure 2. 20 FCL installation at the primary busbar

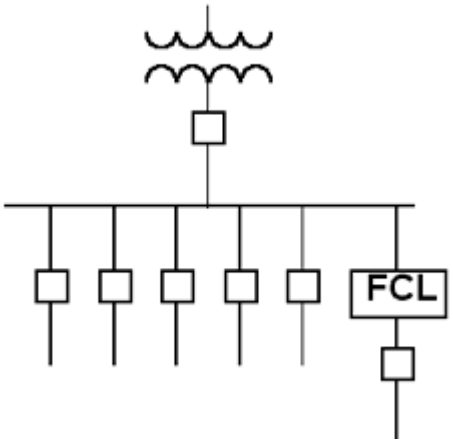

Figure 2. 21 FCL installation at the feeder

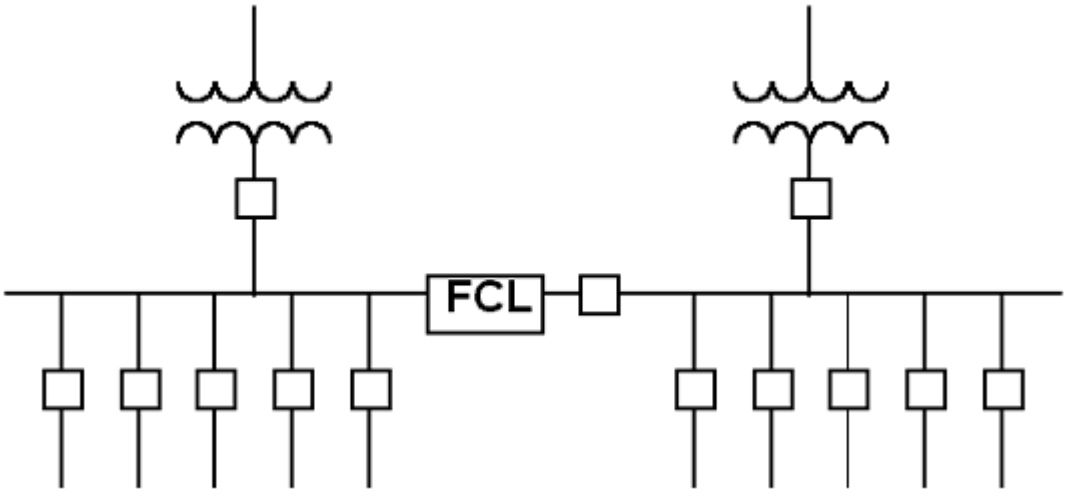

Figure 2. 22 FCL installation at the interconnection between two primary busbars

2.3.1 Resistive Superconductor Fault Current Limiter

Due to the fast development in high temperature superconductor (HTS) material in the 1980s, the HTS based FCL is being developed by researchers and engineers. The original superconductor FCL is designed to insert a piece of superconductor in series with the line. However, due to that the superconductor can generated high magnetic field with small power loss, the superconducting material is further used in the saturated iron core FLC to provide the excitation. The saturated iron core FCL using superconductor dc coils is also sometimes named as superconductor FCL. To distinguish between these two types of superconductor FCL, the superconductor FCL, which inserts the superconductor into the circuit, will be named resistive superconductor FCL (RSFCL) in this thesis.

The figure of the first commercial RSFCL in Europe is shown in Figure 2.23. In normal operation, the superconductor is in the superconducting state and has negligible inserted line resistance. In the fault condition, the superconductor quenches and is no longer superconductive and transform into a high resistance status, limiting the fault current. Due to the inserted resistance, the RSFCL reduces the X/R ratio of the power system, which will lead to less peak value and faster decay of the dc component of the fault current, as shown in Figure 2.24, where the light purple line is the prospective current and the blue line is the limited fault current.

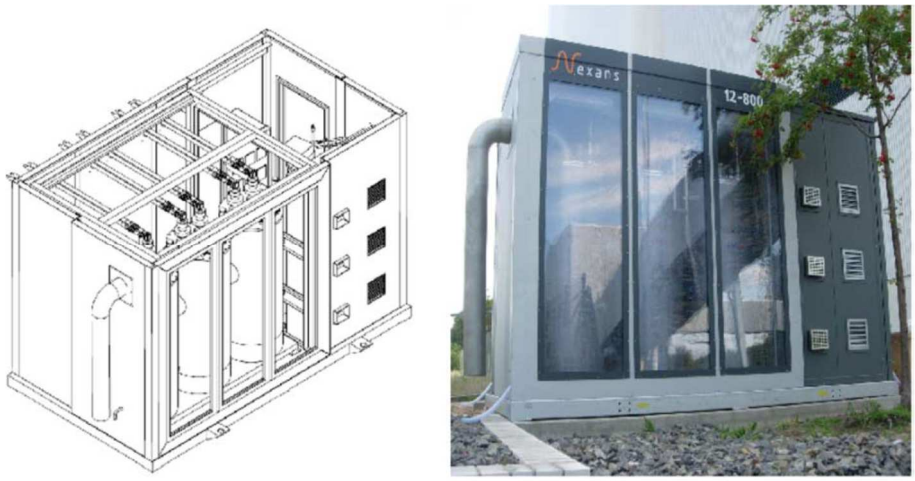

Figure 2. 23 Drawing and complete 3-phase- FLC 12-800 system after installation in Boxberg, Germany [80]

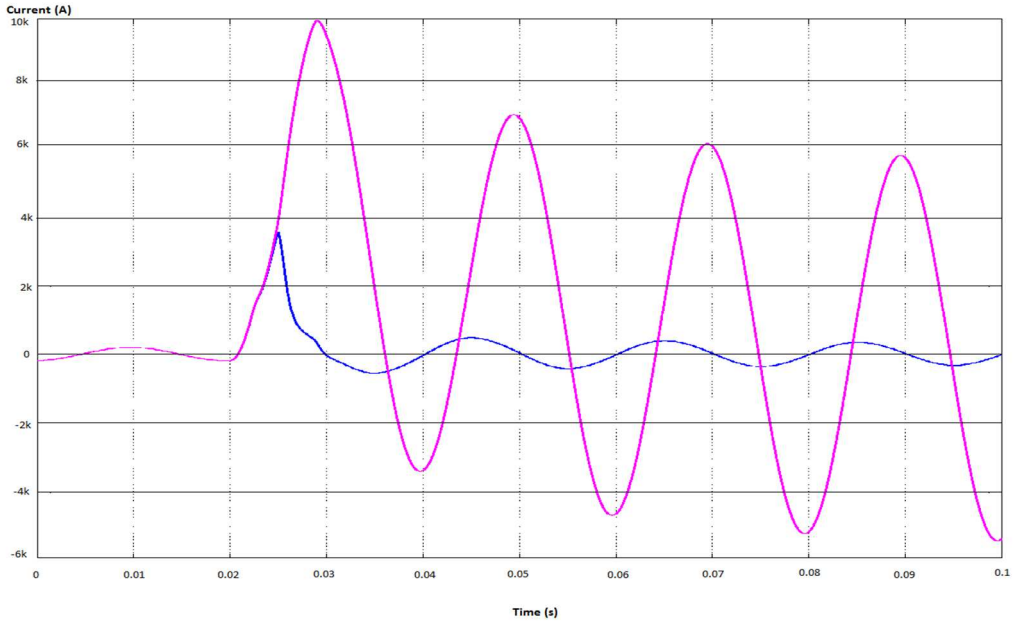

Figure 2. 24 Fault current limiting by a RSFCL [81]

2.3.2 Saturated Core Fault Current Limiter

Each phase of the saturated iron core FCL consists of two iron cores. Each has an ac coil and a dc coil. The diagram of a three-phase saturated iron core FCL is shown in Figure 2.25.

During normal operation, large excitation current in the dc coil drive the core into saturation. This lowers impedance of the ac coil near to that of an air-core coil. During a fault, a large fault current demagnetises the core and drives it from the saturated to unsaturated state (linear B-H region). This increases the primary ac coil impedance. The increased impedance limits the fault current to the desired level. This is equivalent to inject a large inductance into the line. The saturated iron core FCL will further increase the X/R ratio of the system. This leads to a reduction in the amplitude of the fault current but does not have obvious impact on the decay of the fault current, as indicated in Figure 2.25.

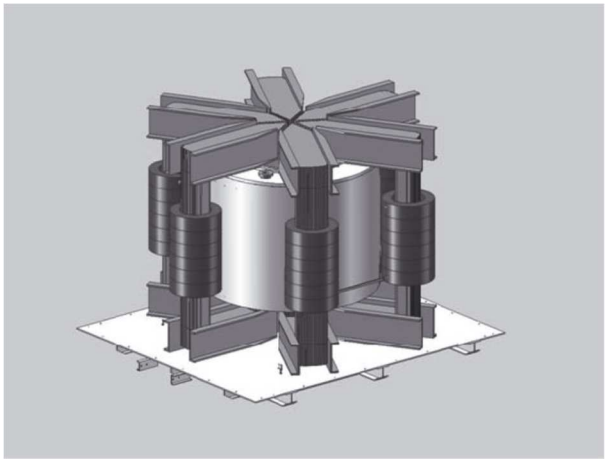

Figure 2. 25 Diagram of a three-phase FCL [82]

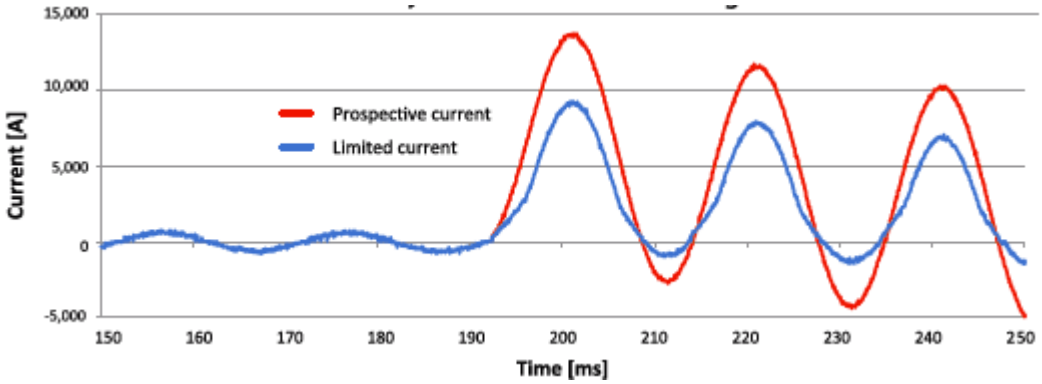

Figure 2. 26 Fault current limiting of a saturated iron-core FCL [83]

Chapter

3 Fault Current Calculation and Estimation with Dynamic Loads and Effects of DG to the Distribution Network

3.1 Fault in Power System

In the power network design, an essential part is the fault current calculation. There are various types of faults and five types are the most commonly seen in the practice, which are illustrated in Figure 3.1.

The single line to ground fault is the most common fault among these but fault analysis is frequently performed with the three-phase, balanced short circuit fault, as shown in Figure 3.1(c) and (e). This is because the three-phase fault is the most severe fault which is incidentally amenable to calculation.

The causes of faults are various and the three most common causes are lighting, gales and fog on the U.K. National Grid System (NGS) in a typical year [8]. For different components in the power network, the number affected by fault also various. According to the statistic from NGS, the most affected component is the overhead line in the UK in a typical year. In MV distribution networks with underground cables, faults per km of the circuit due to environmental or whether conditions may be fewer but can still be caused by equipment degradation, maintenance activities in substations and external intrusions. Such faults must be considered in network design and operation.

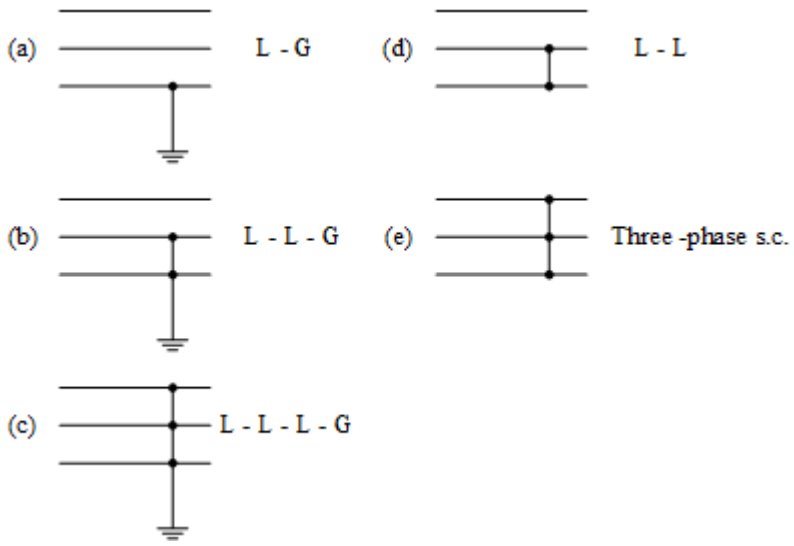

Figure 3. 1 Common types of fault

In network design and operation, the magnitude fault current for the network and power devices is frequently expressed as the fault level (FL), in a unit of MVA.

The three-phase fault level is defined as:

$$FL = \sqrt{3} V_L I_f \tag{3.1}$$

where V_L is the nominal line voltage of the network and I_f is the fault current. The fault level results from the fault analysis for a power system are mainly used to:

1) determine the maximum (make fault current) and maximum ac component (break fault current) of three-phase short circuit currents in the system;
2) determine the asymmetrical fault current for single and double line-to-earth faults, line-to-line faults, and sometimes for open-circuit faults;
3) determine the settings of protective relays;
4) determine the rated rupturing capacity of circuit breakers;
5) and determine fault-current distribution and busbar-voltage levels during fault conditions.

The typical waveform of the short circuit current far (more than 10km in an 11kV network) from the generator is given in Figure 3.2. As indicated in the figure, the short circuit current is the combination of an ac component with a decaying dc component. The dc component is caused by the inductive component in the network. I_p is the peak short circuit current and I_k'' is the initial symmetrical short circuit current. In practice, the network operators will be interested in both the make and break fault current.

The make current relates to the ability of protective devices to withstand the mechanical forced caused by the current flow. The break current relates to the ability of protective devices to interrupt the fault current.

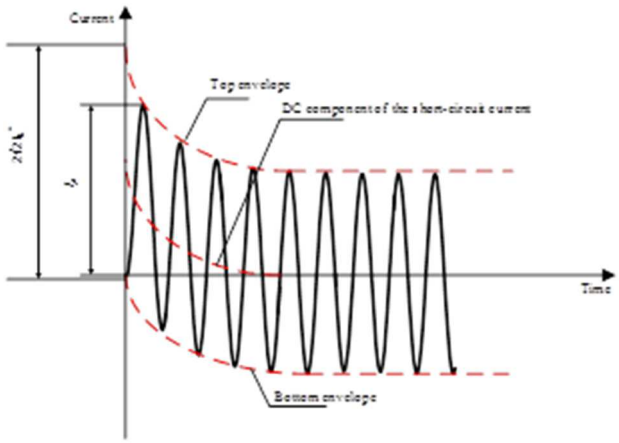

Figure 3. 2 Short circuit current far-from-generator with constant ac component

3.2 Short-circuit Current Calculation in Distribution Network

In different countries, there are many standards used for the fault analysis of power system. Two most widely used standards of short circuit current calculation in an ac system are ANSI standard and IEC standard [83].

The former one is used all over North America and accepted in some other countries. The latter one is widely accepted in most of the European countries. The IEC standard is first published in 1988 as IEC 909 [84-86]. Based on this version, the Engineering Recommendation G74 (ER G74) is developed for computer based fault analysis in 1992 [87-89]. Presently, the subsequent revisions of IEC 909 (IEC 60909) and ER G74 are the commonly applied standards for fault analysis in Europe.

In general, three types of sources can contribute short circuit current to the total fault current in a distribution network: upstream network, distributed generators and dynamic loads, as demonstrated in Figure 3.3.

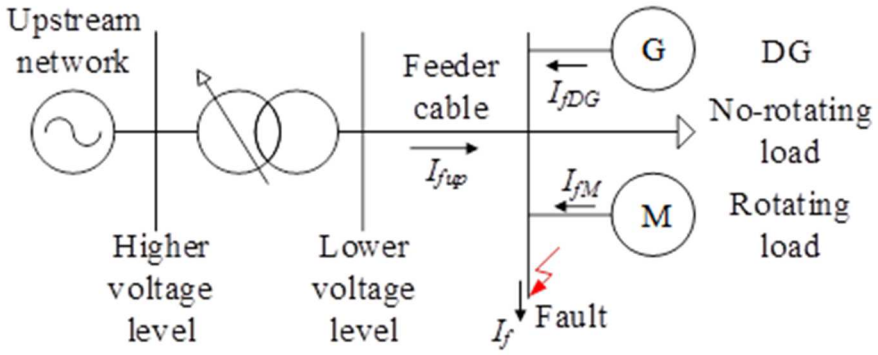

Figure 3. 3 Example of fault in a radial network

In general, the total three-phase short circuit fault current is the sum of all the partial short circuit currents contributed by all branches in a radial network that:

$$I_f = \sum_i I_{fi} \tag{3.2}$$

For instance, for the network shown in Figure 3.3, the total short circuit current is calculated as [85]:

$$I_f = I_{fup} + I_{fDG} + I_{fM} \tag{3.3}$$

This equation can be used for the calculation of the total three-phase symmetrical short circuit fault current, total make current and total break current. Before using this to calculate the total short circuit current, the short circuit currents contributed by each branch should be calculated first.

The initial symmetrical short circuit current I_k'' from a single source is calculated using:

$$I_k'' = \frac{cU_n}{\sqrt{3}Z_f} = \frac{cU_n}{\sqrt{3}\sqrt{X_f^2 + R_f^2}} \tag{3.4}$$

where U_n is the nominal phase-to-phase i.e. line voltage at the fault location and Z_f is the Thevenin equivalent impedance of the fault ($Z_f = R_f + jX_f$). The coefficient c is the voltage factor given by IEC 60909-0 in the calculation. For different sources, the value of c can be found in Table 3.1. The difference between LV and MV and HV network is because of the difference voltage tolerances in the normal operation.

Table 3. 1 Voltage factor c [85]

Nominal voltage U_n	Voltage factor c for the calculation of	
	Maximum short circuit current c_{max} 1)	Minimum short circuit current c_{min}
Low voltage 100V to 1000V	1.05 2)	0.95
	1.1 3)	
Medium voltage 1kV to 35kV	1.1	1
High voltage over 35kV		

1) $c_{max}U_n$ should not exceed the highest voltage U_m for equipment in the power system

2) For low voltage network with tolerance of +6%

3) For low voltage network with tolerance of +10%

For fault far from the generator, the Thevenin equivalent resistance and reactance of the fault are the sum of the series-connected resistances and reactances of the system, as indicated in Figure 3.4, and can be calculated from:

$$R_f = R_s + R_T + R_L \tag{3.5}$$

$$X_f = X_s + X_T + X_L \tag{3.6}$$

where R_s, R_T, R_L, X_s, X_T and X_L are the Thevenin equivalent resistances and reactances of the source, transformer and line.

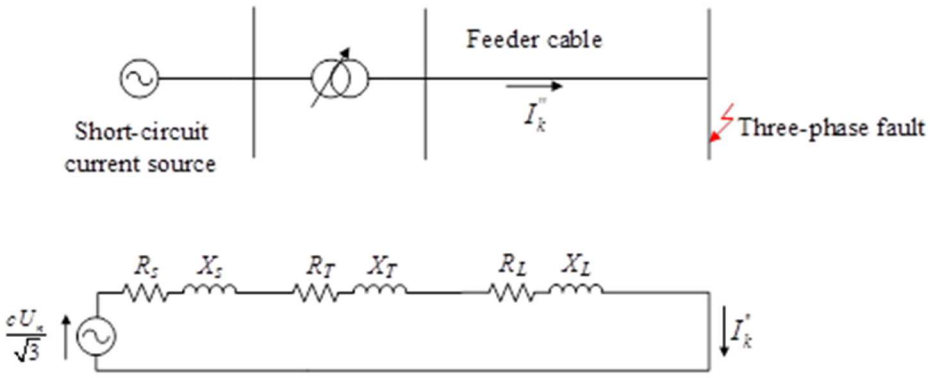

Figure 3. 4 Fault fed from a single source and the equivalent circuit

For each branch, the peak short circuit current contribution of the equivalent source can be calculated using:

$$i_p = \kappa\sqrt{2}I_k'' \tag{3.7}$$

The factor κ is a factor related to the *X/R* ratio of the equivalent circuit to reflect the decay of the dcdc component and can be obtained using the equation:

$$\kappa = 1.02 + 0.98e^{-3R/X} \tag{3.8}$$

Equations (3.7) and (3.8) are used for calculating the maximum value of the peak short-current. This presumes that the fault occurs at zero-crossing of the source voltage, in which the dcdc component contributed by the inductive element in the network will be the maximum. The peak short circuit current is reached approximately after one half-cycle (10ms) as indicated in Figure 3.2.

The total peak short circuit current at the fault location is the sum of the partial short-circuit current from different sources:

$$i_p = \sum_i i_{pi} \tag{3.9}$$

The initial dc component of the short circuit current recommended by IEC 60909 is expressed as:

$$i_{dc} = \sqrt{2} I_k'' e^{-2\pi f t R/X} \tag{3.10}$$

where f is the nominal frequency and t is the time. The break current at the fault location in general consists of a symmetrical current I_b and a dc current at the time t, calculated using Equation (3.11), that:

$$I_{break} = I_b + i_{dc} \tag{3.11}$$

For fault location far from generator, the symmetrical current I_b is equal to the initial three-phase symmetrical current I_k''.

3.3 Short Circuit Current Calculation and Fault Level Estimation of Dynamic loads in Distribution Network

3.3.1 Short circuit Current Calculation of Dynamic Load in Distribution Network

If the detailed composition of the load in distribution network is acknowledged by the DNO, the make and break short circuit currents contributed by downstream distribution dynamic load can be calculated using methods provided in IEC 60909-0. However, in practice, the detailed information of the load composition is not always available. In this situation, a normalised short circuit current contribution for general load is commonly recommended in standards and adopted by DNOs in the network analysis. According to ER G74, the normalised short circuit current contributions for three phase symmetrical short circuit current of general loads connected at different voltages levels are:

1) 1MVA/MVA for loads connected to the low voltage (e.g.400V) busbars and
2) 2.6MVA/MVA for loads connected to the high voltage busbars (e.g. 11kV),

when a fault occurs in 33kV network [87]. This difference because the Thevenin equivalent impedance of high voltage network is always smaller than that of low voltage network. The value 1MVA/MVA is currently adopted by DNOs in fault analysis in their operation of the 11kV distribution network with loads connected on 400V side. However, due to the difference between the equivalent impedances of step-down transformer used in 11kV and 33kV network, it will cause the calculated short circuit current contributed by general load to be smaller when applying this 1MVA/MVA short circuit current contribution in the 11kV network. This is because for the same transformer capacity, the equivalent impedance of the 33kV/400V transformer is generally larger than that of an 11kV/400V transformer due to larger capacity. On the other hand, when the detailed information of the load is available, more accurate fault analysis can be conducted using the method provided by IEC 60909. When using the IEC 60909 to calculate the short circuit current of a dynamic load formed by induction machines, the calculation result correlates with the experiment result for large scale induction machine (rated power ≥50kW) [90]. But the calculation result is conservative when the rated power of the induction machine is less than 50kW. Due to the increasing penetration level of distributed generation, the total short circuit current or fault level contributed by downstream network to the primary 11kV busbar during a three-phase fault is increasingly significant in the recent two decades. The fault level at primary 11kV busbar is approaching the ratings of circuit breakers installed in the 11kV distribution network. To obtain more accurate short circuit current contribution becomes necessary for DNOs to monitor the network fault level and make corresponding decisions in network management.

In the distribution network, the general load can be classified into three types: industrial, commercial and residential loads. Large scale three phase induction motors are commonly used in industrial and commercial applications. Short circuit current calculation using IEC 60909 for industrial and most commercial loads is of adequate accuracy [91]. For some commercial and residential loads, the commonly used electrical machines are small scale (rated power <15kW) single phase electrical machines. The single-phase induction machines are generally divided into single phase induction motor and universal motors.

3.3.1.1 Model of single-phase induction motor

An excited single-phase winding does not naturally produce a rotating magnetic field. Instead, the produced field remains stationary in position and pulsates with time in amplitude. In order to produce a rotating magnetic field, special arrangements are often made in the design of single phase induction machine. Corresponding to the design to cause a net rotating magnetic field effect, single phase induction motors are classified in four types [92]:

- Split-phase winding motor, mainly used in applications which do not require high starting torque, such as fans, blowers and centrifugal pumps;
- Capacitor-start motor, mainly used in applications requiring high starting torque, such as compressors;

- Capacitor-run (permeant split-capacitor) motor, used in similar applications as the capacitor-start motor; and
- Shaded-pole motor, commonly used in small instruments, hair dryers, electrical clocks and etc. the rated power of this type of motor is below 50W and they are not regarded as a source of grid short circuit current because of the small power rating.

In the split-phase induction motor, the rotating magnetic field is produced by the out-of-phase currents in the main and auxiliary windings, as shown in Figure 3.5. The main winding is designed more inductive and less resistive than the auxiliary winding, in order to make the current in the main winding be more out of phase with respect to the supplied voltage. The phase angle difference between the currents in the two windings is usually 35° and 40°. This is enough to produce a net rotating field effect and starting torque. Once the motor reaches about 75% of its rated speed, the auxiliary winding is disconnected from the circuit and the motor continues to operate on the main winding which causes equivalently two rotating magnetic field components but the one in the same direction as the rotor rotation will induce more torque, hence a net driving torque.

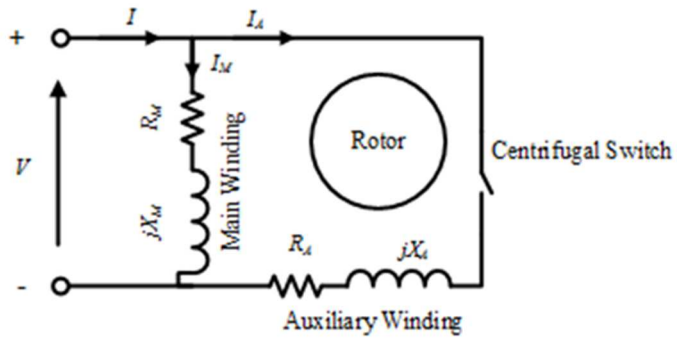

Figure 3. 5 Split-phase winding induction motor

In the capacitor-start induction motor, a capacitor is connected in series with the auxiliary winding, as shown in Figure 3.6. This increase the phase difference between the winding currents in the main and auxiliary windings. With proper selection of capacitor, the phase difference between winding the currents can be 90°, yielding a uniform rotating magnetic field. The operating principle of a capacitor-run motor is the same with the capacitor-start motor, the only difference being that there is no switch to disconnect the auxiliary winding. The design is more efficient and has a higher power factor and smoother torque. To balance the current in both windings in normal operation, the capacitor should be sized carefully.

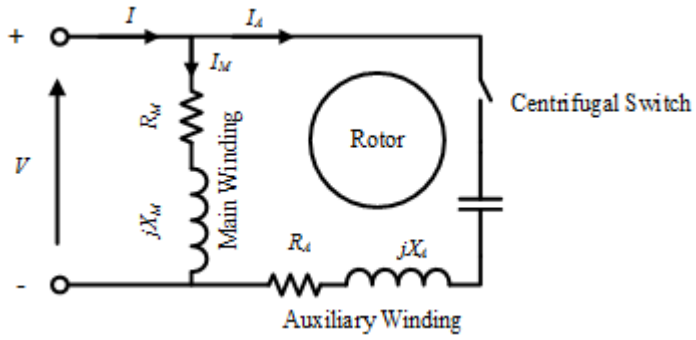

Figure 3. 6 Capacitor-start induction motor

For both split-phase and capacitor-start (run) induction motor, the short circuit behaviour depends on the main winding because the auxiliary winding is switched out when the motor speed is over 75% of the rated speed. The single pulsating magnetising field in the single-phase induction machine generated by only one phase of ac supply can be expressed in two revolving fields in opposite direction. The magnitude of the two fields is half of the original pulsating field. Thus, the analysis of a single-phase induction motor is similar to one phase of a three-phase induction motor. The equivalent circuit of a single-phase induction motor and the torque-speed curve are given in Figures 3.7 and 3.8 [93],

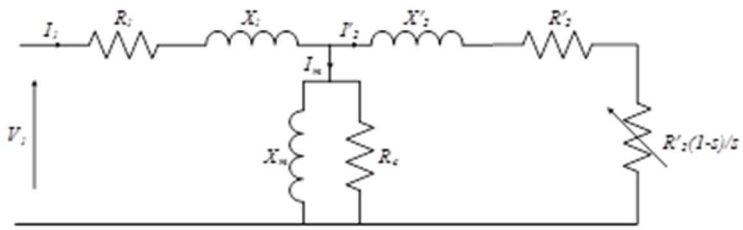

Figure 3. 7 Per phase equivalent circuit of induction motor

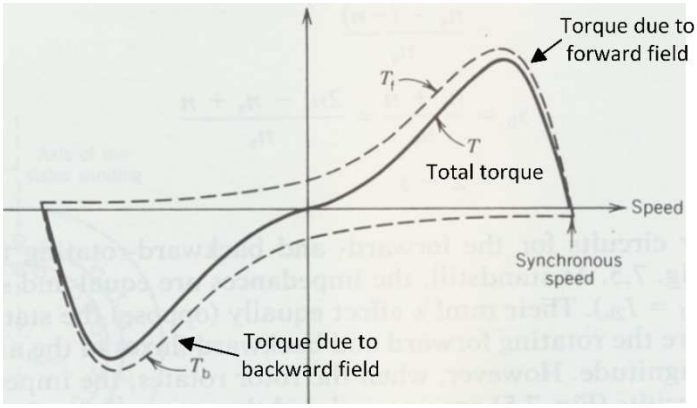

Figure 3. 8 Torque associated with two revolving fields and output torque of single-phase induction machine [94]

where R_1 and R_2' are the stator and rotor winding resistance (per phase) respectively, X_1 and X_2' are the stator and rotor winding leakage reactance (per phase) respectively, R_c is the core loss resistance (per phase) and X_m is the magnetizing reactance (per phase). $R_2'(1-s)/s$ represents the mechanical power and s is the rotor slip. All parameters are referred to the stator winding side. In IEC 60909, the initial symmetrical short circuit current I_k'' of an induction motor is calculated by [85]:

$$I_k'' = \frac{V_1}{X_{k1}''} \tag{3.12}$$

$$X_{k1}'' = X_1 + X_2' \tag{3.13}$$

where X_{k1}'' is the initial positive sequence reactance.

For large induction motor, $X_m >> X_2'$ and the winding X/R ratio is very large. Hence X_m and winding resistances (R_1 and R_2') can be ignored. However, when the capacity of induction machine is scaled down, some assumptions made for large induction machines are no longer valid [95]:

1) The X/R ratio of stator and rotor windings is smaller comparing to large scale induction machines that the stator and rotor winding resistance R_1 and R_2' cannot be ignored in short circuit current calculation for small scale single-phase induction machines;
2) For large induction machines, the pre-fault load current is neglected in the calculation. This is reasonable because for large scale induction machines, the peak value of the short circuit current is around 10 to 20 times of the rated RMS value. For small scale motors used in domestic appliances, the peak short circuit current is 2 to 5 times of the rated current. It is then necessary to consider the pre-fault load current in short circuit current calculation.

3) τ_{ac} increases with time. The actual decay of the ac component is slower than the calculated value based on constant ac time constants given by IEC 60909:

$$\tau_{a.c.} = \frac{X'}{\omega R_2^{'}} \tag{3.14}$$

this is because the reactance corresponding to the elapsed time (t) after the fault is determined from [ER G74]:

$$\frac{1}{X^{'}(t)} = \frac{1}{X^{'}} e^{-\frac{t}{\tau_{a.c.}(t)}} \tag{3.15}$$

, which increases with time. Hence, the ac time constant calculated from this increasing reactance:

$$\tau_{a.c.}(t) = \frac{X^{''}(t)}{\omega R_2^{'}} \tag{3.16}$$

is also increasing with time. The phenomenon is more obvious for small scale motors due to short time constants. Furthermore, the decreasing speed of the rotor affects the peak value of short circuit current which will reduce the frequency of the ac component.

Based on the above considerations, some adjustments to the short circuit calculation method for small scale induction motor are given:

1) The calculation of initial symmetrical short circuit current in RMS value for small scale induction machines is adjusted by:

$$I_k^{"} = \frac{V_1}{Z^{'}} \tag{3.17}$$

where Z is the transient impedance (per phase) of the small-scale induction machine and calculated by:

$$Z^{'} = \sqrt{R^{'2} + X^{'2}} \tag{3.18}$$

$$R^{'} = R_1 + R_2^{'} \tag{3.19}$$

$$X^{'} = X_1 + X_2^{'} \tag{3.20}$$

all parameters are referred to the stator winding side.

2) The adjusted ac time constant is obtained by doubling the value calculated by Equation (3.14) to represent the slower decay of the ac component in the short circuit current, that:

$$\tau_{a.c.}^{'} = 2\tau_{a.c.} \tag{3.21}$$

3) The upper envelope of the asymmetrical short circuit current contributed by the machine at any elapsed time t after the fault is adjusted from:

$$I_{sc}(t) = I_{a.c.}(t) + I_{d.c.}(t) = \sqrt{2}I_k^{"} e^{-\frac{t}{\tau_{a.c.}}} + \sqrt{2}I_k^{"} e^{-\frac{t}{\tau_{d.c.}}} \quad (3.22)$$

to:

$$I_{sc}(t) = I_{a.c.}(t) + I_{d.c.}(t) = \sqrt{2}I_k^{"} e^{-\frac{t}{\tau'_{a.c.}}} + (\sqrt{2}I_k^{"} + I_r) e^{-\frac{t}{\tau_{d.c.}}} \quad (3.23)$$

where I_r is the peak rated current of small scale induction machines in normal operation and $\tau'_{a.c.}$ is the adjusted ac time constant from Equation (3.21). The make short circuit current for small scale induction machines can be estimated by:

$$I_p = 1.1\sqrt{2}I_k^{"} \quad (3.24)$$

3.3.1.2 Simulation and experiment results of the improved model of single-phase induction motor

Short circuit experiments on four fridges/freezers and one washing machine were carried out to verify the adjustments in calculating short circuit current for single phase induction machine in the previous section.

The parameters of these single-phase induction machines are listed in Table 3.2. The test equivalent circuit diagram is given in Figure 3.9. Short circuit current calculations using the adjusted equations were conducted for four the different types of small scale single-phase induction motors. The calculation results were compared with the results from dynamic simulations and experiments. As shown in Table 3.3, I_p is the calculated peak short circuit current using Equation (3.7), I'_p is the peak short circuit current observed in simulation, I''_p is the peak short circuit current measured in the experiment and ΔI is the difference between simulation results and calculation results and between experimental results and calculation results in percentage respectively. The experiment results are given in Figure 3.10. the experiment instruments are given in Appendix V.

According to Table 3.3, the calculated results using the adjusted equations match the simulation results. The differences between the calculated results and the experiment results are within -6.2% and 3.5%. Considering the short circuit current of a single-phase induction machine is relatively small (peak short circuit current is less than 10A, according to Table 3.3), this difference from -6.2% to 3.5% is acceptable.

Table 3. 2 Parameters of four single-phase induction motors

Product Model	GL90AA	GL60TB	TLS5F	TL4G
V_n (V)	220	220	220	220
S_n (W)	184	147	125	110
Frequency (Hz)	50	50	50	50
I_r (A)	2.8	1.45	1.2	1.4
R_1 (p.u.)	0.078	0.13	0.09	0.11
X_1 (p.u.)	0.078	0.16	0.13	0.16
R_2' (p.u.)	0.078	0.14	0.07	0.09
X_2' (p.u.)	0.078	0.12	0.03	0.04
X_m (p.u.)	2.12	2	2.1	2.12

Table 3. 3 Results of the short circuit current calculation for four single-phase induction motors

Product Model	GL90AA		GL60TB		TLS5F		TL4G	
$\tau_{a.c.}$ (ms)	6.4		6.4		7.3		7	
$\tau'_{a.c.}$ (ms)	12.8		12.8		14.6		14	
τ_{dc} (ms)	6.4		7.4		9.2		5.8	
I''_k (A)	4.53		2.62		4.42		3.54	
I_{dc} at 7ms (A)	2.62		1.99		3.58		1.92	
$I_{a.c.}$ at 7ms (A)	3.71		2.14		3.87		3.03	
I_p (A)	6.33	ΔI	4.13	ΔI	7.45	ΔI	4.95	ΔI
$I'p$ (A)	6.39	-0.94%	4.1	3.25%	7.4	0.68 %	4.8	3.13%
$I''p$ (A)	6.36 at 7ms	-0.47%	4.4 at 8ms	-6.14%	7.2 at 7.5ms	3.47 %	5 at 7.6ms	-1.00%

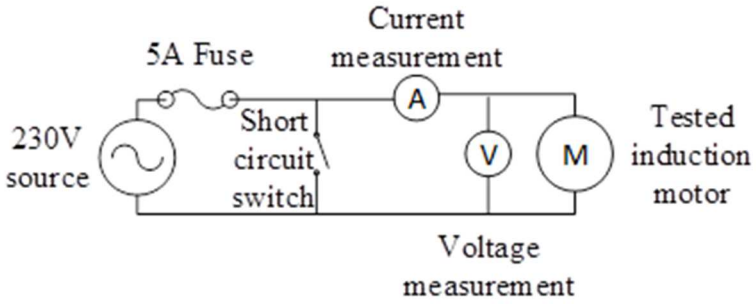

Figure 3. 9 Circuit diagram of the short circuit test equipment

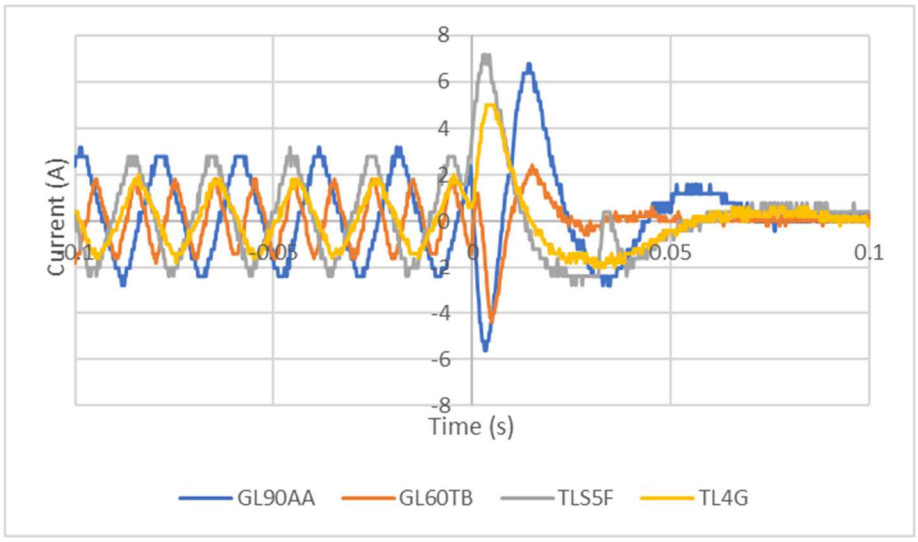

Figure 3. 10 Short circuit experiment results of four tested single-phase induction motors

3.3.2 Effects of Transformer Impedance and Cable Impedance to the Load Fault Current Contribution in Distribution Network

When fault occurs in the network, the total fault current is the summation of all fault currents contributed by different source. These distributed sources include embedded generators and dynamic loads in the distribution network. According to ER G74, parameters should be measured in order to apply the calculation method in the fault current estimation for general loads if dynamic load is part of the total load. However, measurements from load side are commonly not available for DNOs in the normal distribution network operations. Considering this situation, ER G74 provides recommendations for fault current contribution of general loads under peak winter demand in the UK when measurements are not available. The recommendation suggests the initial symmetrical three phase fault current contribution at 33kV busbar is given in the previous section. This is also known as the fault current contribution of general load and is defined as:

$$Fault\,Current\,Contribution = \frac{Fault\ Current\ by\ Load \times Nominal\ Load\ Voltage}{Load\ Power}$$

However, ER G74 does not provide recommendations for calculations of load fault current when fault occurs at an 11kV busbar.

Using the recommendation directly in the case when fault occurs on the 11kV busbar will cause the fault calculation result to be too small. This is because the effects of transformer impedance on fault current of dynamic load are larger in the 33kV network than in the 11kV network. Therefore, simulations are conducted to study the fault current contribution of different types of loads when fault occurs on the 11kV busbar. Meanwhile, the effect of 11kV/400V load transformer on the load fault current is also analysed in the simulations.

In the studies regarding loads, electrical loads are commonly classified into three types: domestic, commercial and industrial loads. In this study, the industrial load is further divided into large (75% of total load is dynamic) and small (35% load of total load is dynamic) industrial loads. The modelling of each type of loads is based on their load composition and load behaviour during fault. All load models are the combinations of dynamic and static loads. The load powers of dynamic and static loads in each type of loads are determined by the load composition and total load power. The dynamic load is modelled as induction motor and static load is modelled as constant impedance load [96-99]. Due to the proportions of dynamic loads are different in different types of loads, the modelling of dynamic loads for each type of loads is adjusted accordingly. Domestic appliance is predominantly supplied by single phase electrical sources, so the dynamic load in domestic load is modelled using solely single-phase induction motors. For electrical utilisations in commercial load, both single phase (for instance freezers, refrigerators etc.) and three phase (for instance central air conditioner, pumps etc.) electrical machines are used.

Hence the dynamic load model in commercial load is the combination of single phase and three phase induction motors. Considering that the small electrical appliances used in domestic and commercial customers are similar, the same-single phase induction motor models are used in both cases. In industrial load modelling, the dynamic load is modelled using solely three phase induction motor models. For each type of the loads, all dynamic loads of the same type are aggregated into one equivalent induction motor and the same for the static loads as indicated in Figure 3.11. The typical load compositions of dynamic and static loads for each types of customer loads are given in Table 3.4 [100, 101]. For each type, the effect of transformer impedance on load fault current contribution is studied by simulations of different cases. In these cases, the load powers are varied from 0.1% to 100% of the fixed transformer capacity. These various ratios of load power to load transformer capacity is the load factor of certain load. Both make and break fault current contributions of each type of load are studied. The same induction machines in Table 3.2 are used in the modelling. The parameters of induction machine and transformer used in the simulations are given in Table 3.5.

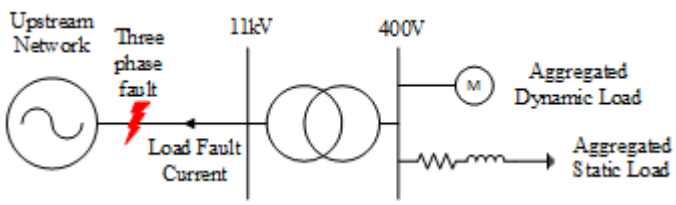

Figure 3. 11 Indicative simulation model

Table 3. 4 Typical compositions of domestic, commercial and industrial loads

Load Type	Load Composition (%)		
	Static Load	Single-phase Dynamic Load	Three-phase Dynamic Load
Domestic	62%	38%	0%
Commercial	43%	18%	39%
Industrial	37%	0%	63%

Table 3. 5 Parameters of transformer and induction machines in the model

Parameters	Transformer	Parameters	Single Phase	Three Phase Induction Machine	
			Induction Machine	Commercial Load	Industrial Load
S_n	10MVA	P_n	184W	37kW	110kW
V_1	11kV RMS ph-ph	V_n	220V RMS ph-n	400V RMS ph-ph	400V RMS ph-ph
V_2	400V RMS ph-ph	R_s	0.078 p.u.	0.01904 p.u.	0.01481 p.u.
R_1	0.001 p.u.	X_s	0.078 p.u.	0.0526 p.u.	0.04881 p.u.
X_1	0.05 p.u.	R_r'	0.078 p.u.	0.01163 p.u.	0.008464 p.u.
R_2	0.001 p.u.	X_r'	0.078 p.u.	0.0526 p.u.	0.04881 p.u.
X_2	0.05 p.u.	X_m	2.12 p.u.	1.97 p.u.	2.241 p.u.
R_m	500 p.u.				
X_m	500 p.u.				

3.3.2.1 Effects of transformer impedance

Figure 3.12 shows the load fault current contribution with the 11kV/400V transformer impedance included, of different types of fault with increasing load factor (the load factor is the ratio of load power to the rated transformer power).

It is generally believed that transformer impedance is relatively small compared to internal impedance of dynamic load. However, from the result given in Figure 3.12, it indicates that with the increase of load factor, the effect of transformer impedance to load fault current becomes more significant in reducing the MVA/MVA fault current contribution of load.

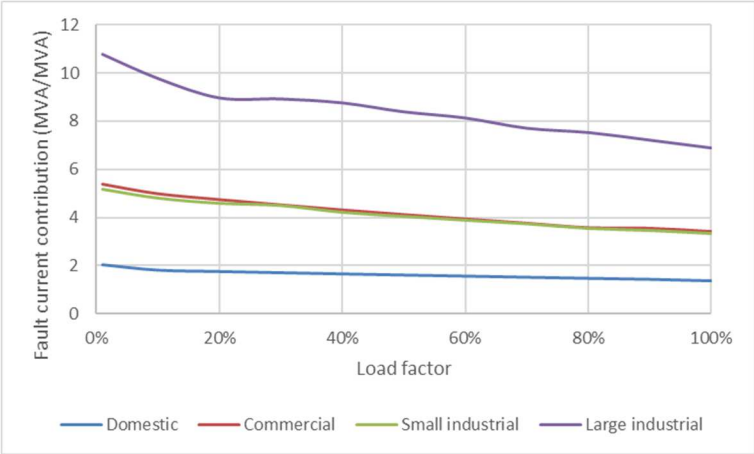

(a)

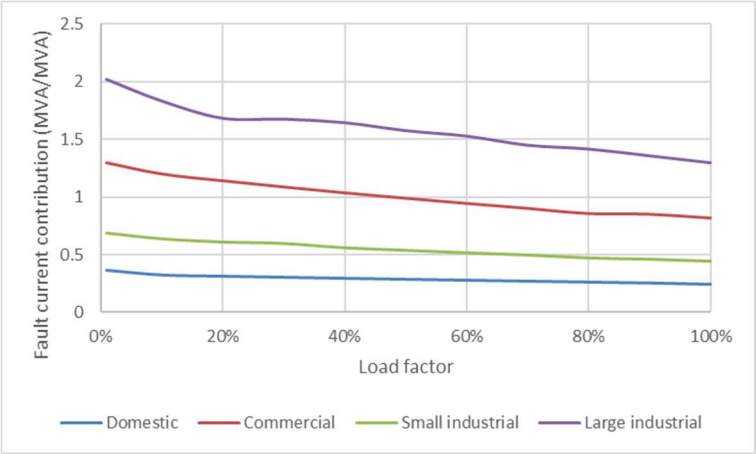

(b)

Figure 3. 12 Impact of transformer impedance on (a) make and (b) break fault current contributions by loads

In Figure 3.12, the make and break fault current contributions demonstrate similar linear manners among all four types of loads when load factor increases. As previously defined, the fault current contribution by load is:

$$FCC_L = \frac{I_{fL} \times V_n}{S_L} = \frac{V_n}{(Z_T + Z_L)} \times \frac{V_n}{S_L} \tag{3.25}$$

where I_{fL} is the fault current by the load, V_n is the nominal load voltage and S_L is the load power. Z_T and Z_L are the equivalent impedances of the transformer and load. For the load power, it can be derived from:

$$S_L = \frac{V_n^2}{Z_L} \tag{3.26}$$

and substituting Equations (3.26) into (3.25) it can be obtained that:

$$FCC_L = \frac{V_n}{(Z_T + Z_L)} \times \frac{V_n}{\frac{V_n^2}{Z_L}} = \frac{1}{\frac{Z_T}{Z_L} + 1} \tag{3.27}$$

When load power is low compared to the transformer rating, the equivalent impedance of load is relatively large compared to the transformer impedance. As the load power increases, the equivalent load impedance is decreasing. As shown in Equation (3.27), it is obviously that when the load impedance decreases, the fault current contribution by load will decrease with fixed transformer impedance. This effect of transformer impedance will be more obviously in the normalised fault current contribution.

The normalised results are obtained by normalising the fault current contributions to the value when load factor is 0.1% (since when load factor is 0%, there will be no fault current), given in Table 3.6. The results are shown in Figure 3.13 for both make and break fault current contribution.

Table 3. 6 Reference fault current contribution

Fault Current	Fault Current Contribution (MVA/MVA)			
	Domestic	Commercial	Small Industrial	Large Industrial
Make	2.03	5.4	5.16	10.78
Break	0.37	1.3	0.69	2.02

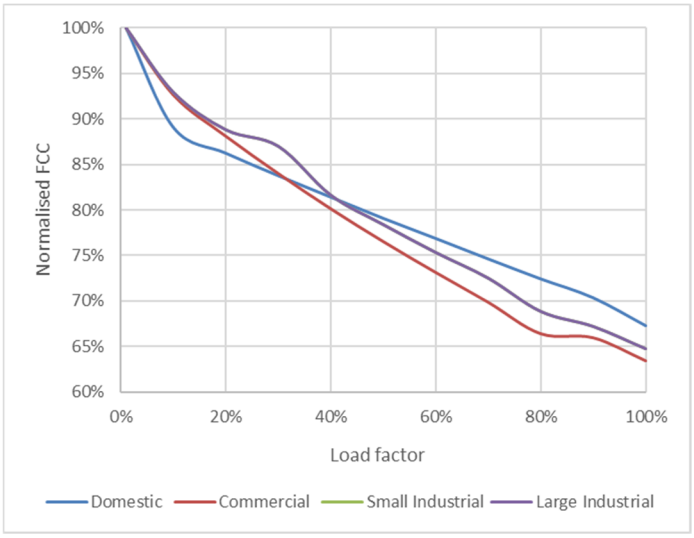

Figure 3. 13 Normalised fault current contribution of load

A linear function can be extracted from linear fitting to represent transformer impedance effects on load fault current contribution for each types of loads:

$$FCC'_{Lk} = A_k \bullet lf_k + B_k \tag{3.28}$$

where FCC_L' is the normalised load fault current contribution, lf is the load power, A and B are the fitting coefficients and k indicates the load type. The fitting coefficients for each type of loads are given in Table 3.7.

Table 3. 7 Fitting coefficients for different types of loads

k	*A*	*B*
Domestic	-0.2756	0.9394
Commercial	-0.3411	0.9689
Small industrial	-0.3562	0.9602
Large industrial	-0.3125	0.9422

3.3.2.2 Effects of Cable Impedance

The effect of cable impedance between the load transformer and load is analysed in this section. For commercial and industrial loads, the power transformer is commonly installed at the site of the load, the length cable between the load and transformer is negligible. Hence the load type analysed in this section focuses on domestic load using the same model in section 3.3.2.1. Some parameters of different types of cables are listed in Table 3.8.

Table 3. 8 Cable parameters

Conductor Cross Sectional Area (mm^2)	Current Carrying Capability RMS (A)		Impedance at 50Hz (Ω/km)	
	Core Material		Core Material	
	Cu	Al	Cu	Al
10	48	34	2.190 + j0.55	3.3 + j0.55
35	95	75	0.628 + j0.18	1.04 + j0.18
70	145	110	0.322 + j0.107	0.533 + j0.107
120	195	150	0.185 + j0.103	0.305 + j0.103
240	290	225	0.084 + j0.08	0.151 + j0.08

The fault location is set at location on the 400V side of the transformer. The impedance of the cable between the fault and the dynamic load depends on the material, size and length of the cables. To analyse the effect, a Matlab/SIMULINK simulation case study is conducted. Figure 3.14 shows the network model.

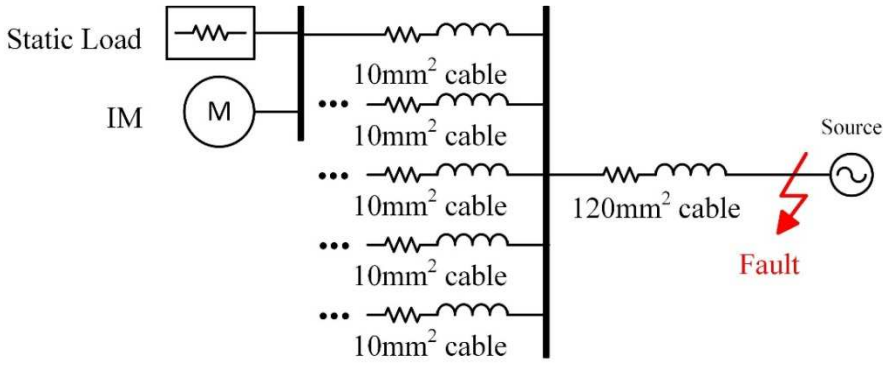

Figure 3. 14 Circuit diagram for simulation

The source voltage is 400V RMS, representing the 400V side of the transformer. The total load is 33.3kVA and further divided into 5 groups. To represent the network of a residential area, each group is fed through a 10mm^2 copper cable with a length increasing from 100m to 200m. All the five groups are connected to the source through a 200m, 120mm^2 copper cable. The initial symmetrical fault current I_k'' is calculated for different cable lengths. The simulation results are given in Table 3.9. all currents are compared to the value without cable.

The results indicate for the cable length up to 200m, the reduction in the fault current is 3.79% maximum. Comparing to the effect of transformer impedance analysed in the previous section, the effect of cable length to the fault current contributed by domestic load is relatively week (no more than 4% reduction). Hence the cable impedance can be negligible in the modelling of load in the network fault analysis.

Table 3. 9 Short circuit current with distribution cable

Cable length	I_k" (kA)	Reduction of I_k" due to cable
0m	0.66	0.00%
100m	0.643	2.58%
150m	0.64	3.03%
200m	0.635	3.79%

3.3.3 Estimation of Fault Level of General Load

3.3.3.1 Methods of the Calculation of Fault Level Contribution and Estimation of Fault Level for General Loads

In a distribution network, the estimation of fault level is significant in the operation management for DNOs. The composition of general load in a 11kV distribution network in the UK is given in Table 3.10 [102, 103]. The load power ratio is the ratio of the load power of a certain load type to the total load.

Table 3. 10 Typical composition of general load

Load type	Load power ratio	Average
Domestic	16%-42%	31.00%
Commercial	24%-65%	44.00%
Industrial	30%-73%	47.53%

By considering the load composition, a substation specified fault current contribution for general load can be calculated by:

$$FCC = \sum_{k} FCC_{ref\_k} \cdot FCC'_{k} \cdot \delta_{k} \tag{3.29}$$

where FCC_{ref_k} is the reference fault current contribution of load type k, FCC'_k is the normalised fault current contribution of load type k and δ_k is the load power ratio of type k. When detailed load composition not available, 1) a general fault current contribution can be obtained by using the typical/average load power ratio of each type of loads; and 2) a peak fault current contribution can be obtained by using the smallest possible load factors of each types of loads for conservative operations. If the range, in which the load power varies, is available, estimations can be obtained about the possible maximum load fault current and the minimum load fault current. These estimations provide useful information about how much fault level headroom would still be available during operation. The maximum is a conservative estimation and the minimum estimation implies the potential benefit that can be achieved if exact load composition information becomes available in real time.

The load fault current depends on the percentage load type composition and the actual load power level. While the composition can be found when all types of load are at their maximum simultaneously, the load type composition could change during operation as the total load power changes. From Table 3.6, the type of loads which has the normalised fault current contributions from highest to lowest are large industrial load, commercial load, small industrial load and domestic load. Hence if the load power increases in a distribution network follows the previous sequence, the network will sustain the highest load fault level. On the contrary, if the load power increases in the opposite sequence, the network will sustain the lowest load fault level. In practice, the load power increases between these two sequences. A band of load fault level can be obtained following these two sequences of load increase.

By following different sequence of load increase, the top and bottom envelopes of this fault level band can be calculated using:

$$FL(S) = \sum_{m} FCC_m \bullet S_m + FCC_n \bullet (S - \sum_{m} S_m) \tag{3.30}$$

where FCC_m is the fault current contribution of load type m, S is the total load, S_m is the peak load power of load type m and FCC_n is fault current contribution of the current increasing load type.

3.3.3.2 Case Study

A case study on the estimation of fault level for general loads were conducted on five 11kV distribution substations in Birmingham. Table 3.11 lists the total load and load composition of these five sample substations, which is provided by a UK DNO. The single line diagram of these substations can be found in Appendix II.

The fault current contribution for each type of load can be developed by Equation (3.29) and fault level band is developed using Equation (3.30). The fault level contribution results are listed in Table 3.12. This fault current contribution is under the condition that three phase fault occurs on 11kV busbar and load are supplied at 400V. Both the make and break fault current contribution are provided. The results of the fault level band are given for substation A as an example.

The fault current bands are developed for one (five in total) of the primary busbars of this substation. This primary busbar is the one that has the average peak load power. The peak load of this busbar is 13.76MVA in which domestic load is 4.38MVA, commercial load is 5.71MVA, small industrial load is 0.78MVA and large industrial is 2.89MVA. The fault current compositions of make and break fault current are shown in Figures 3.15 to 3.18. the fault level bands of the make and break fault current are shown in Figures 3. 19 and 3.20. These bands provide a direct view of the potential headroom for the network in the normal operations.

Table 3. 11 Sample substation data

Substations	Total Load (MVA)	Load Composition			
		Domestic	Commercial	Small Industrial	Large Industrial
A	68.8	31.80%	41.51%	5.65%	21.04%
B	32.2	23.63%	46.49%	4.05%	25.83%
C	40.2	20.14%	48.60%	7.35%	23.89%
D	39.7	57.27%	26.01%	7.58%	9.14%
E	54.6	39.95%	36.55%	10.36%	13.14%

Table 3. 12 Substation specified fault current contribution

Substations	Fault Current Contribution (MVA/MVA)	
	Make	Break
A	4.45	0.92
B	4.88	1.01
C	4.88	1.01
D	3.25	0.65
E	3.88	0.79

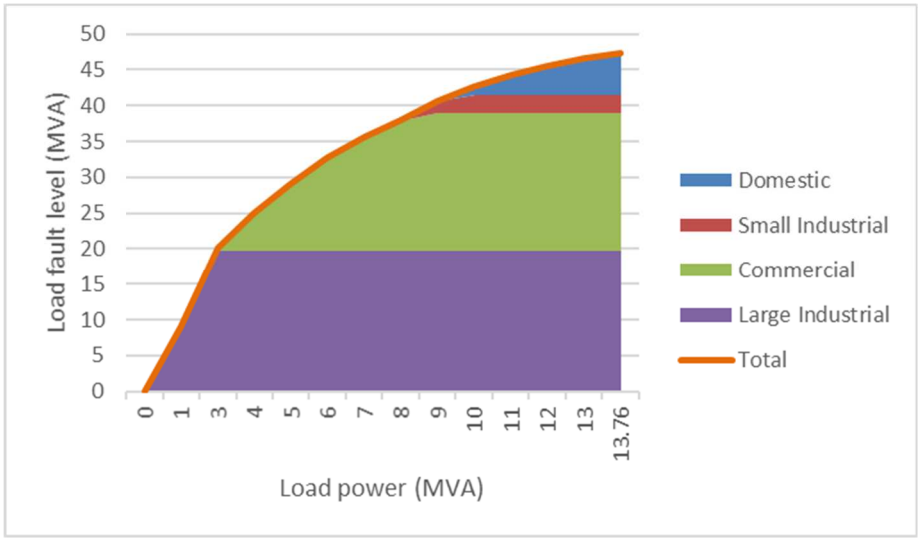

Figure 3. 15 Estimated maximum make fault current compositions

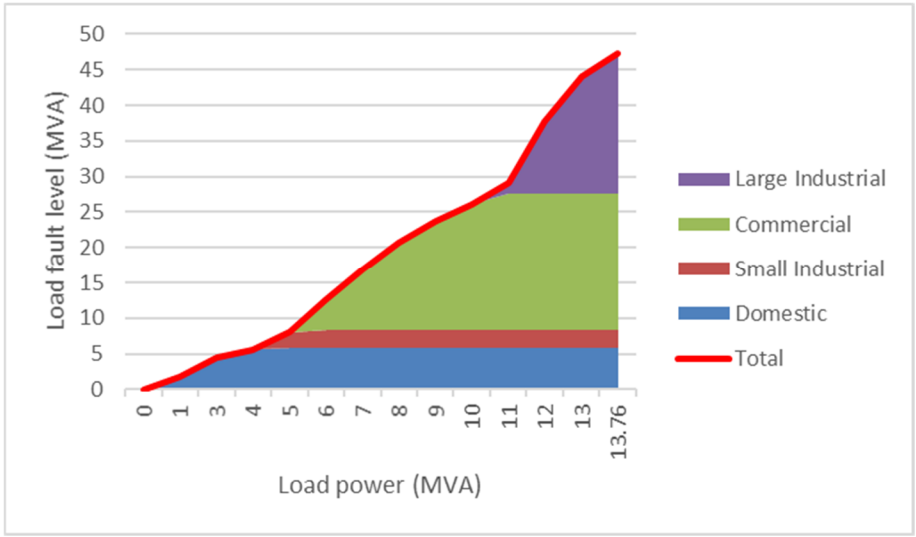

Figure 3. 16 Estimated minimum make fault current compositions

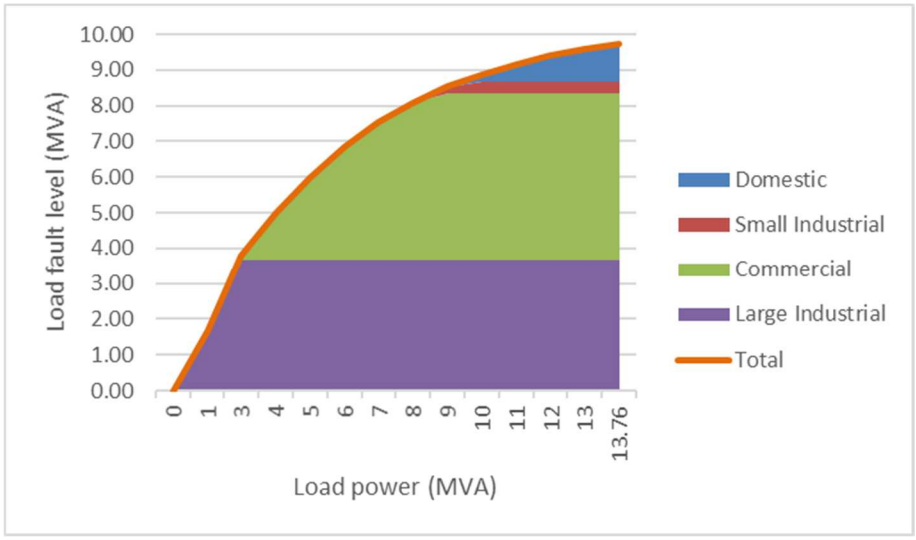

Figure 3. 17 Estimated maximum break fault current compositions

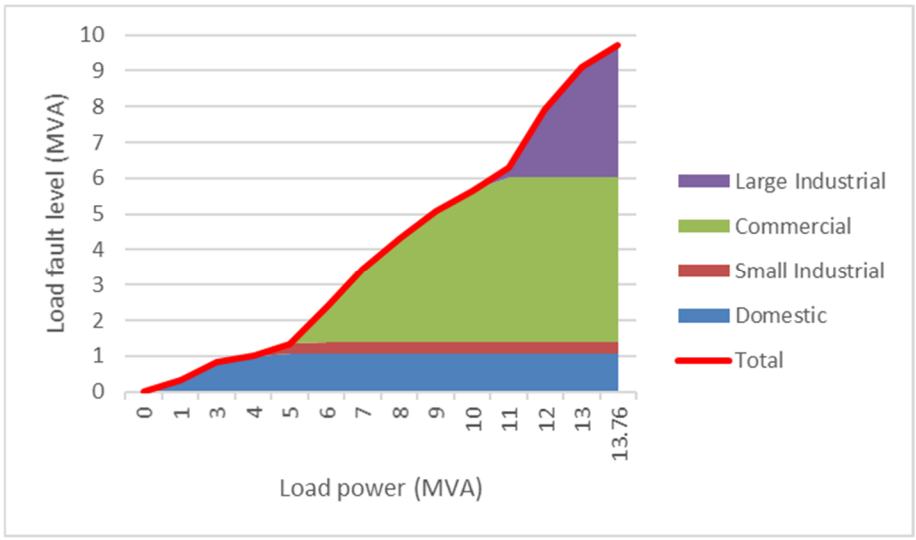

Figure 3. 18 Estimated maximum break fault current compositions

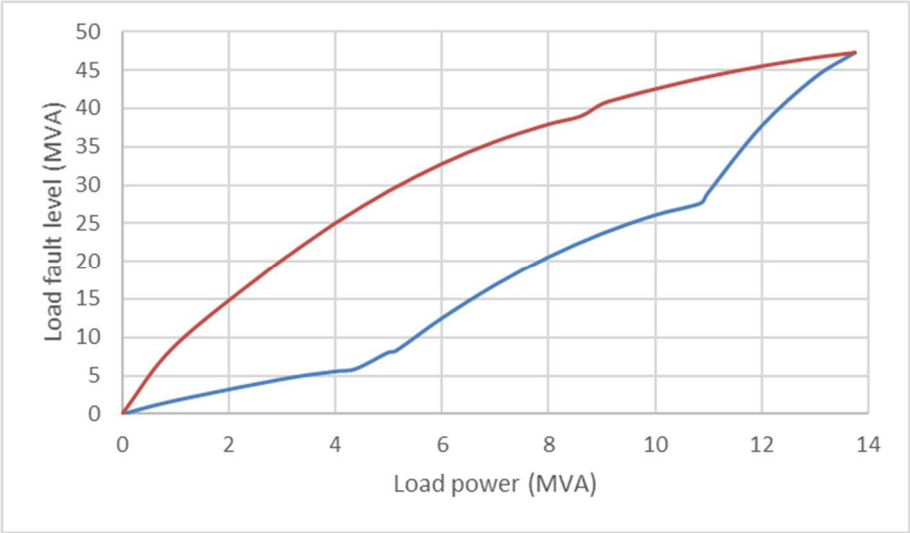

Figure 3. 19 Estimated band of make fault current compositions

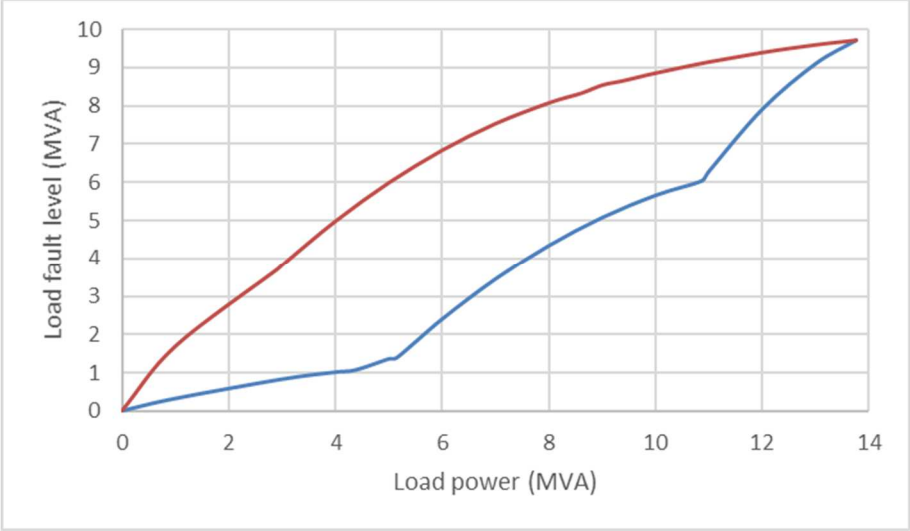

Figure 3. 20 Estimated band of break fault current compositions

3.4 Effects of DG to the Distribution Network

As mentioned in Chapter 2, when DG is connected into the network, it will raise the voltage and increase the fault level of the network. Generally, the voltage rise effect increases as the DG location is moved away from the primary busbar. On the contrary, the effect of fault level increase reduces as the DG location changes like this. Hence regarding different DG locations, the dominant concern for DNOs in network management is different. Furthermore, it is well known that when a fault occurs close to a generation station in the transmission network, the fault current may not cross zero in the first several cycles due to the large dc offset in the fault current contributed by the generation unit and the decaying ac component which changes from subtransient to transient before reaching the steady state. This missing zero-crossing phenomenon will affect the operation of protection devices in the transmission network. When the DG penetration level increases in the distribution network, the total size of DG could reach a considerable level compared to the loads in the distribution network. Whether this missing zero-crossing phenomenon will occur in the distribution network should be analysed regarding to the network protection strategy. In the following sub-sections, the calculation of fault current for synchronous machine based DG is studied. Regarding different DG penetration level and locations, the effects of DG connections to the network voltage profile and fault level are analysed to find the breakeven point when the dominant issue changes from the voltage profile to. The effects of DG to the dc off set of the fault current in distribution network is then studied.

3.4.1 Effects of DGs to the Voltage Profile and Fault Level

3.4.1.1 Fault Level Contribution of DG

The synchronous machine studied in this section is focussed on the medium and small size (10kVA – 5000kVA) three phase 400V synchronous machines. The synchronous generators used in CHP as DG in 11kV distribution network in the UK all belong to this type [10]. Normally these generators are connected to the 11kV network through a step-up power transformer. During fault in the system, the synchronous generator contributes fault current which increases the total fault current experienced by the protection devices. According to IEC 60909 [85], the break short circuit current of a synchronous generator is equal to the subtransient short circuit current of the synchronous generator. For a symmetrical three-phase fault, the break fault current directly contributed by the synchronous generator without transformer can be calculated using:

$$I_{sc}^{"} = I_{sc\_subtransient} = \frac{V_r}{\sqrt{3}X_d^{"}} \tag{3.31}$$

where V_r is the rated voltage and $X_d^{''}$ is the d-axis subtransient reactance of the generator.

The initial symmetrical fault current contributed by the generator represents expressed in fault level is:

$$FL'' = \sqrt{3} V_r I_{sc}'' \tag{3.32}$$

and the normalised initial symmetrical fault current contribution of a synchronous generator is:

$$FCC = \frac{FL''}{S_r} \tag{3.33}$$

where S_r is the rated capacity of the generator. The subtransient reactance X_d'' can be written as:

$$X_d'' = x_d'' \frac{V_r^2}{S_r} \tag{3.34}$$

where x_d'' is the per-unit d-axis subtransient reactance based on the ratingsac of the synchronous generator. Substituting Equations (3.31), (3.32) and (3.34) into (3.33) it can be derived that:

$$FCC = \frac{\sqrt{3} V_r}{S_r} \frac{V_r}{\sqrt{3} x_d'' (V_r^2 / S_r)} = \frac{1}{x_d''} \tag{3.35}$$

Hence the normalised first initial symmetrical fault current contribution of a synchronous machine is inversely proportional to the per-unit d-axis subtransient reactance of the generator.

In order to study how will the normalised break fault current contribution change when the generator size increases, the relationship between the physical design and the parameters of the machine must be considered.

The per-unit d-axis reactance of a synchronous machine includes the per-unit d-axis magnetising reactance (x_{md}) and the per-unit leakage reactance (x_L) of the windings:

$$x_d = x_{md} + x_L \tag{3.36}$$

In the design of synchronous machine, for a given rated voltage V_r, rated output power S_r and magnetising current I_m, the magnetising reactance X_m is calculated by:

$$X_m = \frac{V_r}{I_m} \tag{3.37}$$

and the per-unit magnetising reactance x_m is calculated by:

$$x_m = \frac{X_m}{V_r^2 / S_r} = \frac{X_m}{V_r / I} \tag{3.38}$$

where I is the phase current at rated output power. For a given maximum air gap flux density B_{gmax} and winding layout, I_m is proportional to the stator bore diameter D, V_r is proportional to the stator cross section DL, L is the stator length, and rated current I is proportional to $D^{3/2}$. Hence X_m is proportional to L and x_m proportional to $D^{1/2}$. Assuming that the stator winding current is at rated current I, the leakage-flux linkage per slot is proportional to IL and hence proportional to $D^{3/2}L$.

The corresponding reactance voltage drop is IX_L, and proportional to leakage-flux linkage per slot. Hence the per-unit leakage reactance,

$$x_L = \frac{X_L}{V_r / I} = \frac{IX_L}{V_r} \tag{3.39}$$

is proportional to $D^{1/2}$ [104]. Since both x_m and x_L is proportional to the generator size, the per-unit d-axis sub-transient reactance $x_{d''}$ slightly increases with the generator size. Therefore, according to Equation (3.35), the normalised first initial symmetrical fault current contribution in MVA/MVA slightly decreases with the generator size. This correlates with the calculation results, shown in Figures 3.21 and 3.22, of 154 three-phase 400V synchronous machines varies from 10kVA to 4000kVA, according to the datasheets given in Appendix III. The generators are divided in four groups according the rated capacity: less than 500kVA, 500kVA to 1MVA, 1MVA to 2MVA and 2MVA to 4MVA. The mean fault current contributions of each group are shown in Table 3.13.

Table 3. 13 Mean normalized break FL contributions of synchronous generators to 400V and 11kV networks (MVA/MVA)

DG Size	400V	11kV
<500kVA	9.36	4.8
500kVA-1MVA	8.53	4.58
1MVA-2MVA	8.2	4.47
2MVA-4MVA	7	4.1

The result of the fisrt initial symmetrical fault current contribution to 400V network is shown in Figure 3.21. The normalised three-phase break fault current contribution of a synchronous machine through a transformer is calculated by:

$$FCC' = \frac{V_n}{(a^2 X_d'' + Z_t)S_r} \tag{3.40}$$

where V_n is the nominal voltage of the network where fault occurs, a is the winding ratio of the transformer and Z_t is the equivalent impedance of the transformer. For the same transformer, the normalised break FL contribution decreases with generator size. The calculation results of the initial symmetrical fault current contributions at 11kV busbar of synchronous machines varing from 10kVA to 4000kVA are shown in Figure 3.22.

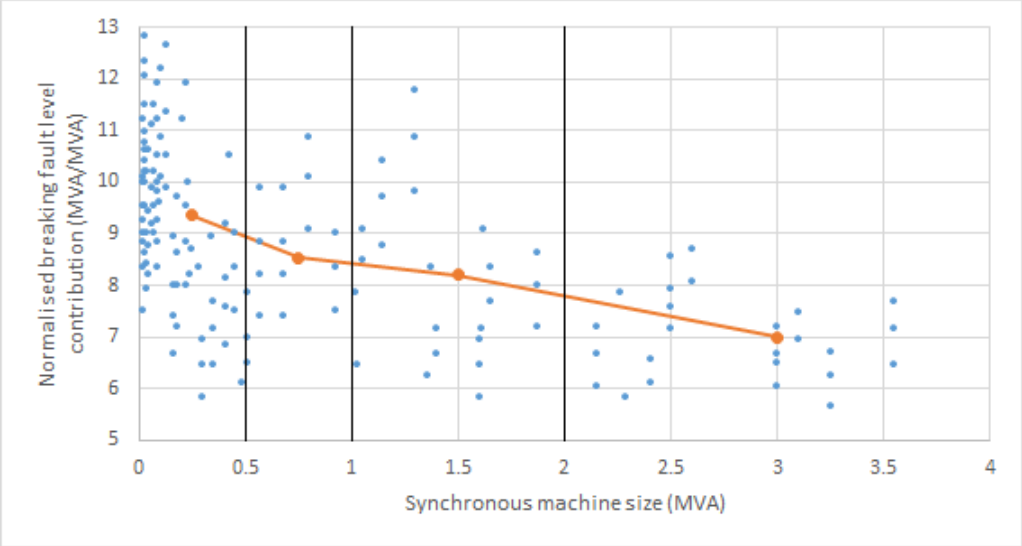

Figure 3. 21 Initial symmetrical fault current contribution to 400V network of different size synchronous machines

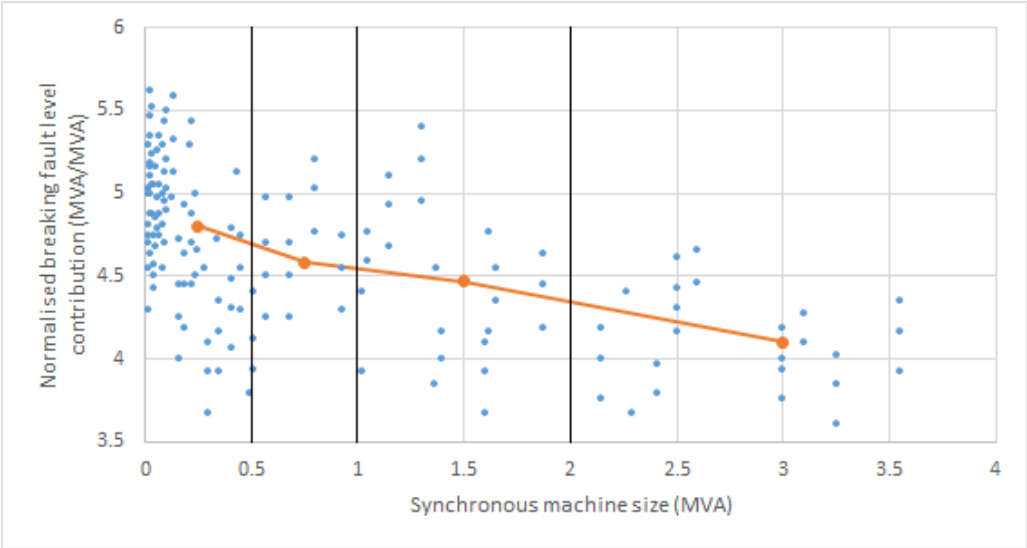

Figure 3. 22 Initial symmetrical fault current contribution to 11kV network of different size synchronous machines

For synchronous machine based DG without knowing the detailed composition, the general normalised first initial symmetrical component of the fault current can be taken as 4.5MVA/MVA on average in the fault analysis for generator size no more than 5MVA in the 11kV distribution network.

3.4.1.2 Effects of DG to Network Fault Level and Voltage Profile with Different DG Locations

In the UK, the peak load fed from a primary substation transformer is typically between 10MVA and 20MVA. The loads are distributed along radial branches, the length of which is usually from 5km to 10km. The busbar voltage should be between +10% and -6% of the nominal value according to ESQC Regulation and the DNOs adopt ±6% in their operation [20]. The ratings of the circuit breaker in an 11kV network is typically 250MVA for break and 625MVA for make. There should be a safety margin of 5% in fault level management.

As DGs are distributed in the network, it will contribute fault current depending on the types of the DG. The type of DG having the highest fault current contribution is usually the synchronous machine which is the choice for many CHP units. The typical first symmetrical fault current contribution of DG using synchronous machine is expressed as the normalised fault level contribution of 4.5MVA/MVA, according to the results in the previous section.

In order to analyse the impacts of DGs at different locations to the voltage profile and fault level of the network, a radial network model is first built based on the data from a UK DNO, as shown in Figure 3.23.

In the model, the 11kV network is fed by the background 132kV grid through a step-down transformer. Three aggregated loads are evenly distributed along the feeder length, at points A, B and C (beginning, middle and end, respectively).

The inductance and resistance per km of the cable are 0.29mH/km and 0.051Ω/km, and the total cable length is 10km. The total load on the feeder is 15MVA at an aggregated power factor of 0.97. In this case, the tap position of the transformer is fixed and set to ensure that the voltage at the end of the feeder is just above the lower voltage limit when the network is at peak load, without DG. The effect of the location of DG (synchronous generator fully generating at a unity power factor) is analysed in the situation when the network is lightly loaded (20% of the peak load). The DG penetration level is increased from 0% to 100% with a 10% step at each location.

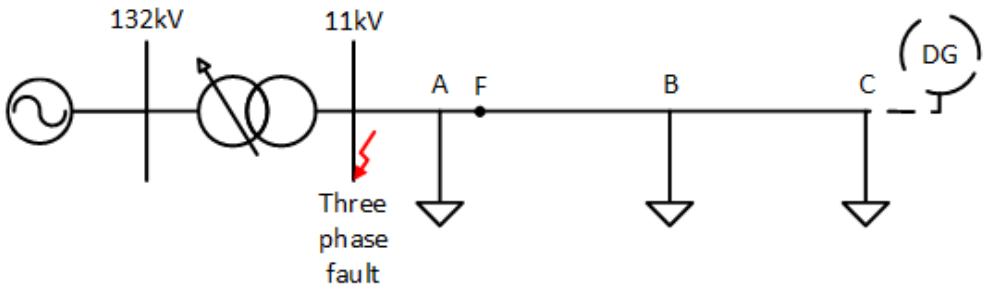

Figure 3. 23 Model of radial distribution network

The simulation results (using Matlab/SIMULINK) are given in Figure 3.24 (a) and (b) where the solid lines indicate the voltage profile at the DG connection point whilst the dashed lines indicate the fault level rise at the primary busbar. Lines with the same colour indicate that the DG is connected at the same location.

Generally, when the DG is connected to the network, the voltage profile is the first constraint to be met. However, when the DG is connected close to the primary busbar, the fault level of the network becomes to the more immediate constraint. The break-over point of location where the fault level becomes the more significant constraint is at somewhere close to location F, which is around 3km from the primary busbar.

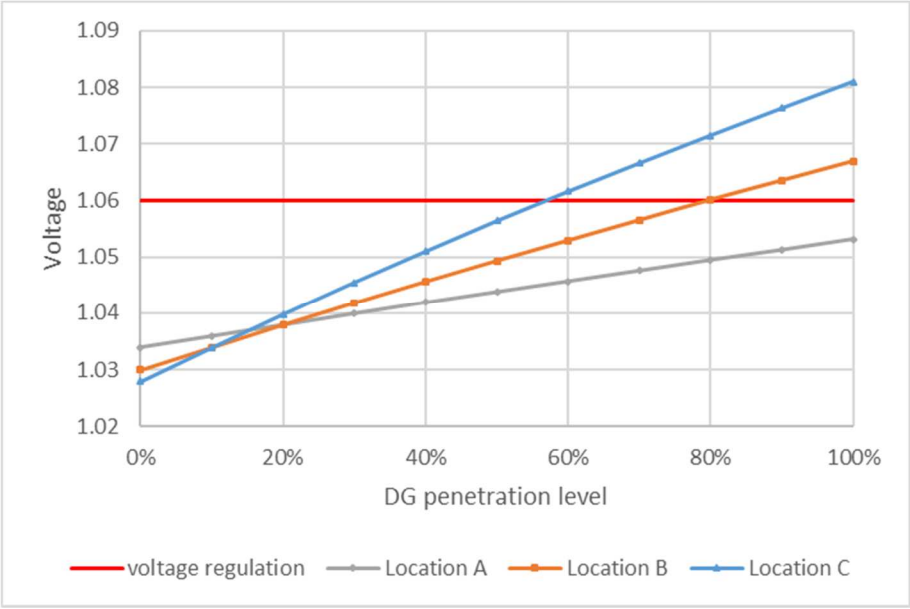

(a)

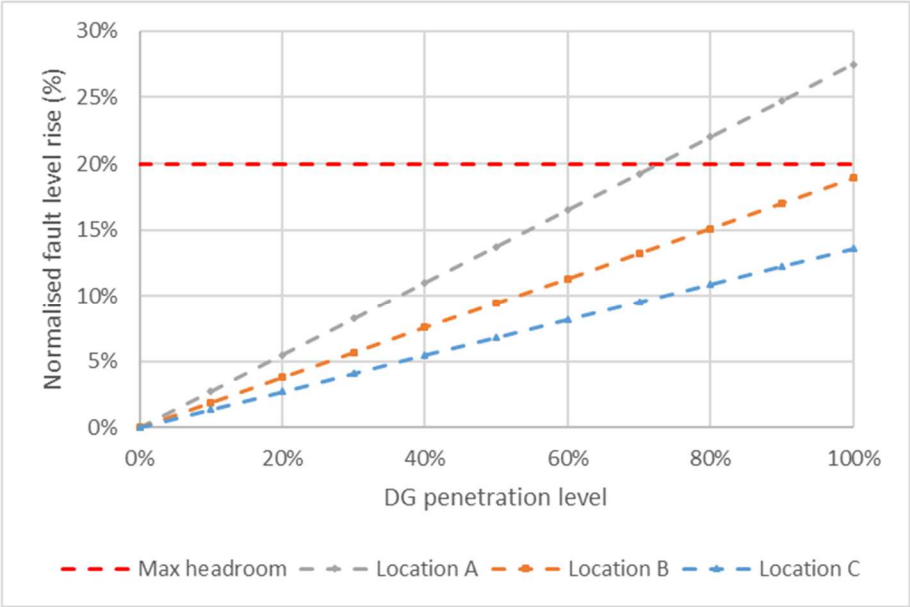

(b)

Figure 3. 24 (a) Voltage variation and (b) fault level caused by DG at different locations in an 11kV network

Regarding the DG capacity, the penetration level can be almost 60% or 70% before the voltage profile or fault level is violated when the network is lightly loaded. The penetration level is defined as the ratio of the installed DG capacity to the peak load on the feeder.

In practice, from the network safety point of view, UK DNOs rarely allow DG to be concentrated close to the primary busbars. Therefore, the most common issue caused by DG connection currently in practice is the voltage violation and the fault level issue should be of concern when the DG penetration level reaches 60%.

3.4.2 Effects of DGs to the Zero-Crossing of Network Fault Current

In a transmission system, when a fault occurs close to a power plant, the missing zero-crossing in the fault current commonly happens, as shown in Figure 3.25 [93].

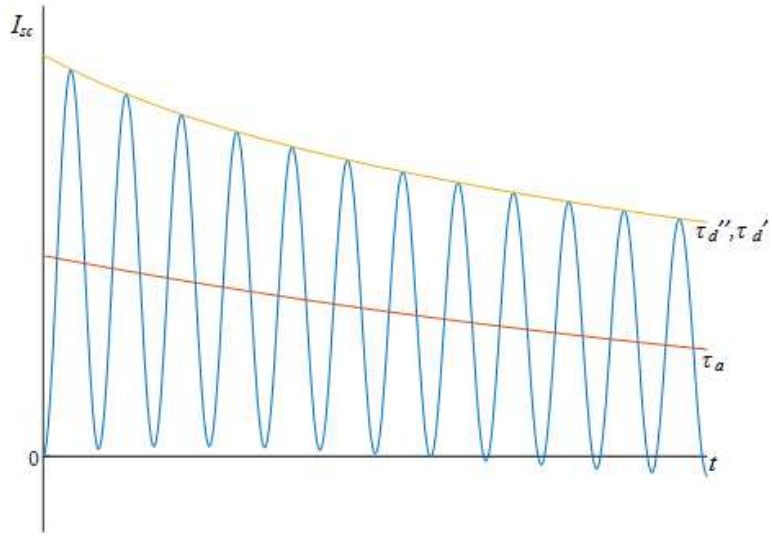

Figure 3. 25 Short circuit current close to power plant

As shown in the figure, the short circuit current misses zero-crossing in several cycles after fault. This is due to the high asymmetrical dc component of the total fault current, and the decay of the ac component.

When DG penetration level increases in the distribution network, this phenomenon is possible to occur if fault happens close to the DG site. For current distribution network conditions, whether this phenomenon will happen is analysed in the following sections for synchronous generator based DG in the 11kV distribution network.

3.4.2.1 Short-circuit Current Analysis of Synchronous Generator

During the fault, the short-circuit current of the synchronous generator consists of two components: a decaying dc component and a decaying acAC component. The envelopes of the short-circuit current for the dc and acAC components are:

$$i_{DC}(t) = \sqrt{2}\frac{V_n}{X_d^{"}}e^{-t/\tau_a} \tag{3.41}$$

$$i_{AC}(t) = \sqrt{2}V_n[(\frac{1}{X_d^{"}} - \frac{1}{X_d^{'}})e^{-t/\tau_d^{"}} + (\frac{1}{X_d^{'}} - \frac{1}{X_d})e^{-t/\tau_d^{'}} + \frac{1}{X_d}] \tag{3.42}$$

and the total short circuit current of a synchronous generator is:

$$I_{sc}(t) = I_{AC}(t) + I_{DC}(t) = i_{AC}(t)\cos(\omega t + \theta_0) + i_{DC}(t)\cos(\theta_0) \tag{3.43}$$

where V_n is the rated voltage of the synchronous generator, X_d'', X_d' and X_d are the sub-transient, transient and steady-state reactances of the generator respectively and τ_d'', τ_d' and

τ_a are the sub-transient, transient and armature time constants of the synchronous machine respectively.

As mentioned in the previous section, the total short circuit current of a synchronous generator includes a decaying dcdc component and a decaying acAC component, shown in Figure 3.26. As indicated in the figure, during the first cycle after fault, if the amplitude of the peaks of ac component are smaller than the amplitude of the dcdc component at the same time, the missing zero-crossing phenomenon will happen. Otherwise, the short circuit current will not miss the zero point. From Equation (3.43), it can be derived that if:

$$|I_{DC}| > |I_{AC}| \tag{3.44}$$

there will be the missing zero-crossing of short circuit current.

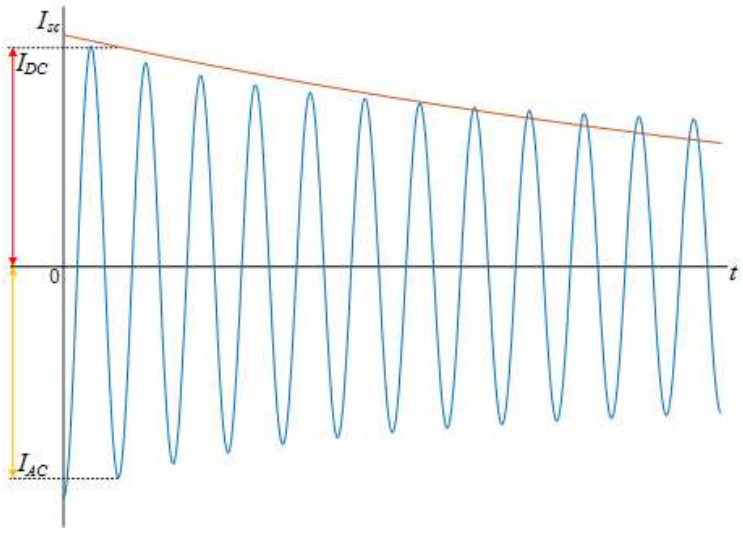

Figure 3. 26 dc and ac components of the short circuit current from a synchronous machine

For the ac component, it consists of three components: sub-transient current, transient current and steady state current, as shown in Figure 3.27. The whole short circuit period, according to the decay of ac component, can be divided into sub-transient, transient and steady state periods. In the sub-transient period (During the first cycle after fault [94]) the sub-transient current is the dominant component of the total short-circuit current for synchronous machines sized between 500kVA and 20MVA (datasheets are given in Appendix IV) as shown in Figure 3.28. The results are the ratio of the calculated sub-transient current to the total short-circuit current. As shown in the figure, the ratio of the sub-transient current to the total current at 20ms after fault is all above 90% for synchronous generators between 500kVA and 20MVA.

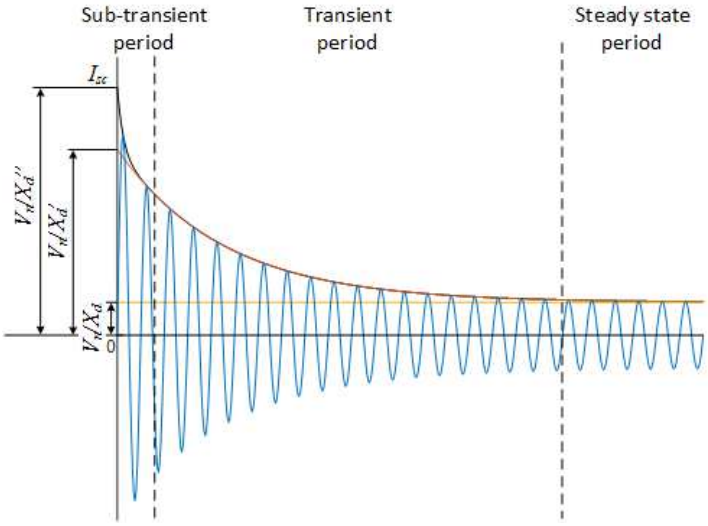

Figure 3. 27 ac components of synchronous machine short circuit current

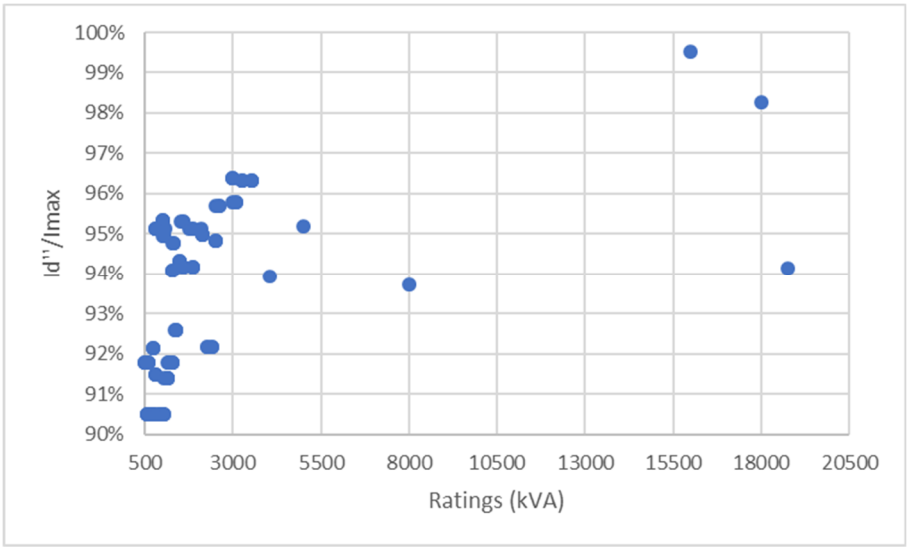

Figure 3. 28 Ratio of sub-transient current to total current of synchronous machine

Hence for the first cycle after fault, the decay of the transient current is neglected and the total short circuit current is reduced to:

$$I'_{AC}(t) = \sqrt{2}V_n[(\frac{1}{X''_d} - \frac{1}{X'_d})e^{-t/\tau''_d} + \frac{1}{X'_d}]\cos(\omega t + \theta_0) \tag{3.45}$$

and Equation (3.44) can be rewritten as:

$$\frac{\sqrt{2}V_n}{X''_d}e^{-t/\tau_a} > \sqrt{2}V_n[(\frac{1}{X''_d} - \frac{1}{X'_d})e^{-t/\tau''_d} + \frac{1}{X'_d}] \tag{3.46}$$

It is further derived as:

$$\frac{1}{X''_d}e^{-t/\tau_a} + (-\frac{1}{X'_d}) > \frac{1}{X''_d}e^{-t/\tau''_d} + (-\frac{1}{X'_d}e^{-t/\tau''_d}) \tag{3.47}$$

It is obvious that for larger than zero:

$$-\frac{1}{X_d^{'}} < -\frac{1}{X_d^{'}} e^{-t/\tau_d^{''}} \tag{3.48}$$

Hence for all synchronous generators having smaller dc time constant compared to sub-transient ac time constant, the short circuit current will not have the missing zero-crossing phenomenon. Even for synchronous generator having larger dc time constant, it must be 'large enough' to have the missing zero-crossing phenomenon according to Equations (3.47) and (3.48).

3.4.2.2 Case Study on Short Circuit of Synchronous Generator

In order to find out the ratio of τ_a to τ_d'' which is 'large enough' to missing zero-crossing, synchronous generators of different sizes from 500kVA to 20MVA are studied, the parameters are given in Appendix IV. Synchronous machine models using Park's equation are developed using Matlab/SIMULINK and three-phase faults with different inception angles are applied to obtain the short circuit current. The results of the zero-crossing time of the short-circuit current are shown in Figure 3.29.

As shown in the figure, the zero-crossing time varies for different time constant ratios. Generally, it can be observed for most of the synchronous machine with a time constant ratio smaller than 2.5, the zero-crossing time of short circuit current is before 20ms, that is within one cycle after fault. For time constant ratio larger than 2.5, most of the zero crossing times are around 40ms, which is two cycles after fault. Due to particular design in the synchronous machine, the zero-crossing time could be even longer for some machines with time constant ratio larger than 2.5.

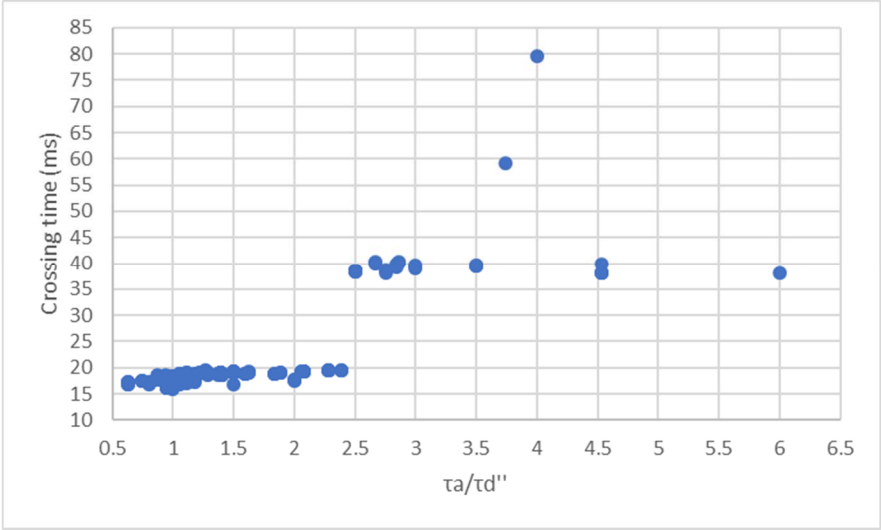

Figure 3. 29 Zero-crossing time of short circuit current for different time constant ratios

As indicated in Figure 3.30, for most of the synchronous machines sized less than 2MVA, the time constant ratio is less than 2.5, while generators larger than that would have larger time constant ratio.

Hence for synchronous generators sized between 500kVA and 2MVA, the missing zero-crossing phenomenon will not occur in the short circuit current while for synchronous generator larger than 2MVA, this phenomenon will occur in most of the cases.

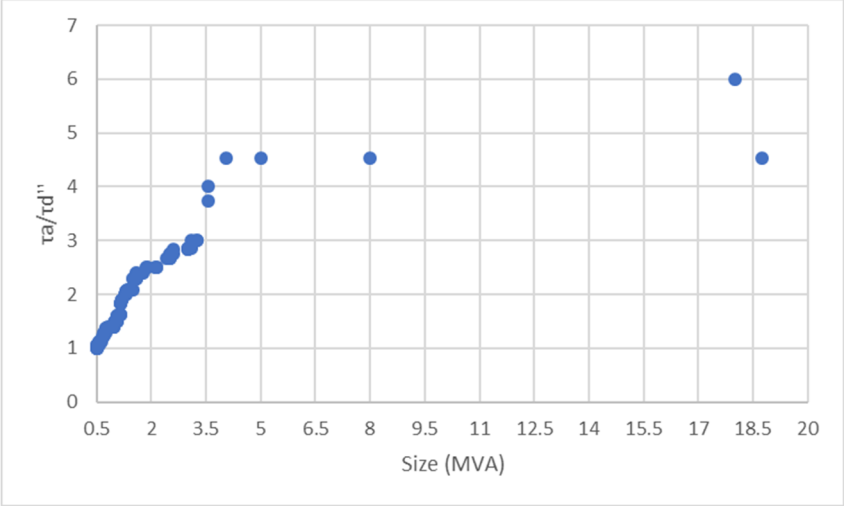

Figure 3. 30 Time constant ratios for synchronous generators in different sizes

3.4.2.3 Effects of Synchronous Generator Type DG to Total Fault Current in 11kV Distribution Network

As discussed in the previous section, when fault occurs at the DG location, the occurrence of missing zero-crossing phenomenon in the short circuit current of the synchronous generator depends on the size of the individual generator.

However, when a fault happens in the 11kV distribution network with DG installation, this effect from fault current contributed by synchronous machine to the total fault current requires further analysis, considering the effect of distance from the DG to the fault and the number of generation units. In order to analysis the mentioned two effects, the same network model as in Subsection 3.4.1.2 is used.

The total fault current is the summation of the fault currents contributed by both the upstream network and DGs. Since the X/R ratio of the upstream network of a typical 11kV distribution network is between 7.5 and 15, the fault current contributed by the upstream network does not have the zero-crossing missing phenomenon. Compared to the fault current contributed by the upstream network in 11kV network, the fault current from a single synchronous machine between 500kVA and 20MVA is less than 20% of the upstream current calculated using the same generators in Subsection 3.4.1.2. Hence the most significant case when missing zero-crossing is possible to occur is that the DG is installed at the end of the feeder and the fault happens just at the DG location. The simulation results of the zero-crossing time for a single synchronous generator in different sizes is listed in Table 3.14.

Table 3. 14 Zero-crossing time of fault current in 11kV network with fault at DG site

Size (kVA)	Crossing Time (ms)
2100	0.0145
4050	0.0146
5000	0.0146
8000	0.0147
16000	0.0148

As shown in the table, the zero-crossing time of total fault current is still within one cycle after fault, which means the upstream fault current is dominant in the total current. as the fault location moves away from the DG location, the zero-crossing time becomes even shorter. The results from simulations on a 16000kVA synchronous machine is shown in Table 3.15.

Table 3. 15 Zero-crossing time of fault current with different distance between fault and DG

Length (km)	Crossing Time (ms)
0	0.01475
5	0.0138
10	0.01355
15	0.01347
20	0.01338

For DG with more than one generators, the zero-crossing time of fault current reduces with the increase of generator numbers. As shown in Subsection 3.4.2.2, with the increase of size of a single synchronous machine, the zero-crossing time of the short circuit current increases. For DG with fixed size, the increase in the generator number means a reduction in the size of a single generator. For all smaller synchronous generators, the zero-crossing time of the short circuit current of each one is smaller than one synchronous generator with the size equalling the summation of sizes of all smaller generators.

Hence the zero-crossing time of the total short circuit current of all these smaller generator is smaller than one large generator. This is also confirmed by the simulation results listed in Table 3.16.

Table 3. 16 Zero-crossing time of fault current contributed by different numbers of generators

Number x MVA	Crossing Time (ms)
4x4	0.01445
2x8	0.0145
1x16	0.01475

3.5 Summary

The short circuit current calculation method for induction machines and short circuit current contribution estimation method in IEC 60909 were reviewed. For small scale induction machines, the winding R/X ratio is relatively large compared to that of large scale induction machines. Using the equations in IEC 60909 in short circuit current calculations for small scale three/single phase induction machines leads to a conservative calculation result. Adjustment of taking the winding resistance into short circuit current calculation for small scale induction machines can achieve a 10% more accurate result.

In ER G74, which is an alternative of IEC 60909 for computer based short circuit current estimation commonly used by DNOs in the UK, provides a recommendation on the short circuit current contribution to 33kV busbar from general loads connected at low/high voltage busbar at peak winter demand (1MVA/MVA and 2.6MVA/MVA). Using these values in 11kV system causes the results of fault current contributed by general load to be smaller. The fault current at 11kV busbar contributed by 400V loads in different types are studied. With the increasing of load power factor, the fault current contribution reduces in a linear manner. Using this linear manner, substation specified estimation of load fault current can be obtained if specified load composition and load power factor are acknowledged. Further, if the changing range of load power can be acknowledged, the fault current bands of specified busbar/substation can be developed which can be beneficial in the network operation management for DNOs.

When DG is connected into distribution network, the fault level issue will not occur until the penetration level is over 60%. With heavy DG penetration in a typical 11kV distribution network with 10km-llong feeder, the fault level issue becomes the dominant issue when DG is concentrated installed within 3km from the primary busbar. If the detailed composition of this concentrated DG is unable to acknowledge, the normalise fault level contribution of 4.5MVA/MVA can be applied for the initial symmetrical current in the network fault analysis.

For a single synchronous generator, if the time constant ratio of τ_a to τ_d'' is larger than 2.5, the short circuit current of it will have the missing zero phenomenon. When connecting the synchronous generator as DG, sized between 500kVA and 20MVA, into the distribution network, the total fault current of the network will not have the missing zero phenomenon in all circumstances due to the fault contributed by DG is still apparently small compared to that from the upstream network. Hence the installation of DG will not affect the action of circuit breaker on the zero-crossing time of fault current.

.

Chapter

4 Analysis on the Changes of the Electrical Network in the UK in the Future

4.1 Analysis on the Upstream Generation

The UK government has set targets for carbon emission reduction from 2013 to 2050 in the 2050 Pathway Analysis [15]. In order to achieve the target, large coal-fired power stations without carbon capture technology have to be closed from 2013 to 2023 [15]. The map of power stations in the UK is shown in Appendix I. As shown in the map, currently there are 13 coal-fired stations left in the UK, one in Scotland, one in Wales and one in Northern Ireland and the rests are in England [105].

In synchronism with the closing down of these power stations, the generation capacity provided by these stations are to be replaced by power stations with carbon capture technology, renewable energy and DGs [29]. However, these changes in the power generation landscape will cause the fault level of primary distribution substations to change accordingly. This chapter is going to study about how the fault levels of 11kV primary substations will change when the upstream generation is replaced by local DG.

4.1.1 Network Model of the Sample Substations

Fifteen 11kV primary substations in Birmingham provided by WPD are chosen in the study. The whole network diagram is shown in Appendix II. According to the network models, these 15 substations are supplied by four 132kV upstream networks. There are interconnections between these four 132kV networks but the interconnections are normally open. Each of the 132 kV networks is supplied by a 275kV network further upstream. All the 275kV networks are modelled in one or two Thevenin equivalents. The single-line diagram of the network model for a primary 11kV busbar is shown in Figure 4.1.

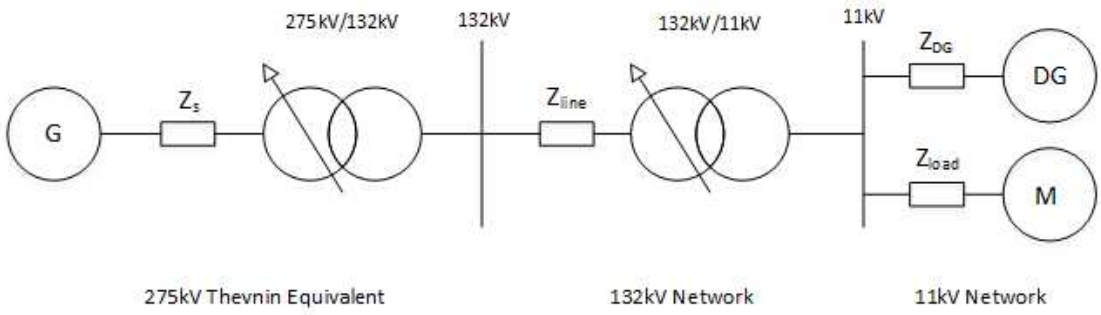

Figure 4. 1 Single line diagram of the simplified model

where Z_s is the equivalent Thevenin impedance viewed into the 275kV network, Z_{line} is the equivalent impedance of the 132kV network, Z_{DG} is the equivalent impedance of the DG and Z_{load} is the equivalent impedance of the general load. The calculation method is based on the G74 and the fault level infeed of the DG and general load are 4.25 MVA/MVA and 1.445 MVA/MVA respectively. In the model, both the 275kV Thevenin equivalent impedance and DG are modelled as a synchronous generator.

Therefore, in the study, the 15 11kV primary substations are divided into four groups according to the equivalent 275kV unit, as listed in Appendix II. The analysis focuses on how the fault level will change as the penetration level of DG increases while the generation capacity of upstream decreases accordingly. All 15 11kV substations are operated in the most common configurations given in the latest network models. The load demands of all 11kV primary substations are at their peak. The load composition is assumed to be unchanged from what it is now.

The upstream network structure is also assumed to be unchanged and only the generation capacity decreases according to the increase of DG capacity.The simulation studies only consider the most significant case: all the DGs are provided by synchronous machines which are directly connected to the primary 11kV busbars of the primary substations. The DG capacity connected to each substation is amended according to the peak load demand of the substation. The DG penetration level is defined as the ratio between the DG capacity and the peak load. Simulation runs were conducted on cases when penetration level increased from 0% to 100% with a step of 10% in each case.

4.1.2 Fault Level Compositions of Different Networks

In order to analyse the fault level change when DG increases in the network, the fault level composition of 11kV busbar without DG is analysed first. The sources of fault current are divided into the upstream network and downstream network. The upstream network refers to the 132kV background network. The downstream network refers to the local 11kV distribution network for each 11kV primary busbar. The IEC 60909 is applied to calculate the fault current contribution of the upstream contribution using the model in Figure 4.1.

The adjusted normal fault level contribution of general load in Chapter 3 is applied to calculate the downstream contribution for each primary 11kV busbar. For each primary 11kV busbar, the total fault current is the sum of the upstream fault current and the downstream fault current.

The weights of the upstream contribution and downstream contribution to the total fault current are further calculated for each primary 11kV busbar to obtain the fault level composition. The results of the fault level composition for each primary 11kV busbar are shown in Figures 4.2 to 4.5.

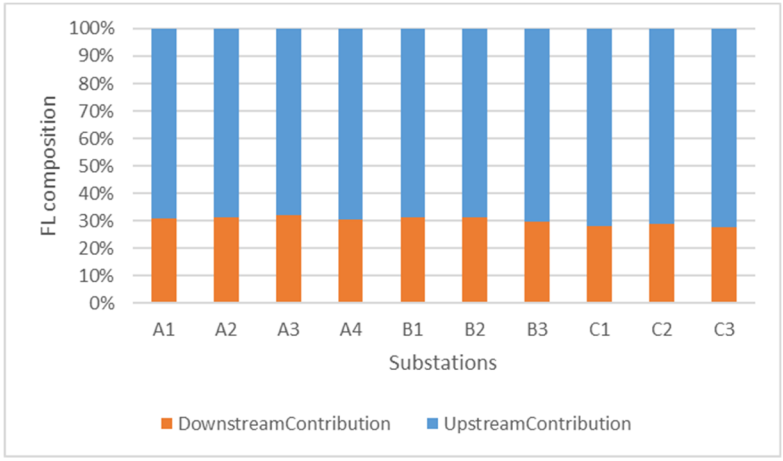

Figure 4. 2 Fault level composition of Group 1

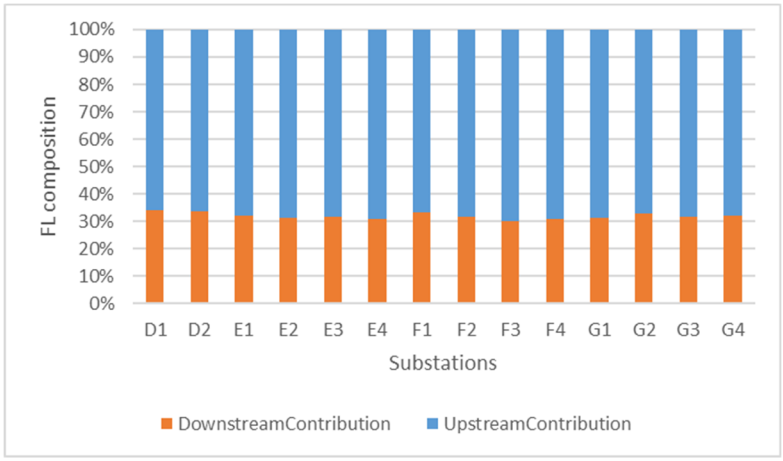

Figure 4. 3 Fault level composition of Group 2

According to the simulation results, with no or very small DG penetration level, the fault level is dominantly contributed by the upstream network. For substations connected in the same 132kV network, the fault level compositions are almost the same. Since the upstream network is usually strong, the compositions of fault level at 11kV the primary busbars are 70% to 80% caused by the upstream network and 20% to 30% by the downstream network (dynamic load and generally the contribution from DG is relatively small, which is negligible in the current situation) respectively, as shown in Figures 4.2 to 4.4. The difference in fault level composition between different groups is caused by the different equivalent upstream network impedance and source impedance. However, when the upstream network is relatively weak, the contribution of the upstream network to the fault level can reduce to about 50% to 60%, as shown in Figure 4.5. In the studied substations, the location of the equivalent impedance 275kV generation equivalent is relatively large comparing to the general situation. This is affected by the location of the connection point between the 275kV network and the 132kV network that the upstream generation is relatively far from the 132kV network in the electrical distance comparing to other 132kV networks.

On the other hand, the equivalent impedance of the 132kV network in Group 4 comparing to the other 132kV networks is relatively large. This can be caused by the network topology, the location of the 11kV substations and the overhead lines and cables used in the network. Considering the downstream network, some of the substations in this group currently have DG connections. This increases the fault level contribution from downstream network of relevant substations.

Furthermore, some substations in the Group 4 have interconnections between each other. These interconnections also increase the contribution of the downstream network to the total fault level.

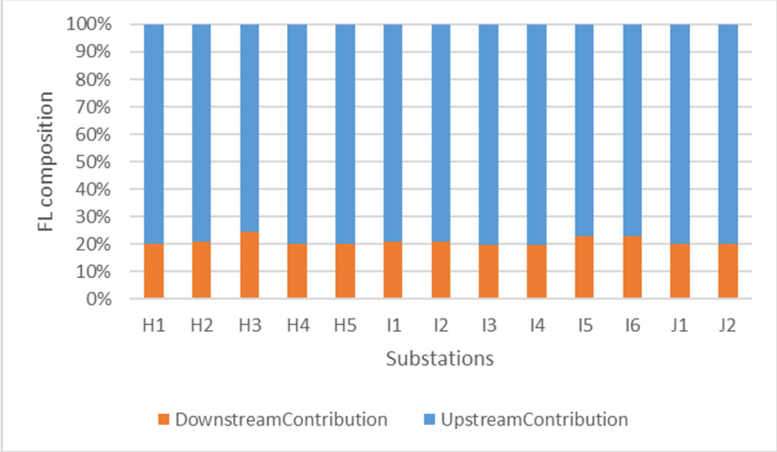

Figure 4. 4 Fault level composition of Group 3

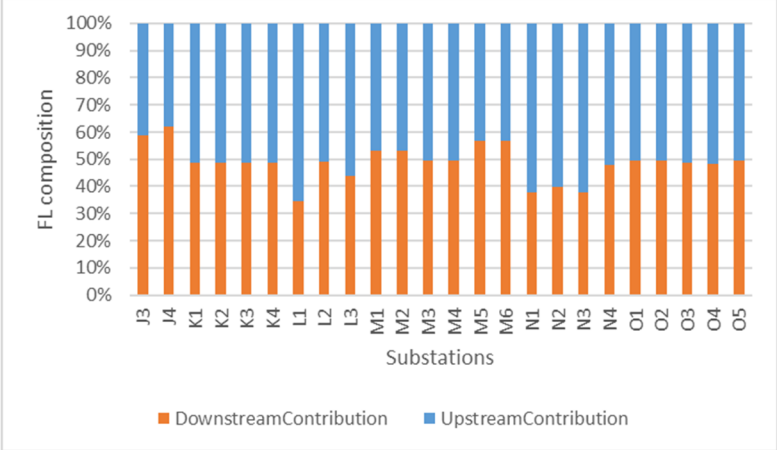

Figure 4. 5 Fault level composition of Group 4

4.1.3 Fault Level Changes due to the Increase of DG

The simulation results about the fault level changes with respect to the DG connected at the 11kV primary busbar are shown in Figures 4.6 to 4.9. The fault level results of each primary busbar are normalised to the value when the DG penetration level is 0%. This fault level at 0% penetration level is regarded as the base value later in the analysis.

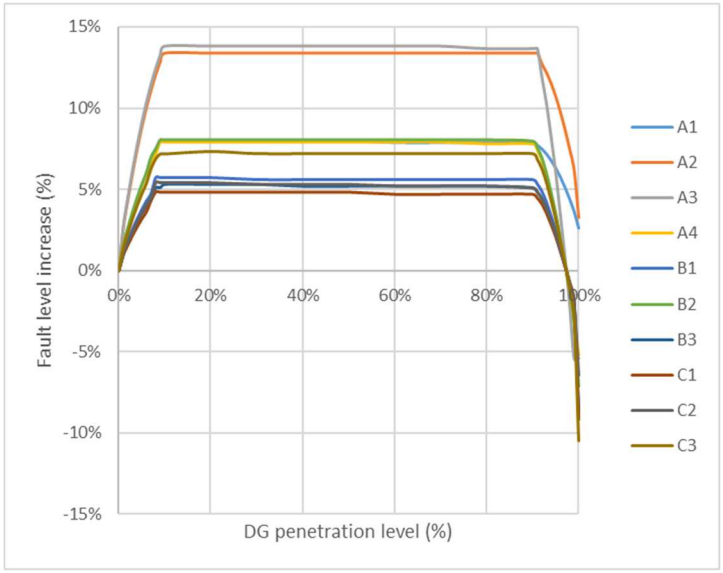

Figure 4. 6 Normalized fault level change of Group 1

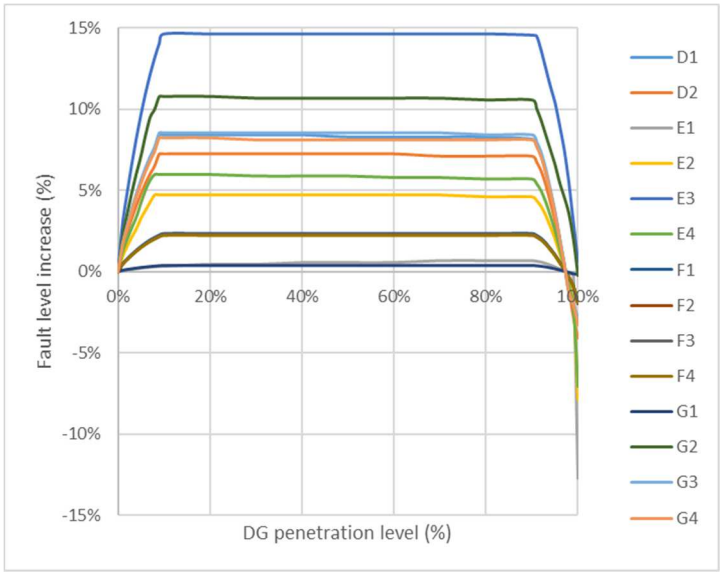

Figure 4. 7 Normalized fault level change of Group 2

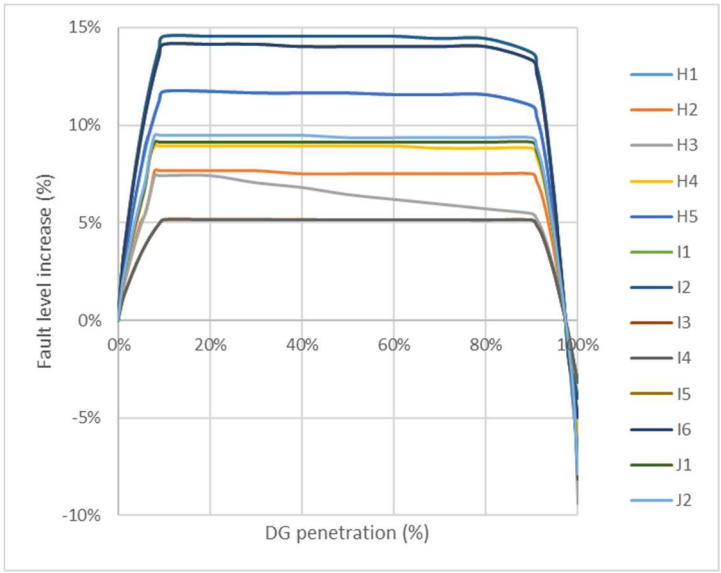

Figure 4. 8 Normalized fault level change of Group 3

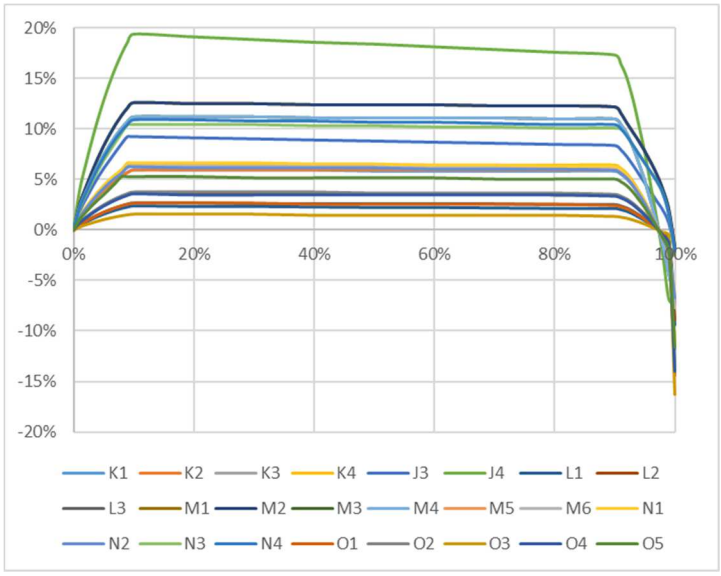

Figure 4. 9 Normalized fault level change of Group 4

All the results indicate that when DG is connected into the distribution network, there will have an obvious increase of the fault level at 11kV primary busbar. As the DG further increases and upstream generation decreases correspondingly, the fault level at the primary 11kV primary busbar does not change very much. When the penetration level reaches 100%, i.e. all the load demand of the distribution network is supplied by DG and no power consumption from upstream network, the fault level at 11kV primary busbar will reduce to a value less than the base value.

As shown in Figures 4.6 to 4.9, the fault level increase caused by DG is approximately 5% to 15% of the base value. This variation in the fault level increase is mainly affected by the added DG capacity. Since the upstream network topology is unchanged, the 10% reduction in the upstream generation will cause the upstream network to reduce.

In the model, this 10% reduction refers to the 10% reduction in the 275kV generation equivalent. This can be from centralised generation, localised generation of both, as long as the generation supplies the 132kV network through the 275kV network. But comparing to the base value, this reduction is approximately 1% to 2%, which is negligible.

As the added DG capacity is proportional to the load demand of the substation, when the peak load demand of one single primary busbar is relatively large, normally more than 15MVA, the added DG capacity is relatively large. This leads to a larger fault level contribution of DG. Since the DG is directly connected to the primary busbar, the fault level increase caused by DG can be more than 10% of the base value when the peak demand of the substation is large. When the peak load demand of the substation is relatively smaller, the fault level increase caused by DG will be smaller, as explained in the former. Normally, for substations with peak demand of a single primary busbar less than 7MVA, the increase caused by connecting DG can be approximately 5% to 8%. For DG penetration level between 10% and 90%, the total fault level is decreasing for approximately 0.5% of the base value per 10% increase in the DG penetration level. However, this reduction comparing to the base value is relatively small that this change can hardly be observed in the figures. This is because when the DG increases, the upstream generation decreases accordingly. Though for a single primary busbar, 10% increase of DG is not much, normally between 0.5MVA to 2MVA, the 10% reduction of upstream generation can be 20 to 30MVA. This generation reduction will cause the equivalent impedance of the further upstream network to increase approximately 10%, which leads to a reduction of appositely 2% to 4% in the upstream network contribution comparing to the base value.

On the other hand, as the DG is directly connected to the primary busbar, a 10% increase in the DG will cause the fault level contributed by the DG to increase approximately 10%. Comparing to the base value, this 10% increase in fault level contribution of DG is approximately 1.5% to 3.5% of the base value. The increase of fault level contributed by 10% DG of a single substation is approximately equal to the reduction of contribution by 10% of the total upstream generation. Therefore, the total fault level does not have obvious variations when the upstream generation and DG are changing correspondingly.

However, when the penetration level of the DG reaches 100% that all downstream load can be supplied by the DG, the power consumption from the upstream network will be very small. This causes the equivalent source impedance seen by the downstream network to be almost infinity which means the fault level contribution from upstream network can be negligible. This will cause the total fault level at a primary busbar to decrease approximately 5% to 10% comparing to the base value. Depending on the generation capacity of DG, the fault level at the 11kV primary busbar will varies between 90% and 95% of the base values when penetration level of the DG is 100%.

4.1.4 Fault Level Composition Change due to the Increase of DG

Though the fault level at the 11kV primary busbar does not change when DG capacity increases from 10% to 90%, the composition of the fault level is changing. The percentage of upstream contribution keeps decreasing while the contribution from DG is increasing. The results are shown in Figures 4.10 to 4.13.

The results indicate the fault level composition in terms of the average of each group. As shown in Figures 4.10 to 4.13, the contribution from DG is increasing by approximately 3% for every 10% increase of the penetration level. When the upstream generation is completely closed down from the network, the fault level compositions are approximately 60% to 70% contributed by the DG and 40% to 30% by downstream dynamic loads. During the increase of DG, as the total fault level does not change, the contribution of other downstream sources keeps almost steady.

When the penetration level of DG is 100%, as explained in 6.1, the equivalent impedance of the upstream network seen by the downstream network is almost infinity. Hence the fault level from the upstream network is negligible. Since the equivalent impedance of DG is larger than that of upstream network, when the penetration level is 100%, the fault level contribution from DG is less than that from the upstream network when no DG is connected. This also leads to the total fault level of 100% penetration level is approximately 5% to 10% less than the base value.

When the downstream network is relatively strong, the DG contribution can be about 60% of the total fault level when DG penetration level is 100%, as shown in Figure 4.13.

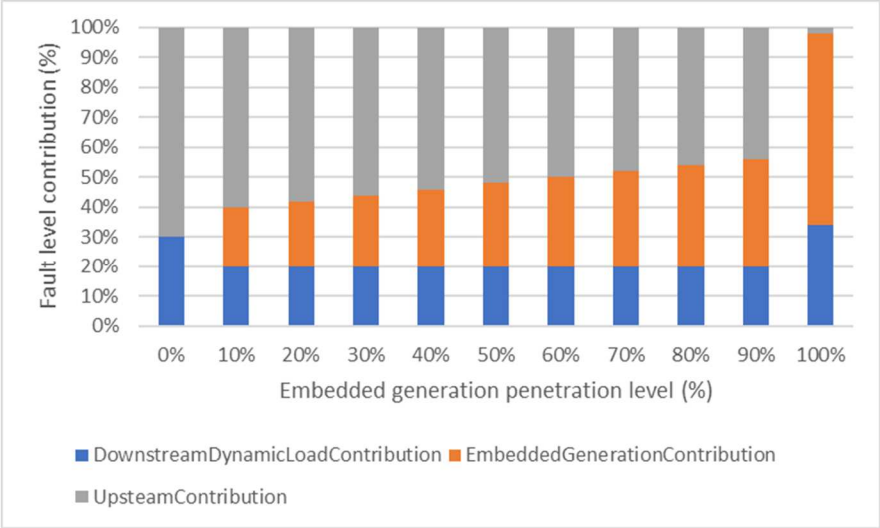

Figure 4. 10 Fault level composition when DG penetration level is increasing of Group 1

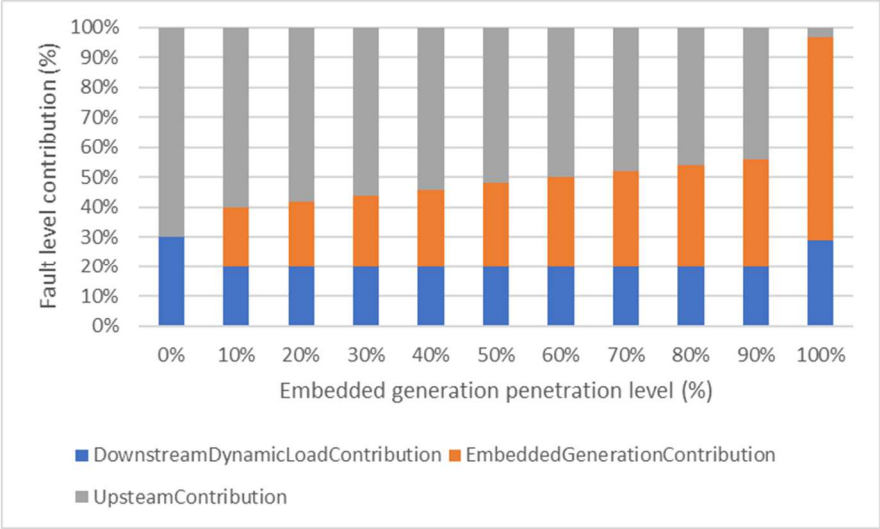

Figure 4. 11 Fault level composition when DG penetration level is increasing of Group 2

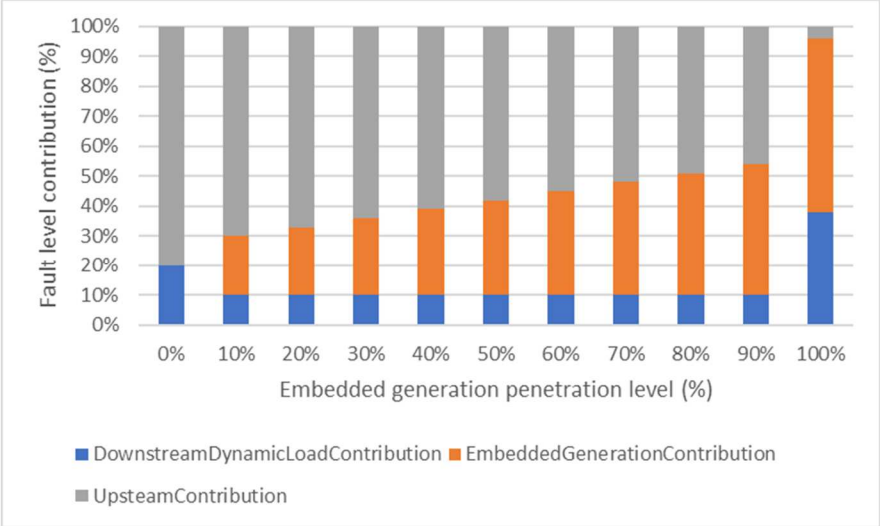

Figure 4. 12 Fault level composition when DG penetration level is increasing of Group 3

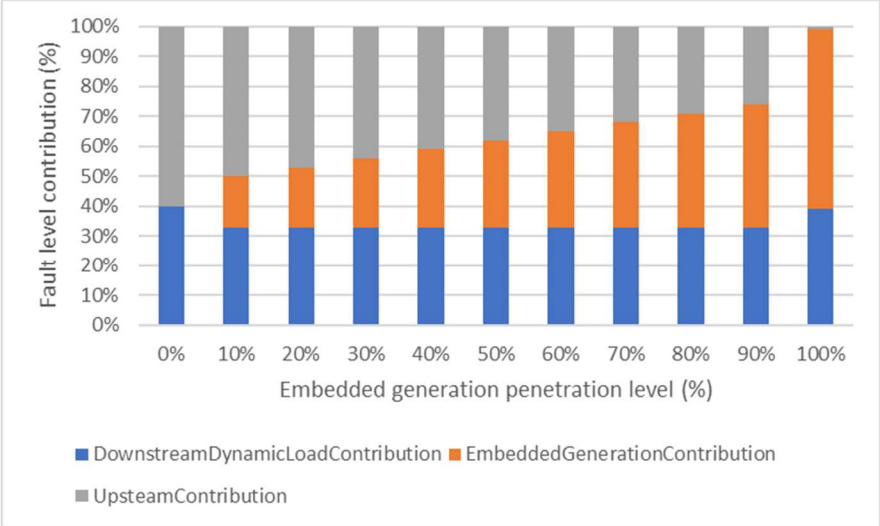

Figure 4. 13 Fault level composition when DG penetration level is increasing of Group 4

4.2 Analysis on the Downstream Load

To meet the targets on carbon emission reduction set in the 2050 Pathway Analysis, use of technologies with higher efficiency, which utilise renewable energy sources is encouraged. These low-carbon devices are mostly electrically powered, and this change will affect the load composition, and consequently affect the fault current contribution by the downstream load. Regarding domestic and transportation loads, it is also anticipated that there will be changes in the behaviour of consumers, caused by improvements in the efficiency and technology of electrical appliances and electrical vehicle. The adoption of high efficiency devices will have an effect on the general load characteristics. However, the change in the load behaviour of industrial and commercial loads are mainly to be affected by the economic environment and the main effect is on the total demand rather than the composition.

According to the Future Energy Scenarios 2015 (FES 2015), there are four scenarios estimated by National Grid [106]. These four scenarios refer to different levels of economy and low-carbon technology development. In the following section, the scenario, Gone Green, with moderate economic growth and focused innovation on low-carbon technologies, and the scenario, No Progression, with slow economic growth and little innovation in low-carbon technologies, are used in the analyses. This is because these two scenarios represent the most optimistic and pessimistic prediction of the UK economies and the other two scenarios are between the chosen two.

The predicted peak power demand changes in domestic, commercial and industrial categories, which are expressed as percentages of the comparable 2013 values; these are shown in Figures 4.14 and 4.15. In the Gone Green scenario, due to the economic growth, domestic and commercial loads are predicted to increase after 2019. The reduction in industrial load is caused by the adoption of high efficiency equipment in the manufacturing sector. Raised by the domestic load increase, the total load in the Gone Green scenario will increase by about 15% by 2035, compared to the 2015 demand. In the No Progression scenario, due to slow economic growth, both commercial and industrial loads continue to decrease. The total load will continue to decrease until 2025 and slowly recover to the current demand. In the following sections, the detailed analyses on domestic and transportation loads are carried out.

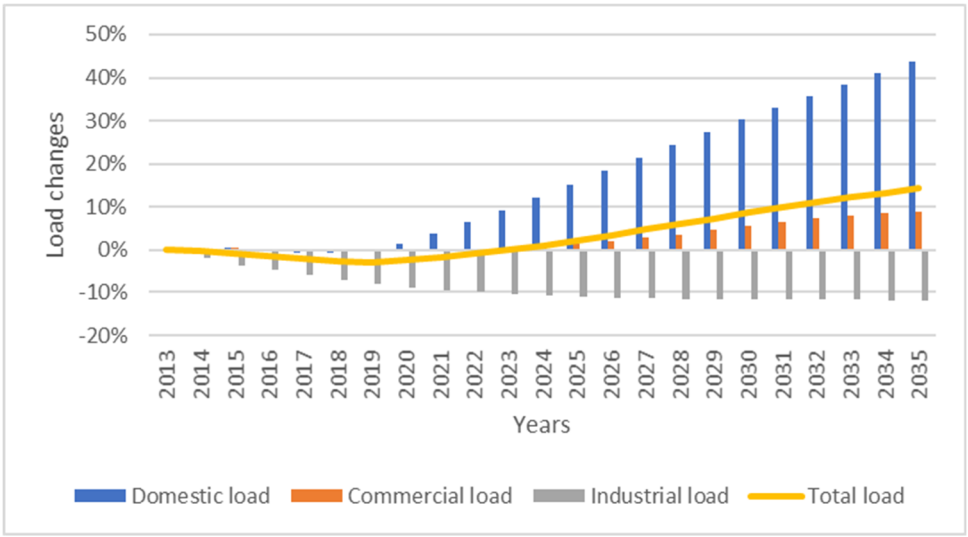

Figure 4. 14 Predicted power demand changes - Gone Green

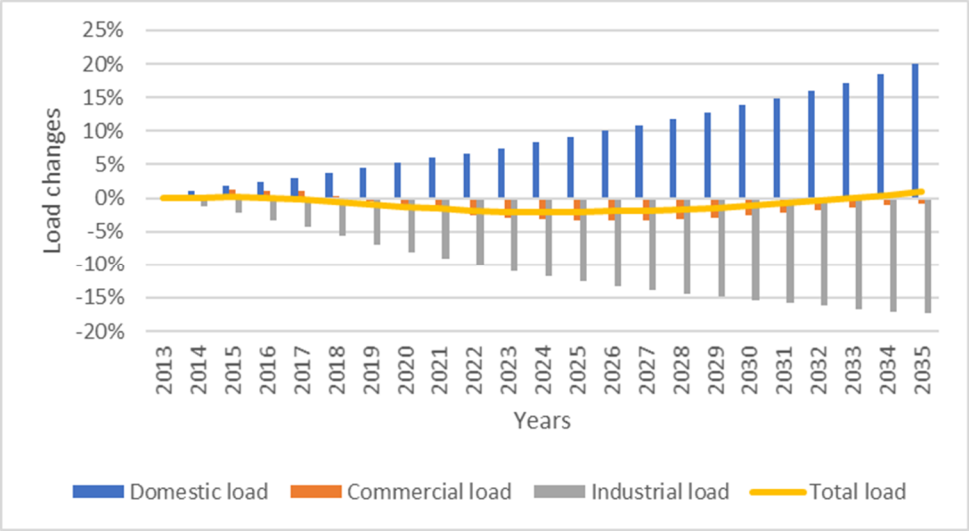

Figure 4. 15 Predicted power demand changes - No Progression

4.2.1 Changes in the Load Composition of the Downstream Load

4.2.1.1 Domestic Load

The change in domestic load occurs in both the peak load demand and the load composition. Following the Government policies, many more houses need to be built in the UK as the total number of residents is set to grow significantly over the next two decades.

This leads to more domestic appliances being connected to the network causing the peak load demand to increase. On the other hand, new technologies and devices are developed for daily usage. Motivated by Government policies, more energy efficient devices are being developed and pushed to market. The adoption of energy efficient devices will eventually replace current, less efficient devices and add more electrical devices into the network. This will cause the contribution of load composition from lighting, domestic appliances and heating in UK houses to change.

4.2.1.1.1 Lighting

Lighting currently accounts for approximately 12% of residential demand, down from approximately 15% in 2007. Changes in European and UK Government policies and consumer choice have driven the changes in the light bulbs used in homes and the amount of power consumed.

The 4TWh reduction in lighting consumption accounts for approximately half of the total 9TWh reduction in the weather corrected residential consumption achieved since 2007 [29]. Hence the effect of changes in lighting should be considered in the load composition analysis. EU standards for lighting are continuously evolving in order to reduce carbon emissions. The ban on larger incandescent bulbs was the main cause of the reduction in power consumption from 2007 to 2012.

Customers' preference has a huge impact, with Government data showing rapid adoption of halogen lighting since 2009 (halogen consumption increased from 4TWh/year to 7TWh/year between 2009 and 2012) as customers adopt spot-lights and replace single downlighters with multiple halogens [29].

LEDs could be widely adopted if their prices continue to fall and this would cause significant further reduction in power consumption (the average annual consumption of a halogen light is 26kWh/year compared to 7kWh/year for an equivalent LED). Table 4.1 shows the current average annual power consumption and rated power of commonly used lighting bulbs, for the same lumen level. Figures 4.16 and 4.17 show the estimation of numbers of different types of lighting in the next two decades in Gone Green and No Progression scenarios.

Table 4. 1 Average annual power consumption and rated power of different types of lighting

	Annual Consumption (kWh/year)	Rated Power (W)
Incandescent Light Bulbs	21	50
Halogen	26	36
Fluorescent Strip Lighting	25.5	35
Compact Fluorescent Light (energy saving)	11	15
LED	7	10

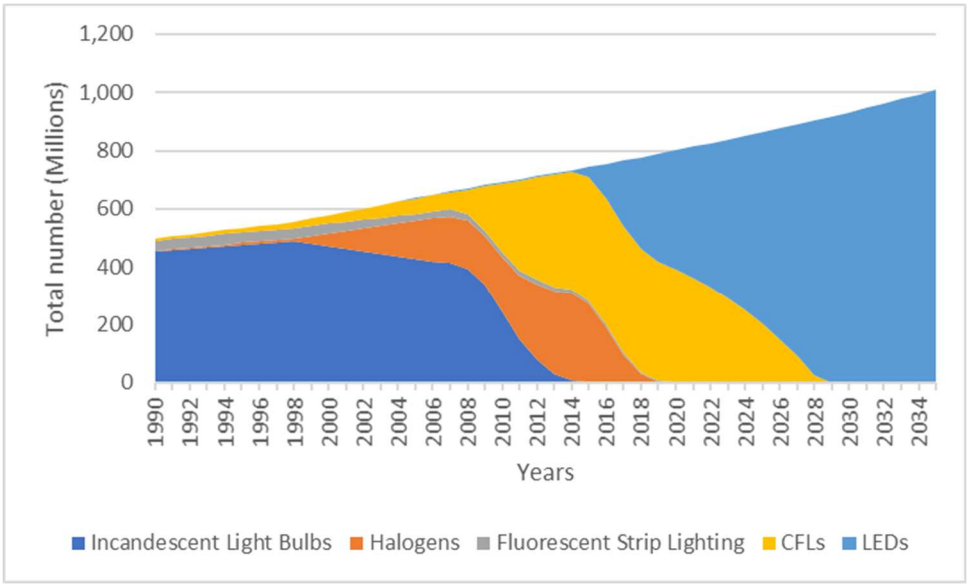

Figure 4. 16 Domestic lighting technology estimation - Gone Green

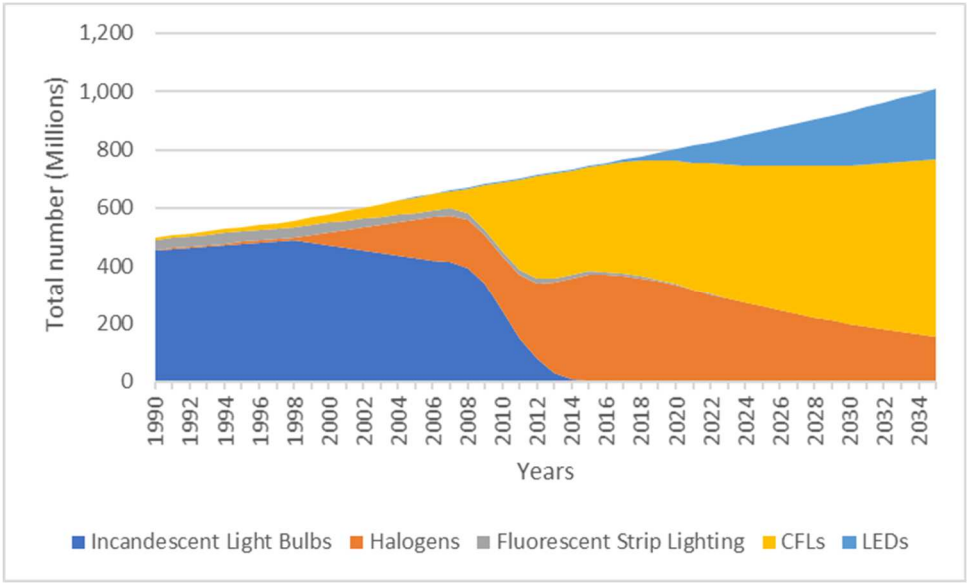

Figure 4. 17 Domestic lighting technology estimation - No Progression

In both the Gone Green and No Progression scenarios there is a terminal decline in electricity demand by filament light bulbs, and there is also a decline in halogen bulbs depending on the scenario. In terms of bulb numbers LEDs and CFLs become the dominant light source respectively and they represent over half of all the bulbs in use by 2035. The overall effect is a decline in both the power demand and energy consumption by lighting.

In the Gone Green scenario, LEDs are adopted almost universally by 2030, driven by higher electricity prices, higher technological innovation, which will also drive down the unit price, and the policy banning of selected halogen bulbs. Compact fluorescent lights (CFL) will be eliminated in the more prosperous Gone Green scenario. The opposite environment will exist in No Progression, with its lower electricity prices, lower technological innovation and low policy drivers. This slows the LED development and adoption rate and, by default, prolongs halogen usage.

Based on the data above, the average power demand of lighting for a single house in the UK can be estimated for the next two decades as shown in Figure 4.18. This result is further used in the estimation of peak load demand and load composition of domestic load.

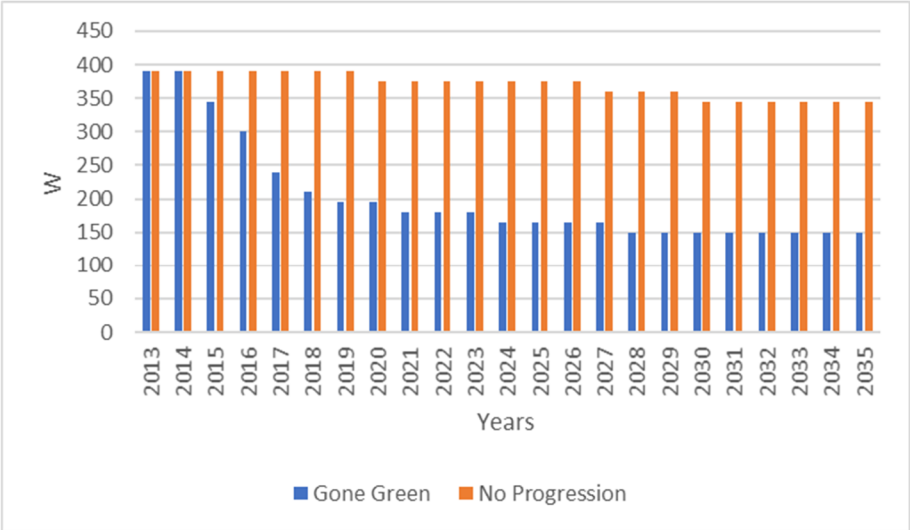

Figure 4. 18 Average lighting power demand of a single house in the UK

4.2.1.1.2 Domestic Appliance

Domestic appliances are divided into five general types: cold, wet, electronics, home computing and cooking, as shown in Table 4.2.

With improvements in the energy efficiency of these appliances, the rated power demand of each major type is estimated for two decades according to the Future Energy Scenarios 2014 [107], as shown in Figures 4.19 and 4.20. The results of the total difference between these two scenarios are shown in Figure 4.21. It can be seen from Figure 4.21 that for each house, the total load demand can save about 1.5kW by 2035.

When accumulate this by the total number of residential houses, it will be a huge reduction in the load demand for house appliance. These estimations are also used in the further analysis of future peak load demand and load composition of domestic load.

Table 4. 2 Appliances of different types of appliance

Appliance type	Appliances
Cold	Chester freezers, fridge-freezers and refrigerators
Wet	Washing machine, washer-dryers and dishwashers
Electronics	TV, DVD/VCRs and games consoles
Home Computing	Desktops and laptops
Cooking	Ovens, microwaves and kettles

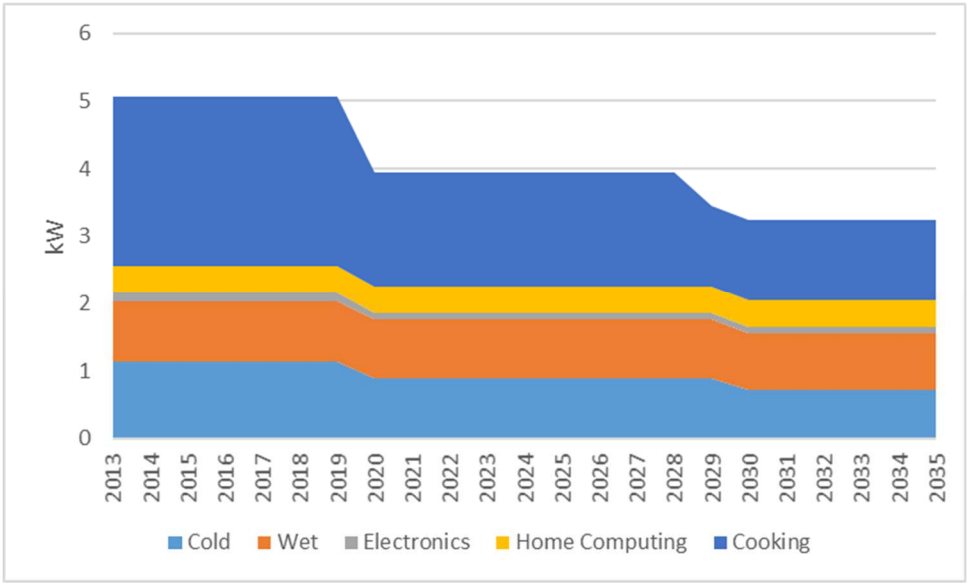

Figure 4. 19 Average power demand of different types of domestic appliance - Gone Green

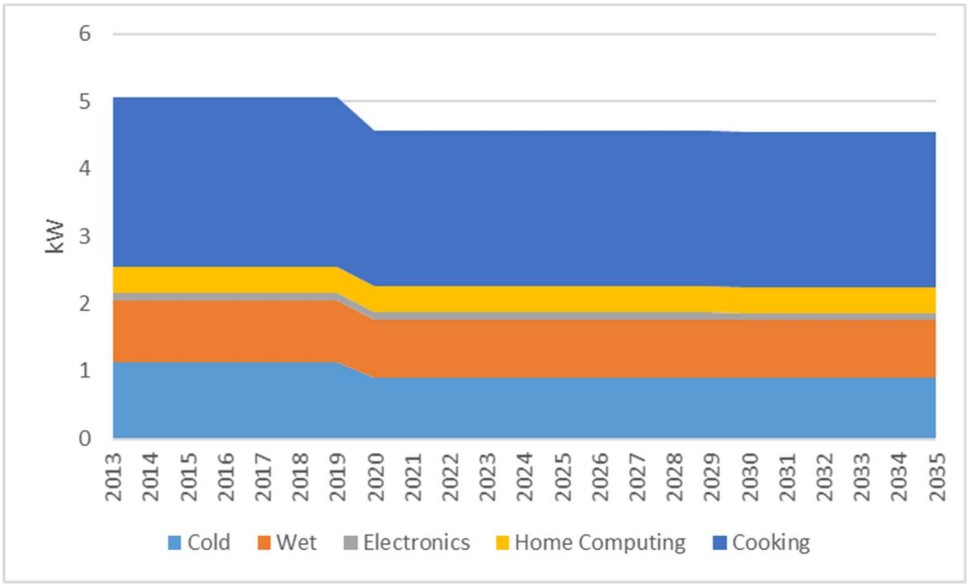

Figure 4. 20 Average power demand of different types of domestic appliance - No Progression

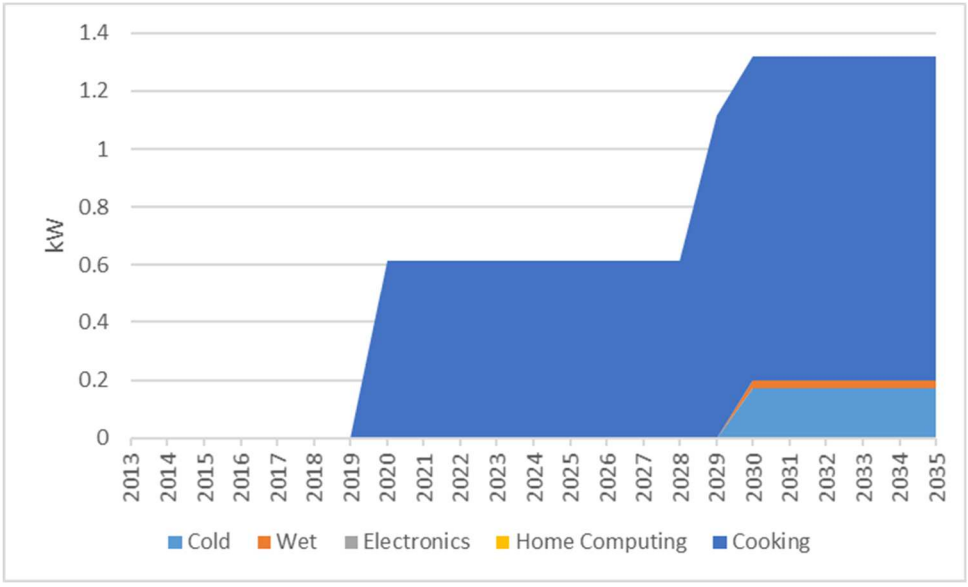

Figure 4. 21 Average power difference between two scenarios

4.2.1.1.3 Domestic Heating

Heating currently accounts for 8% of total electricity demand and 28% of gas demand [106]. Changes in heat demand, such as the introduction of new technologies with improved efficiencies, have a substantial impact on overall gas and electricity consumption. The introduction of new heating technologies could displace the traditional gas boiler. The main new heating technology considered here is the heat pump.

A heat pump is a device that provides heat energy from a source of heat to the heat sink. Heat pumps are designed to move thermal energy opposite to the direction of spontaneous heat flow by absorbing heat from a cold space and releasing it to a warmer one. A heat pump uses external power to accomplish the work of transferring energy from the heat source to the heat sink. Similar to a refrigerator, heat pumps generally draw heat from the cooler external air or from the ground and transfer the heat to the warmer internal destination [108]. In heating mode, heat pumps are three to four times more efficient in their use of electric power than simple electrical resistance heaters. Currently the installation cost for a heat pump is about 20 times greater than for resistance heaters [109, 110].

Figure 4.22 shows the working cycle of a heat pump. The refrigerant, is pressurised and circulated through the system by the compressor. The heat pump makes the refrigerant hotter by compressing it using the compressor. On the discharge side of the heat pump, the hot and highly pressurised refrigerant is cooled in a the condenser to provide heat for consumers.

The refrigerant cools down but maintain the high pressure when flows out of the condenser. The condensed refrigerant then passes through an expansion valve to release the pressure. The low-pressure refrigerant then enters the evaporator, in which the refrigerant absorbs heat. The refrigerant then returns to the compressor and the cycle is repeated. This is a dynamic load because of the motor-compressor set operated direct-on-line.

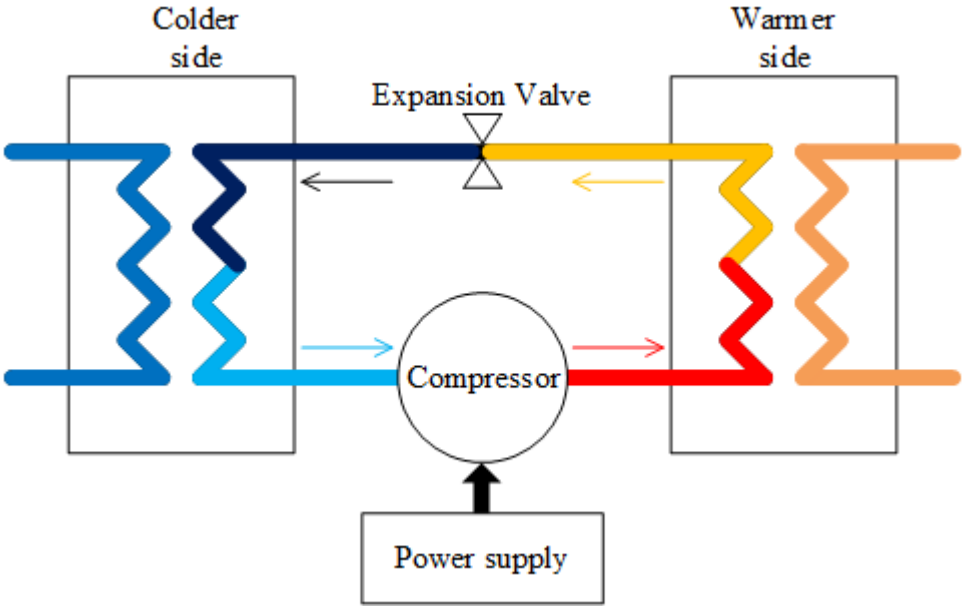

Figure 4. 22 Working cycle of heat-pump

Due to the use of a compressor, the behaviour of a heat pump during fault is similar to an air-conditioner and refrigerator in that it contributes fault current to the network. Generally, according to the heat source, the heat pump is classified into air source heat pump (ASHP), gas source heat pump, ground source heat pump (GSHP) and hybrid heat pump.

The analysis of the effects of the adoption of heat pumps on the domestic load demand and composition is based on the estimated numbers of heat pumps installed for domestic heating. The estimated numbers of residents and heat pumps for the next two decades are shown in Figures 4.23 to 4.25.

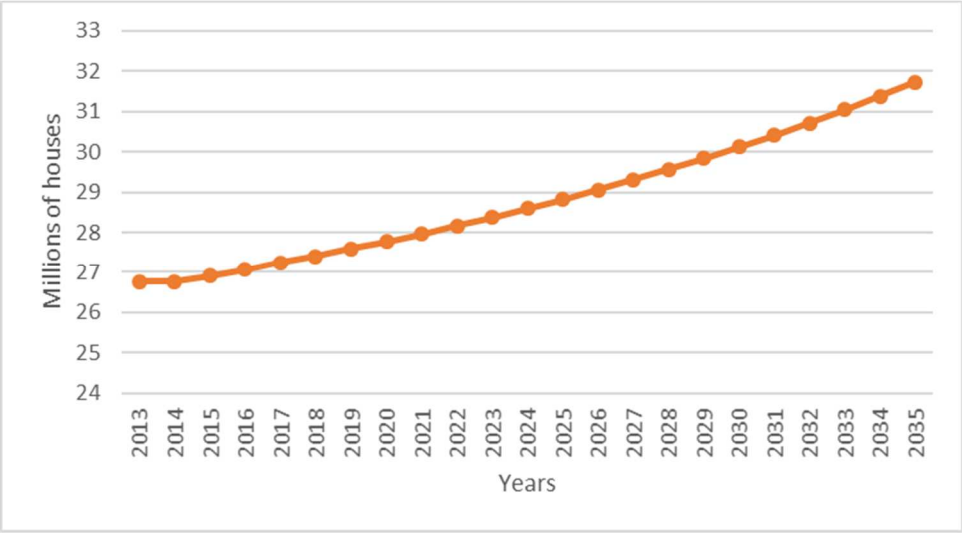

Figure 4. 23 Estimated UK resident house growth

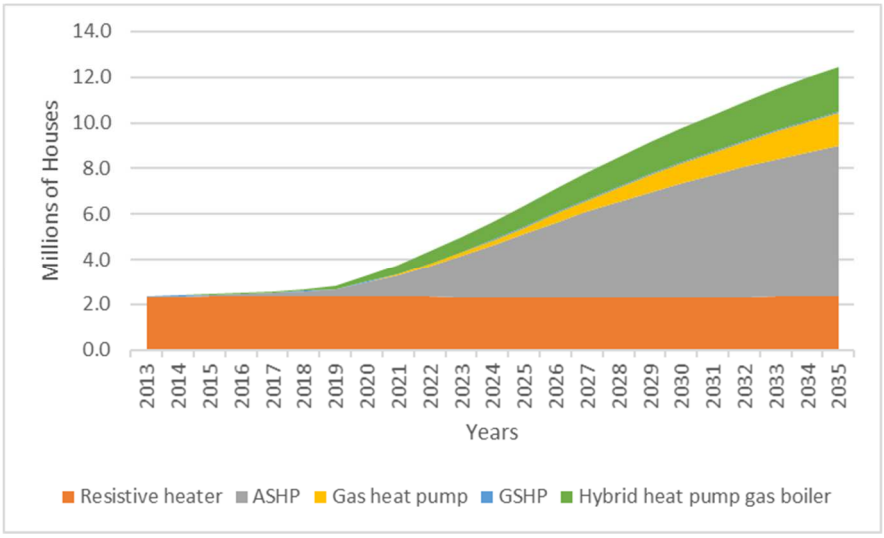

Figure 4. 24 Estimation of numbers of different types of electrical powered heaters - Gone Green [106]

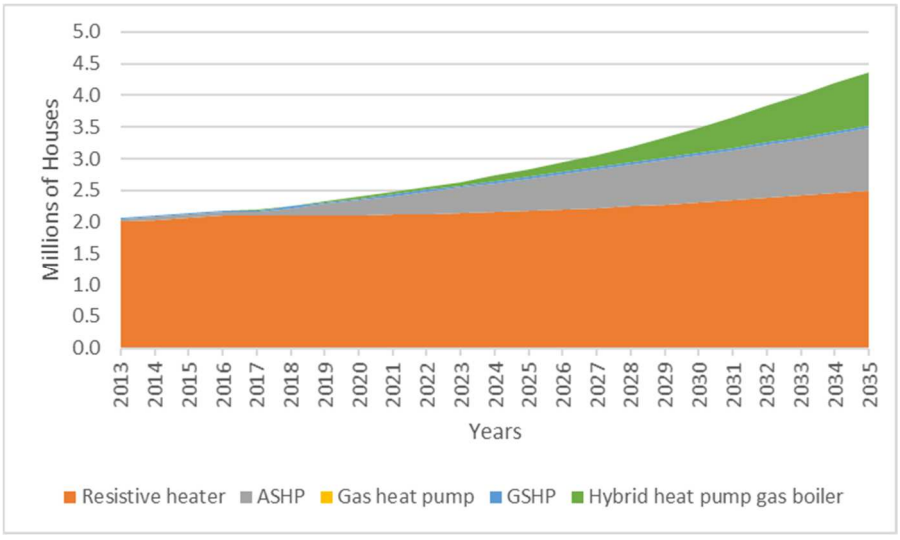

Figure 4. 25 Estimation of numbers of different types of electrical powered heaters - No Progression [106]

There is a rapid increase in the number of heat pumps after 2020 in the Gone Green scenario and by 2035, around one third of the houses in the UK will use a heat pump for the house heating (As indicated in Figures 4.24 and 4.25, it is estimated to be nearly 32 million houses in the UK and approximately 11 million of houses using heat pump for heating. While in the No Progression scenario, the uptake of heat pumps is very slow and by 2035, the total number of heat pump users is approximately two thirds of those using resistive heaters. Considering the weights of electrical resistive heaters and heat pumps in the total number of houses, the average electrical power demands in house heating for the next two decades can be calculated and are shown in Figure 4.26. The increase in the power demand from domestic heating follows the trend of the utilisation of heaters in both scenarios. However, the rate of increase in the power demand is less than (about half of) that for the number of heaters. This is because of the high energy efficiency of a heat pump in heat generation; it consumes half of the energy of a resistive electrical heater to generate the same amount of heat.

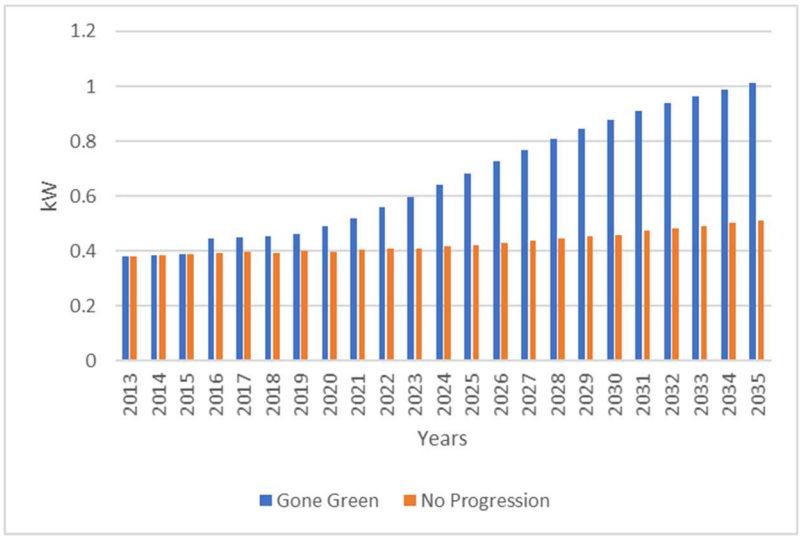

Figure 4. 26 Average Electrical Power Demand in House Heating

4.2.1.1.4 Domestic Load Composition

Based on the analysis above, the change in domestic load composition over the next 20 years can be calculated. The assumption for the calculation is that for a common UK residential house, the domestic electrical appliances include all types of appliance listed in Table 4.2, and one heater per house (resistive heater or heat pump). The appliances which contribute fault current during fault include cold, wet and heating appliances. The composition results in terms of static and dynamic loads are shown in Figures 4.27 and 4.28.

In the Gone Green scenario, the proportion of dynamic load continues to increase. This is mainly driven by the rapid growth of the utilization of heat pumps for domestic heating. The percentage of dynamic load will be approximately 44% of the general load by 2035. In the No Progression scenario, since the living status is not changing significantly, the dynamic component in domestic load varies slightly around 32%.

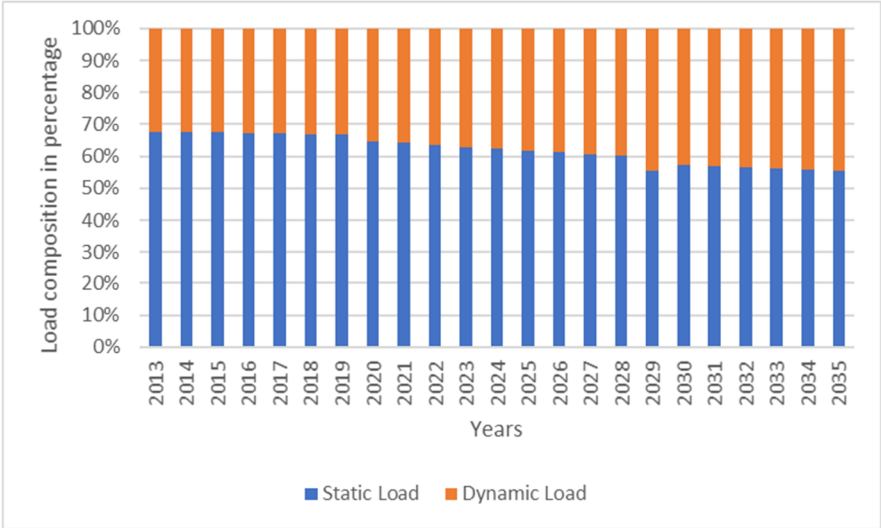

Figure 4. 27 Estimated load composition - Gone Green

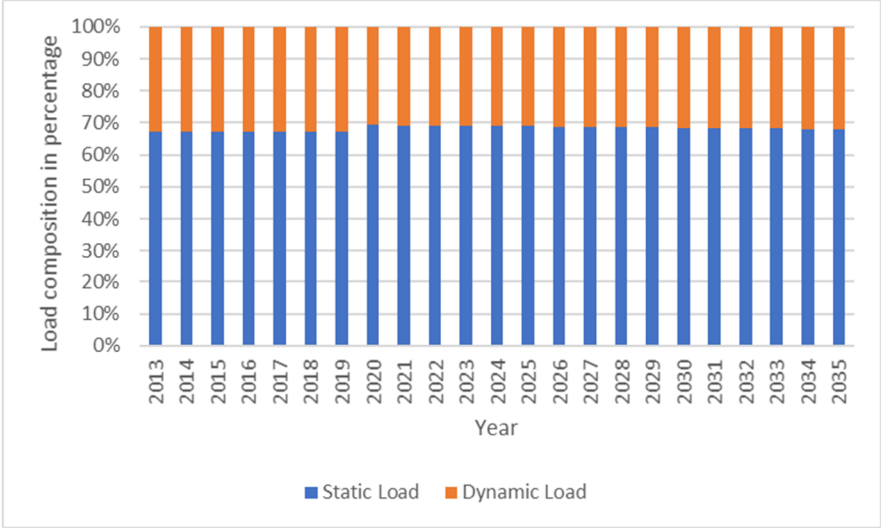

Figure 4. 28 Estimated load composition - No Progression

4.2.1.2 Transportation Load

According to the latest statistical data, the total peak transportation load on the distribution networks in the UK is 11.24MW, which is only 0.0187% when compared to the total peak load [29]. Hence the transportation load was not included in the previous load analysis. Since Government policy is to encourage the uptake of electrical vehicles, a technology which is starting to mature, over the next 20 years the number of electrical vehicles will undergo rapid growth, as shown in Figure 4.29.

This will cause a considerable increase in the load demand of transportation use in the distribution network. The estimated peak load demand increase caused by electrical vehicles is shown in Figure 4.30. This is obtained from the calculation of the percentage of the estimated peak demand of electrical vehicles in the estimated total peak demand, over the next two decades, using the data from National Grid's Future Energy Scenarios 2015. The slight trough in the Gone Green scenario in 2020 is due to the TOUTs (Time of Use Tariffs) that will come into effect in that year. This tariff causes the electrical vehicle customer to optimise the time when they charge the vehicle. Therefore, the TOUT will increase the efficiency in the use of electricity, which causes a slight dip in the load demand of electricity compared to before in a short term of time [106]. Although the peak demand of electrical vehicles is increasing, the contribution from electrical vehicles to the total load demand is less than 2% for both scenarios [106].

The effect of electrical vehicles on the total load demand is therefore likely to be negligible compared to the other types of loads. Though the effect to the total load demand is slight, the effect of electrical vehicle will increase the stress to the voltage profile in the distribution network operation [111].

When an electrical vehicle is connected into the network and is in the charging mode, during a grid fault, the vehicle will not contribute fault current to the network. The structure of a charger used in an electrical vehicle is shown in Figure 4.31. As shown in the figure, the power supply is the distribution network. With the IGBTs gated off, the diode rectifier charges the battery. When a short circuit fault occurs on the grid side, the diodes in the converter prevent current flowing back to the network from the battery [112, 113]. Hence it is not necessary to be concerned about the effect of electrical vehicle chargers on the fault level.

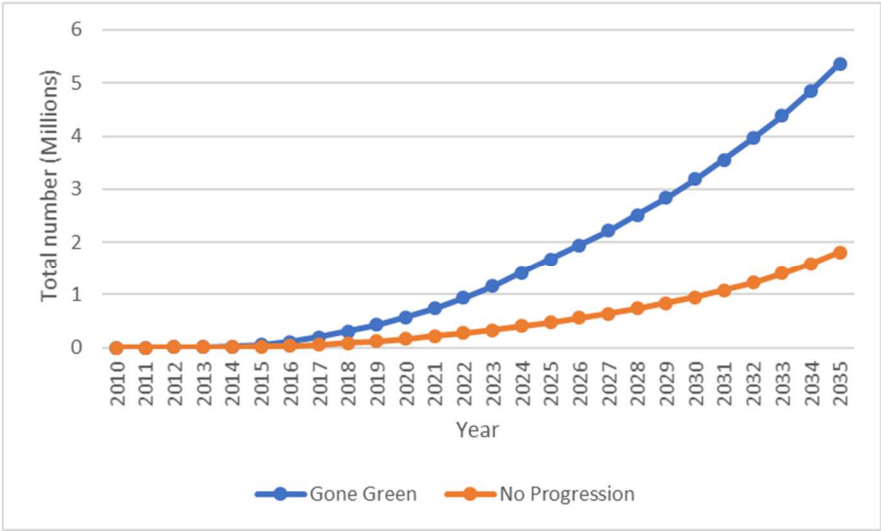

Figure 4. 29 Estimated number of electrical vehicle on road [106]

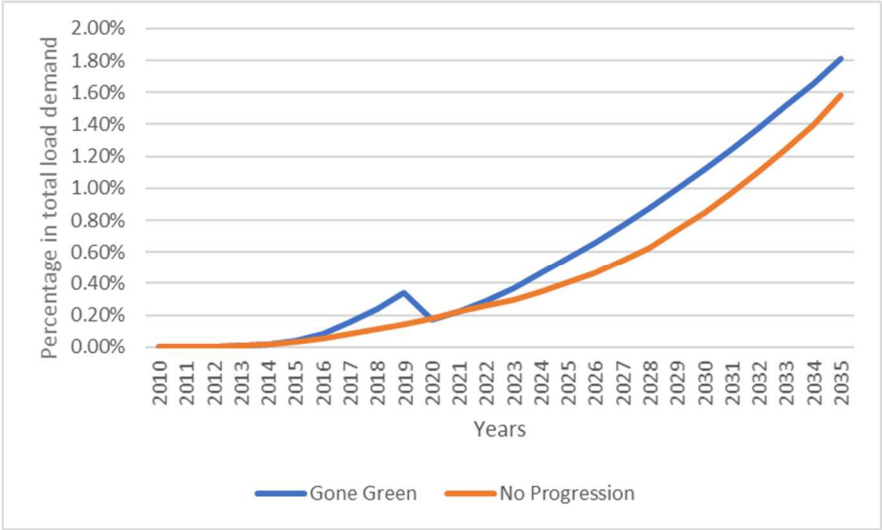

Figure 4. 30 Percentage of electrical vehicle in total load demand [106]

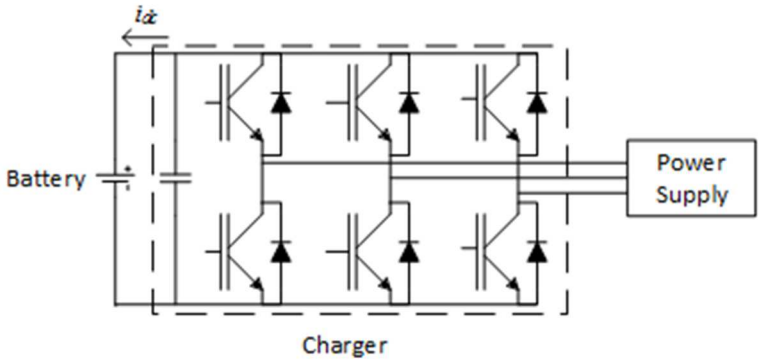

Figure 4. 31 Indication of electrical vehicle charger circuit

4.2.2 Effects of Changes in Downstream Load on the Fault Current Contribution

As shown in the previous section, the dynamic load will comprise a higher percentage in the Gone Green scenario. This leads to an increase in the fault level contribution of domestic load. Models of domestic loads are built to analyse the effect on fault level contribution (MVA/MVA). The modelling and analysis methods in Chapter 3 are used in this analysis. The fault level contributions of each type of load are required. For commercial and industrial loads, since the static-dynamic composition is assumed to be the same as before, the fault level contributions suggested in Chapter 3 are used, as shown in Table 4.3. For the transportation load, the contribution is negligible according to the analysis in Section 4.2.1.2. For the domestic load, there is a considerable increase in the percentage of dynamic load in the estimation. Hence the fault level contribution of domestic load is recalculated using time domain simulation under different percentages of dynamic component.

The domestic load is modelled as the combination of a constant impedance static load and a single-phase induction motor. The motor parameters used in the simulation are taken from Chapter 3. The results of the fault level contribution from domestic load are shown in Figures 4.32 and 4.33.

Table 4. 3 Normalized fault level contribution of commercial and industrial loads (MVA/MVA)

	Commercial	Industrial	Large industrial
Make	5.4	5.16	10.78
Break	1.3	0.69	2.02

From the results, it can be seen that in the Gone Green scenario, the normalised fault level contribution increases due to large scale adoption of heat pumps. In the No Progression scenario, the normalised fault level (make) is slightly reduced. This is because of the reduced power consumption in traditional dynamic load (cold and wet types of electrical appliances) in domestic use.

With the updated fault level contribution of domestic load, the estimation of fault level contribution of a general load for the next two decades can be developed. As discussed in Deliverable 8, the load composition varies from substation to substation. Hence the fault level estimation is substation specific. The results for the sample substation (data from a UK DNO) in the normal circuit breaker configuration (split mode) is given here as an example, as shown in Figures 4.34 to 4.39. The estimated fault level results take both upstream and downstream changes into the consideration.

As shown in Figures 4.34 and 4.35, in both scenarios, the peak demands of domestic load will increase over the next two decades. The peak load demand of commercial load remains relatively constant at around the present level. For industrial load, the peak load demand keeps decreasing for the next 20 years. In general, however, the total load demand increases.

In both scenarios, this results in the normalised fault level contribution, MVA/MVA, of the general load decreasing slightly. The main reason for the decline in the normalised fault level contribution of a general load is the decreasing peak load demand of industrial load, which is the main contribution of fault level from load in the distribution network. In the Gone Green scenario, the fault level will decrease until 2020 then rebound slightly. The fault level will then increase from 2020 to 2035. The reduction in the fault level is mainly due to the decrease of commercial and industrial loads. The increasing domestic load demand will not affect the total load demand until 2020. The large-scale adoption of heat pumps with the continuous increase of domestic load demand will cause the fault level to keep increasing. But for the No Progression scenario, the adoption of heat pumps is quite limited. Adding the effects of the reduced commercial and industrial load demand, the total fault level continues to decrease for the next twenty years. The results are shown in Figures 4.36 to 4.39.

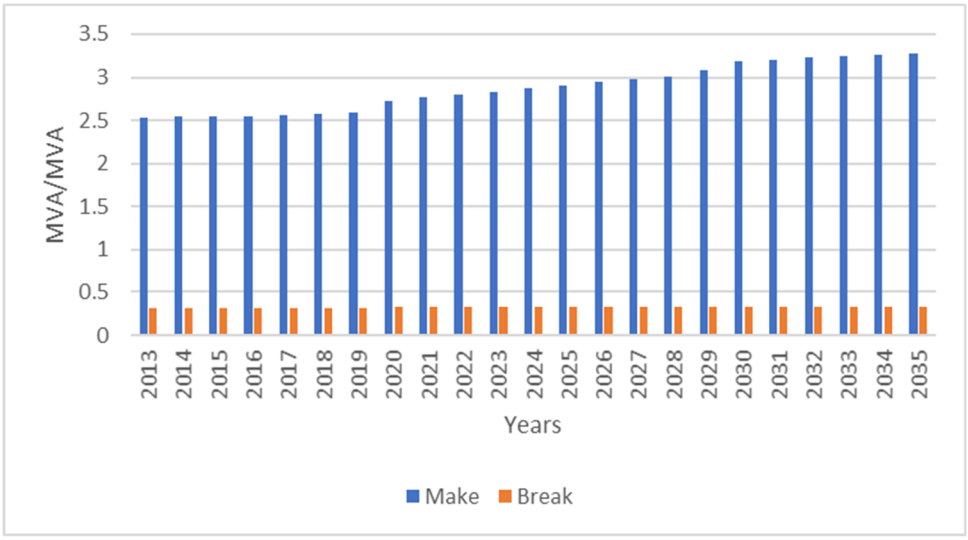

Figure 4. 32 Estimated fault level contribution - Gone Green

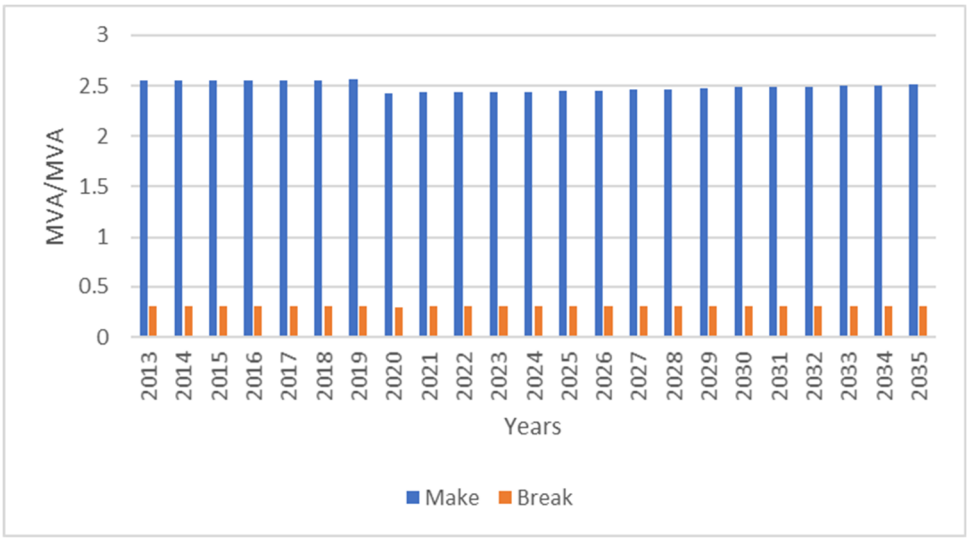

Figure 4. 33 Estimated fault level contribution - No Progression

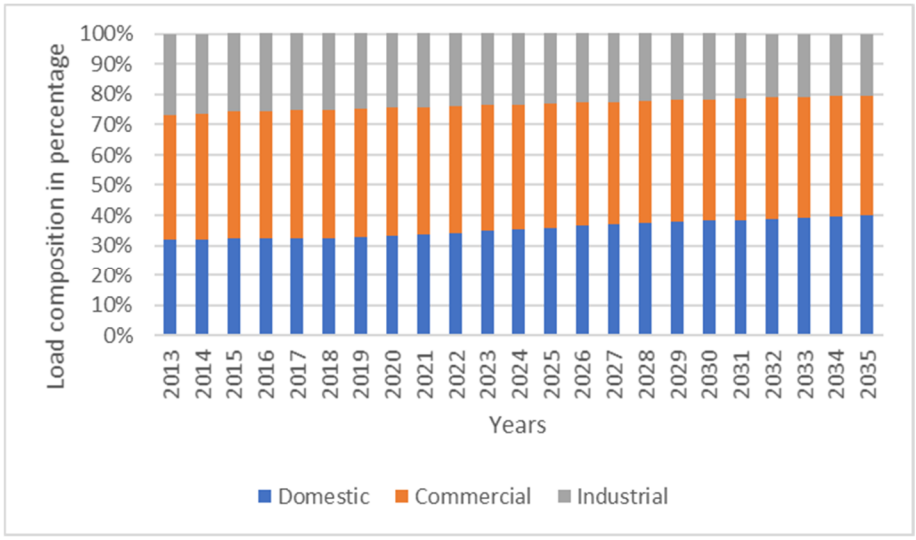

Figure 4. 34 Estimated load composition - Gone Green

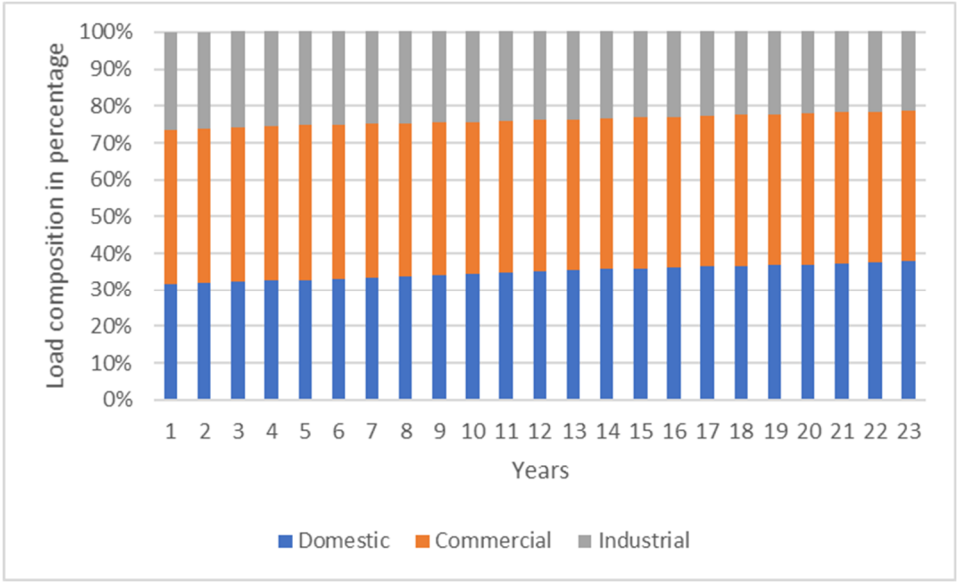

Figure 4. 35 Estimated load composition - No Progression

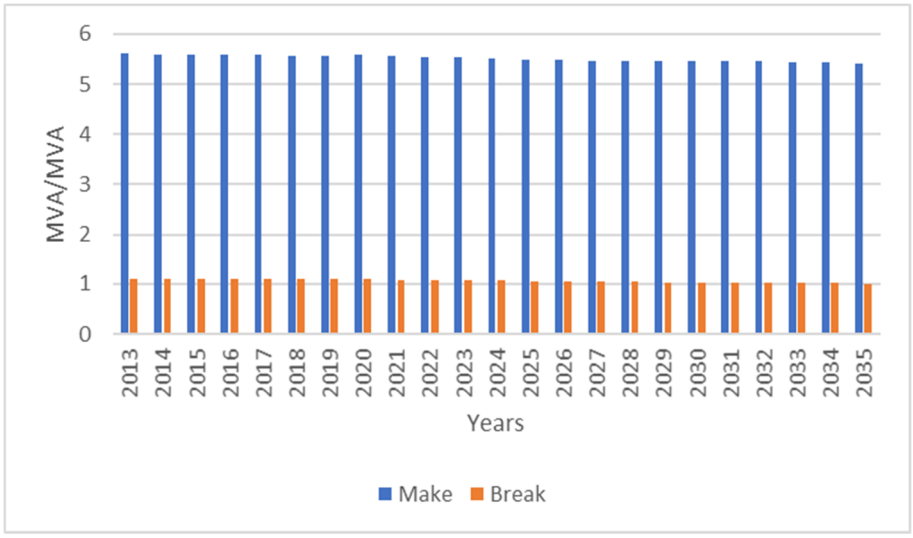

Figure 4. 36 General Load Fault Level Contribution (MVA/MVA) – Gone Green

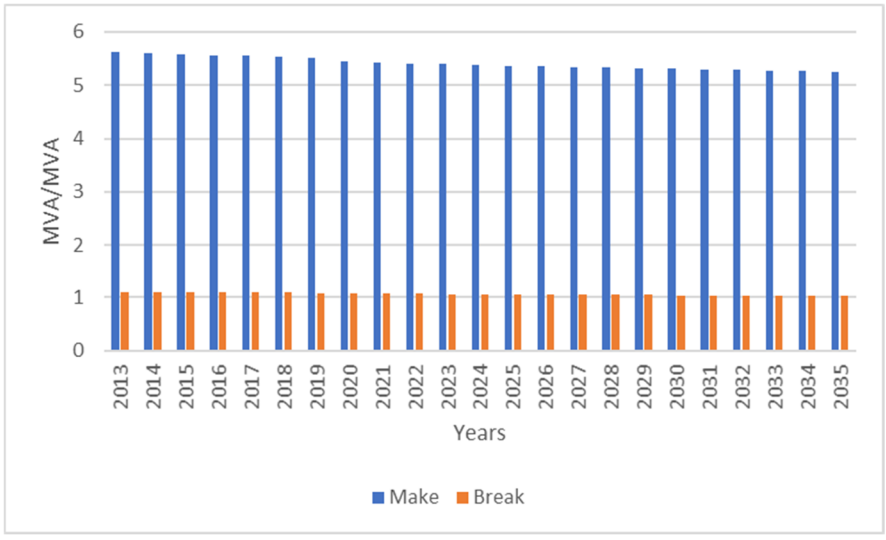

Figure 4. 37 General Load Fault Level Contribution (MVA/MVA) - No Progression

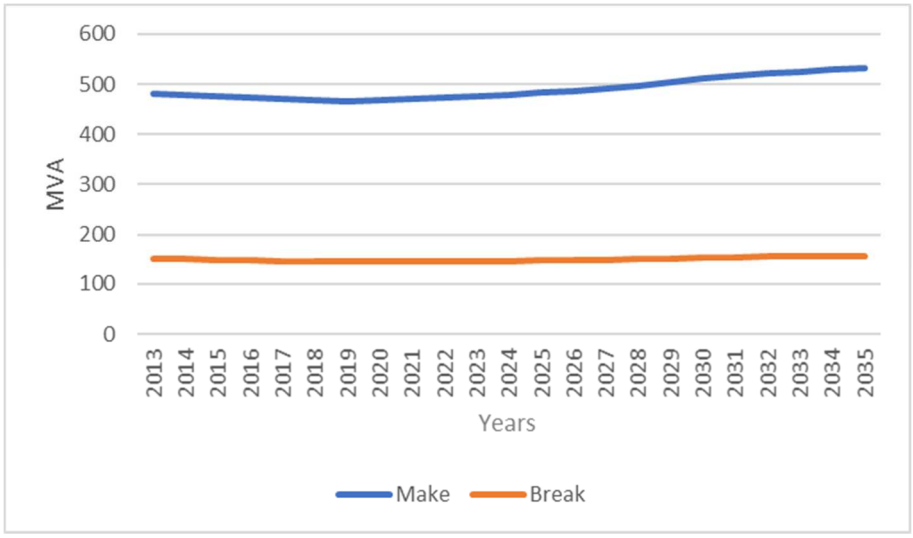

Figure 4. 38 Estimated general load fault level contribution – Gone Green

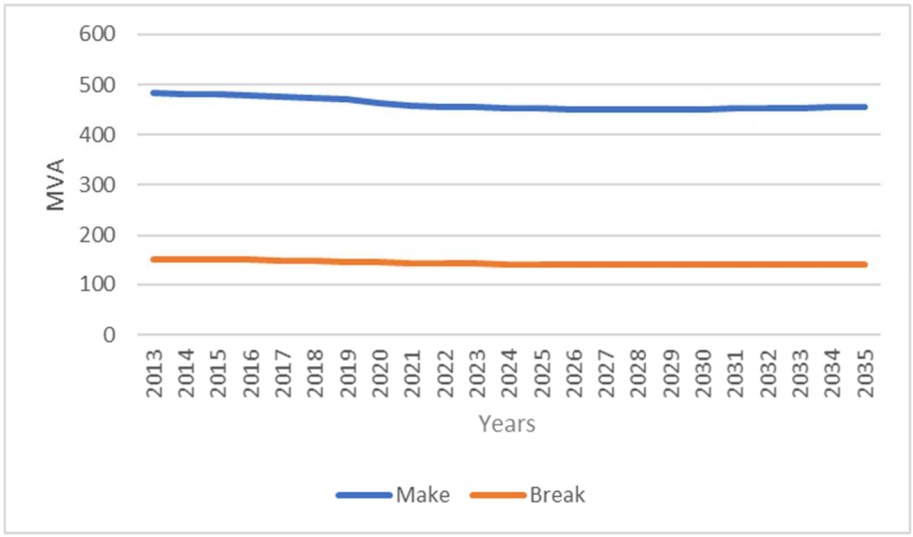

Figure 4. 39 Estimated general load fault level contribution – No Progression

4.3 Summary

In general, the present fault level at a primary 11kV busbar is 70% to 80% contributed from the upstream network, and 20% to 30% from the downstream network. For a weak upstream network and downstream network with interconnections, the composition of the fault level can be 60% from the upstream network and 40% from downstream. When the connected embedded generation reaches a certain amount, e.g. 10% of the total peak load demand, the fault level at the primary 11kV busbar will show a considerable increase, approximately 5% to 15% of the base value, depending on the local peak load demand. During the increase of embedded generation, the fault level at the primary 11kV busbar does not vary considerably until the total embedded generation penetration level reaches 100%, so that all load demand can be supplied by the embedded generation and the upstream generation is almost totally closed down.

In this situation, the fault level at the primary 11kV substation will reduce to 90% to 95% of the base value depending on the peak load demand of the 11kV substation. If the peak load demand is large, above 15MVA per primary busbar, the fault level under 100% embedded generation penetration level is close to the base value. If the peak load demand is small, e.g. less than 15MVA per primary busbar, the fault level under 100% embedded generation penetration level will be approximately 10% less than the base value.

The compositions of the fault level at the primary 11kV busbar when the embedded generation penetration level is 100% will be 60% to 70% contributed by the embedded generation, and 30% to 40% by downstream dynamic loads. Generally, the fault level head room for primary 11kV network is 20%, exclude 5% safety margin. With existing fault level headroom, the 10% penetration of embedded generation will generally cause the fault level to be approaching to the switchgear rating. In the most significant case, the increase can be 15% of the base value, which is equals to 10% of the switchgear rating. This leaves only 10% headroom even in the split operations. Hence, solutions have to be developed to solve this potential problem. However, once a solution has been applied, further increase of embedded generation penetration could be accommodated in the distribution network, and further solutions may not be necessary if the upstream generation is gradually closed down. There will be closing down of centralised power plants within the next 10 years. This will increase the equivalent impedance and reduce the fault level contribution from the upstream network to some extent.

For the predicted changes in the loads, two scenarios: Gone Green and No Progression are analysed. In the Gone Green scenario, the UK economy will have a moderate growth and renewable and low-carbon generation is high. The society will have increased focus on green innovation. Hence the peak load demand of industrial type is predicted to decrease. For domestic load, heat pumps are widely adopted for home heating. In this situation, the general load composition changes so that the percentage of domestic load increases and the percentage of industrial load decreases.

The percentage of dynamic load in the general load will also increase causing the total fault level to increase by approximately 5% by 2035, as compared to the present (2015) value. In the No Progression scenario, the UK economy will have a slower economic growth. Innovation in, and adoption of, low-carbon technologies are assumed to be low. In this situation, the peak power demand of industrial and commercial loads will keep decreasing. For domestic load, the power demand is increasing, but the heating method for UK residents will remain as predominantly gas powered. Hence the total load increases but the percentage of dynamic load reduces. This causes the total fault level contributed by load to decrease. Hence if the economic climate in the UK does not improve significantly, the fault level will decrease, with a reduction in industrial load demand being the main reason.

As for the adoption of electrical vehicles, even in the Gone Green scenario, the percentage of electrical vehicles in total peak load demand will be less than 2% by 2035. Hence it is anticipated that the total contribution made by electrical vehicles to peak load demand is unlikely to be of significant concern.

Chapter

5 Feasibility Study of the Protection for Series Compensators Using Shunt Thyristor Crowbar

5.1 Introduction

Due to the increase in load demand and DG installation in the recent years, improvement of voltage stability and power quality have been a concern of many DNOs. Many studies have been conducted to fulfil these requirements. A popular idea is to introduce soft open point (SOP) into the distribution network. An SOP is the inter-connection between two feeders using power electronic devices in the distribution network, which ideally provides connection during normal operation but isolation between the feeders during a fault.

The most common technologies used are back-to-back voltage source convertor (B2B VSC), static synchronous compensator (STATCOM) and static synchronous series compensator (SSSC). A comparison between functions of the three technologies is given in Table 5.1.

Table 5. 1 Functions of commonly used power electronic compensators in SOP [69]

	B2B	STATCOM	SSSC
Real power exchange	Y	N	Limited
Post-fault restoration	Y	N	Y
Reactive power support	Y	Y	Limited
Fault current restrain	Y	N	Limited
VSCs per device	2	1	1

Compared with STATCOM and SSSC, a B2B VSC has advantages, other than those listed in Table 5.1, in isolating incompatible ac networks due to issues in phase angle or frequency and completely blocking fault current from critical customers in the distribution network [114]. However, being relatively expensive in construction and of relatively high power loss in operation is the drawback of the B2B VSC scheme as compared to STATCOM and SSSC especially in medium-voltage network applications [115]. As shown in Table 5.2, the cost of installing B2B VSC in the transmission networks is much higher than STATCOM and SSSC [116]. The capacity shown in the table is the power manipulated across the network. The costs are the total capital costs for B2B VSCs, STATCOMs or SSSCs used in the network.

Considering that applying B2B VSC is still under trial in the distribution network, this data can be used as a reference and from this it can be concluded that using STATCOM and SSSC would be more cost effective to achieve the same control effect within their capabilities. Also, Table 5.3 shows that the power loss in B2B is much more than STATCOM or SSSC for the same power exchange. Therefore, this study will investigate the use of SSSC in an MV distribution network for full control capability.

Table 5. 2 Construction cost comparison between B2B VSC and STATCOM/SSSC [117]

Capacity (MW)	B2B VSC 2 terminal cost (Million $)	STATCOM/SSSC cost (Million $)
200	40-50	05-10
500	75-100	10-20
1000	120-170	20-30
2000	200-300	30-50

When two feeders are connected without using SOP, the fault levels of both feeders are added together. Since SSSC has limited capability in restricting fault current as indicated in Table 5.1 and is vulnerable during a network fault, external protection devices should be installed for the safe operation of SSSC. This is a further development. In term of fault protection, mechanical circuit breakers are the most conventional devices. However, in comparison with power electronic switches they have slow reaction to fault. Therefore, power electronic thyristor crowbars have been employed in cooperation with mechanical circuit breakers in the protection of SSSC based SOP.

Table 5. 3 Comparison between B2B VSC and STATCOM/SSSC [117]

	B2B VSC	STATCOM/SSSC
Losses	Medium+	Low+
Social implications	Low	Low
Operation cost	High	Medium

Two topologies using thyristor crowbar(s) to protect the SSSC in distribution network is proposed for this application. The diagrams of these two topologies are shown in Figures 5.1 and 5.2. In Topology 1, the thyristor crowbar provides a by-pass for the fault current to protect the SSSC during a network fault. In Topology 2, the thyristor crowbar creates alternative path to the ground for the fault current from Feeder 2, if the fault location is at Feeder 1 and vice versa. Both topologies prevent the fault current from directly flowing through the SSSC during the network fault.

The operation process for Topology 1 when a fault is detected in the network is as follows:

1) The thyristor crowbar is switched on;

2) The circuit breakers ① and ② are open to cut the SSSC out of the network; and

3) The thyristor crowbar is switched off.

For Topology 2, the protection process is as follows:

1) Both thyristor crowbars are switched on when a fault is detected;

2) Circuit breakers ① and ② of very low switching duties are opened to cut out the SSSC;

3) The thyristor crowbars are switched off; and

4) Circuit breakers ③ and ④ are open to cut out the whole equipment.

In the following sections, the feasibility is analysed for both protection topologies in several aspects. Regarding different coupling technologies of the SSSC, with transformer or using filter, the consideration of both types of SSSC is conducted in the feasibility analysis regarding the following aspects:

1) The fault level change due to the application of SOP with different protection topologies;

2) The over-voltage effects of transformer during fault period; and

3) The thermal capability of thyristor.

Another important aspect is that due to the installation of DG, if the fault location is close to the generator, the missing zero-crossing phenomenon may occur in the distribution network, affecting the operation of circuit breakers and increasing the operation time for the thyristor crowbars. This issue has been analysed regarding the effects of DG to network fault level part, in Chapter 3. Hence this aspect is not further analysed in the feasibility study in the following sections of this chapter.

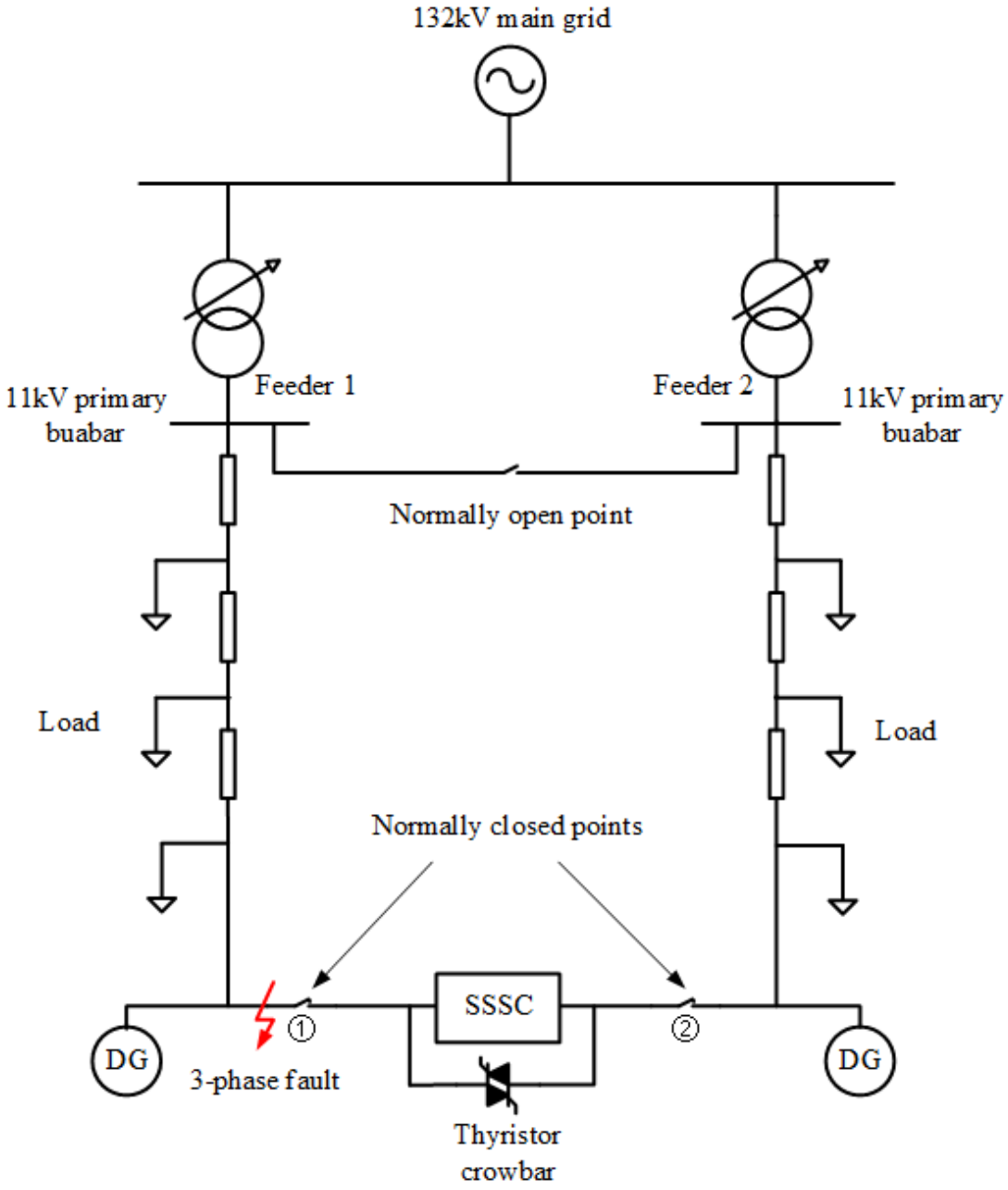

Figure 5. 1 Topology 1 using shunt thyristor crowbar in SSSC protection

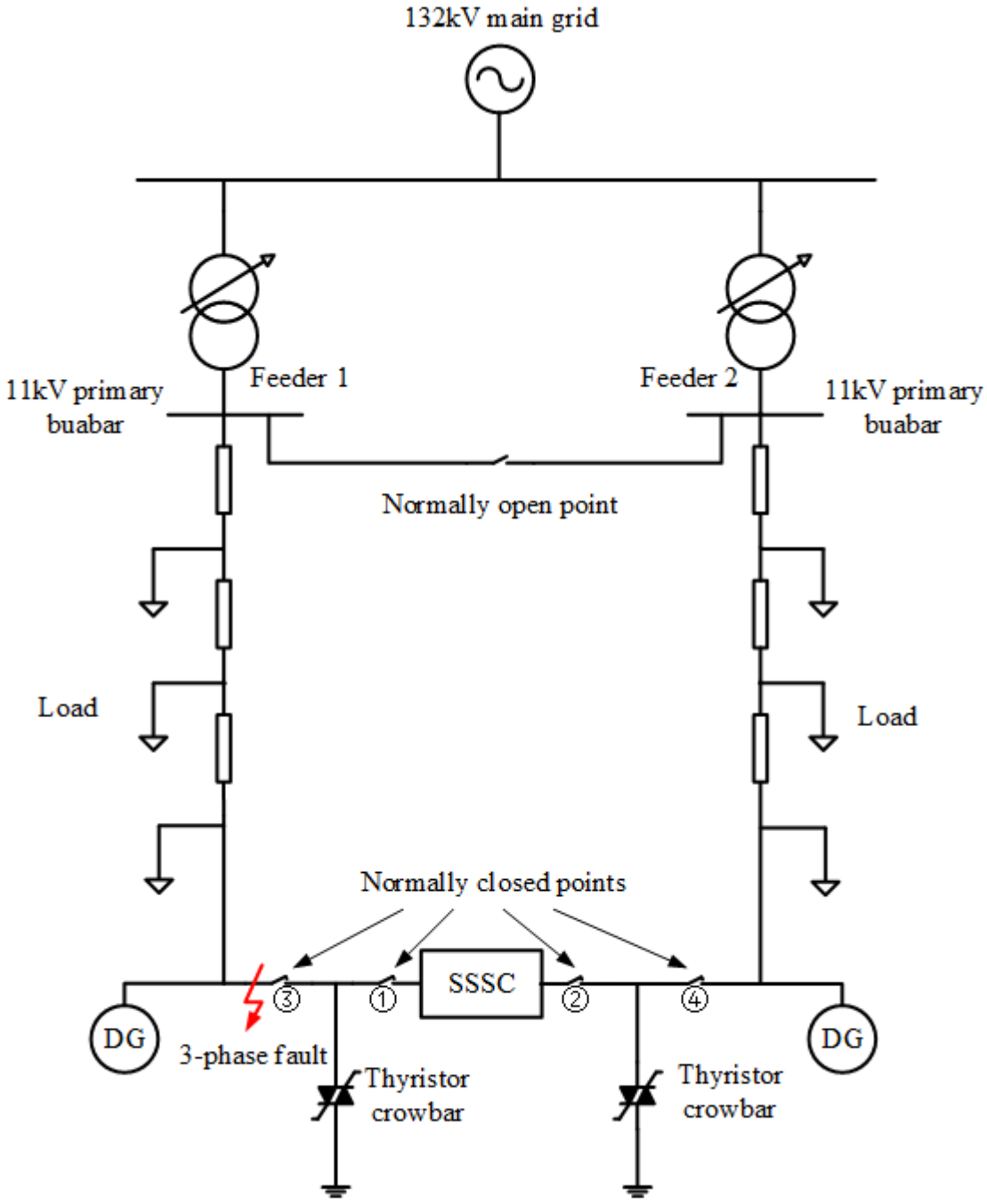

Figure 5. 2 Topology 2 using shunt thyristor crowbar in SSSC protection

5.2 Fault Level Study

Generally, when two feeders are in parallel connection, fault levels of both feeders are increased since both feeders will contribute fault current if a fault occurs in the network. In Topology 1, as indicated in Figure 5.1, when a three-phase fault occurs close to the SSSC on the side of Feeder 1, the shunt thyristor crowbar is switched on to protect the SSSC by by-passing the fault current. This by-passed fault current still flows into the fault location, which almost doubles the fault level of Feeder 1. It is the same when a fault happens on the side of Feeder 2. However, in Topology 2, both thyristor crowbars are switched on to divert the fault current away from the SSSC. If a fault occurs on Feeder 1, as indicated in Figure 5.2, the fault current contributed by Feeder 2 flows to the ground through the thyristor crowbar at Feeder 2 side without flowing into the fault location at Feeder 1. The fault current experienced by Feeder 1 does not increase compared to a split connection. Hence Topology 2 will not increase the fault level for either feeders connected by the SOP.

An 11kV network model with two feeders connected using the SOP at the end of both feeders is developed using Matlab/SIMULINK to verify the above analysis. The single line diagram of the 11kV distribution network model is shown in Figure 5.3. The parameters for the 11kV network are listed in Table 5.4.

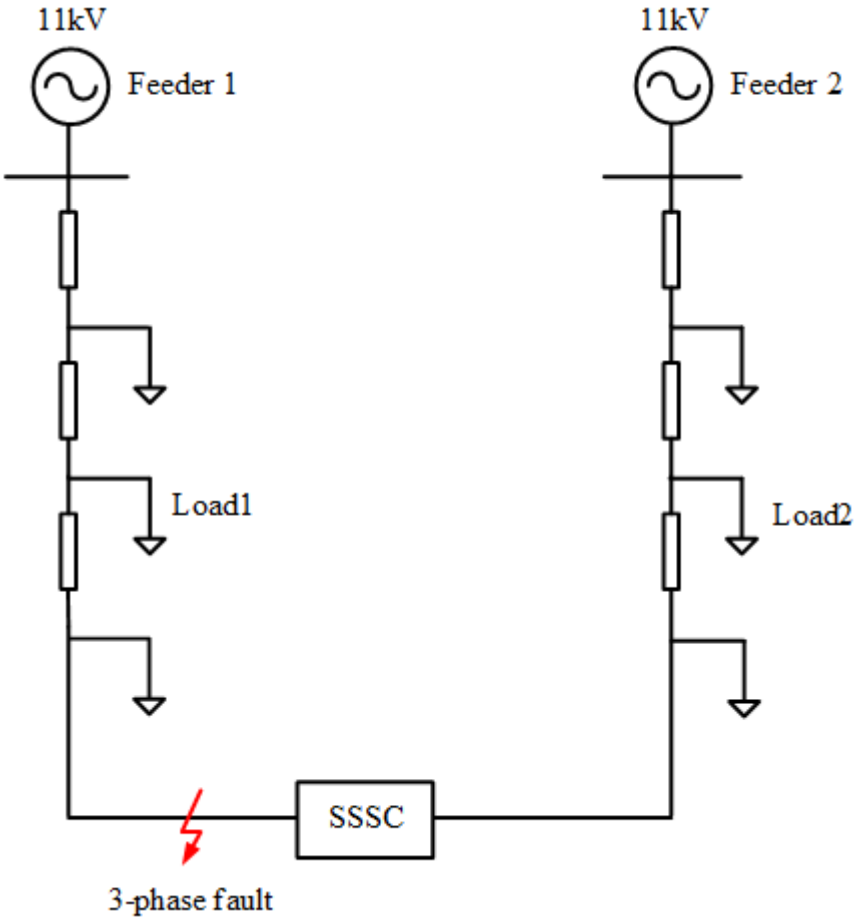

Figure 5. 3 SLD for the 11kV distribution network

Table 5. 4 Parameters for 11kV network model

		Feeder 1	Feeder 2
Voltage level		11kV	11kV
Source fault level		250MVA	250MVA
Cable Impedance	Resistance	0.06Ω/km	0.06Ω/km
	Inductance	0.314mH/km	0.314mH/km
Cable length		10km	10km
Load		15MVA	10MVA

For both feeders, the loads are modelled as static and distribute evenly along the feeder. The sources for both feeders are modelled as 11kV three phase voltage sources with the same fault level of 250MVA and background X/R ratio of 15. Both feeder have the same cable length and impedance. However, the total loads on the two feeders are different to create power exchange, controlled by the SOP, between both feeders. A three-phase fault is applied close to the SOP on the side of Feeder 1 as indicated in Figure 5.3. The simulation results of the total fault current at the fault location are given in Figure 5.4 for both topologies.

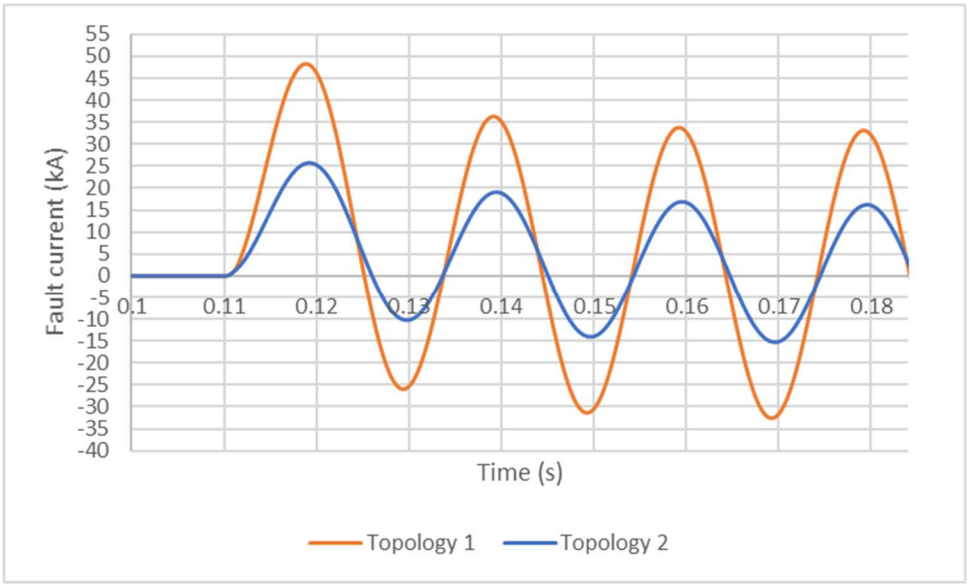

Figure 5. 4 Total fault current of Topologies 1 and 2

From Figure 5.4, it can be observed that the peak value of the total fault current in Topology 1 is approximately 48kA and in Topology 2 is just above 25kA. The steady state fault current, more than 70ms after the fault is 33kA in Topology 1 and 16kA in topology 2. It is obvious that the total fault current experienced at the fault of Feeder 1 is doubled in Topology 1 compared to that in Topology 2. Topology 1 cannot limit the fault level increase caused by the interconnection between feeders, but Topology 2 can.

5.3 Fault Detection

In practice, DNOs have monitoring devices installed in the distribution network to monitor the network voltage and current in real time. The abnormality in the monitored network voltage and current will be analysed and used in the network management. Commonly in the fault detection, if the monitored voltage or current changes by at least 20% compared to the nominal voltage or current of the network, it is regarded that a fault has occurred in the network and further protection actions are conducted [118]. Since two options of detection are available, a case study has been conducted to determine which one between voltage and current is better to be used in the fault detection in the protection of SSSC.

The working voltage and current of the SSSC are measured as the input for the fault detection. Two separate fault detection system are developed based on the monitored voltage and current, as shown in Figures 5.5 and 5.6. As shown in Figure 5.5, the working voltage of the SSSC, V_{sssc} is the amplitude of the voltage difference between the measured phase voltages on the two sides, V_1 and V_2. Then V_{SSSC} is compared to the rated voltage of the SSSC, V_n. If V_{sssc} is equal to or larger than 1.2 times of the rated voltage, it is regarded that a fault has occurred in the network. If not, the next V_{sssc} is calculated and performing the same judging process. When a fault is detected in the network, the amplitudes of measured V_1 and V_2 are compared to determine the fault location. If V_1 is larger than V_2, the fault is on the Feeder 2 side. Otherwise, the fault is on the Feeder 1 side. For the fault detection using current measurement, as shown in Figure 5.6, the working current of the SSSC on both sides are measured. The current, I_{sssc} is equalled to the measured current I_1 and I_2. Then I_{sssc} is compared to the rated current of the SSSC, I_n. If I_{sssc} is equal to or larger than 1.2 times of the rated current, it is judged that a fault has occurred in the network. If not, the next I_{sssc} is obtained to perform the same judging process. The fault location cannot be determined using current as reference.

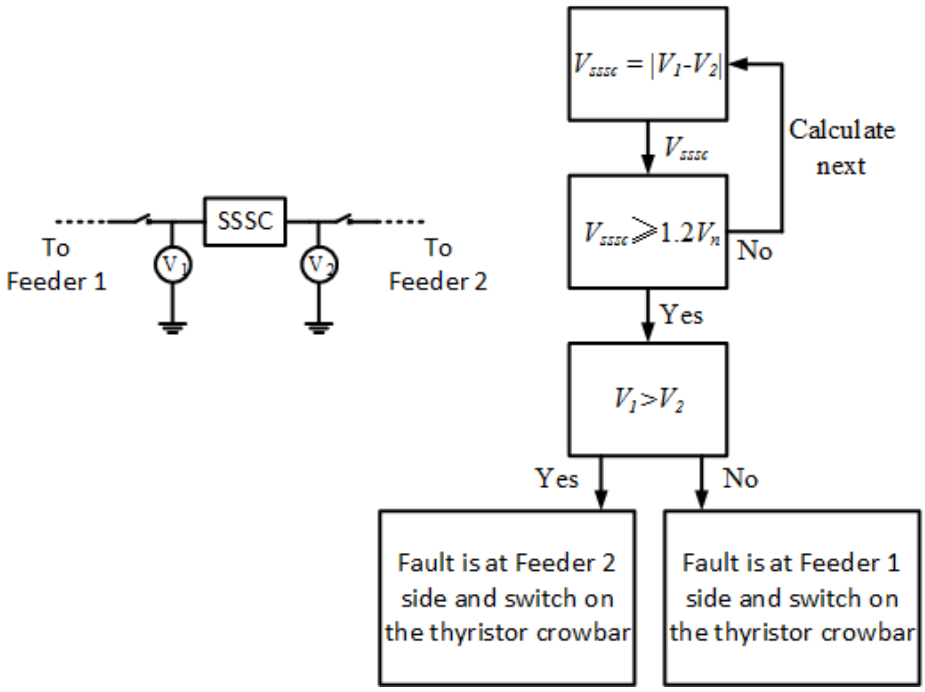

Figure 5. 5 Fault detection using voltage reference

The speed in fault detection of both methods is compared through simulations. The same network model as in Section 5.2 is used for the simulation. The time for signal transmission is ignored in the simulation. The results of the time when fault is detected by each method are shown in Figure 5.7. The fault occurs on the side of Feeder 1 at 0 ms. By using the voltage reference, the fault is detected approximately 9ms after the fault. The detected time by using current reference is approximately 9.8ms after fault. The results indicate that fault detection using voltage reference is faster than using voltage reference. The reason why current response to fault is slower than voltage is that the inductance in the network prevents sudden change in the current.

Since fault detection using voltage reference has the advantages in detecting speed and location determination to that using current reference, the working voltage of the SSSC is used as the reference in the fault detection in the simulations in the following sections.

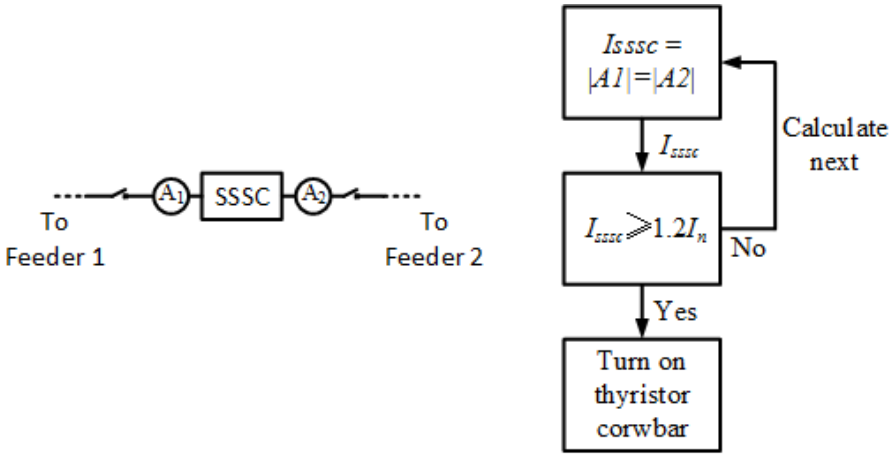

Figure 5. 6 Fault detection using current reference

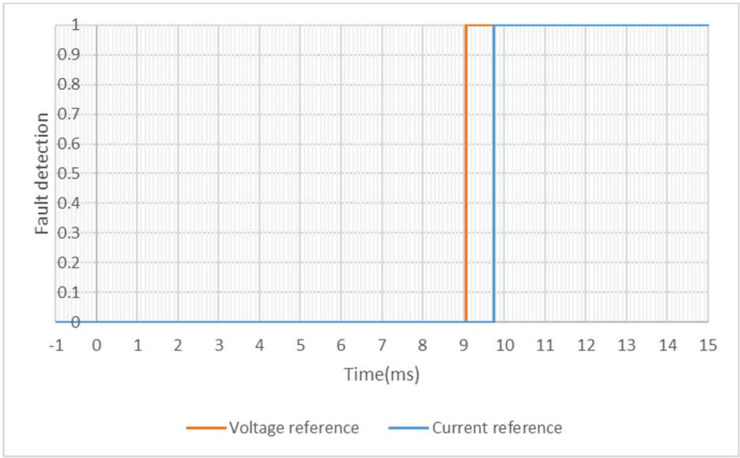

Figure 5. 7 Results for fault detection speeds using voltage and current reference

5.4 Transformer Over-voltage

When using a transformer in the SSSC, the primary winding is connected in series into the network. By controlling the output voltage of the converter connected to the secondary winding of the transformer, functions like voltage compensation and power flow control can be realised. The rated primary winding voltage in the SSSC transformer is determined according to the maximum power exchange between the connected feeders.

During fault condition, the phase voltage on the fault side is approximately zero while the phase voltage of the other side is almost the full voltage of the network. Before the SSSC is cut out from the network, the series transformer must withstand almost the whole voltage of 11kV on the primary side. This over voltage during fault may cause the transformer core to saturate. If the transformer core is saturated, the equivalent mutual impedance of the transformer will decrease significantly leading to a large increase in the magnetizing current. This magnetizing current will heat up the winding and cause damage to the transformer and converter. Hence to understand whether the transformer will saturate during fault is important in the feasibility study of the application of SSSC in SOP. The equivalent circuit referring to the primary side of a transformer is shown in Figure 5.8.

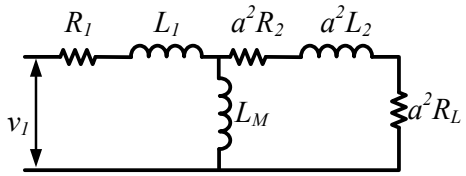

Figure 5. 8 Equivalent circuit of a transformer referring to the primary winding

As shown in Figure 5.8, v_1 is the primary winding voltage, R_1 and R_2 are the resistances of the primary and secondary windings. L_1 and L_2 are the leakage inductances of the primary and secondary windings. L_M is the mutual inductance and R_L is the load resistance. a is the winding ratio. The voltage over the mutual inductance v_M can be calculated by:

$$v_M = v_1 \frac{Z'}{Z_1 + Z'} \tag{5.1}$$

where:

$$Z_1 = R_1 + j\omega L_1 \tag{5.2}$$

and

$$\frac{1}{Z'} = \frac{1}{j\omega L_M} + \frac{1}{a^2 R_2 + j a^2 L_2 + a^2 R_L} \tag{5.3}$$

The saturation of a transformer core is determined by the magnetic flux density, B, of the core. It can be calculated by the integration of the voltage over the mutual inductance using the following equation:

$$B(t) = \frac{1}{N_1 A_c} \int v_m(t) dt \tag{5.4}$$

where N_1 is the number of turns of the primary winding and A_c is the cross-section area of the transformer core. During fault, when the thyristor crowbar is switched on, the load (the IGBT converter for a SSSC) at the secondary winding of the transformer is short-circuited, which results in R_L being zero. Hence, during fault, the equation (5.3) reduces to:

$$\frac{1}{Z'} = \frac{1}{j\omega L_M} + \frac{1}{a^2 R_2 + j a^2 \omega L_2} \tag{5.5}$$

Generally, for a power transformer produced by silicon lamination steel, the transformer core will saturate when the magnetic flux density is more than 2T [119]. The network model in Figure 5.3 is used to conduct simulations to study whether the iron core saturates due to the over-voltage of the transformer. Parameters of the transformer used in the simulation are listed in the Table 5.5. Several scenarios with different cable lengths of the network are studied. The simulation results of the magnetic flux density of the transformer iron core are shown in Figure 5.9.

Table 5. 5 Transformer parameters

Size	5 MVA	R_1	0.002 p.u.	N_1	125
V1	2.2k V	L_1	0.05 p.u.	N_2	39
V2	690 V	R_2	0.002 p.u.	A_c	0.04 m^2
L_M	500 p.u.	L_2	0.05 p.u.		

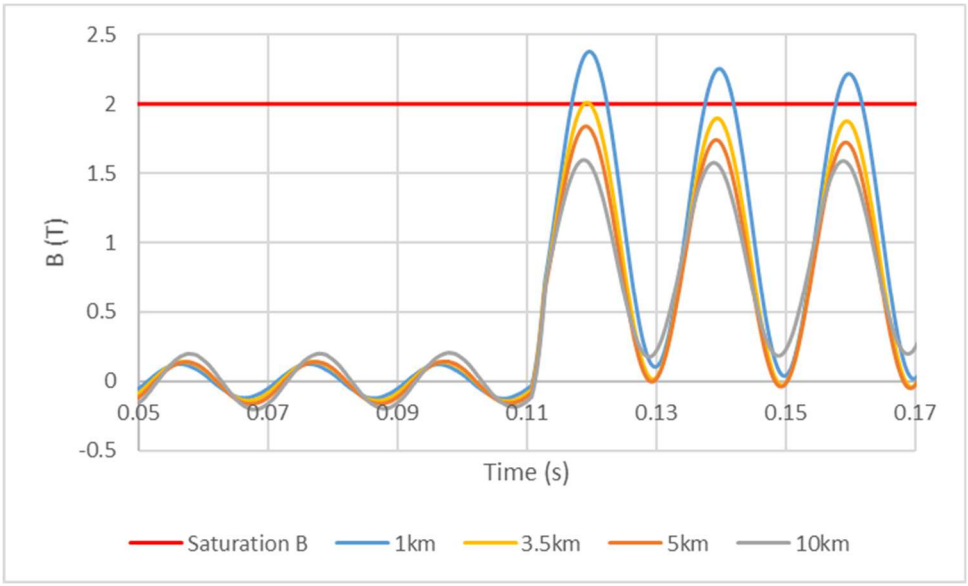

Figure 5. 9 Core magnetic flux density during fault

The result indicates that when the protection functions normally, the iron core of the transformer becomes saturated only if the SOP is close to the primary busbar. As shown in Figure 5.9, when the cable length is longer than 3.5km, the iron core will not saturate, otherwise the core saturates due to the over-voltage on the primary side. The low magnetic flux density during normal operation is due to the low working voltage, as shown in Figure 5.10.

When the location of the SOP is moved away from the 11kV background network, the magnetic flux density of the transformer core during fault is decreasing. This is because when the thyristor crowbar is switched on, the SSSC is equivalent to being short-circuited by the thyristor crowbar. After the switching on of the thyristor crowbar, the voltage of the SSSC will have an obvious reduction due to the low on-state impedance of the thyristor crowbar. Though the on-state voltage of the thyristor crowbar is low, if the SOP is close to the primary busbar (cable length is short), the overvoltage of the SSSC on the primary side of the transformer can still drive the transformer core into saturation, as shown in Figure 5.9 for cable length of 1km. With the increase of the cable length, the cable impedance is increasing. This leads to a decreasing voltage over the thyristor crowbar and a decreasing magnetic flux density in the transformer core due to decreasing voltage. When the cable length is longer than 3.5km, the overvoltage of transformer will not cause saturation in the iron core if the thyristor crowbar can be switched on during fault. Therefore, when the SOP is installed close to the primary busbar, transformers with high primary winding leakage inductance (L_1) can be used to prevent the iron core from becoming saturated. Simulation result of the magnetic flux density of the iron core when cable length is 3.5km using a transformer with L_1 equalling 0.1 p.u. is shown in Figure 5.11. As shown in Figure 5.11, the magnetic flux density of the iron core is reduced and does not saturate during fault. This is because the increased L_1 reduces the voltage across the mutual inductance of the transformer and further reduces the magnetic flux density of the transformer core during fault.

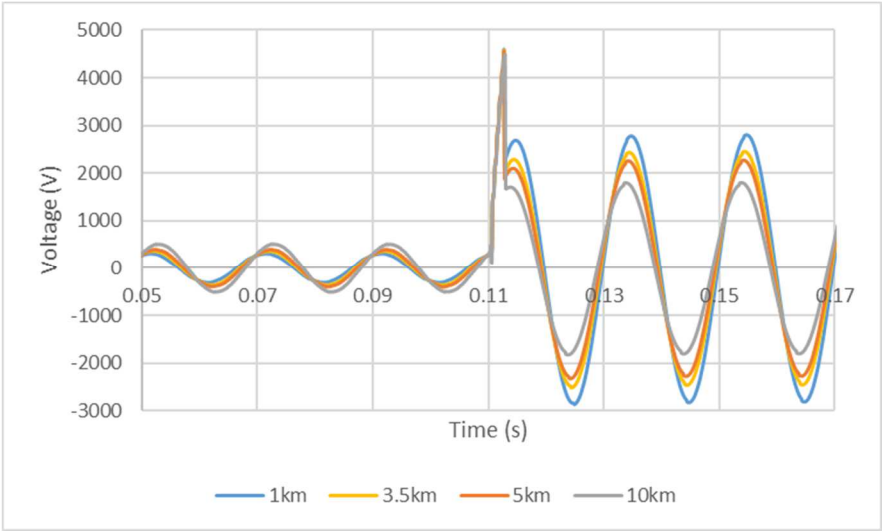

Figure 5. 10 Voltage of the SSSC during fault

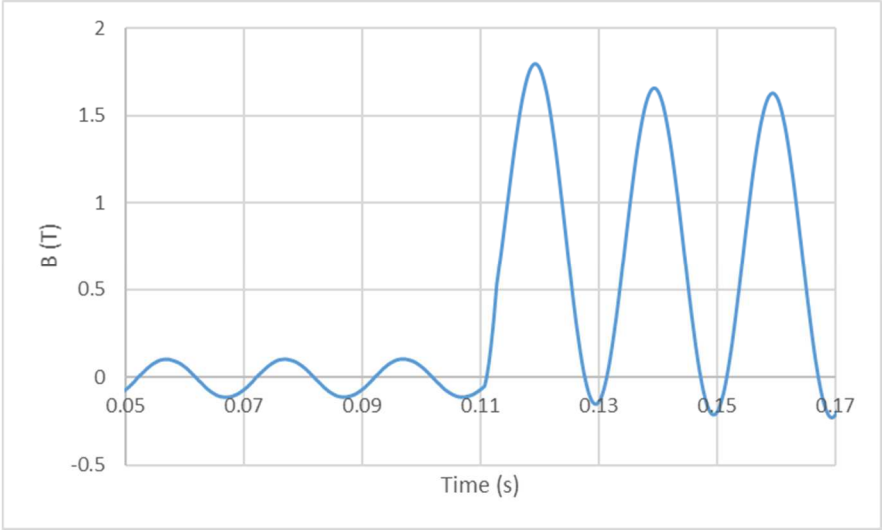

Figure 5. 11 Magnetic flux density of the transformer with doubled primary winding leakage inductance and 3.5 km cable length

However, if the thyristor crowbar fails to operate during fault, the SSSC has to withstand the whole voltage of the network due to the large equivalent impedance, which leads to deep saturation of the transformer core, as shown in Figure 5.12 for cable length of 10km. The voltage at the primary winding of the transformer is shown in Figure 5.13. Even using transformer with high leakage inductance, the iron core is still saturated, since the winding voltage is far more (5 times) than the ratings, as shown in Figure 5.14 for the flux density of the high impedance transformer with cable length of 10km. Hence backups must be prepared in case of the failure of the thyristor crowbar.

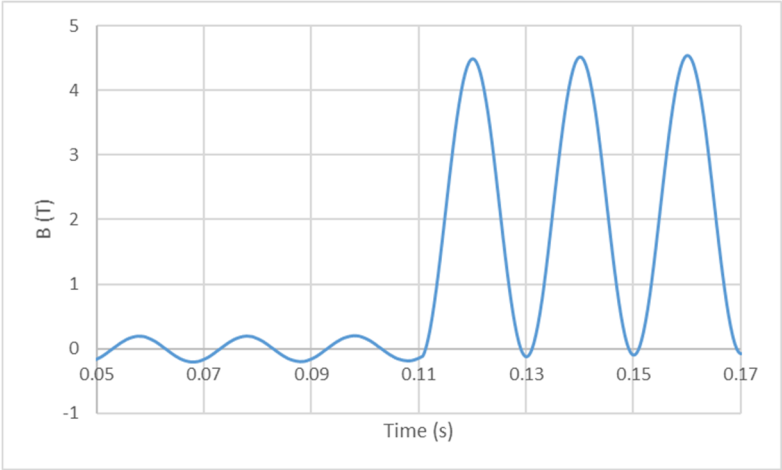

Figure 5. 12 Core magnetic flux density during fault (protection failure)

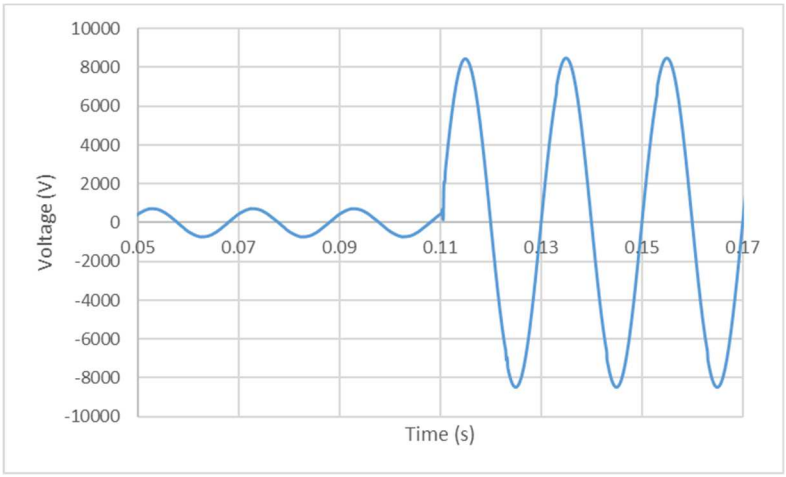

Figure 5. 13 Voltage of the SSSC during fault (protection failure)

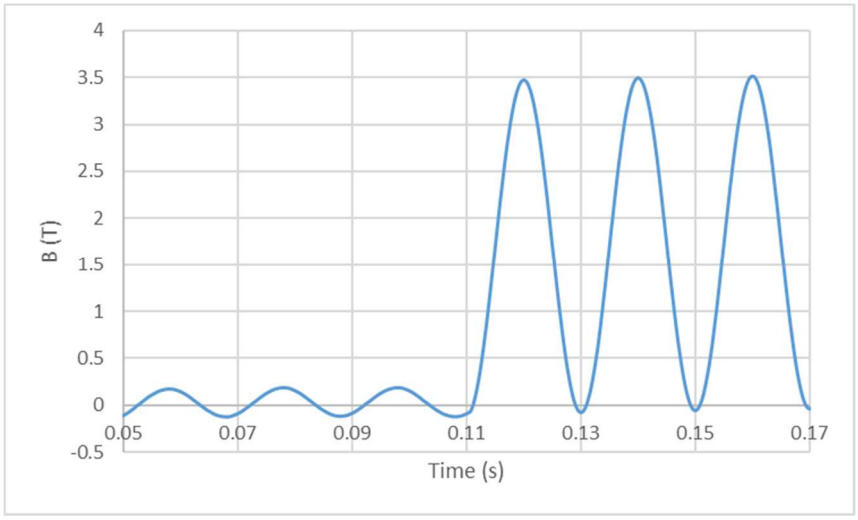

Figure 5. 14 Calculated magnetic flux density of the transform core during fault (protection failure)

5.5 Thermal Capability of Thyristor Crowbar

For the chosen thyristors of the thyristor crowbar, it is not cost effective to have the ratings of the on-state current of the thyristor higher than the make fault current of the network. In the design of thyristor, it is designed to withstand a short-term surge current, which is normally maximum 10 times of the rating without reapplied voltage for half a cycle and maximum 8 times with reapplied voltage for several duty cycles (commonly five cycles), without causing failure of the thyristor [120]. The mechanism of failures of a thyristor caused by a surge current is classified into three categories [121]:

1) The temperature swing caused by the surge current introduces thermal stress to the thyristor, which will cause damage due to the cumulated thermal fatigue of the thyristor. The degradation of the thyristor will cause an increase of the forward voltage or a degradation of blocking capability of the thyristor.

2) If the junction temperature is too high during the surge current event, the damage to the silicon wafer could be so large to cause the device to be not operational.

3) The temperature rise caused by the surge current affects the carrier lifetime of the thyristor and gradually causes a lower on-state voltage and an increased reverse recovery charge.

Categories 1) and 3) are failures during continuous operations of thyristor, which is not considered in the operation of thyristor during network fault. Category 2) is considered in the operation of thyristor during network fault and this mechanism is related to the absolute junction temperature of the thyristor during network fault. In the datasheet given by manufactures, the value of I_{TSM} is based on the destruction limit of the device following the mechanism 2). This value reflects the thermal capability of thyristor crowbar during network fault. However, in most of the cases, the manufacturer only provides the peak value of the I_{TSM} of a half cycle sine wave. It is difficult to determine whether the thyristor will be damaged with smaller surge current which lasts for more than half a cycle. Therefore, if the peak temperature during the surge current test conducted by the manufacturer can be acknowledged through the thermal model of a thyristor, it will provide a reference in the selection of thyristor.

5.5.1 Thermal model of a thyristor

The transient thermal behaviour of semiconductor components is described in two dominant thermal network models: partial fraction circuit model (Foster model) and continued fraction circuit model (Cauer model). The thermal equivalent circuit diagrams are shown in Figures 5.15 and 5.16. Both models can be used to represent the thermal behaviour of a one, two or three-dimension system.

The basic assumption for the use of both models is that the heat is generated from a single source with unit-step heating and the heat flows perpendicular to the surface of the semiconductor device [122].

The mathematical expressions for the Foster model is:

$$Z_{thF}(t) = \sum_{i=1}^{n} R_{thFi}(1 - e^{-t/\tau_{thi}}) \tag{5.6}$$

$$\tau_{thi} = R_{thFi} C_{thFi} \tag{5.7}$$

where R_{thFi} and C_{thFi} are the equivalent thermal resistance and capacitance and τ_{thi} is the equivalent time constant for Foster model.

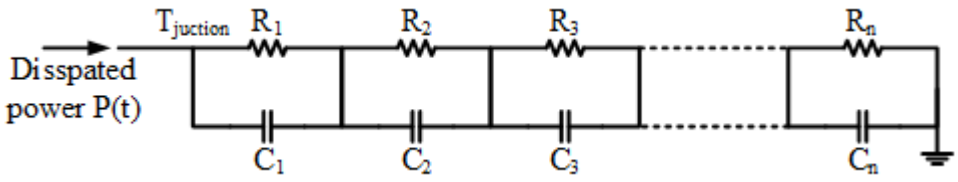

Figure 5. 15 Foster thermal equivalent circuit model

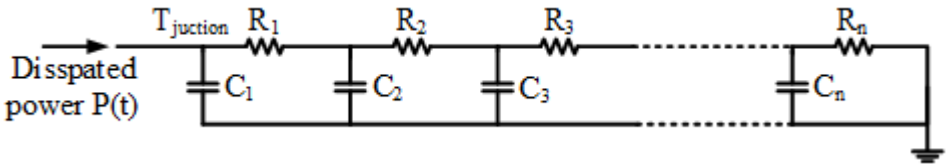

Figure 5. 16 Cauer thermal equivalent circuit model

The values of the thermal resistance R_{thFi} and thermal time constant τ_{thi} can be obtained from the standard curve fitting algorithm from the measured thermal impedance [123]. This information is always available in the datasheet provided by the manufacturer for semiconductor devices. However, the Foster model is only valid for a single thermal system to describe the thermal behaviour at the input node (commonly the device junction). It cannot be used to determine the temperature distribution within the device, nor to combine the thermal network with extended thermal system. This is because the Foster model is only a description of thermal behaviour of the measured system but not a true physical description. In the Foster model, the heat enters the left-hand side and leaves the right-hand side of the thermal system at the same time. In reality, it takes time for heat generated from the device junction to propagate into the external cooling system. As the manufacturers commonly only provide the equivalent thermal impedance of the thermal system from the device junction to the case or heat sink, therefore these parameters cannot be directly used in combined thermal systems.

The Cauer model can describe the same thermal impedance as the Foster model in case of same constant temperature at the right-hand side of the thermal circuit. Unlike the Foster model, the Cauer Model is so closely related to the concept of "structure function" that it can correctly describe the internal temperature distribution and the propagation of heat between nodes in a more complete thermal system [124]. For a thermal system including more than one sub-thermal system, the total system can be the series connection using the Cauer circuits of these sub-thermal systems.

Although the Cauer model has some advantages compared to the Foster model, it has a more complicated mathematical representation in the time domain unlike Equation (5.2) for Foster model and it is difficult to determine the parameters of R_i and C_i based on experiments for a Cauer model, as the direct calculation of these parameters relates to the material properties of the device. This is the reason why manufacturers only provide the thermal impedance in Foster Model. But the transformation from Foster model to Cauer model for the same thermal system is available by using the standard circuit transformations built in some simulators [125].

5.5.2 Transformation from Foster Model to Cauer Model

The transformation from Foster model to Cauer model is performed in the frequency domain. By applying Laplace transformation to Equation (5.2), the transfer function of a Foster model is:

$$Z_{thF}(s) = \sum_{i=1}^{n} \frac{R_{thi}}{1 + sR_{thi}C_{thi}} \tag{5.8}$$

From the recursive definition of the Cauer model, the transfer function of a Cauer model in continued fraction expression is written as:

$$Z_{thC}(s) = \cfrac{1}{s_1 C_{th1} + \cfrac{1}{R_{th1} + \cfrac{1}{sC_{th2} \cdots + \cfrac{1}{R_{thn}}}}} \tag{5.9}$$

To perform the transformation, the recurrence relation of Equation (5.5) is used in the form:

$$\frac{1}{Z_{thCn}(s)} = sC_{thC1} + \frac{1}{R_{thC1} + Z_{thCn-1}(s)} \tag{5.10}$$

The partial fraction representation of the transfer function of the Foster model, shown in Equation (5.4) can be equated into the rational function as:

$$Z_{thFn}(s) = \frac{f_n(s)}{g_n(s)} \tag{5.11}$$

$$\frac{f_n(s)}{g_n(s)} = \frac{f_1 s^{n-1} + f_2 s^{n-2} + \cdots + f_{n-1} s + f_n}{g_1 s^n + g_2 s^{n-1} + \cdots + g_n s + g_{n+1}} \tag{5.12}$$

The polynomial degree of $f_n(s)$ is one degree smaller than that of $g_n(s)$. Since $Z_{thCn}(s)=Z_{thFn}(s)$, by substituting Equation (5.7) into Equation (5.6), the following equation can be deduced:

$$\frac{g_n(s)}{f_n(s)} = sC_{thC1} + \frac{1}{R_{thC1} + Z_{thCn-1}(s)} \tag{5.13}$$

By substituting Equation (5.8) into Equation (5.9) and decomposing Equation (5.9) using the standard Euclidean algorithm into a polynomial linear *s* and a rational function $rem_n(s)/f_n(s)$ as the remainder, it can be deduced:

$$\frac{g_n(s)}{f_n(s)} = \frac{g_1}{f_1}s + \frac{rem_n(s)}{f_n(s)} \tag{5.14}$$

$$\begin{aligned} rem_n(s) &= g(s) - \frac{g_1}{f_1}s \bullet f_n(s) \\ &= (g_2 - \frac{g_1}{f_1}f_2)s^{n-1} + (g_3 - \frac{g_1}{f_1}f_3)s^{n-2} + \cdots + (g_n - \frac{g_1}{f_1}f_n)s + g_{n+1} \end{aligned} \tag{5.15}$$

The functions $rem_n(s)$ and $f_n(s)$ have the same polynomial degree. Comparing Equation (5.10) with Equation (5.9), the first Cauer thermal capacitance can be determined by:

$$C_{thC1} = \frac{g_1}{f_1} \tag{5.16}$$

and

$$\frac{1}{R_{thC1} + Z_{thCn-1}(s)} = \frac{1}{\frac{f_n(s)}{rem_n(s)}} \tag{5.17}$$

By substituting Equation (5.11) into (5.13) and applying the Euclidean algorithm, the rational function $f_n(s)/rem_n(s)$ can be decomposed into:

$$\frac{f_n(s)}{rem_n(s)} = \frac{f_1^2}{g_1 f_2 - g_2 f_1} + Z_{thCn-1}(s) \tag{5.18}$$

and

$$R_{thC1} = \frac{f_1^2}{g_1 f_2 - g_2 f_1} \tag{5.19}$$

The new $Z_{thCn-1}(s)$ can be defined by $f_{n-1}(s)/g_{n-1}(s)$. by applying the same transformation method, the value of R_{thC2} and C_{thC2} can be obtained. The algorithm continues until all Cauer R_{th} and C_{th} are calculated for required modelling term n.

The transferred Cauer model from the Foster model using the parameters from datasheet can be used with further connections of the Cauer model of the heat sink or other cooling systems.

5.5.3 Critical Temperature of Different Types of Thyristor during Surge Current Test

As mentioned in the previous section, the damage of thyristor crowbar during a network fault is caused by the high junction temperature when the fault current (surge current) flows through. To understand the critical temperature during the surge current test with the I_{TSM} provided in the datasheet becomes important in the selection of thyristor.

Hence simulations are conducted based on the test environment in manufactures' surge current test to study the critical temperature for different types of thyristors. The structure of the surge current test model is shown in Figure 5.17.

As indicated in the figure, the model can be divided into three sections: the on-state voltage calculation section, the power loss calculation section and the junction temperature calculation section. The on-state voltage V_T is obtained for given on-state current I_T and junction temperature V_j using a lookup table developed from the I-V curve provided in the datasheet. The loss of thyristor is calculated by:

$$P(t) = V_T(t) I_T(t) \tag{5.20}$$

The calculated loss is input into the Cauer model to calculate the junction temperature V_j. The Cauer model, as indicated in Figure 5.18, is developed using the parameters transferred from Foster parameters.

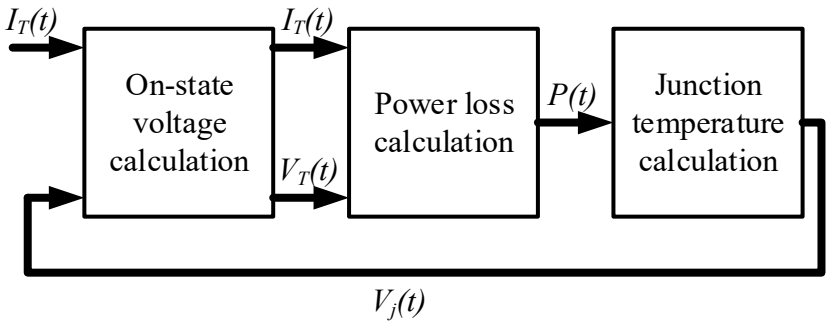

Figure 5. 17 Structure of the surge current test model

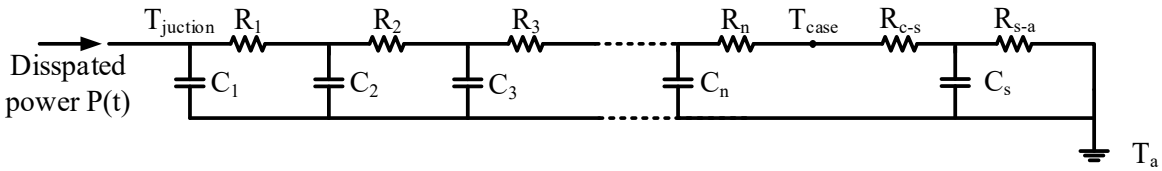

Figure 5. 18 Cauer model for thyristor with heat sink

5.5.3.1 Model verification

This thermal model is verified in the experiment which is to test the thermal behaviour of thyristor during high current. The equivalent circuit and figure of the test bench are shown in Figures 5.19 and 5.20. The power is provided by the 240V source through the 240V/10V transformer with 3kVA rated capacity. The maximum current provided by the transformer is 300A RMS on the secondary side. A 30mΩ resistive load (paralleling 6 x 180mΩ resistors) is connected into the test circuit to control the current. The thyristor module, having two thyristors anti-parallel connected, is connected into the circuit with the gate control circuit. The current and voltage are monitored the whole time during the experiment using an oscilloscope. The surge current test is tested using three different air cooling systems: air cooling withnot heat sink and air cooling with two different types of heat sinks. The case temperature of the thyristor module is measured using a thermocouple and recorded using PicoLog Recorder software installed on the laptop. The parameters of the equipment used in the experiment is shown in Table 5.6.

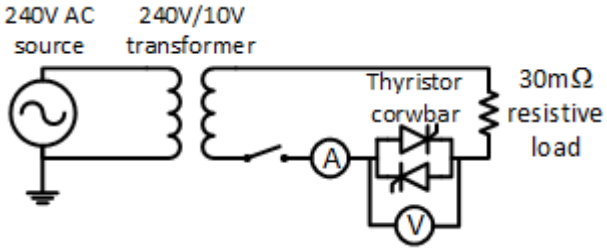

Figure 5. 19 Test circuit

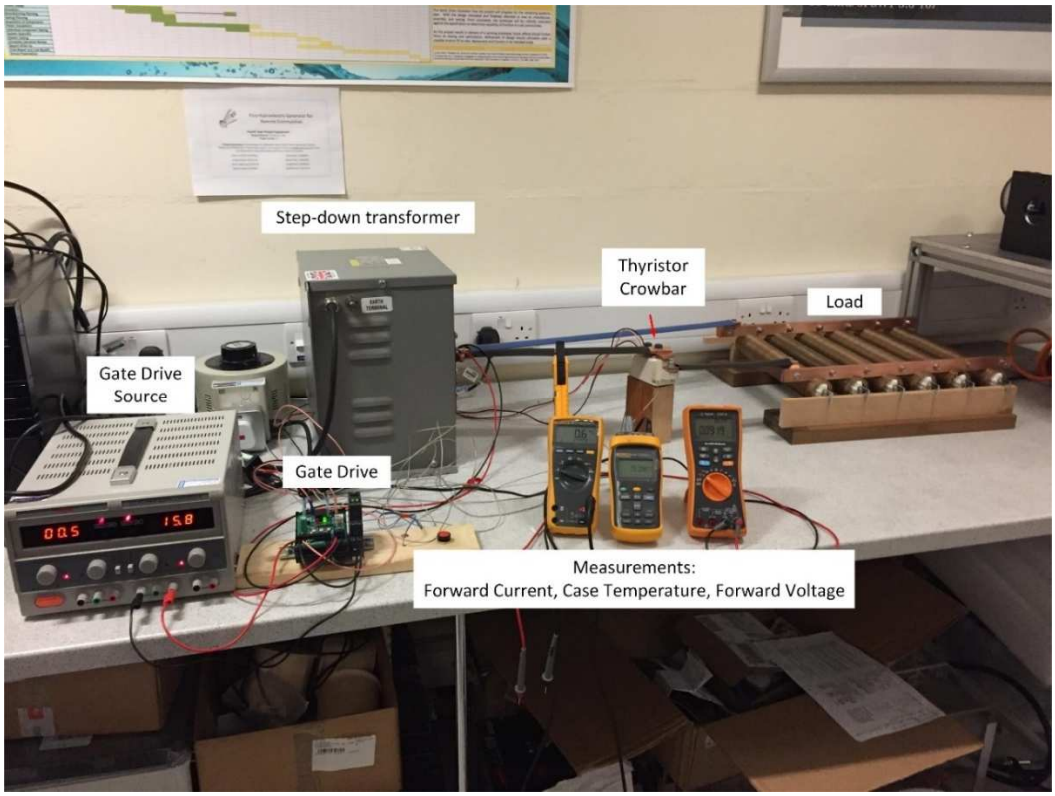

Figure 5. 20 Thyristor crowbar surge current test bench

The thyristor modules are turned on for 3 seconds and the forward current, voltage and case temperature during this period are measured. The experimental result and simulation result are shown in Figures 5.21, 5.22 and 5.23.

Table 5. 6 Experiment equipment parameters

Transformer		Thyristor		Resistor	
Size	3kW	Model	Semikron SKKT 273	Model	Ohmite PFE5KR180E
V1	230V				
V2	20V	V_{RRM}	1.2kV	Size	1.012kW
r1	0.02 p.u.	I_{TAV}	273A	R	180mΩ
r2	0.02 p.u.				
x1	0.05 p.u.				
x2	0.05 p.u.				
x_M	500 p.u.				

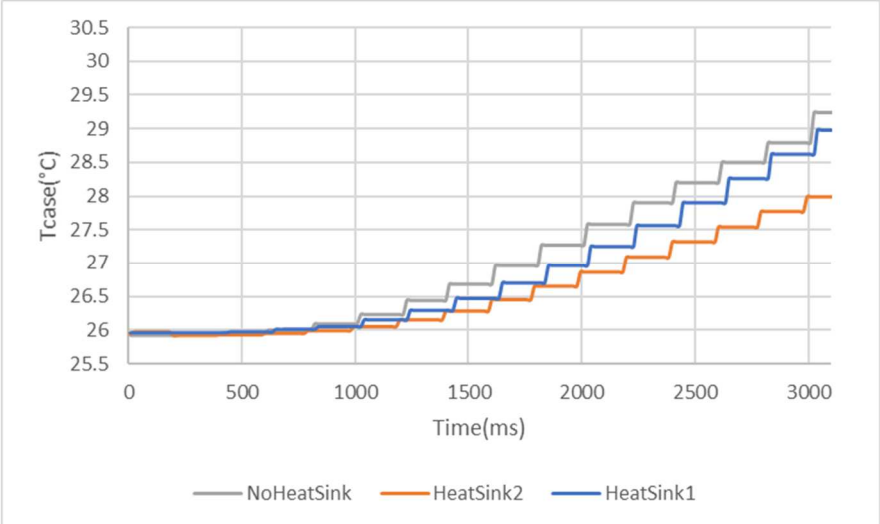

Figure 5. 21 Case temperature during experiment @ 300A RMS

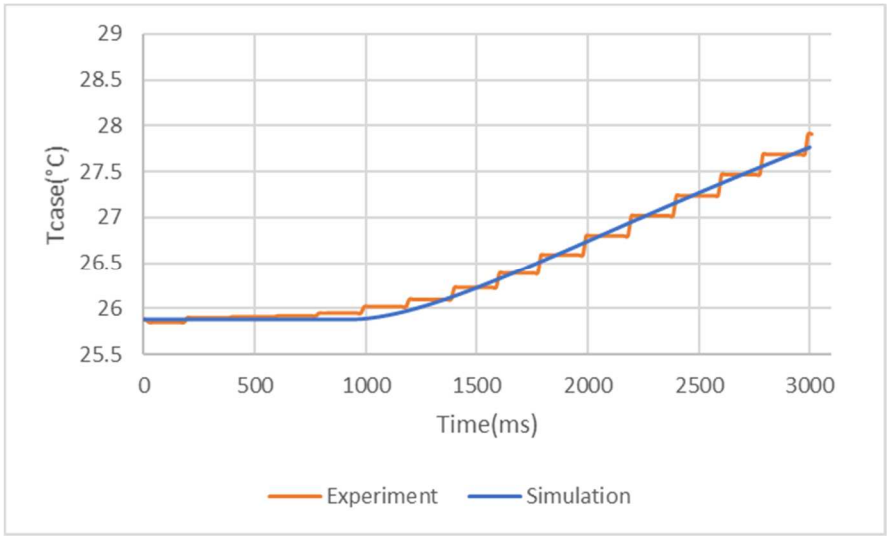

Figure 5. 22 Case temperature simulation vs experiment (Heat sink 2)

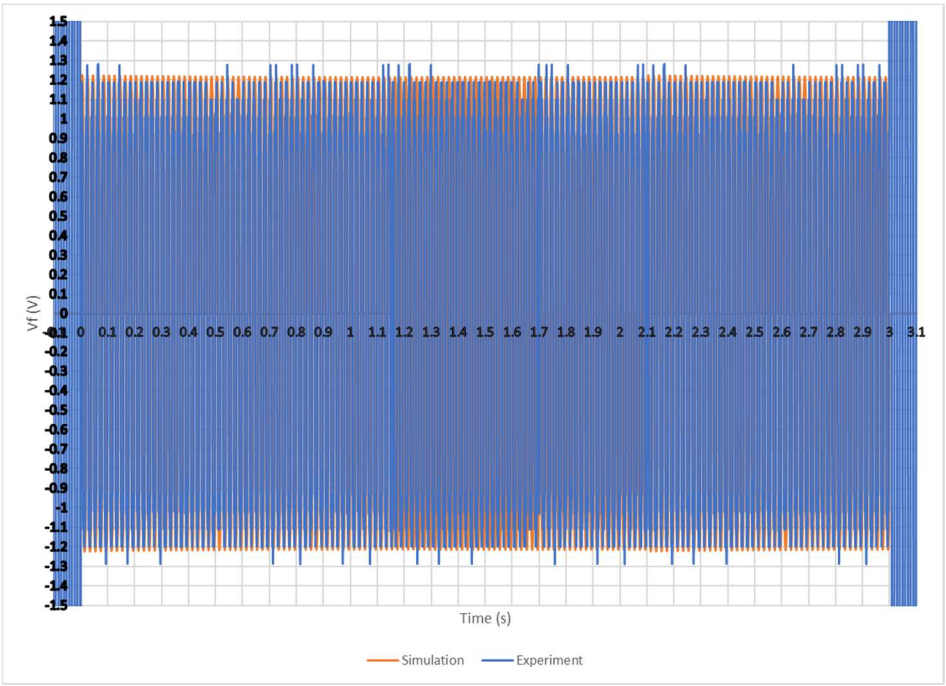

Figure 5. 23 Forward voltage during turning on simulation vs experiment

The average discrepancies between the simulation results and experiment results of the forward voltage is 6.26% and of the case temperature is 1.673%. These errors are within acceptable range. Hence the thermal model proposed in Section 5.5.1 is valid in the surge current study. Furthermore, from Figure 5.22, it can be observed from the experiment results that during the initial 500 ms after the switching on of the thyristor crowbar, the case temperature rise is negligible. Since 500 ms is five times of 100 ms which is five-cycle in a 50Hz system, it is reasonable to assume that the case temperature rise is not significant during the first five-cycle period after switching on of the thyristor crowbar in the fault of a 11kV distribution network. Hence the thermal model of thyristor crowbar in the following simulations is based on the assumption that the case temperature is constant and the value is the ambient temperature.

5.5.3.2 Simulations on different types of thyristors

With this verified thermal model approach, simulations are conducted on different types of power thyristors to study the critical current during surge current test. All simulations use the same heat sink model. The basic parameters of thyristors used in the simulation are listed in Table 5.7. The Foster model parameters of thyristors used in the simulation are listed in Tables 5.8 and 5.9.

All press packed thyristors selected for this simulation have the rated peak reverse voltage around 1.7kV, as this would be the most common voltage rating for thyristors used in SSSC for 11kV distribution network application [126]. The maximum surge currents I_{TSM} at maximum working junction temperature for these selected thyristors are all higher than the typical make current of a three-phase fault in the 11kV network, which is 32kA, equivalent to 625MVA fault level. The ambient temperature, which is also the initial junction temperature, is set to be the maximum working junction temperature. This is because that the surge current test conducted by the manufactures for all thyristors is at this temperature [127]. The surge current is a half cycle (10ms at 50Hz) sine wave with the peak value shown in Table 5.7 in the simulations for each type of thyristor. It is applied to the thyristor when time is t=10ms. The simulation ends 10ms after the surge current. The junction and case temperature of each type of thyristor is measured for the whole simulation period. The simulation results of the junction and case temperature of each type of thyristor are given in Figures 5.24 and 5.25 [].

Table 5. 7 Ratings of different types of thyristors

Manufacture	Type	V_{RRM} (V)	I_{TAV} @ T_c (A @ °C)	I_{TSM} @ T_j (A @ °C)	R_{c-s} (k/W)
ABB	30H1801	1800	3108 @ 70	47000 @ 125	0.003
	34T1600	1600	3370 @ 70	49000 @ 125	0.003
	34T1601	1600	3370 @ 70	49000 @ 125	0.003
	42L1800	1800	4390 @ 70	64000 @ 125	0.0015
	50Q1801	1800	6100 @ 70	94000 @ 125	0.001
Semikron	SKET800	1800	808 @ 85	32000 @ 130	0.001

Table 5. 8 Foster thermal resistance of different type of thyristors

Type	R_{th} (k/W)				
	R_1	R_2	R_3	R_4	R_5
30H1801	0.00673	0.00144	0.00065	0.00084	0.00032
34T1600	0.007	0.00161	0.00092	0.00047	
34T1601	0.00673	0.00144	0.00065	0.00084	0.00032
42L1800	0.0047	0.00085	0.00107	0.00049	
50Q1801	0.00336	0.00094	0.00048	0.00022	
SKET800	0.0044	0.00845	0.0097	0.01806	

Table 5. 9 Foster time constants of different types of thyristors

Type	τ_{th} (s)				
	τ_1	τ_2	τ_3	τ_4	τ_5
30H1801	0.4871	0.1468	0.0677	0.0079	0.0021
34T1600	0.3225	0.1186	0.0095	0.0025	
34T1601	0.4871	0.1468	0.0677	0.0079	0.0021
42L1800	0.4787	0.0824	0.0104	0.0041	
50Q1801	0.4069	0.0854	0.0118	0.003	
SKET800	0.00981	2.287	2.476	22.8	

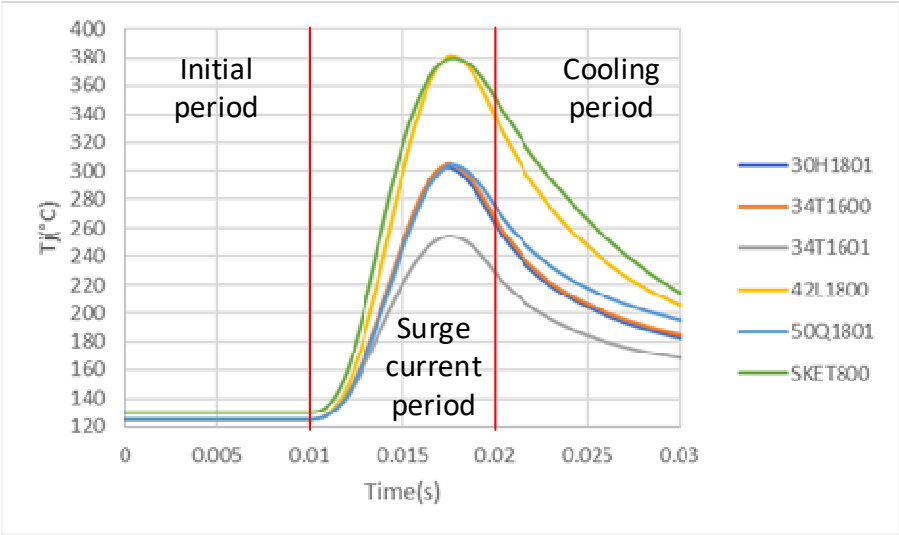

Figure 5. 24 Junction temperature in the surge current test

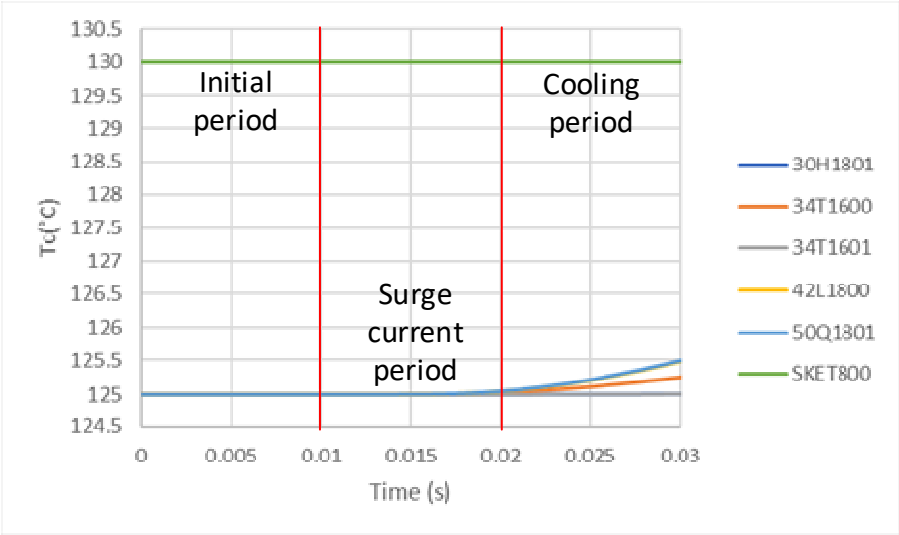

Figure 5. 25 Case temperature in the surge current test

As indicated in Figure 5.24, due to the differences in the structure and ratings of thyristors design, the critical temperature (peak junction temperature) during surge current test is different. The maximum critical temperature can be 380°C which is approximately three times of the maximum working temperature, for ABB 42L1800 and Semikron SKET800 thyristor. The minimum critical temperature can also be 255°C, twice of the maximum working temperature for ABB 34T1601 thyristor. The time for junction temperature to reach peak value is approximately 0.002s after the peak surge current, which is at 0.015s. this is due to the thermal capacitance of the silicon used in the thyristor, which will cause a delay in the temperature rise compared to the power loss of the thyristor. However, when checking on the temperature rise of the case temperature shown in Figure 5.22, during the surge current period, the temperature is hardly to be observed for any of these types of thyristors, while a slight temperature rise can be observed in the first 10ms during the cooling period for some of these thyristors. As the surge current period is only 10ms, which is relatively small in the thermal system in high power electrical system, it is too short for the heat generated in the junction to propagate to the case despite of the different designs for power thyristors rated around 1.7kV.

5.5.4 Thyristor Crowbar Thermal Capability during Fault

With the results of the critical temperatures of different types of thyristors, the thermal capability of thyristor crowbar during fault is studied using simulations. The 11kV distribution network model used in the simulation is the same as the one shown in Figure 5.3. The fault current passing through the thyristor crowbar is input into the thermal network model of these different types of thyristors to study the junction temperature rise of these thyristors. Simulations are conducted for different cases, as listed in Table 5.10. The tested thyristor is listed in Table 5.11.

Table 5. 10 Case details

Case No.	Cable length (km)	Ta (°C)
1	1	25
2	1	40
3	10	25
4	10	40

Table 5. 11 Thyristor models

A	ABB34T1600
B	ABB34H1601
C	ABB30H1801
D	ABB50Q1801
E	ABB42L1800
F	Semikron SKET800

For different cases, the distance from the source to the SOP increases from 1km to 10km. For each distance, two ambient temperatures of 25°C and 40°C are set for the thermal model in the simulation. For Topology 1, the fault currents passing through the thyristor crowbar are shown in Figures 5.26 and 5.27.

As shown in figures above, the fault current passing through the thyristor crowbar of the SSSC using transformer is much larger than that through the transformerless SSSC. This is because to the thyristor crowbar used in the SSSC with transformer is installed on the secondary side of the transformer. Due to that the voltage level is decreased on the secondary side of the transformer, the current is increased according to the same ratio between the winding voltages. For the transformerless SSSC, the fault current flowing through the thyristor crowbar is the same as that in the network. Hence for transformerless SSSC, the number of series connected thyristors used in the thyristor crowbar is more than that compared to SSSC using transformer. While the requirement of the current ratings of thyristor in the transformerless SSSC is lower than that in SSSC with transformer. The junction temperature of the thyristor crowbar in Topology 1 for the SSSC using transformer is shown in Figures 5.28 to 5.35. The thyristor crowbar is switched off five cycles after switching on.

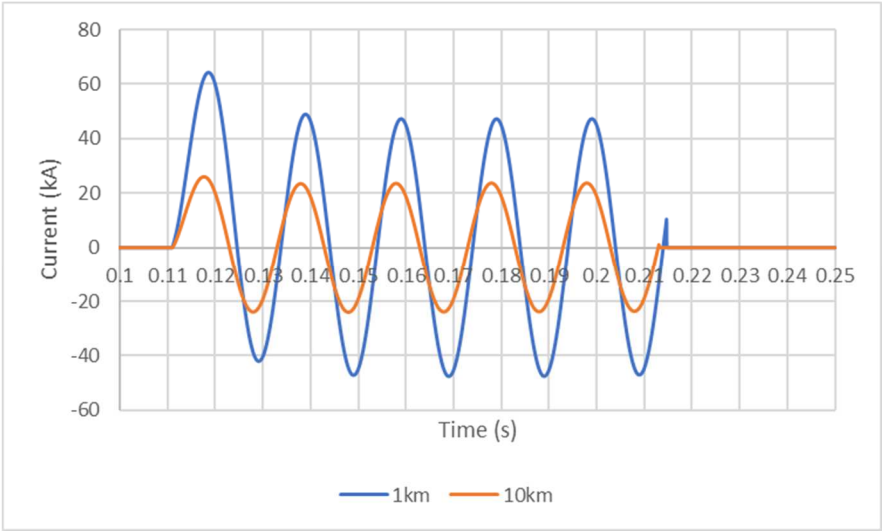

Figure 5. 26 Fault passing through the thyristor crowbar of the SSSC with transformer - Topology 1

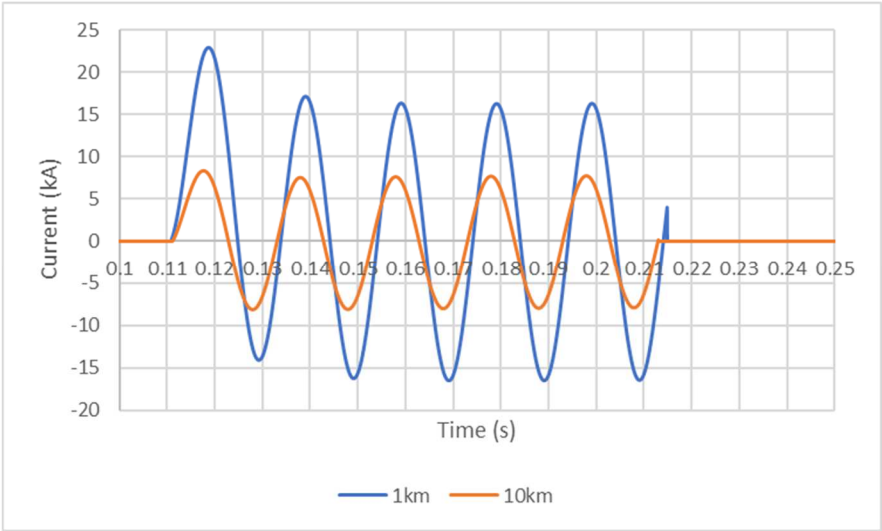

Figure 5. 27 Fault current passing through the thyristor crowbar of the transformerless SSSC - Topology 1

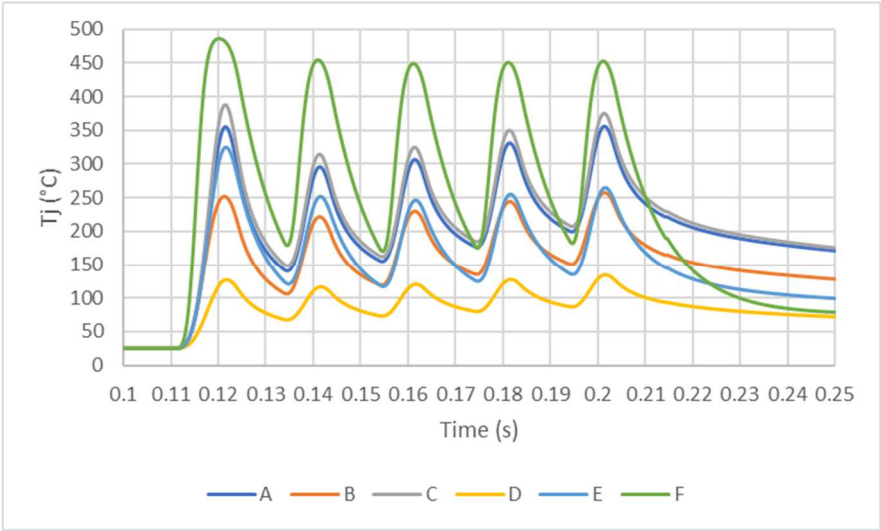

Figure 5. 28 T_j of forward thyristor (1km cable and 25°C) - Topology 1

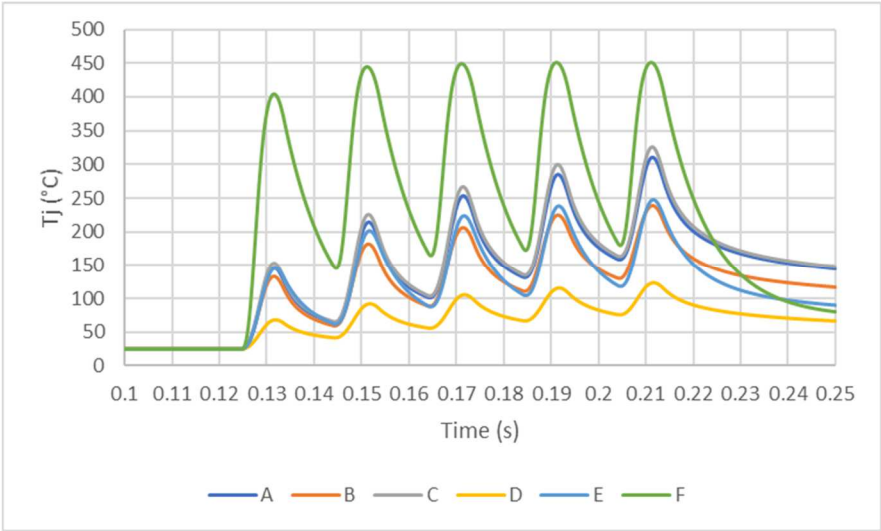

Figure 5. 29 Tj of reverse thyristor (1km cable and 25°C) - Topology 1

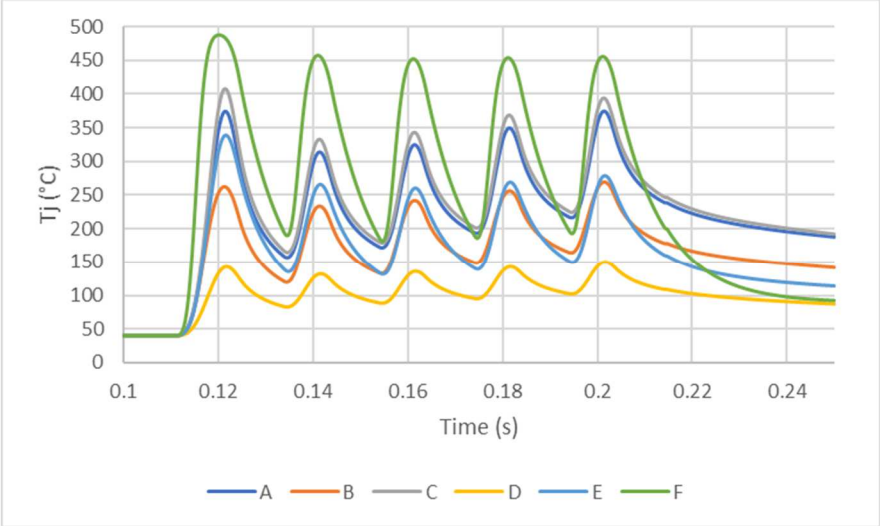

Figure 5. 30 Tj of forward thyristor (1km cable and 40°C) - Topology 1

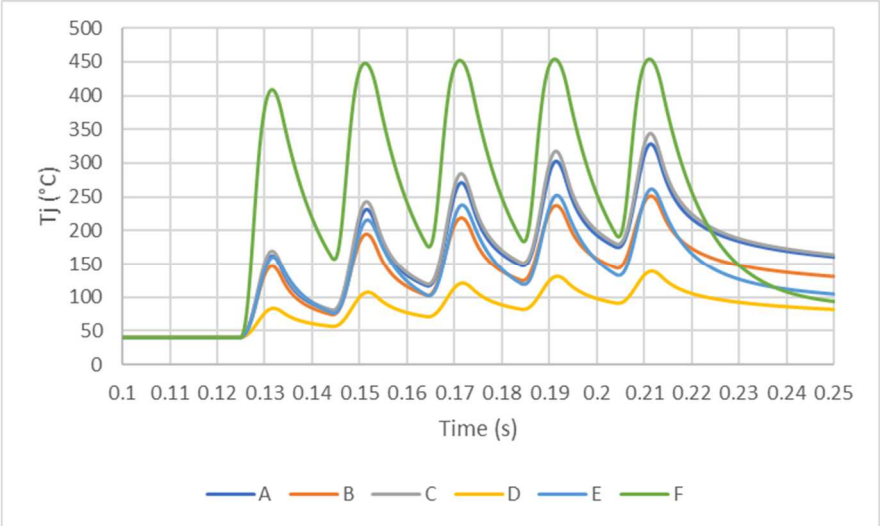

Figure 5. 31 Tj of reverse thyristor (1km cable and 40°C) - Topology 1

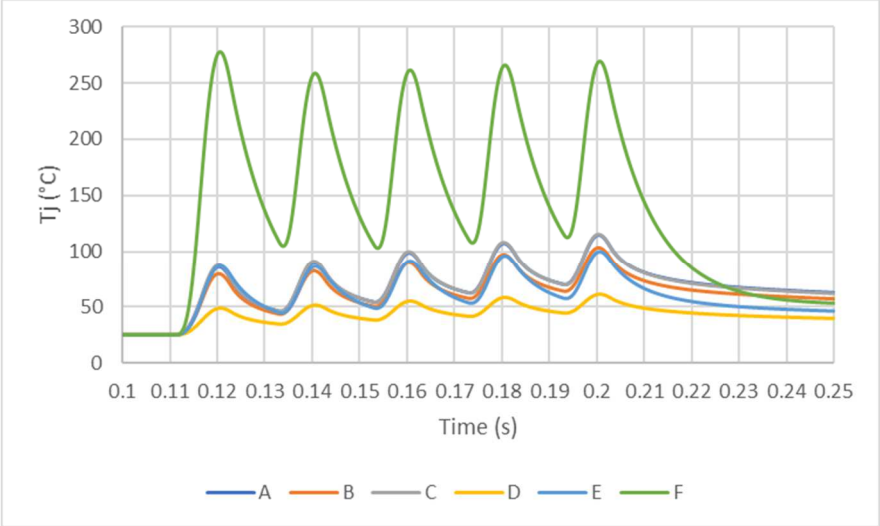

Figure 5. 32 Tj of forward thyristor (10km cable and 25°C) - Topology 1

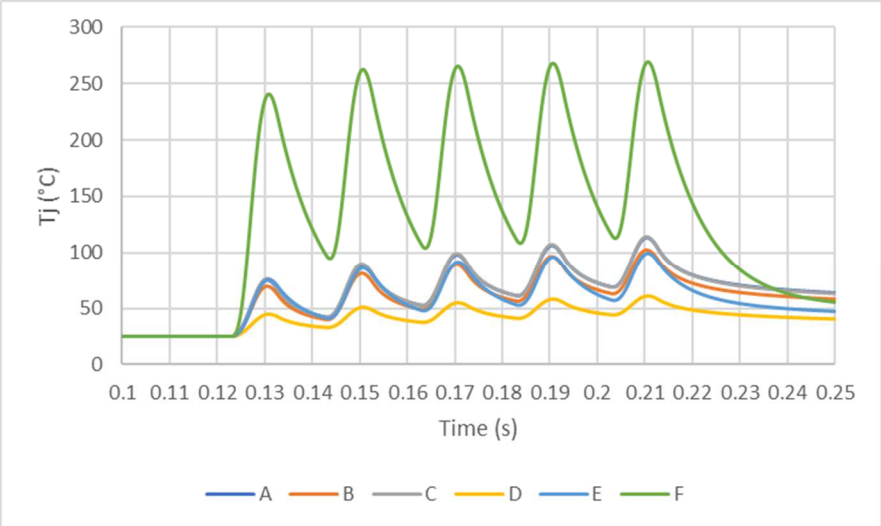

Figure 5. 33 Tj of reverse thyristor (10km cable and 25°C) - Topology 1

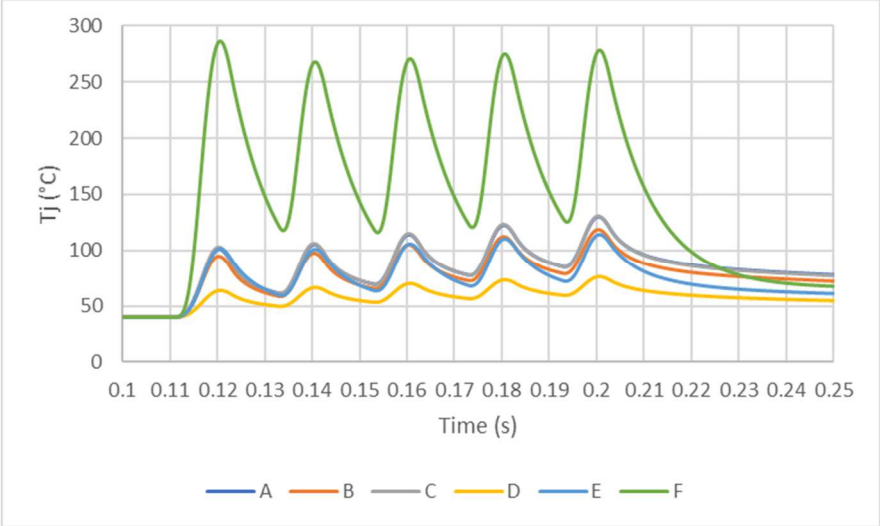

Figure 5. 34 T_j of forward thyristor (10km cable and 40°C) - Topology 1

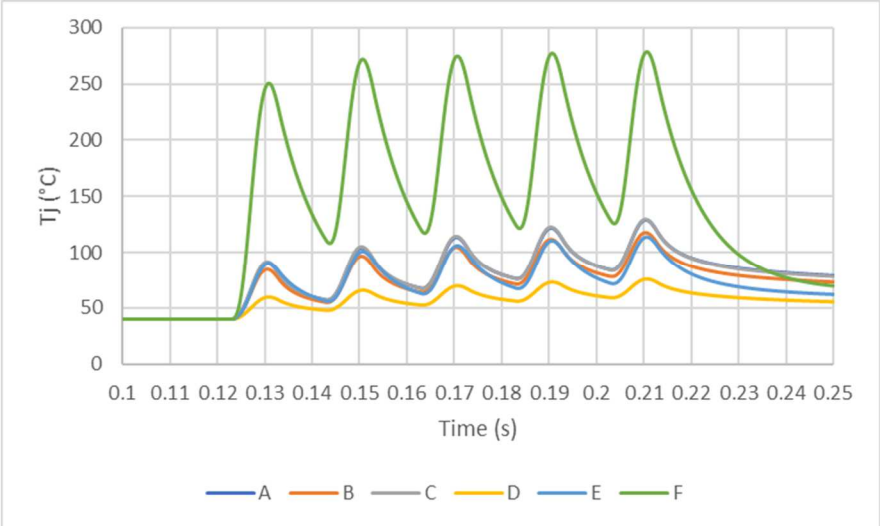

Figure 5. 35 Tj of reverse thyristor (10km cable and 40°C) - Topology 1

As indicated in Figures 5.28 to 5.31, except for Model D thyristor, the peak junction temperatures of all models of thyristors will exceed their critical junction temperatures shown in Figure 5.24 during five cycles after switching on. This is due to the fault current for 1km cable on the secondary side of the transformer exceeds or be close to (Model E) their I_{TSM}, given by the datasheet. Since the I_{TSM} given in the datasheet is tested using a half cycle sine wave, even the fault current is close to but smaller than the I_{TSM}, the junction temperature will still exceed the critical junction temperature for five cycles of fault current. For model D, the peak fault current is 2/3 of the I_{TSM} given in the data sheet. During the five-cycle period after switching on, the peak junction temperature during fault is approximately 2/5 of the critical junction temperature. When the cable length is increased to 10km, the fault current reduced to approximately 1/3 of that of 1km cable network. In this situation, the fault current is reduced to approximately 1/2 (Model A, B and C) or even less (Model D and E) compared to the I_{TSM} given in the datasheet, as shown in Figures 5.31 to 5.35. Hence the peak junction temperatures during five cycles after switching on of all these models are far less (less than 50%) than their critical junction temperatures. For thyristor Model F, the junction temperature is still close to the critical junction temperature. This is because the fault current in the 10km network is still close to its I_{TSM}, 80% of the I_{TSM}, given in datasheet.

The junction temperature of the thyristor crowbar during fault for the transformerless SSSC is shown in Figures 5.36 to 5.43. For these results, all junction temperatures are within the critical junction temperatures of all models of thyristor.

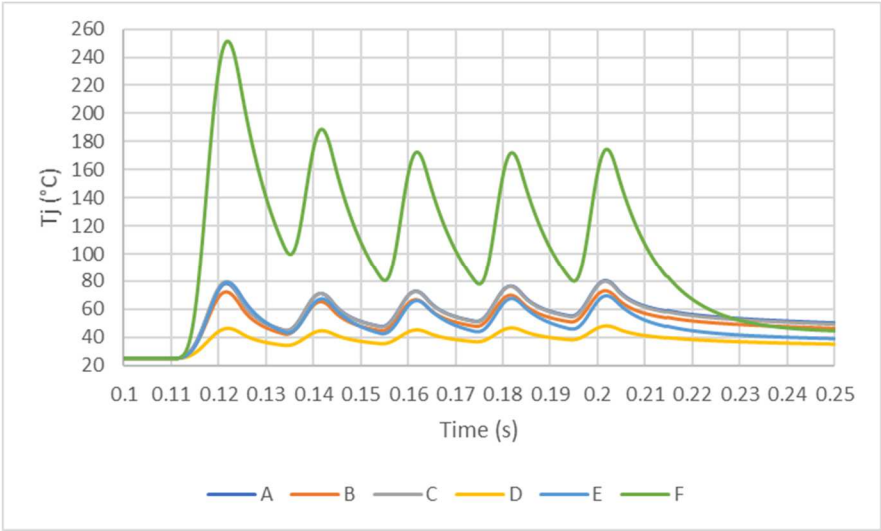

Figure 5. 36 T_j of forward thyristor (1km cable and 25°C) - transformerless SSSC, Topology 1

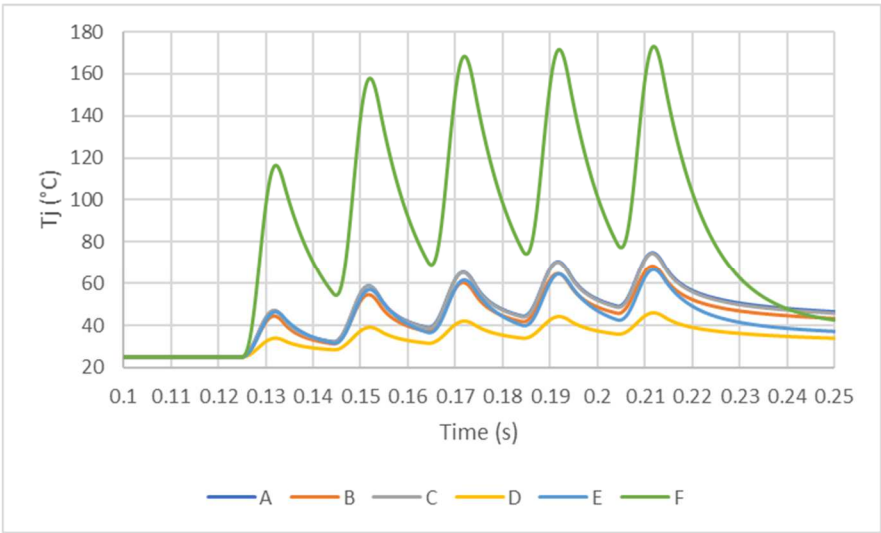

Figure 5. 37 T_j of reverse thyristor (1km cable and 25°C) - transformerless SSSC, Topology 1

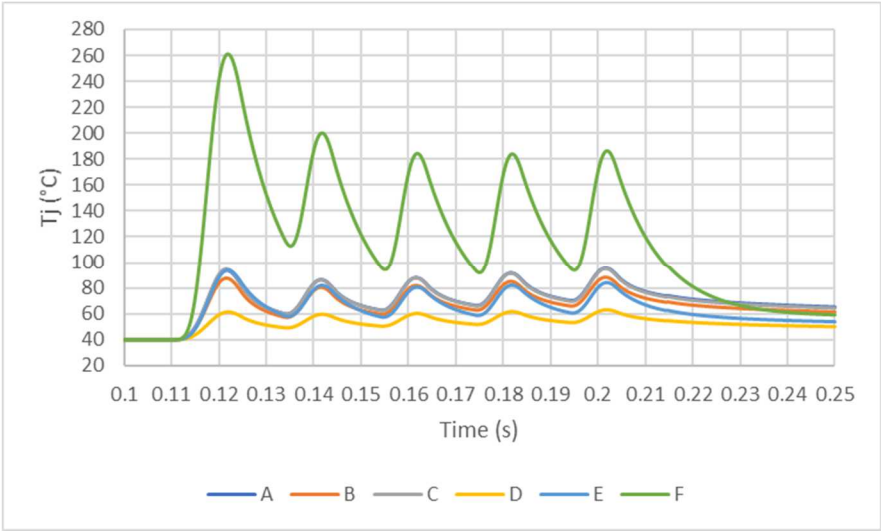

Figure 5. 38 T_j of forward thyristor (1km cable and 40°C) - transformerless SSSC, Topology 1

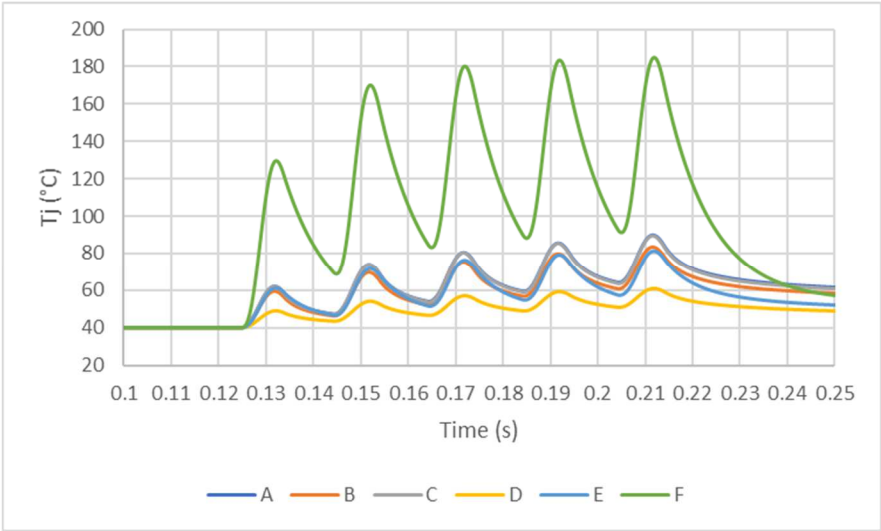

Figure 5. 39 T_j of reverse thyristor (1km cable and 40°C) - transformerless SSSC, Topology 1

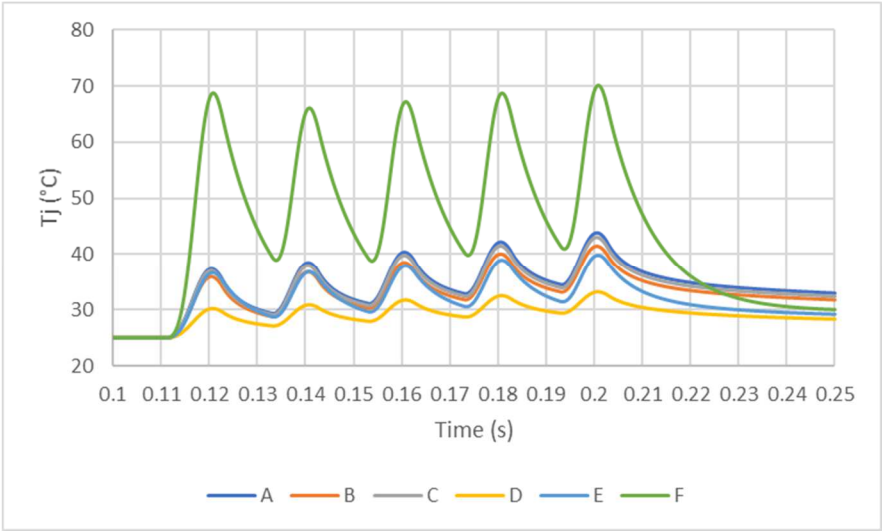

Figure 5. 40 T_j of forward thyristor (10km cable and 25°C) - transformerless SSSC, Topology 1

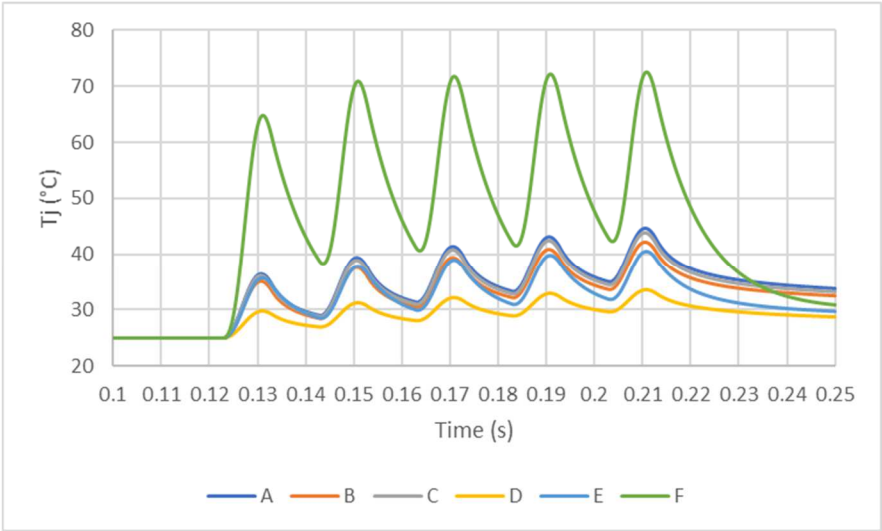

Figure 5. 41 T_j of reverse thyristor (10km cable and 25°C) - transformerless SSSC, Topology 1

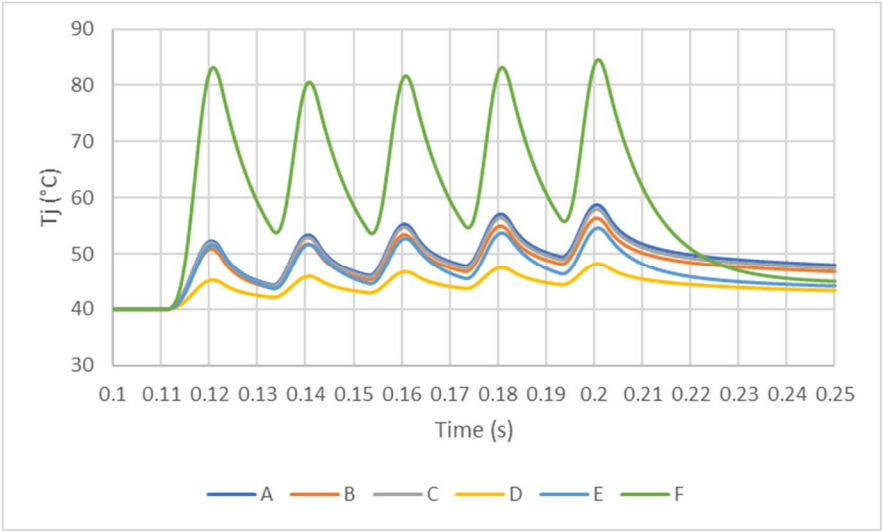

Figure 5. 42 T_j of forward thyristor (10km cable and 40°C) - transformerless SSSC, Topology 1

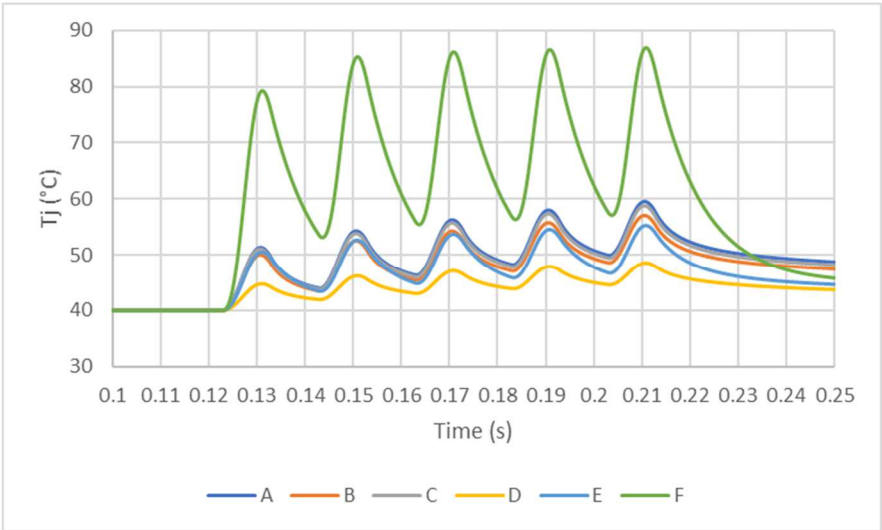

Figure 5. 43 T_j of reverse thyristor (10km cable and 40°C) - transformerless SSSC, Topology 1

Figures 5.36 to 5.39 show the results of the network with 1km cable and Figures 5.40 to 5.43 show the results of the network with 10km. For transformerless SSSC, since there is no voltage transfer between the VSC side and the network side, the fault current is not amplified as that in the SSSC using transformer. Hence if the given I_{TSM} is at least 25% larger than the peak fault current of the fault current, the thyristor crowbar can withstand the fault current for at least five cycles in a 50Hz network without failure in the protection of SSSC.

For Topology 2, the results fault current flowing through the thyristor crowbar are shown in Figures 5.44 and 5.45. As indicated in the two figures below, the fault current is similar for both types of SSSC in Topology 2. This is because in Topology 2, the fault current will not pass through the SSSC but to the ground by the thyristor crowbar.

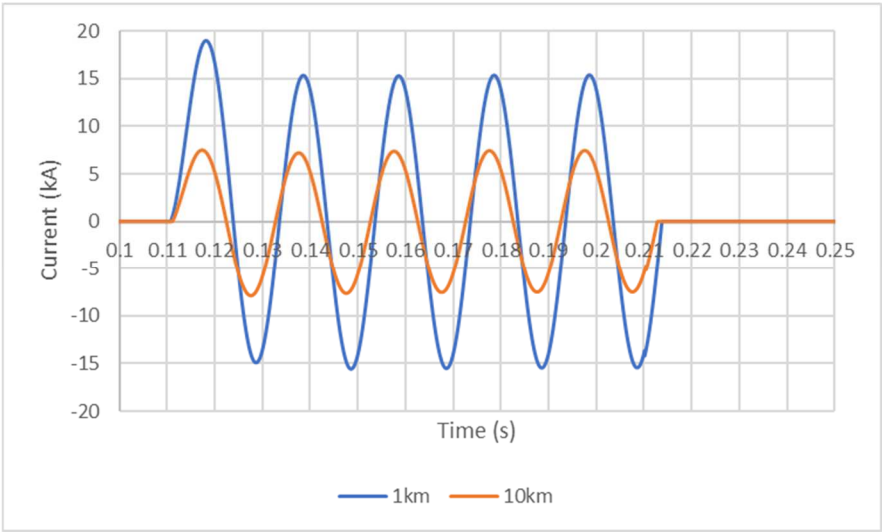

Figure 5. 44 Fault passing through the thyristor crowbar of the SSSC with transformer - Topology 2

The junction temperature results are shown in Figures 5.46 to 5.53 for SSSC using transformer and Figures 5.54 to 5.61 for transformerless SSSC. In all cases of Topology 2, the peak junction temperature during the five-cycle period of all models of thyristor is within the critical junction temperature. As indicated in Figures 5.44 and 5.45, the peak fault current is no more than 65% of the I_{TSM} given by the datasheet. The peak junction temperature during five-cycle after thyristor switched on does not exceed 60% of the critical junction temperature shown in Figure 5.24.

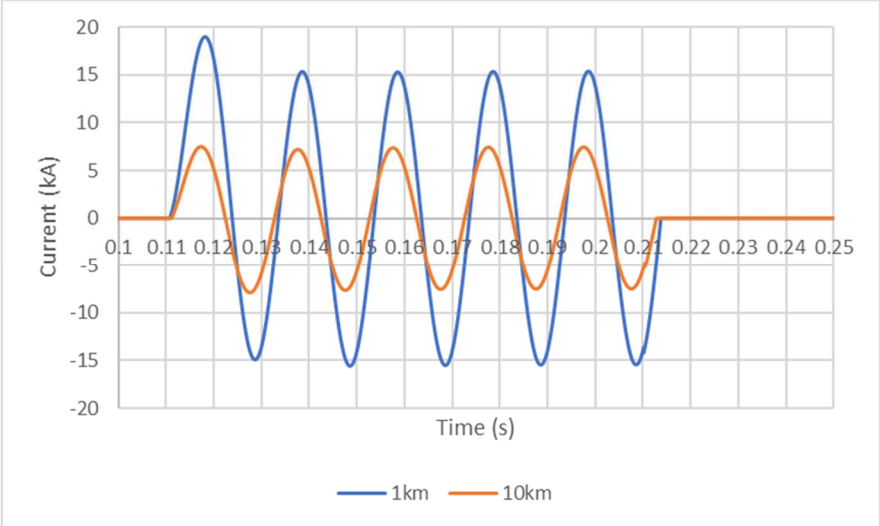

Figure 5. 45 Fault passing through the thyristor crowbar of transformerless SSSC - Topology 2

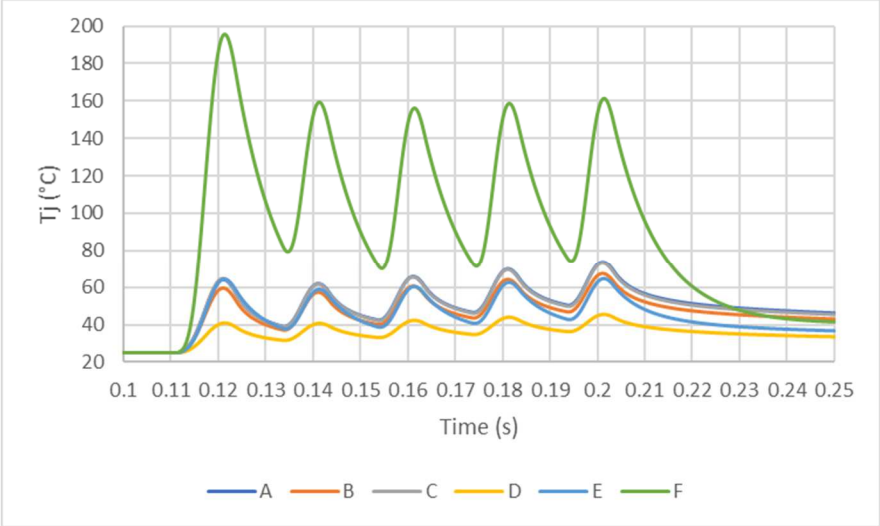

Figure 5. 46 Tj of forward thyristor (1km cable and 25°C) - Topology 2

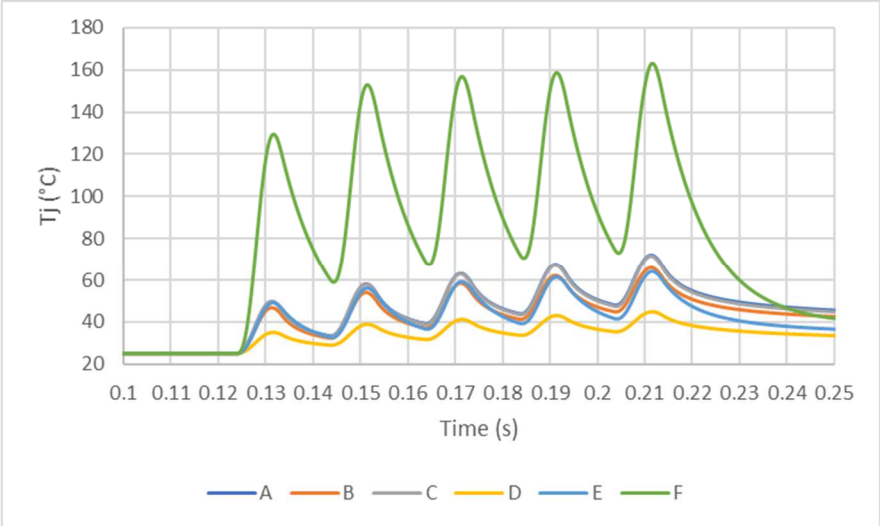

Figure 5. 47 Tj of reverse thyristor (1km cable and 25°C) - Topology 2

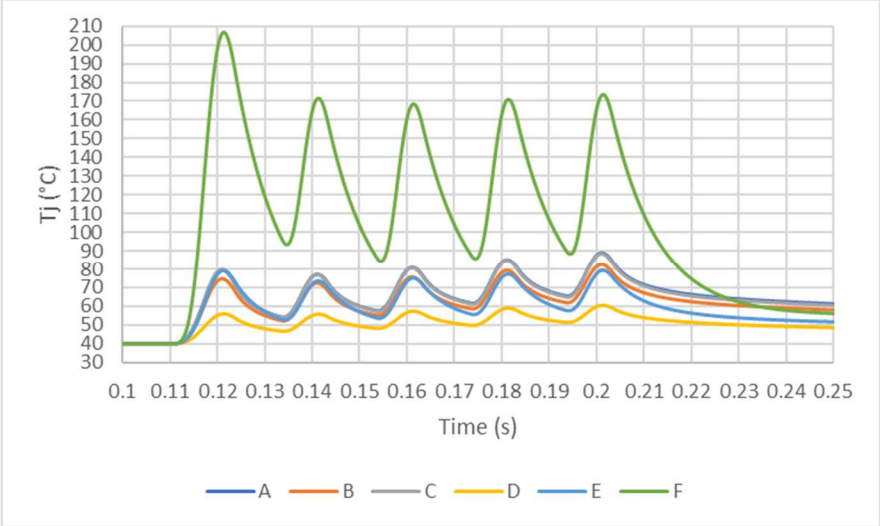

Figure 5. 48 Tj of forward thyristor (1km cable and 40°C) - Topology 2

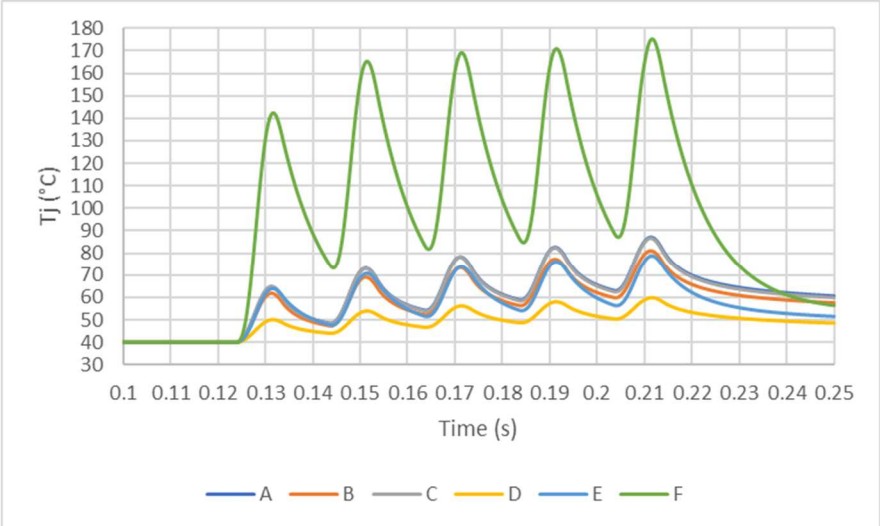

Figure 5. 49 Tj of reverse thyristor (1km cable and 40°C) - Topology 2

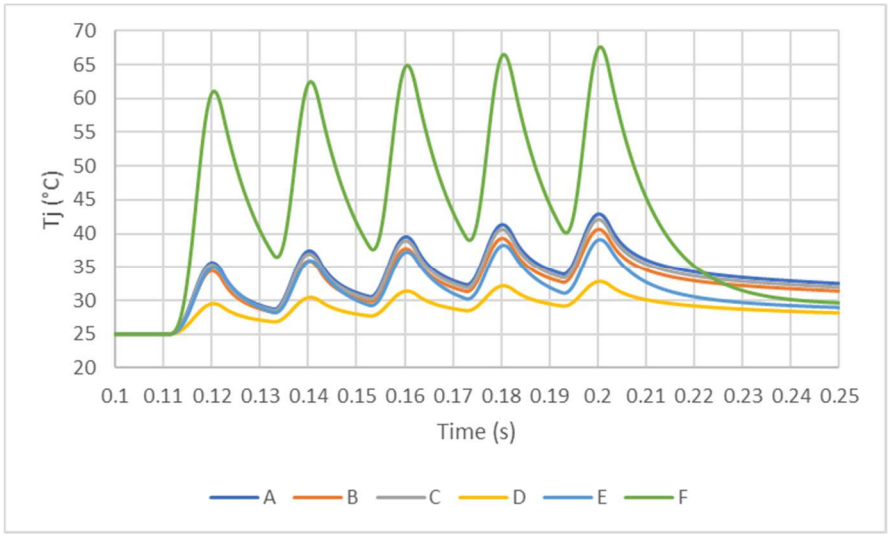

Figure 5. 50 Tj of forward thyristor (10km cable and 25°C) - Topology 2

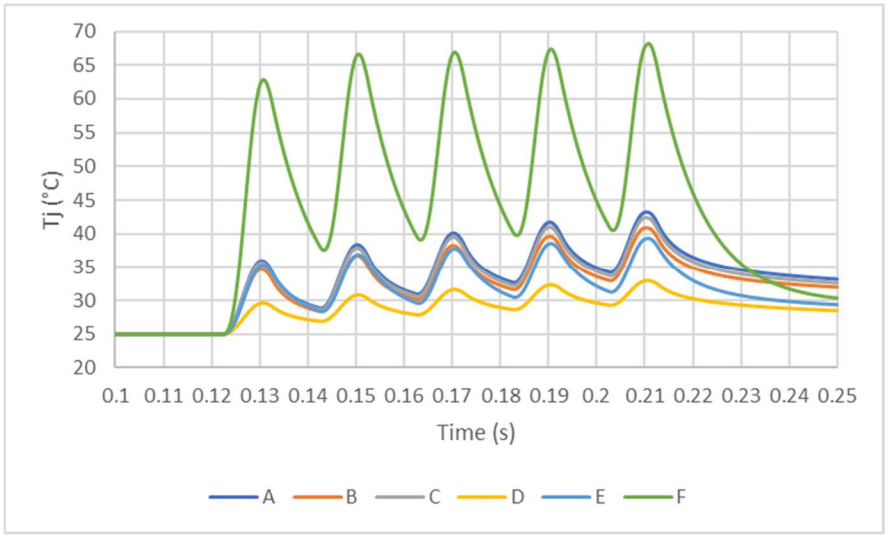

Figure 5. 51 Tj of reverse thyristor (10km cable and 25°C) - Topology 2

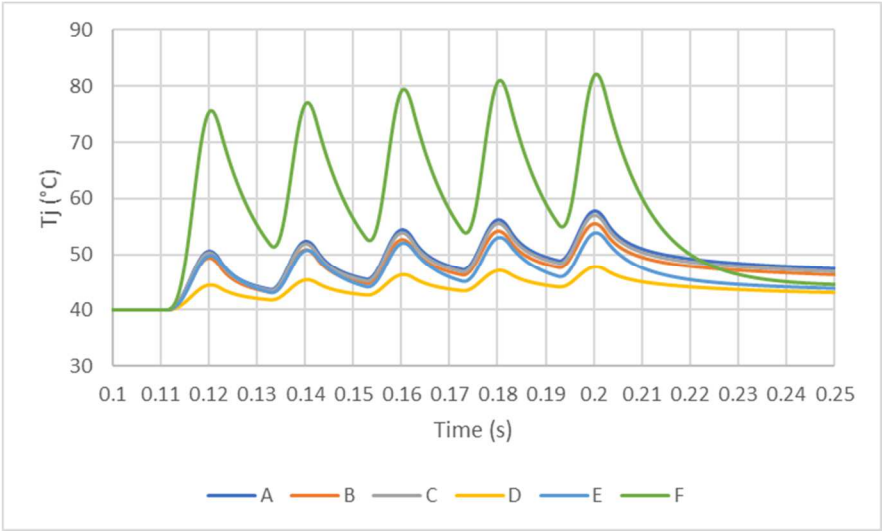

Figure 5. 52 Tj of forward thyristor (10km cable and 40°C) - Topology 2

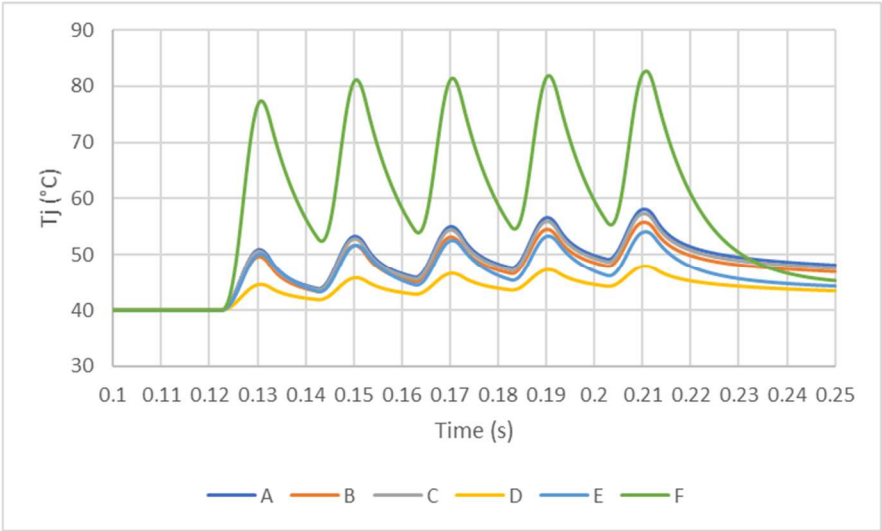

Figure 5. 53 Tj of reverse thyristor (10km cable and 40°C) - Topology 2

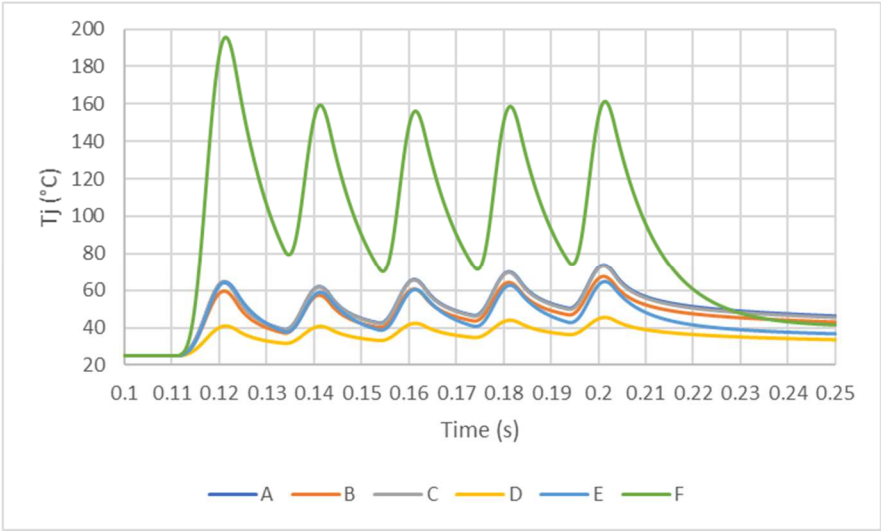

Figure 5. 54 Tj of forward thyristor (1km cable and 25°C) - transformerless SSSC, Topology 2

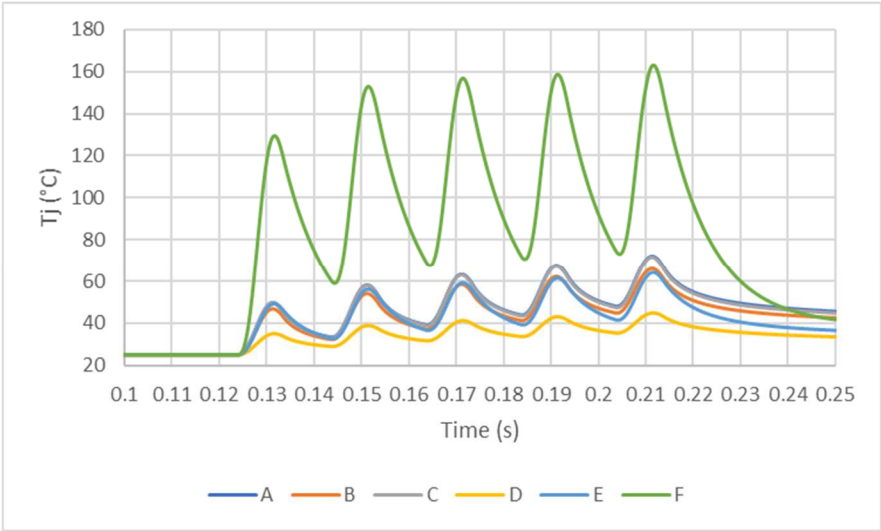

Figure 5. 55 Tj of reverse thyristor (1km cable @ 25°C)-transformerless SSSC, Topology 2

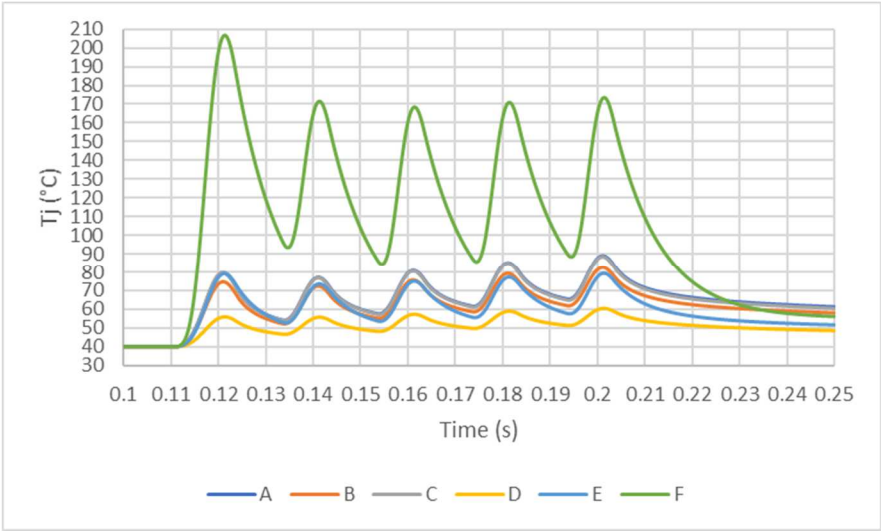

Figure 5. 56 Tj of forward thyristor (1km cable @ 40°C)-transformerless SSSC, Topology 2

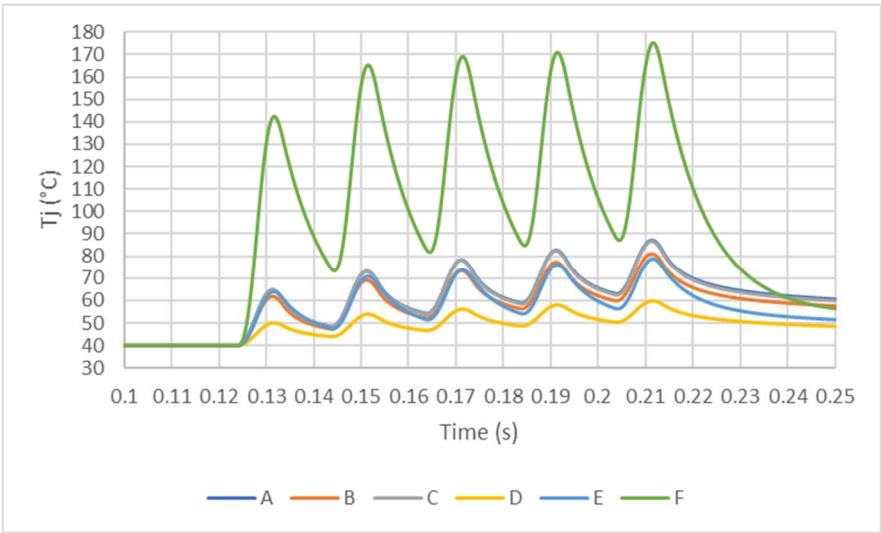

Figure 5. 57 Tj of reverse thyristor (1km cable @ 40°C)-transformerless SSSC, Topology 2

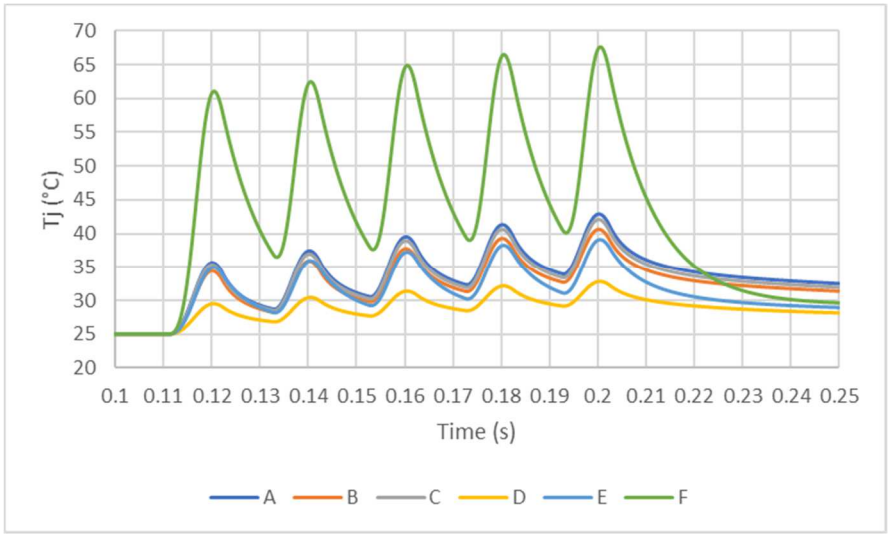

Figure 5. 58 Tj of forward thyristor (10km cable @ 25°C)-transformerless SSSC, Topology 2

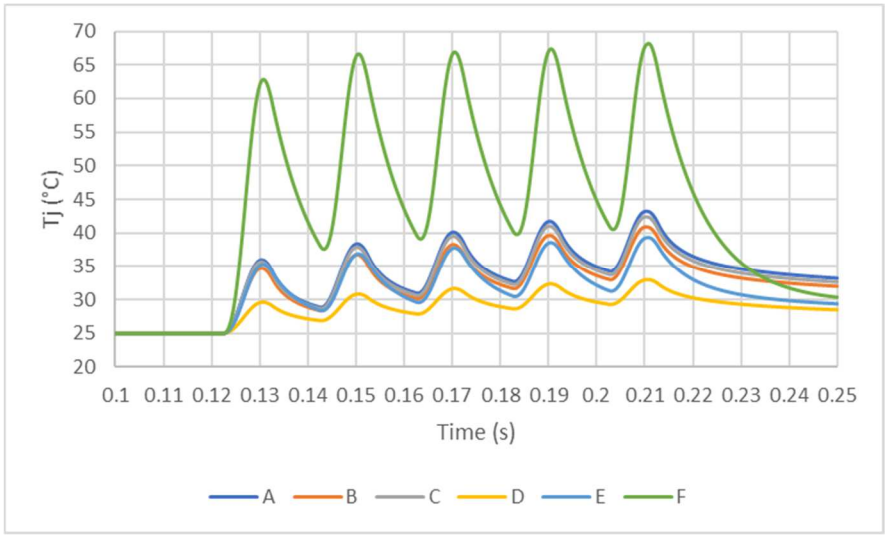

Figure 5. 59 Tj of reverse thyristor (10km cable @ 25°C)-transformerless SSSC, Topology 2

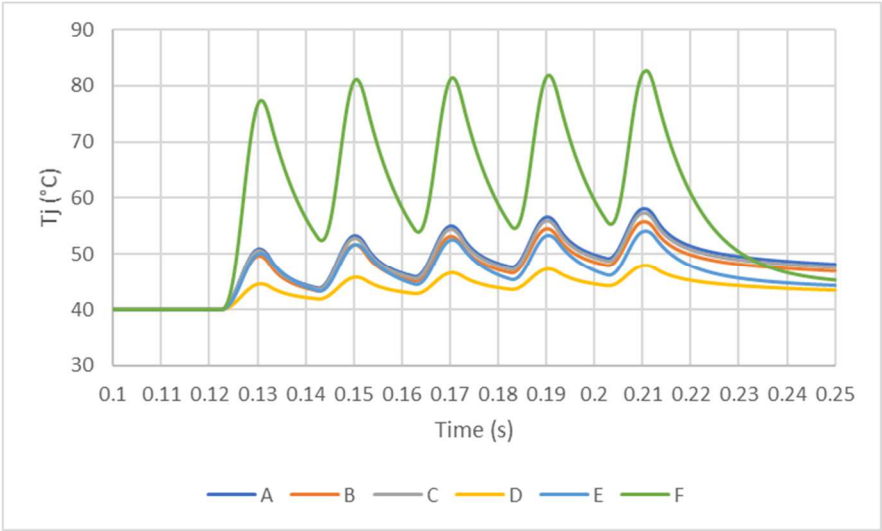

Figure 5. 60 Tj of forward thyristor (10km cable @ 40°C)-transformerless SSSC, Topology 2

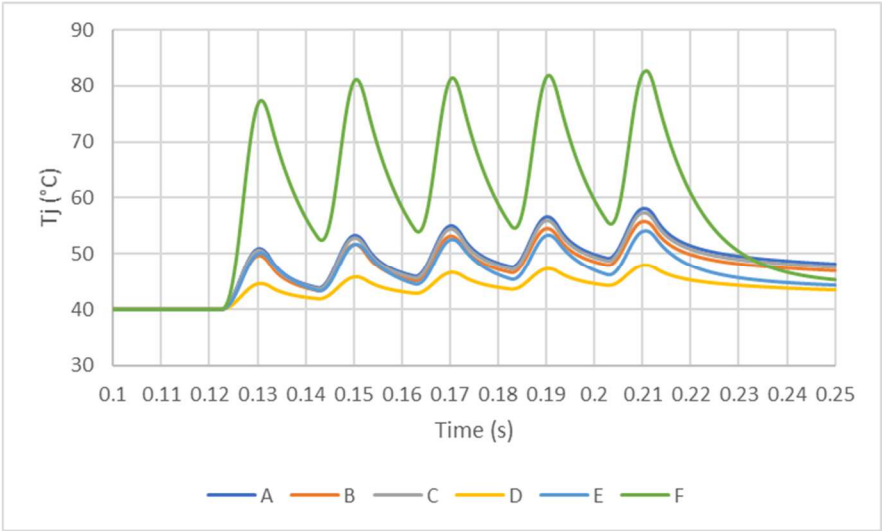

Figure 5. 61 Tj of reverse thyristor (10km cable @ 40°C)-transformerless SSSC, Topology 2

5.6 Summary

In summary, using thyristor crowbar in the protection of SSSC based SOP is feasible if:

1) The SOP is installed 3.5km away from the primary busbar or using a high impedance transformer to prevent core saturation when using transformer for the coupling; and

2) The I_{TSM} of the thyristor crowbar is at least 1.5 times of the peak fault current of the network.

For Topology 1, the original protection device of the 11kV distribution network, where the SOP is installed, should be updated to double ratings since the fault levels of the looped feeders are doubled due to the use of SOP. For Topology 2, the protection device does not require updating since no fault level change caused by the use of SOP.

Regarding the types of SSSC, the fault current used in the thyristor selection for SSSC using transformer in Topology 1 should consider the transformer winding ratio, if the thyristor crowbar is installed on the secondary side (VSC side) of the transformer but not the network fault current.

Chapter

6 The Utilisation of Back-to-back VSC in Distribution Network

Regarding to the results of DG capacity in Chapter 3, the penetration level can be almost 60% or 70% before the voltage profile or fault level is violated when the network is lightly loaded. In practice, from the network safety point of view, UK DNOs rarely allow DG to be concentrated close to the primary busbars. Therefore, the most common issue caused by DG connection currently in practice is the voltage violation. To concentrate DG at the location far from the primary busbar will lead to the most significant violations of voltage at the load busbars. Hence the following solution is focused on voltage violations and the consequential fault level rises caused by concentrating the DG at the far end of the feeder. Thereafter, a loss analysis based on this voltage profile solution is conducted.

Solutions to the voltage problem caused by DG connection have been studied by many researchers using different compensators. Recent solution involves direct connection between, i.e. paralleling, two feeder circuits in one form or another, as illustrated in Figure 6.1, using mechanical switches traditionally, and more recently power electronic controllers or compensators.

In this topology, the back-to-back VSC is capable of voltage compensation and power flow control between these two feeders. This can be realised in the control strategy, which is explained in the following section.

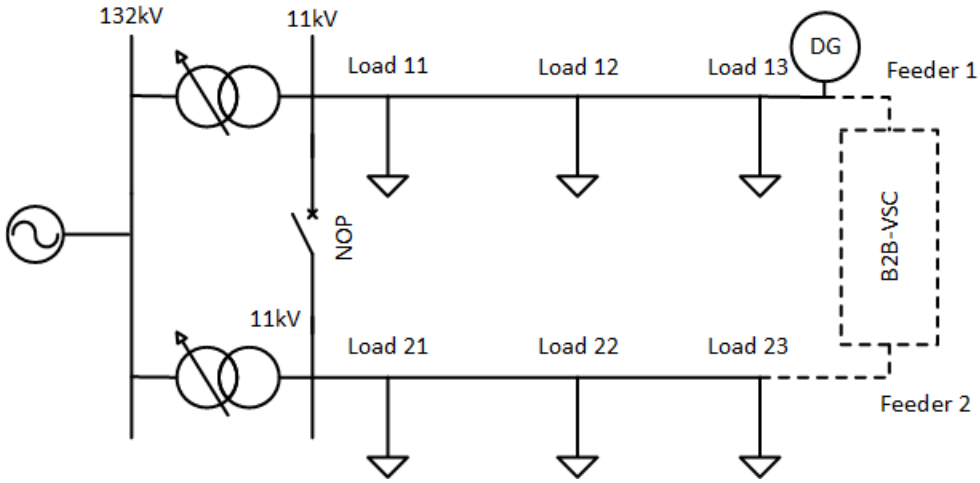

Figure 6. 1 The 11kV distribution network model

6.1 Control of Back-to-Back VSC

These functions of voltage and power flow controls are achieved by the control of the open/close of IGBT switches in the inverter. The diagram of the control system of the right-hand side VSC is shown in Figure 6.2. It is the same diagram of the control system for the left-hand side VSC. It is indicated in the diagram that the control system measures the dc bus voltage, $v_{d.c.}$, and the grid voltage, v_{gabc}. The three phase grid voltage, v_{abc} is transformed into v_{gd} and v_{gq}, using the Park transformation. v_{gd}, v_{gq} and the dc voltage $v_{d.c.}$ are then used in the following control loop.

With the control loops indicated in Figure 6.2, the VSC can control the active and reactive power flowing through it in order to control the output voltage at the grid and block the short circuit current during the network fault. The two VSC used in the B2B work as inverter and rectifier regrading to the direction of the controlled power flow. If the power flows from right to left, the right side VSC functions as rectifier and the i_d reference is input from source 1. If the power flows in the opposite direction, the VSC works as an inverter and i_d reference is input from source 2. For the VSC on the left-hand side, the functioning is as the reverse of the right-hand side VSC. The designs of each control loop are expressed in detail as follows.

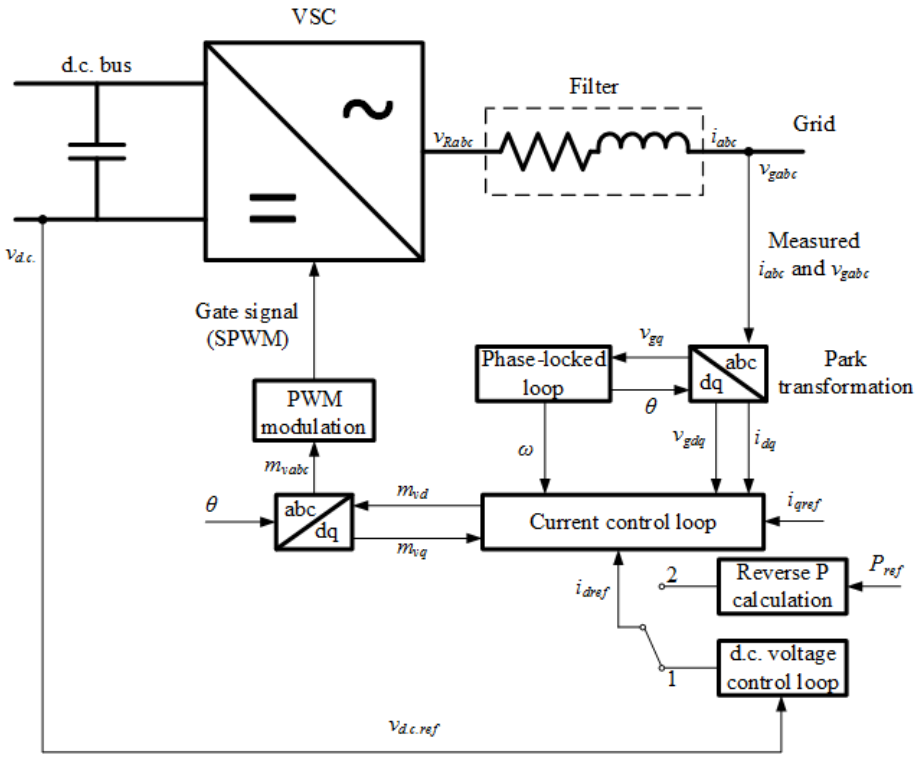

Figure 6. 2 Schematic diagram of the control system of the right-hand side VSC of the B2B

6.1.1 Park Transformation

Park Transformation or dq0 transformation is a transformation that converts three phase stationary coordinate system to the dq0 rotating coordinate system, which is firstly introduced in the late 1920s, and developed over the next 50 years [128-131]. It is often used to simplify the analysis of the three-phase synchronous machine or the calculations of the control of three-phase converters.

In dq0 coordinate system, the reference frame is not stationary but keeps rotating. In three-phase balanced condition, Park Transformation reduces three ac quantities (parameters for phases a, b and c) to two dc quantities (parameters for d and q). Figure 6.3 shows the abc stationary coordinates and the dq0 rotating coordinates.

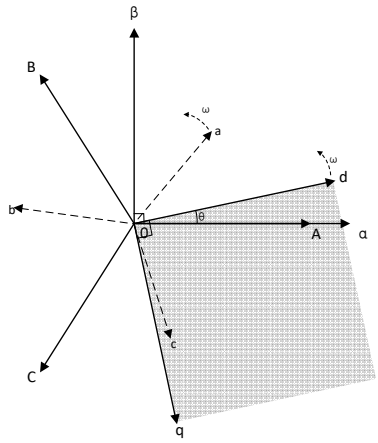

Figure 6. 3 Plane graph of dq0 coordinates system

θ is a time dependent variable, assuming the initial angle between d-axis and α-axis is ψ_0, then θ can be described as:

$$\theta = \omega t + \phi_0 \tag{6.1}$$

where ω is the angular frequency of the grid. The Park Transformation is defined as:

$$\left[x_{dq}\right] = \left[T\left(\theta\right)\right] \cdot \left[x_{abc}\right] \tag{6.2}$$

Matrix [x_{dq}] and [x_{abc}] are the correlated expressions of the three phase quantities in dq0 and abc coordinates and [T(θ)] is the transformation matrix. For a balanced three phase system, Equation (6.2) can be expanded as:

$$\begin{bmatrix} x_d \\ x_q \end{bmatrix} = \frac{2}{3}\begin{bmatrix} \cos\theta & \cos(\theta-\frac{2}{3}\pi) & \cos(\theta+\frac{2}{3}\pi) \\ \sin\theta & \sin(\theta-\frac{2}{3}\pi) & \sin(\theta+\frac{2}{3}\pi) \end{bmatrix}\begin{bmatrix} x_a \\ x_b \\ x_c \end{bmatrix} \tag{6.3}$$

And the inverse transformation is as follows:

$$\begin{bmatrix} x_a \\ x_b \\ x_c \end{bmatrix} = \begin{bmatrix} \cos\theta & \sin\theta \\ \cos(\theta-\frac{2}{3}\pi) & \sin(\theta-\frac{2}{3}\pi) \\ \cos(\theta+\frac{2}{3}\pi) & \sin(\theta+\frac{2}{3}\pi) \end{bmatrix}\begin{bmatrix} x_d \\ x_q \end{bmatrix} \tag{6.4}$$

6.1.2 The Phase-locked Loop

The phase-locked loop is used to lock the θ of Park Transformation to the grid angular frequency. It aims to maintain the rotate speed of the dq0 coordinates at the grid angular velocity. To lock the component at q axis of the voltage to zero is an alternative way to achieve this goal. The component at q-axis of the voltage is:

$$v_q = -V_m \sin(\theta - \theta_{ref}) = V_m \sin(\theta_{ref} - \theta) \tag{6.5}$$

where V_m is the peak amplitude of the nominal voltage of the grid, θ is the grid angular velocity of the Park Transformation and θ_{ref} is the angular velocity of the grid. According to Taylor's expansion, when θ - θ_{ref} is close to zero, sin (θ_{ref} - θ) is approximately equal to θ_{ref} - θ [132]. Hence Equation (6.5) can be approximately written as:

$$v_q = V_m(\theta_{ref} - \theta) = x_e \tag{6.6}$$

where x_e is the error of the reference and feedback values. According to Equation (6.6), the block diagram of the phase-locked looped can be structured as shown in Figure 6.4. the closed-loop transfer function is:

$$\frac{\theta_{ref}(s)}{\theta(s)} = \frac{V_m \cdot G_{PLL}(s)}{s + V_m \cdot G_{PLL}(s)} \tag{6.7}$$

$G_{PLL}(s)$ is the designed proportion integration (PI) controlled, which is expressed as:

$$G_{PLL}(s) = K_{PG} + \frac{K_{IG}}{s} \tag{6.8}$$

where K_{PG} and K_{IG} are the proportion and integration gains of the PI controller. Substituting Equation (6.8) into (6.7), the transfer function of the phase locked loop is derived as:

$$\frac{\theta_{ref}(s)}{\theta(s)} = \frac{V_m(K_{PG} + \frac{K_{IG}}{s})}{s + V_m(K_{PG} + \frac{K_{IG}}{s})} = \frac{V_m K_{PG} s + V_m K_{IG}}{s^2 + V_m K_{PG} s + V_m K_{IG}} \tag{6.9}$$

By comparing Equation (6.9) with the normal form of a two-dimension transfer function:

$$\frac{\theta_{ref}(s)}{\theta(s)} = \frac{2s\xi\omega + \omega^2}{s^2 + 2s\xi\omega + \omega^2} \tag{6.10}$$

the gains of the PI controller can be calculated:

$$\begin{cases} K_{PG} = \dfrac{2\xi\omega}{V_m} \\ K_{IG} = \dfrac{\omega^2}{V_m} \end{cases} \tag{6.11}$$

where ω is the natural angular velocity and ξ is the damping factor of the phase locked loop system.

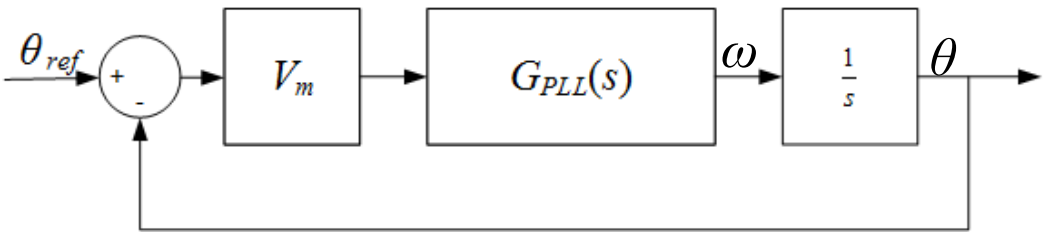

Figure 6. 4 Block diagram of the phase-locked loop

6.1.3 The dc Voltage Control Loop

The dc voltage control loop is to determine the demand power in order to maintain the dc bus at the required voltage. The dc bus is usually built using a capacitive energy storing device, according to the characteristic of capacitor $E = \frac{1}{2}CV^2$, the relation of the energy stored in the dc bus and its voltage is:

$$E_{d.c.} = \frac{1}{2}Cv_{d.c.}^2 \tag{6.12}$$

Since power is the time derivative of energy, the power flowing into the dc bus can be expressed as:

$$P_{d.c.} = \frac{dE_{d.c.}}{dt} = \frac{1}{2}C\frac{d(v_{d.c.}^2)}{dt} \tag{6.13}$$

By replacing $v_{d.c.}^2$ by F and conducting Laplace transformation to Equation (6.13), the power flowing into the dc bus can be expressed as:

$$P(s) = \frac{1}{2}sCF(s) = \frac{F(s)}{H_{d.c.}(s)} \tag{6.14}$$

Hence the transfer function of the system $H_{d.c.}(s)$ is calculated as:

$$H_{d.c.}(s) = \frac{2}{sC} \tag{6.15}$$

Set the PI controller $G_{d.c.}(s)$ to be:

$$G_{d.c.}(s) = K_{Pd.c.} + \frac{K_{Id.c.}}{s} \tag{6.16}$$

The transfer function of the closed loop voltage control system can be expressed as:

$$\frac{F(s)}{F_{ref}(s)} = \frac{G_{d.c.}(s)H_{d.c.}(s)}{1+G_{d.c.}(s)H_{d.c.}(s)} = \frac{sK_{Pd.c.} + K_{Id.c.}}{\frac{1}{2}Cs^2 + sK_{Pd.c.} + K_{Id.c.}} \tag{6.17}$$

where F_{ref} is the required dc bus voltage. By comparing Equation (6.17) with:

$$Y(s) = \frac{2s\xi\omega + \omega^2}{s^2 + 2s\xi\omega + \omega^2} \tag{6.18}$$

The value of the gains of the PI controller can be obtained:

$$\begin{cases} K_{Pd.c.} = C\xi_{d.c.}\omega_{d.c.} \\ K_{Id.c.} = \frac{1}{2}C\omega_{d.c.}^2 \end{cases} \tag{6.19}$$

where $\omega_{d.c.}$ and $\xi_{d.c.}$ are the natural angular velocity and damping factor of the dc voltage control loop system respectively. The block diagram of the dc voltage control loop is illustrated in Figure 6.5.

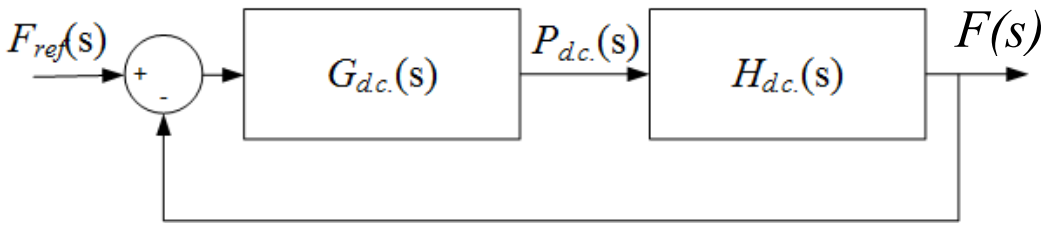

Figure 6. 5 Block diagram of the dc voltage control loop

The dc voltage control loop can adjust the power flowing through the VSC in order to maintain the dc bus voltage at the required value. Since the q axis voltage v_q is locked to be zero by the phase-locked loop, the current flowing through the VSC can be obtained from the power calculation expressed in dg0 coordinates, as given in Equation (6.20):

$$\begin{cases} P = \frac{3}{2}(v_d i_d + v_q i_q) \\ Q = \frac{3}{2}(v_d i_q - v_q i_d) \end{cases} \tag{6.20}$$

6.1.4 The Current Control Loop

The current control loop is used to generate the voltage reference for the PWM modulation process and eventually control the output of the VSC. The reference current input to current control loop is obtained from the output of the dc voltage control loop using the Equation (6.20).

As indicated in Figure 6.2, the voltage drop on the filter can be described as:

$$v_{fabc} = v_{gabc} - v_{Rabc} = R_f i_{abc} + L_f \frac{di_{abc}}{dt} \tag{6.21}$$

where R_f and L_f are the resistance and inductance of the RL filter. Applying the Park Transformation to each component in the Equation (6.21), it can be obtained:

$$\begin{bmatrix} v_{fd} \\ v_{fq} \end{bmatrix} = \begin{bmatrix} v_{gd} \\ 0 \end{bmatrix} - \begin{bmatrix} v_{Rd} \\ v_{Rq} \end{bmatrix} = R_f \begin{bmatrix} i_d \\ i_q \end{bmatrix} + L_f \frac{d}{dt} \begin{bmatrix} i_d \\ i_q \end{bmatrix} + L_f \begin{bmatrix} 0 & -\omega \\ \omega & 0 \end{bmatrix} \begin{bmatrix} i_d \\ i_q \end{bmatrix} \tag{6.22}$$

The value 0 is the output q axis voltage of the VSC, which is locked to be zero by the phase locked loop as mentioned in section 6.1.3. Hence the Laplace Transformation of Equation (6.22) can be expressed as:

$$\begin{bmatrix} V_{fd}(s) \\ V_{fq}(s) \end{bmatrix} = \begin{bmatrix} sL_f & 0 \\ 0 & sL_f \end{bmatrix} \begin{bmatrix} I_d(s) \\ I_q(s) \end{bmatrix} + \begin{bmatrix} R_f & 0 \\ 0 & R_f \end{bmatrix} \begin{bmatrix} I_d(s) \\ I_q(s) \end{bmatrix} + \begin{bmatrix} 0 & -\omega L_f \\ \omega L_f & 0 \end{bmatrix} \begin{bmatrix} I_d(s) \\ I_q(s) \end{bmatrix} \tag{6.23}$$

The transfer function of the current control loop, with current as input and the voltage at the rectifier side as output, can be obtained from Equation (6.23):

$$[H_C(s)] = \frac{[I_{dq}(s)]}{[V_{fdq}(s)]} = \begin{bmatrix} sL + R & -\omega L \\ \omega L & sL + R \end{bmatrix}^{-1} \tag{6.24}$$

In order to obtained the transfer function of this current control loop system, the coupling quantities $-\omega L i_q$ and $\omega L i_d$ must be decoupled using the decoupling process:

$$\begin{bmatrix} V_{Rd}(s) \\ V_{Rq}(s) \end{bmatrix} = \begin{bmatrix} -V_{fd}(s) + V_{gd}(s) - \omega L_f I_q(s) \\ -V_{fq}(s) + 0 + \omega L_f I_d(s) \end{bmatrix} \tag{6.25}$$

By substituting the decoupling Equation (6.25) into Equation (6.23), the following relation can be obtained:

$$\begin{bmatrix} I_d(s) \\ I_q(s) \end{bmatrix} = \begin{bmatrix} \frac{1}{sL+R} & 0 \\ 0 & \frac{1}{sL+R} \end{bmatrix} \begin{bmatrix} V_{fd}(s) \\ V_{fq}(s) \end{bmatrix} \tag{6.26}$$

Therefore, the transfer function of the current control loop system in Equation (6.24) is reduced as Equation (6.27) without the coupling quantities:

$$[H_C^{'}(s)] = \frac{[I_{dq}(s)]}{[V_{fdq}(s)]} = \begin{bmatrix} \frac{1}{sL_f + R_f} & 0 \\ 0 & \frac{1}{sL_f + R_f} \end{bmatrix} \tag{6.27}$$

For the ease of the design of the control system, an internal model control method is applied to simplify the parameter settings [133]. The PI controller, according to the internal model control method, can be defined as:

$$K_{PI}(s) = K_P + \frac{K_I}{s} = nL_f + \frac{nR_f}{s} \tag{6.28}$$

where 1/n is the time contestant of the current control loop. The closed-loop transfer function of the current control loop can be written as:

$$\frac{I_{dq}(s)}{I_{dqref}(s)} = \frac{K_{PI}(s)H_c^{'}(s)}{1 + K_{PI}(s)H_c^{'}(s)} = \frac{n}{s+n} \tag{6.29}$$

As indicated in Equation (6.29), by using the internal model control method, the transfer function of the current control loop is reduced to one-dimensional system with only one parameter of n. This increases the robust of the control system and reduce the difficulty in the design of the control system. The block diagram of the control loop is shown in Figure 6.6.

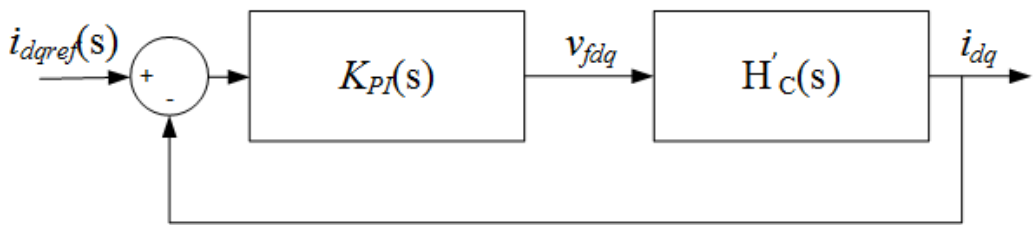

Figure 6. 6 Block diagram of the current control loop

6.2 Functions of B2B VSC

The functions of B2B in voltage regulation, power flow control and fault restrain are analysed in simulations. the simulations are conducted in models developed using Matlab/SIMULINK. The network topology is as indicated in Figure 6.1. Based on the model used in the study on the effects of synchronous generator type DG in Chapter 3, an expanded network is simplified into two main feeders each with three aggregated loads evenly distributed along each feeder, as shown previously in Figure 3.27.

The interconnection is between load busbars 13 and 23. Feeder 1 changes again from the peak loaded to the minimum load, i.e. 20% of the peak load. The voltage changes of load busbar 13 caused by the increasing DG penetration level is given in Figure 6.7.

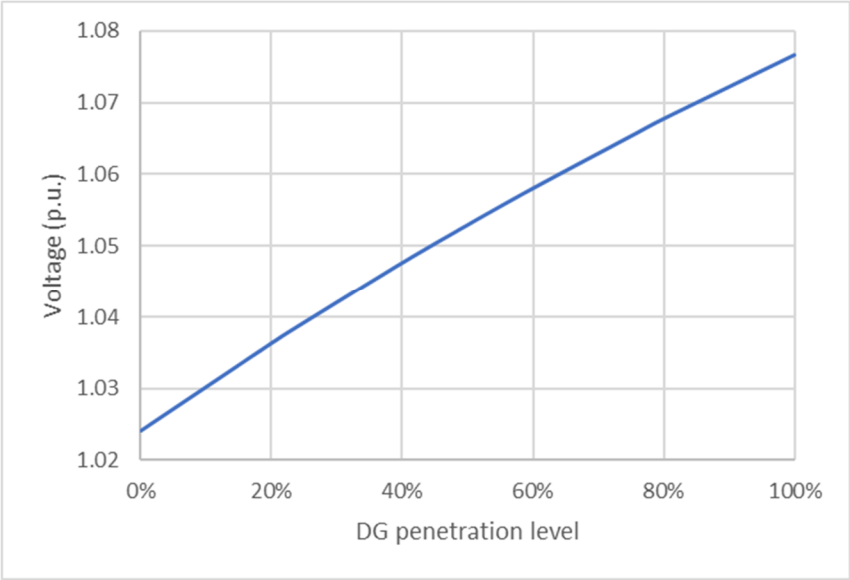

Figure 6. 7 Voltage of load busbar 13 at minimum load with increasing DG penetration

It was shown in Figure 6.7 that when the DG penetration level is approximately 55%, the voltage will exceed the upper limit of 1.06 p.u.. With the connection to feeder 2 using a power electronic controller (B2B-VSC), the voltage of load busbar 13 can be regulated within the limit, as shown in Figure 6.8 for transferred power (to another feeder) at 1-6MW. For the fault level limit at the primary busbar (i.e. load busbar 11), the result is shown in Figure 6.9, for a 4.2MW, 400V, 50Hz synchronous generator STAMFORD P80. The three-phase short circuit fault is at the primary busbar.

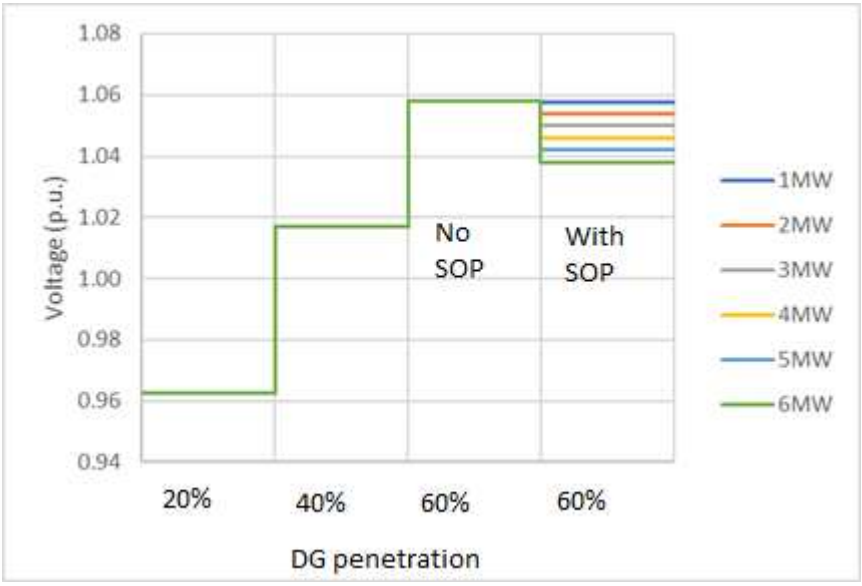

Figure 6. 8 Voltage variation at load busbar 13 with interconnection using a B2B-VSC power electronic controller to transfer power

Figure 6.9 shows the current from the other feeder connected through a mechanical switch or B2B-VSC, and the fault current at the primary busbar for both cases regarding the connection at the far ends of the two feeders. As shown in Figure 6.9, direct connection without using the B2B-VSC power electronic controller will certainly cause the fault level to exceed the switchgear rating (13kA break, at 100ms after fault inception) due to the connection of DG and the connection of the other feeder. With the power electronic controller for power transfer, the fault current contributed by the other feeder can be reduced to a low set value to keep the fault level within the switchgear capability limit, due to the current control loop of the voltage source converter. Due to unbalanced loading between the two feeders, this is a load current in the normal operation of the B2B VSC, which is indicated as the small current before fault in the second figure in Figure 6.9.

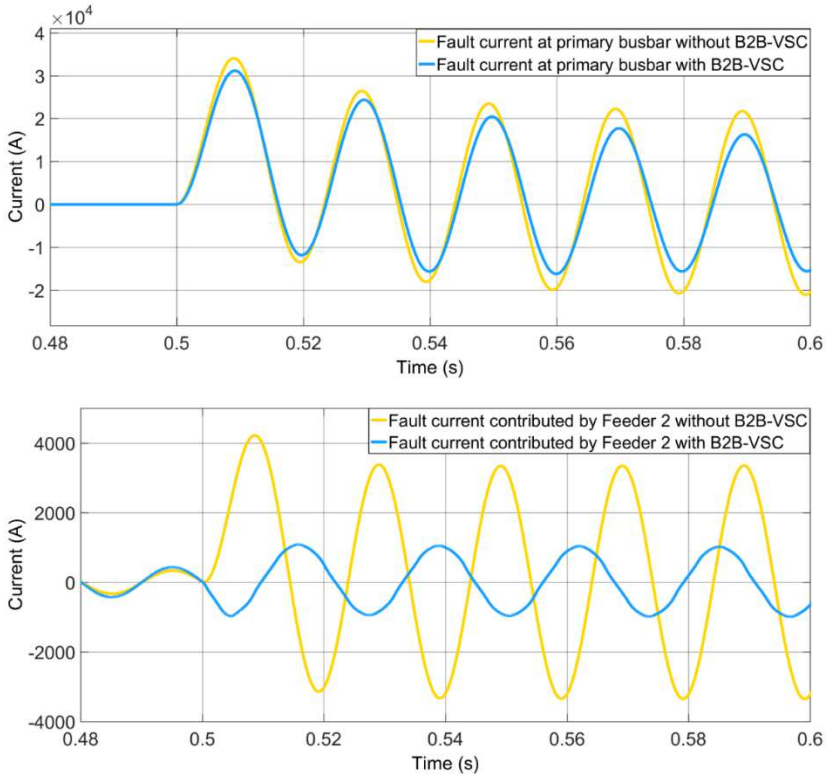

Figure 6. 9 Fault current limiting using B2B-VSC for the interconnection

6.3 Network Power Loss with Feeder Connection Using B2B-VSC

As analysed in the previous sections, voltage regulation and fault current limiting can be provided by a B2B-VSC device. Furthermore, a reduction of the network loss could be achieved in some cases, by balancing the current flow when the far ends of the two feeders are connected in such a controlled manner.

It is noteworthy that the B2B-VSC could introduce considerable power losses compared to the network loss that can be saved. Therefore, the device loss needs to be included when investigating the network loss reduction. In this study, simulations are carried out to calculate the conduction and switching losses of the semiconductors and analyse the effect on the control strategy for loss reduction. Firstly, appropriate power semiconductor devices need to be selected. For the network model in the previous section, the extreme case (with one feeder at peak loading of 20MVA and the other feeder with almost no load) requires the B2B-VSC to transfer a maximum power of 9.68MW to balance the current in the network which corresponds to a peak current of 719A at 11kV. So, the power module 'ABB HiPak IGBT Module 5SNE 0800M170100' which has the rating of V_{ce} = 1700V and I_c = 800A is selected for the study. For the simplicity of first analysis, the two-level VSC structure is adopted with 15 IGBT modules connected in series for each arm. The dc link voltage is set at 20kV. 90 modules in total for one ac-dc converter, are required for direct connection to the 11kV network. The total device loss consists of the turn on and off losses of the IGBTs, the IGBT conduction loss, the diode conduction loss and the diode reverse recovery loss which depends on the current.

All these losses can be obtained from the datasheet of the selected module for a determined current level and junction temperature. In the simulation, the junction temperature is assumed to remain at 125℃ for the worst scenario. As the junction temperature is considered to be constant, all the losses can be regarded as the functions of the current.

The total energy loss of the B2B VSC includes: the on-state power loss of the IGBT and diode; and the turn on/off power loss of the IGBT and the reverse recovery power loss of the diode. For on time instinct *dt*, the total energy loss of an individual IGBT power module can be calculated as:

$$\begin{aligned} E_{total} &= (P_{on-state\_IGBT} + P_{on-state\_diode} + P_{on} + P_{off} + P_{rec})dt \\ &= (v_{ce} \cdot i_c + v_f \cdot i_f + \frac{e_{on}}{t_r} + \frac{e_{off}}{t_f} + \frac{e_{rec}}{t_{rr}})dt \end{aligned} \tag{6.30}$$

where, v_{ce}, v_f, e_{on}, e_{off} and e_{rec} are the on-state voltage, diode forward voltage, turn on loss, turn off loss and the diode reverse recovery energy respectively; v_{ce} , e_{on} and e_{off} are functions of the collector current i_c. Similarly v_f and e_{rec} are the functions of the diode forward current; t_r, t_f and t_{rr} are the rise time, fall time and reverse recovery time which are characteristics of the module that can be found in the datasheet. The equations for calculating v_{ce}, v_f and so on are determined by curve fitting the characteristic plots in the datasheet. In addition, the logic part needs to be built to ensure that the conduction losses are only calculated when the IGBT or diode is conducting, the switching losses are only calculated when the IGBT is turned on or off, and the reverse recovery energy is only calculated when the diode is turned off. Besides the loss in the device, the loss in the filter of the converter should also be included. A well-designed filter introduces power loss about 0.65% of the power flow through the device.

Therefore, the total power loss of a single IGBT module is, by definition, the integral of the total energy loss over one second, which is:

$$P_{total} = \int_0^1 E_{total} \tag{6.31}$$

For a network includes two feeders with imbalanced loading conditions (load current $I_1 \neq I_2$), as indicated in Figure 6.10, the total network loss can be calculated by:

$$P_{Loss\_total} = P_{Loss\_1} + P_{Loss\_2} = I_1^2 R_1 + I_2^2 R_2 \tag{6.32}$$

If the network load is balanced by end connection of these two feeders, the load current is also balanced to be:

$$I_1^{'} = I_2^{'} = \frac{I_1 + I_2}{2} \tag{6.33}$$

Hence the total power loss of the balanced network can be obtained by:

$$\begin{aligned} P_{Loss\_total}^{'} &= P_{Loss\_1}^{'} + P_{Loss\_2}^{'} = I_1^{'2} R_1 + I_2^{'2} R_2 \\ &= \left(\frac{I_1 + I_2}{2}\right)^2 R_1 + \left(\frac{I_1 + I_2}{2}\right)^2 R_2 \end{aligned} \tag{6.34}$$

Assuming the line resistances are the same, that $R_1 = R_2 = R$ for both feeders, by subtracting Equation (6.34) from Equation (6.32), the difference of total power loss of the network can be obtained as:

$$\Delta P_{Loss\_total} = P_{Loss\_total} - P_{Loss\_total}^{'} = \frac{(I_1 - I_2)^2}{2} R > 0 \cdots\cdots (I_1 \neq I_2) \tag{6.35}$$

Therefore, by balancing the loading conditions between two feeders in a network using the B2B VSC based SOP, the total network loss can be reduced.

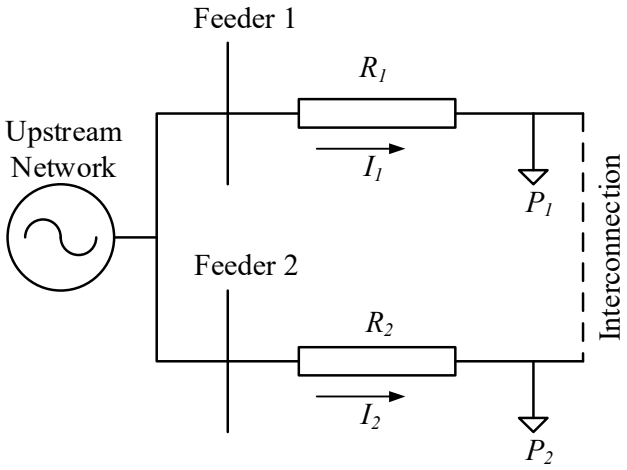

Figure 6. 10 Single line diagram of a network with imbalanced feeder loadings

To investigate the loss reduction with different unbalancing levels, i.e. different power exchange through the B2B-VSC, the scenarios considered in this paper are: the load level on Feeder 1 varies from 20% to 90% with a step size of 10%, while the load level on the other feeder remains at 100%. The network condition is the same as in Section 6.2. Three DG penetration levels are concentrated at the end of Feeder 1, and these penetration levels (PL) are 20%, 40% and 60%. Basically, the greater is the load difference between the two feeders, the more power transfer is needed to balance the currents and hence reduce the network loss.

The comparisons between the original network loss and the 'minimised' network loss when the two feeders are connected using the B2B-VSC are given in Tables 6.1, 6.2 and 6.3. The results indicate that the connection between the feeders can significantly reduce the system active power loss. This reduction decreases with the increase of the load level on Feeder 1 but increases with the increase of DG penetration. A comparison among the reduced network losses including the loss of the B2B-VSC is shown in Figure 6.11.

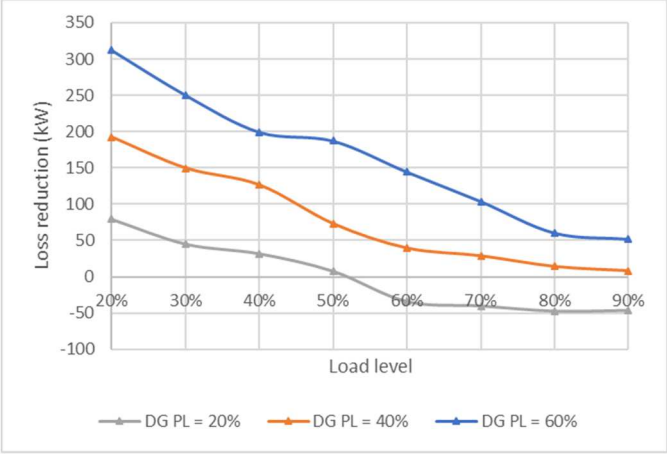

Figure 6. 11 Total network loss reductions under different DG penetrations

*Table 6. 1 Network loss reduction (**kW**) at DG penetration of 20%*

Load level of Feeder 1	20%	30%	40%	50%	60%	70%	80%	90%
Transferred power	6520	5920	5330	4740	4180	3610	3060	2520
Original network loss	610	600	610	630	660	700	740	800
Reduced network loss	320	360	400	460	540	600	660	730
Converter loss	211	195	178	163	154	140	128	117
Loss reduction	79	45	32	7	-34	-40	-48	-47

*Table 6. 2 Network loss reduction (**kW**) at DG penetration of 40%*

Load level of Feeder 1	20%	30%	40%	50%	60%	70%	80%	90%
Transferred power	8100	7490	6900	6310	5730	5160	4600	4050
Original network loss	650	630	620	610	620	640	670	710
Reduced network loss	200	240	270	330	390	430	490	550
Converter loss	258	240	224	207	191	181	166	152
Loss reduction	192	150	126	73	40	29	14	8

*Table 6. 3 Network loss reduction (**kW**) at DG penetration of 60%*

Load level of Feeder 1	20%	30%	40%	50%	60%	70%	80%	90%
Transferred power	9680	9070	8460	7870	7280	6710	6140	5580
Original network loss	770	720	680	670	650	640	650	680
Reduced network loss	140	180	210	230	270	310	380	434
Converter loss	318	289	271	253	236	226	210	194
Loss reduction	312	251	199	187	144	104	60	52

The figure shows that with the increase of load level on Feeder 1 (as the loads on two feeders are more balanced), the total network loss reduction effect decreases. For the same load level given, the total loss reduction increases with the increase of DG penetration. Furthermore, when the DG penetration is below 20%, the total network loss reduction is negative when the load level on Feeder 1 is above 50%.

This negative loss reduction means the total network loss increases compared to the original network loss due to the power loss of B2B-VSC. However, with large load unbalance, when the load level of Feeder 1 is below 50%, the total network loss reduction becomes positive. This means that the total network loss is reduced due to the connection of the two feeders even including the power losses of power electronic devices. For DG penetration of 40% and more, the total system reduction is always positive. This indicates that with this connection between the two feeders using the B2B-VSC, the network loss can be significantly reduced with the increasing DG penetration. Different B2B-VSC configurations may differ in efficiency.

6.4 Summary

This section presents results on a typical 11kV distribution network in the UK. When DG is concentrated close to the primary busbar in a distribution network, the fault level is the more significant constraint regarding further increasing the DG penetration level. When the DG penetration is over 70% it will cause the fault level to exceed the current switchgear ratings, particularly the break rating. When DG is concentrated at the far end of the distribution feeder, the voltage profile becomes the most critical constraint regarding further increasing the DG penetration level. The voltage violation occurs when the DG penetration level is over 60%.

The break over location of the voltage constraint and the current constraint is about 3km from the primary busbar. These fault level and voltage violation issues caused by DG can be solved by implementing a B2B-VSC in the distribution network.

Utilising the B2B-VSC in the distribution network can effectively regulate the voltage violation caused by the DG penetration when the feeder power is transferred from the heavily loaded to the lightly loaded. It can also avoid the consequential further rise of the fault level. Furthermore, due to the connection of the two feeders, the power flow is balanced to some extent which reduces the total network loss, even including the loss of the B2B-VSC. This reduction of network loss is positively correlated to the level of load unbalance between the two feeders. It is also proportional to the unbalanced DG penetration level in the network. It is noteworthy that the B2B-VSC can increase the network loss when the load unbalance or DG penetration level is low.

Chapter

7 Loss Study on the Saturated Iron Core Fault Current Limiter in Normal Operation

The saturated iron core fault current limiter (FCL) consists of two ac windings connected in series with the network and a dc winding to provide the excitation current. As the structure of the saturated iron core FCL is similar to a power transformer, the loss of a saturated iron core FCL also includes: no-load loss and load loss, as the transformer. To be in detail, the no-load loss includes: eddy current loss and hysteresis loss. The load loss includes the copper loss and the stray loss.

The causes of all these types of loss are explained in detail in the following sections. Based on these causes, the loss of a saturated iron core FCL is analysed and compared to a transformer with the same capacities.

7.1 Different Types of Loss of a Transformer

7.1.1 Eddy Current Loss

When ac current is flowing through the coils, the current generates a changing magnetic field subject to the cross section of the iron core. According to Faraday's Law, this changing magnetic field will induce current within the iron core as shown in Figure 7.1. This induced current is the eddy current. Due to the resistance of the iron core, the eddy current does work and this work dissipates as heat. This type of energy loss is the eddy current loss of the transformer.

The eddy current increases with the width of current loop. To reduce the loss, transformer core nowadays is commonly manufactured using stacked coated laminations. For a single lamination with unit volume and mass, the eddy current loss can be calculated using [134].

$$Loss_E = (\frac{\pi^2}{6}) \frac{f^2 B_{\max}^2 l^2}{\rho D} \tag{7.1}$$

where f is the frequency of current, B_{max} is the peak flux density, l is the length of the lamination, ρ is the resistivity of the material and D is the density of the material. Hence the total eddy current loss of a transformer is:

$$P_E = Loss_E VMN \tag{7.2}$$

where V is the volume of a single lamination, M is the mass of a single lamination and N is the number of laminations of the transformer. The value of VN is also the volume of the transformer core.

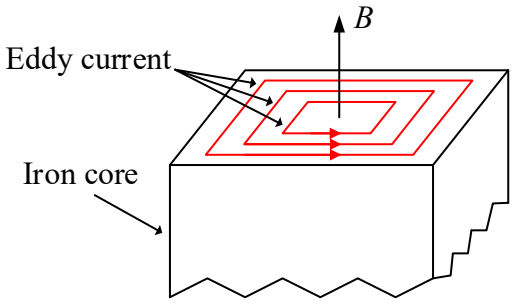

Figure 7. 1 Eddy current

7.1.2 Hysteresis Loss

The phenomenon of magnetic hysteresis refers to that in the magnetisation or demagnetisation of a ferromagnetic material, the change of the flux density (B) of the material lags the applied external field excitation (H). When an external field excitation is applied to a demagnetised ferromagnetic material, domains having the direction closest to

that of the applied field grow due to the motion of domain walls. At the initial stage, the motion of domain wall is reversible so that the phenomenon of magnetic hysteresis does not occur.

Due to that the crystal structure of the ferromagnetic material contains imperfections, the domain boundaries will encounter these imperfections during their movement. The applied magnetic field excitation can provide the energy for the domain wall to eliminate the magnetostatic energy associated with the imperfections when the domain wall moves past the imperfections. Eventually, all domains will align towards the same direction as the applied field excitation for the whole material, which behaves like a single domain [135]. When further increasing in the applied magnetic field excitation, this domain rotates away from the easy direction to an orientation parallel to that of the external applied field. This stage of magnetisation is the saturation stage of the material. If the external applied field excitation is removed, the single domain will return to the easy direction in the crystal. During the demagnetisation process, a demagnetising field is set up due to the single domain. The magnetising field excitation is not strong enough for the domain walls to grow past the crystal defects so that they cannot reverse back to the original growth path. This results in the magnetic hysteresis. The full *B*-*H* curve of a hysteresis loop is shown in Figure 7.2. When the external field is totally removed, some magnetisation remains, which is the remnant magnetisation. To neutralise this magnetisation, extra magnetomotive force (mmf) is required, which is the coercive force. Hence in the operation of a transformer, this extra mmf causes extra work, which is known as the hysteresis loss of transformer [134].

Considering a transformer core having a *N*-turn winding with current *I* A, as shown in Figure 7.3, has an equivalent magnetic path of *L* m. The mmf generated by the current is:

$$\oint Hdl = NI \tag{7.3}$$

which leads to that:

$$H = \frac{NI}{L} \tag{7.4}$$

where *H* is the magnetic field of the iron core. At this instant, the magnetic flux density of the iron core is *B*. Therefore, the total magnetic flux through the transformer core is:

$$\Phi = A_T B \tag{7.5}$$

where A_T is the cross-section area of the iron core. According to Faraday's Law, the induced electromotive force (EMF) is:

$$\varepsilon = -N\frac{d\Phi}{dt} = -NA_T\frac{dB}{dt} \tag{7.6}$$

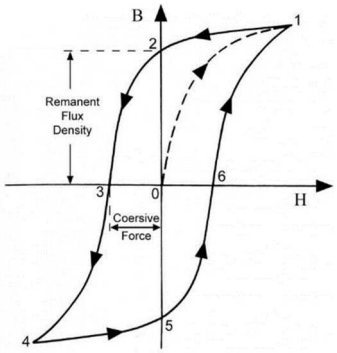

Figure 7. 2 Schematic of the hysteresis curve

This induced EMF is opposing to the flow of the applied current and hence to maintain the current flow, an opposite EMF must be supplied by the source. Hence the energy consumed in this instant *dt* is:

$$E^{'} = -\varepsilon I dt = NA_T \frac{dB}{dt}\frac{HL}{N}dt = A_T LHdB \tag{7.7}$$

For one cycle of the ac current, the total energy consumption by the transformer iron core is:

$$E = \int_0^{B_{\max}} E^{'} = A_T L \int_0^{B_{\max}} HdB \tag{7.8}$$

As shown in the Figure 7.4, $\int HdB$ is the area enclosed by the Hysteresis loop. Therefore, the hysteresis loss of transformer can be calculated using:

$$P_H = fA_T LA_{B-H} = fVA_{B-H} \tag{7.9}$$

where f is the frequency of the current, V is the volume of the transformer iron core and $A_{B\text{-}H}$ is the area of the full B-H curve of the transformer.

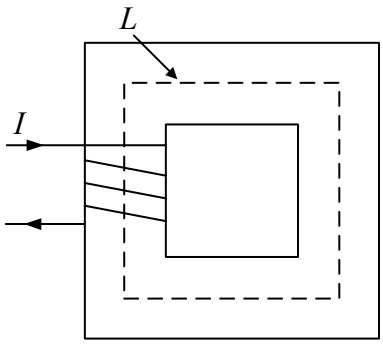

Figure 7. 3 Schematic of the transformer core with winding current I

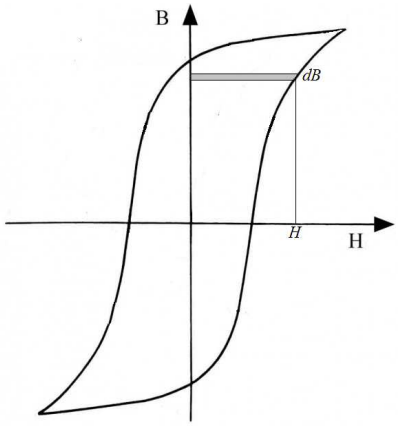

Figure 7. 4 Schematic of one-cycle of the hysteresis loop

7.1.3 Copper Loss and Stray Loss

Copper loss is the loss dissipated as heat due to the resistance of transformer windings. It is calculated by:

$$P_C = I_1^2 R_1 + I_2^2 R_2 \tag{7.10}$$

where I_1 and I_2 are the current of the primary and secondary windings of the transformer and R_1 and R_2 are the winding resistances of the primary and secondary windings. The stray loss is caused by the link of leakage flux of the winding current with transformer tanks and clamps.

7.2 Loss Analysis of the Saturated Iron Core FCL

7.2.1 Load Loss

The structure of a saturated iron core fault current limiter (FCL) is shown in Figure 7.5. Like the transformer, the loss of a saturated iron core FCL also includes the no-load loss (eddy current and hysteresis losses of the core) and load loss (copper loss and stray loss of the windings).

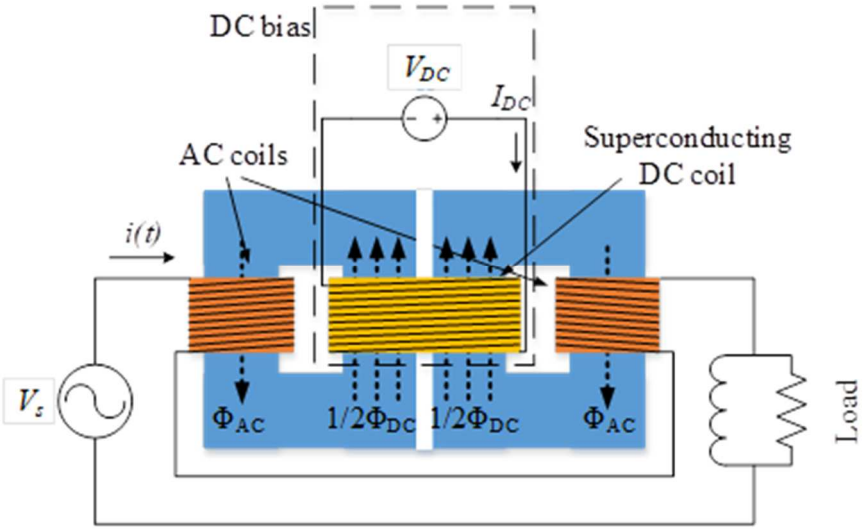

Figure 7. 5 Schematic of a saturated iron core FCL

Compared to the transformer, the load loss will increase in a saturated iron core FCL. With the fixed winding resistance, the copper loss does not change compared to that of a transformer. However, due to the permeability of the core is reduced if the core is in saturation, the leakage inductance of the ac winding will increase, which results in the increase of the stray loss of a saturated iron core FCL compared to the transformer.

7.2.2 No-load Loss

As indicated in Figure 7.6, with same increase in the applied magnetic field excitation, the change of magnetic flux density, ΔB, of the unsaturated core and saturated core is different.

Compared to the unsaturated core, the change of magnetic flux density regarding the same change in the applied field excitation will reduce significantly in a saturated core. The relation between the magnetization of the material and the applied field can be expressed as:

$$B = \mu H = \mu_r \mu_0 H \tag{7.11}$$

where μ is the magnetic permeability of the material, μ_0 is the permeability of vacuum and μ_r is the relative permeability of the material, which is the ratio of μ to μ_0. The permeabilities of some common materials are listed in Table 7.1.

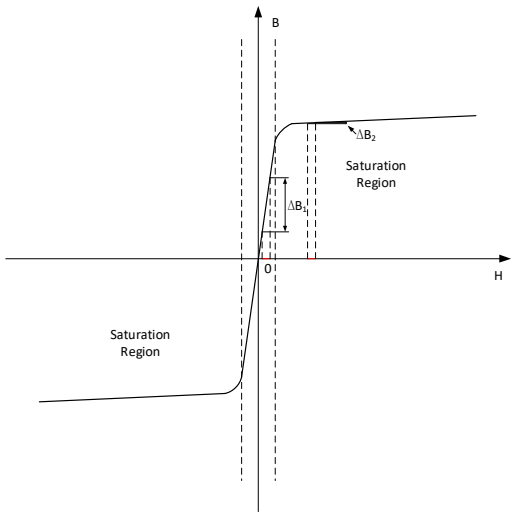

Figure 7. 6 Schematic of B-H curve

For the ferromagnetic materials, it can build strong magnetism with applied external magnetic field excitation. This results in large magnetic permeability when the material is demagnetised, like the electrical steel (also known as silicon steel, which is an iron alloy with silicon up to 6.5%), iron and permalloy (nickel-iron alloy) listed in the Table 7.1.

However, when the material is saturated, the permeability will reduce significantly, which can be 2% of or even less than that of material in the normal status [136]. Hence for the same increase in the magnetic field excitation H, the increase of the induced magnetic flux density B when the material is saturated is only 2% of that in normal status.

Since both the eddy current loss and hysteresis loss is related to the peak induction of the iron core, it is obvious that for a saturated core, the no-load loss will be much smaller compared to an unsaturated core. But the reduction differs in the level of the magnetisation of the material and this is further analysed based on the experiment results.

Table 7. 1 Permeability of common materials [137]

Material	Permeability, μ(H/m)	Relative permeability, μ/μ_0
Air	1.25663753×10^{-6}	1.00000037
Aluminium	1.256665×10^{-6}	1.000022
Copper	1.256629×10^{-6}	0.999994
Electrical steel	5.0×10^{-3}	4000
Hydrogen	1.2566371×10^{-6}	1
Iron (99.8% pure)	6.3×10^{-3}	5000
Permalloy	1.0×10^{-2}	8000
Platinum	1.256970×10^{-6}	1.000265
Vacuum	$4\pi \times 10^{-7}$ (μ_0)	1, exactly
Water	1.256627×10^{-6}	0.999992
Wood	1.25663760×10^{-6}	1.00000043

7.2.3 Experiment and Results

To analyse the reduction in the loss of a saturated iron core FCL, a transformer core manufactured using permalloy is used. The parameter of the core is listed in Table 7.2. The test circuits are shown in Figures 7.7 and 7.8 and the test bench is shown in Figure 7.9.

Table 7. 2 Transformer core parameter

Core type	Shell-type construction
Dimensions	228mmL x 100mmD x 180mmH
Number of turns	115 primary winding
	5 secondary winding
Resistivity (25°C)	0.55e-6 Ωm
Permeability	0.0111 H/m
Density	8750kg/m^3

An open circuit test is conducted firstly to obtain the magnetic characteristic of the transformer core. Then a test coil with the same number of turns as the secondary winding is added to the transformer core to measure the induced voltage. For the loss test, a dc excitation current is supplied to the primary winding of the transformer core to saturate it. Then a 100Ω load is connected to the secondary winding supplied by the ac voltage source through a variac. The induced voltage and total loss are measured for different excitation currents. From the open circuit test, the magnetic field, *H*, can be calculated using Equation (7.4) from the measured current. The magnetic flux density, *B*, can be calculated by integrating the measured winding voltage from:

$$B = \frac{1}{AN}\int vdt \tag{7.12}$$

where A is the cross-section area of the transformer core and N is the number of turns of the primary winding.

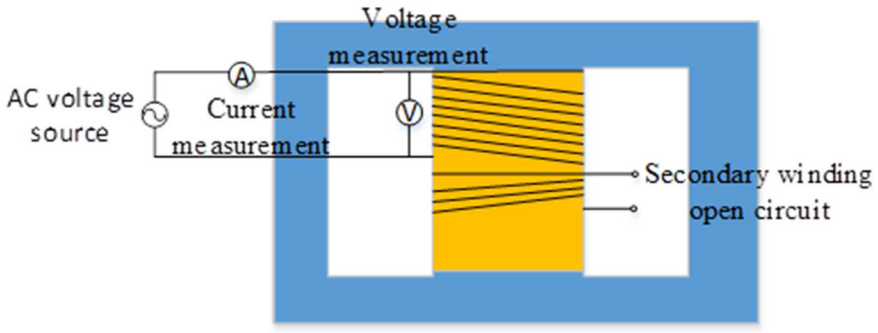

Figure 7. 7 Test circuit of open circuit test of the transformer core

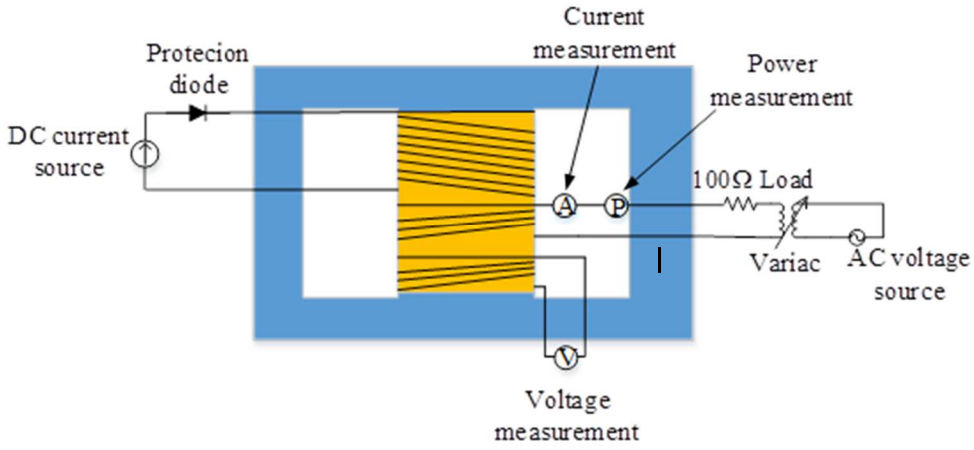

Figure 7. 8 Test circuit of the loss test

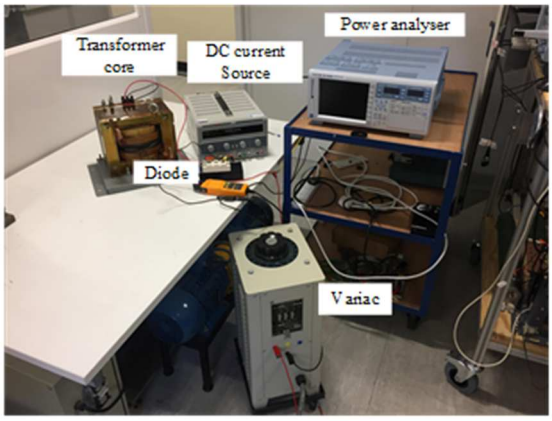

Figure 7. 9 Test bench

Figure 7.10 shows the hysteresis loop of the transformer core extracted from the calculation. The permeabilities extracted from the *B-H* curve of the transformer core are approximately 0.001 H/m in saturation (the magnetite of the magnetic field, $100<|H|<400$), which is about 10% of the permeability of 0.0111 H/m when the core is unsaturated ($|H|<100$) and 0.00027H/m in deep saturation ($|H|>400$), which is about 2% of unsaturated core.

The measured results of the total loss in the loss test are listed in Table 7.3. A detailed comparison in each type of loss between the normal status and status with core saturation (with excitation current of 2A dc) of transformer core is demonstrated in the follows.

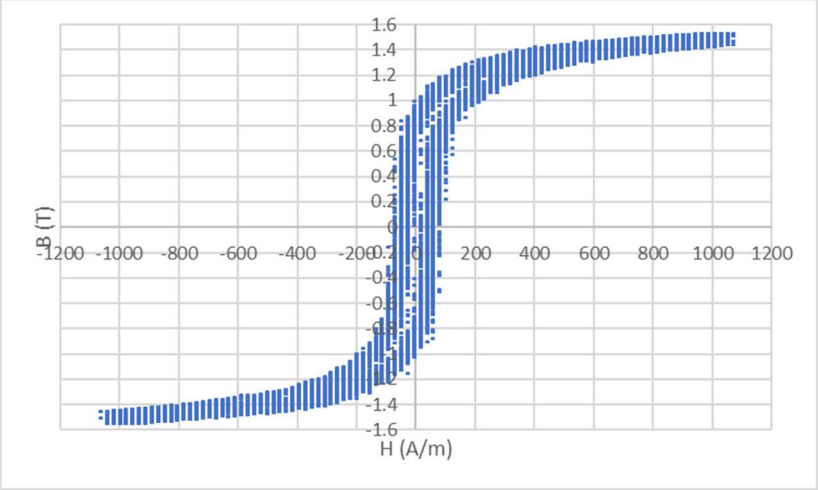

Figure 7. 10 Transformer core hysteresis loop

Table 7. 3 Loss test measurements

Transformer core status	Excitation current (A)	Load current (A, RMS)	Induced voltage (V, RMS)	Total loss (W)
Normal	0	1	10.131	10.816
Saturation	1.5	1	2.52	2.654
	1.75	1	1.41	1.326
	2	1	1.06	0.732

For each status, the magnetic flux density of the transformer core can be calculated using Equation (7.11) with the relative permeability. For the saturation status, the applied magnetic field H is calculated using:

$$H_{total}L = N_1 I_{dc} + N_2 I_{load} \tag{7.13}$$

From the calculated magnetic flux density, B_0, the maximum change of the magnetic flux density can be obtained for the calculation of eddy current loss. By using the fitting equation:

$$B = B_0 + \lambda \frac{dH}{dt} \tag{7.14}$$

to the hysteresis loop shown in Figure 7.10, the hysteresis loop can be obtained using the following parameters in Table 7.4. The obtained hysteresis loops by the curve fitting of both statuses are shown in Figures 7.11 and 7.12.

Table 7. 4 Fitting coefficients

Range of H	d*H*/d*t*	λ
H<-100	>0	-2.28E-07
	<0	-4.83E-07
-100≤H≤0	>0	-4.72E-08
	<0	-2.94E-08
0<H≤100	>0	2.47E-08
	<0	4.78E-08
H>100	>0	-7.07E-07
	<0	-3.06E-07

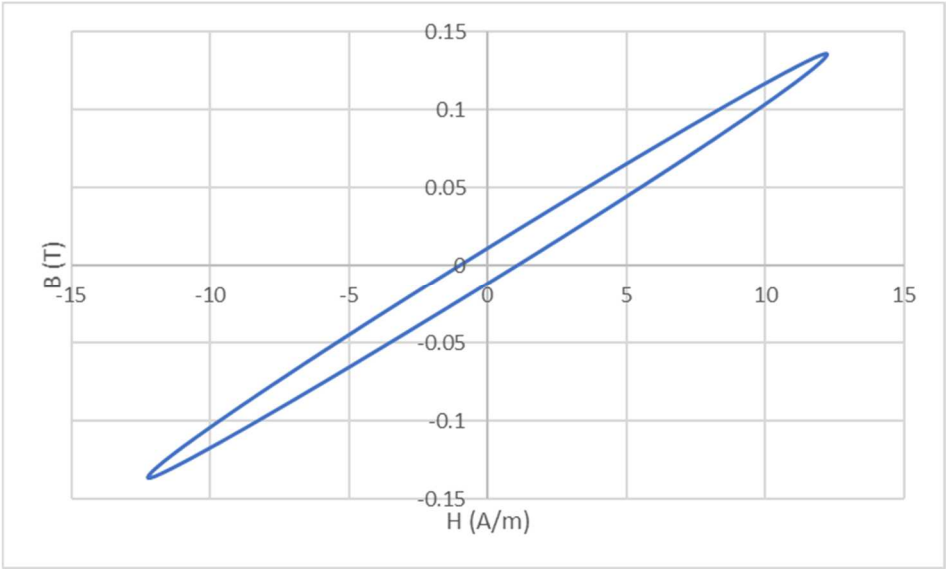

Figure 7. 11 Hysteresis loop - normal status

With the hysteresis loop calculated using the measurements in the experiment, the no-load loss of the tested transformer in both normal status and saturation status can be calculated using Equations (7.2) and (7.9). the copper loss of the tested transformer in both statuses are calculated using Equation (7.10). Since the stray loss is related to the leakage induction of the winding current, it is difficult to calculate explicitly using certain equations in practice.

The stray loss is obtained by subtracting all the other types of losses from the total loss. The experimental results of the total loss and the calculated results of these four types of loss of the tested transformer in the normal and saturation statuses are given in Table 7.5.

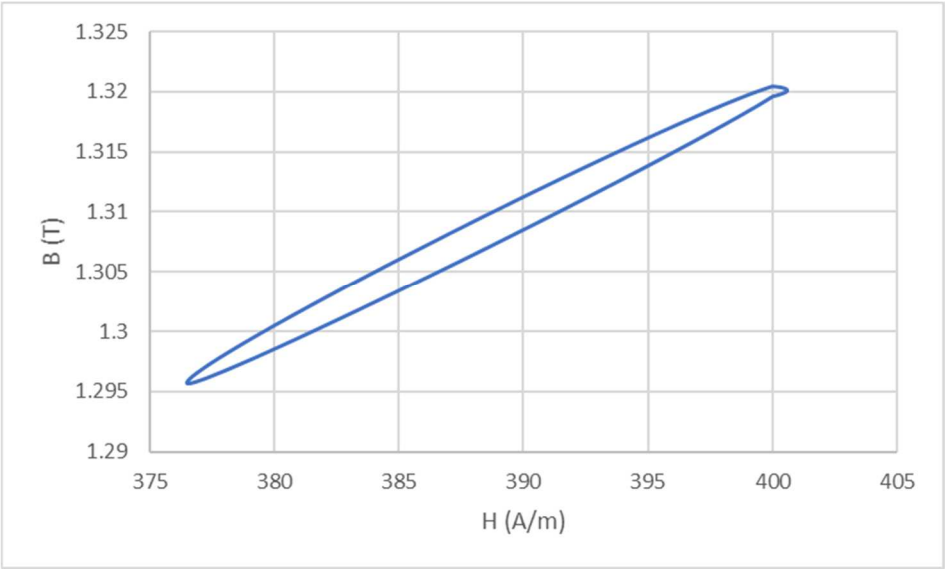

Figure 7. 12 Hysteresis loop - saturation status

The efficiency of the unsaturated iron core is approximately 90%, while of a saturated iron core is approximately 99%, without considering the loss in the dc coil. It can be obtained from Table 7.5 that the dominant loss of an unsaturated iron core is the eddy current loss, while for the saturated iron core, it should include the stray loss.

Compared with the unsaturated core, there is a significant reduction in the no-load loss. This is because both type of no-load losses are related to the magnetic flux density B of the iron core. For the eddy current loss, according to Equation (7.1), it is proportional to the square of the peak flux density variation caused by the applied field, B_{max}, of the iron core.

Since the permeability in saturation is 10% of that in the normal status, regarding the same change in the applied magnetic field excitation, the peak induction of a saturated core is 10% of that in an unsaturated core. Hence the eddy current loss in saturation is approximately 1% of that in normal status, as shown by the results in Table 7.5.

For the hysteresis loss, it is proportional to the area enclosed by hysteresis loop which is equivalent to the product of the the applied field and the field excitation. Hence for the same change in the applied field excitation, the hysteresis loop is proportional to the induction. When the iron core is saturated, the induction is about one tenth compared to unsaturated core, as mentioned before. Hence the hysteresis loss in a saturated core is about 10% of that in an unsaturated core, as shown in Table 7.5. For the load loss, both types are related to the load current. Hence for the same load current, the copper loss does not change with the status of the iron core. For the stray loss, it is proportional to the leakage induction of the winding. With the iron core becoming saturated, the permeability of the iron core reduces which results in the increase of the leakage flux linkage of the winding current. This will increase the stray loss of the saturated core FCL compared to that of a transformer. This also coincides with the calculation results in Table 7.5. Due to the significant reduction in the no-load loss in a saturated iron core, the total loss of a saturated iron core FCL decreases largely compared to the transformer. For the core in deep saturation, the loss will reduce even further.

The sum of the no-load and load losses of a saturated iron core FCL is less than 1% of its capacity. For the recent technologies, the dc wind is always designed to be superconducting to reduce the loss in the dc winding [138]. The loss of the superconductive dc winding is approximately 0.25% of the FCL capacity [139].

To remove this heat, extra power is required and ratio of the power of the heat generation to the cooling system is approximately 1/4 according to practical experience [140]. Hence the total operation loss including the no-load loss, load loss and the dc winding cooling loss is about 2% of the capacity of the FCL.

Table 7. 5 Analysis result of the loss breakdown

	Normal status		Saturation status	
	(W)	(%)	(W)	(%)
Load	100		100	
Total loss	10.816	10.82	0.732	0.73
Eddy current loss	10.167	10.17	0.082	0.08
Hysteresis loss	0.596	0.6	0.05	0.05
Copper loss	0.02	0.02	0.02	0.02
Stray loss	0.032	0.03	0.58	0.58

7.3 Summary

Compared to a transformer, the total operational power loss of a saturated iron core FCL is reduced significantly. Although the copper loss does not change for transformer or saturated iron core FCL, the stray loss in the saturated iron core FCL increases about five times compared to that of a transformer due to the decrease in the permeability of the iron core.

However, the significant reduction in the no-load loss results in the reduction in the total loss of the saturated iron core FCL compared to the transformer. Both eddy current loss and hysteresis loss of a saturated iron core FCL decreases significantly (99% and 90% respectively).

Even including the cooling power for the superconducting dc coil of the saturated iron core FCL, the approximately total loss of the FCL reduces from 10% of its capacity for a transformer to 2% (dc winding cooling loss included) of its capacity for the FCL (for the small transformer tested). The dominant loss in the FCL is the stray loss and cooling loss while that of a transformer is the no-load loss.

Chapter

8 Conclusions and Future Work

8.1 Conclusions

As response to the increasing energy demand and global climate change, the distribution network is adopting an increasing penetration of distributed generation using renewable energy sources. This increasing DG penetration causes network issues in both the network voltage profile and fault level. In this thesis, several studies have been conducted regarding these issues. Firstly, it is important to estimate the fault level of distribution network for DNOs in order to inform DG penetration.

Since the commonly used standard in short-circuit current calculation for small scale induction machine is not of adequate accuracy, an improvement has been made to the short-circuit calculation method for small induction machine. Based on this improvement, a method to estimate the fault level contributed by general load in the distribution network has been developed.

Secondly, in the technologies applied for DG, synchronous generator based CHP unit is one of the most commonly used technology in practice. The behaviour of small and medium synchronous machines during system fault has been studied. Also, whether the adoption of synchronous machine with deep penetration in the distribution network will cause the fault current to miss the zero-crossing has been analysed. Thirdly, with the carbon emission reduction policies, large changes in both the power generation and load composition of electrical network will happen. The effect of these changes to the distribution network fault level has been analysed. A solution to the voltage problem caused by DG is to employ power electronic based SOP in the distribution network. Two topologies using shunt thyristor crowbars to protect the power electronic device during network fault have been proposed and the feasibility has been evaluated. Finally, the power lost in normal operation of B2B VSC based SOP and saturated iron core FCL have been analysed.

8.1.1 Short-circuit Current Calculation and Fault Level Estimation of Dynamic Loads

- In the distribution network, the load is typically divided into industrial, commercial and domestic loads. Traditionally, dynamic loads (mainly small-scale single-phase induction motors) in domestic load may be regarded similar to that (medium, and large scale three-phase induction motors) in industrial and commercial loads. However, the fault behaviour of the small-scale single-phase induction motor is quite different from the medium and large-scale induction motors. Since the X/R ratio of the small-scale single-phase induction motor is relatively small compared to that of medium and large induction motors, the winding resistance should be included in the fault current calculation for small scale induction motors, which is often ignored for medium and large scale three-phase induction motors. The results of the fault analysis with this improvement agree better with the experimental results.
- The recommended normalised fault level contribution for general loads given by the standard used by UK DNOs is with respect to the 33kV network, which generally leads to conservative result in calculation. As the study shows that with increasing load power factor, the fault current contribution reduces in a linear manner. Hence, if the load composition and power factor is available, the substation specified estimation of load fault current can be obtained by including the effects of transformer and cable length.

- Furthermore, based on this substation specified fault current of dynamic load, the fault current bands of a specified busbar/substation can be obtained, which can be used as references in network operation management by DNOs.

8.1.2 Analysis of the Effects of Synchronous Machine to Total Fault Current in Distribution Network

- For DGs using small and medium sized synchronous generators directly connected to the 11kV network through a step-up transformer, the normalised fault current contribution with respect to the initial symmetrical fault current can adopt 4.5MVA/MVA if detailed parameters of the generator are not available.
- The effects on the voltage profile and fault level of the network are different when DGs are installed in different locations in the distribution network. When the DG is concentrated close to the primary busbar of the distribution network, the fault level increase becomes the more series issue than voltage profile violation, while when the DG is concentrated at the end of the feeder, the voltage profile violation is the most significant issue.

- For an 11kV network, the break-even point when the most significant issue changes from fault level to voltage profile is approximately at the location which is 3 km away from the primary 11kV busbar with a typical feeder length of 10 km. Furthermore, violations in voltage profile or fault level is likely to appear when the DG penetration level is over 60%.
- When the ratio of time constants τ_a to τ_d'' is larger than 2.5, the missing-zero-crossing phenomenon would occur in the three-phase short-circuit current with the synchronous machine. The missing zero-crossing becomes more significant with the increasing size of the generator. For a single DG generation unit, the size is commonly less than 20MVA. Due to the fault current from the upstream network is relatively large compared to that from the generator, the missing zero-crossing phenomenon will not occur in the total fault current even the fault location is close to the DG site.

8.1.3 Analysis of the Network Changes in the UK in the Future

- At present, the fault current composition of a three-phase fault at the primary busbar in an 11kV network in the UK in most of the substations is 20% to 30% from the downstream network and 70% to 80% from the upstream network respectively.

- Due to the government policy, centralised fire power plants are going to be closed down in the future with the generation filled up by DG. The fault level will increase approximately 10% of the present level with the DG penetration level increasing to around 10% of the peak load and decrease to 95% to 90% of the present level when the DG penetration is approximately 100%, which means that all the upstream generation is closed down. At 100% DG penetration level, the compositions of the fault level at the 11kV primary busbar is 60% to 70% contributed by DG and 30% to 40% contributed by other downstream sources such as the dynamic loads respectively.
- Solutions have to be prepared in response to the potential fault level issue caused by the changes in both the upstream and downstream generation. However, once the solution has been developed, it is not always necessary to adopt further solutions for the accommodation of increasing DG penetration in the network if the upstream generation is gradually closed down.
- In the prediction of the changes of loads, it is assumed that the total electrical power demand is increasing with the fault current contribution of the load also increasing due to the widely adoption of heat pumps in domestic heating, if the UK economy has a moderated growth and low-carbon penetration is high in the next two decades. However, if the UK economy is growing slowly and the adoption level of low-carbon technology is very low, the fault current contribution of load will decrease, mainly caused by the reduction in industrial load demand.

8.1.4 Feasibility Study on the Protection of SSSC Based SOP Using Shunt Thyristor Crowbar

- The two topologies proposed in Chapter 5 have different effects on the fault level of the two feeders. Topology 1 will double the fault level of both feeders while Topology 2 does not cause changes in the fault level.
- When the SOP is connected close to, with cable length less than 3.5km, the primary busbar, the over-voltage at the primary side of the transformer will cause the iron core to saturate. This can be solved by using transformers with high leakage impedance. Backups are required in case of the failure of the thyristor crowbar.
- The I_{TSM} of the thyristor selected for the protection must be 1.5 times larger than the make fault current of the network to withstand the 5-cycle surge current without damaging. However, when the SSSC uses a transformer, the make fault current should be adjusted according to the transformer winding ratio if the thyristor crowbar is connected at the secondary side of the transformer using Topology 1.

8.1.5 Utilisation of Back-to-back VSC Base SOP in Distribution Network

- The B2B VSC can eliminate the voltage violation of a feeder by transferring certain real power to the other feeder connected by the SOP.
- The B2B VSC can block the fault current from the other feeder if fault occurs on one feeder. This means, unlike the SSSC based SOP, no further external protection other than the conventional mechanical circuit breakers is required in the protection of B2B VSC based SOP during fault.
- The B2B VSC can reduce the system power losses by balancing the power flow of both feeders connected by the SOP. However, if the load difference is less than 20% compared to the larger one or the DG penetration level is less than 40%, the total loss may increase due to the power loss in the B2B VSC.

8.1.6 Loss Study of Saturated Iron Core FCL

- In general, the power losses of a saturated iron core FCL will reduce compared to a transformer of the same capacity. For the no-load loss, both the eddy current loss and hysteresis loss will decrease significantly in the saturated iron core of the FCL. Regarding to different core material, the reduction of eddy current loss can be approximately 99% and that of the hysteresis loss can be 90% for permalloy. For the load current, the copper loss does not change with the same load current due to the winding resistance is not affected by the status of the iron core. The stray loss will increase about 5 times in the saturated iron core FCL. This is because the reduction in the permeability of the iron core during saturation.

8.2 Future Work

Based on the work reported in this thesis, the following work is identified as to be extended in the future.

Firstly, the fault current estimation of a dynamic load is based on the current load composition of each type of loads. With the development of the electrical appliances used in different types of loads, the ratio of dynamic load to each type of loads will change in the future.

These changes in load compositions will have effects on the fault current contribution of each type of load. Hence the load change is worthy to be modelled to obtain an estimation of the load composition in the future. With this estimation of load composition, an estimation of the fault current contributed by the dynamic load in the distribution network can be obtained for DNOs in their planning of the design and operation management of the network in the future.

Secondly, the effects of DG locations on the network profile and fault level are studied in the situation when DG is assumed somewhat concentrated. This indicates the worst cases in DG connections. It is also worthwhile to know how will the increasing DG penetration affect the network voltage profile and fault level when the DG is more evenly distributed along the branches in the network. Such a case is more realistic for DNOs DG management.

Furthermore, the assumption is made that the load composition will remain the same, in the analysis of the fault level change; the change of fault level is only caused by the change in the upstream and downstream generation. The estimated load composition is not used in the analysis due to that the time-dependent change in the generation is not available. Hence if this information becomes available in the future, more accurate result can be obtained in the analysis of fault level composition estimation.

As for the SSSC based SOP, the proposed Topology 2 has many advantages over Topology 1 in the finalities. However, in Topology 1, one set of thyristor crowbar is required while in Topology 2, two sets of thyristor crowbar are required. Compared to Topology 1, the construction and maintenance costs of Topology 2 is larger.

An evaluation on the costs between these topologies can be further analysed to have better understanding in the selection of protection topology in practice. Also, if the thyristor crowbar is failed to switch on, the large over-voltage on the SOP will cause series damage to the devices. The backup strategies in case of the failure of thyristor crowbar can be further studied.

In addition, the evaluation of utilising power electronic devices in the distribution network is focused on the B2B VSC for its capability in both voltage control and fault current limitation. However, high temperature superconducting fault current limiter (HTSFCL) is also a possible choice that can be used for the connections between the ends of two feeders. Though it normally cannot control the power flow, the loss of the HTSFCL during normal operation is smaller compared to power electronic devices. Hence an evaluation between different types of protection/compensation devices in response to the increasing DG penetration is worthy to be studied.

Finally, the evaluation of the utilising B2B VSC in the distribution network has only analysed the network loss. For the further studies, the reliability and cost of the B2B VSC is also worthy to be evaluated in order to optimise the performance of power electronic devices in the operation of distribution networks.

Reference

[1] J. Harris., The electricity of Holborn. *New Scientist*. 80., 1982

[2] L. de Andrade and T. P. de Leao, "A brief history of direct current in electrical power systems," in *History of Electro-technology Conference (HISTELCON), 2012 Third IEEE*, 2012, pp. 1-6.

[3] T. P. Hughes *Networks of Power:Electrification in Western Society, 1880-1930*. JHU Press, 1993.

[4] R. Cochrane, "Cradle of Power - The Story of Deptford Power Stations," CEGB, 1986.

[5] R. Kahnt, "Entwicklung der Hochspannungstechnik—100 Jahre Drehstromübertragung," *Elektrizitätswirtschaft,* vol. 90, no. 11, pp. 558-576, 1991.

[6] T. J. Hammons *et al.*, "State of the Art in Ultrahigh-Voltage Transmission," *Proceedings of the IEEE,* vol. 100, no. 2, pp. 360-390, 2012.

[7] W. H. Kersting, *Distribution System Modelling and Analysis*, Second Edition. Boca Raton: CRC Press Taylor & Francis Group, 2007, p. 421.

[8] B. Weedy *et al.*, *Electric Power Systems*, 5th edition. John Wiley & Sons, Incorporated, 2012.

[9] N. Jenkins, R. Allan, P. Crossley, D. Kirschen, and G. Strbac, *EMBEDDED GENERATION*. The Institution of Electrical Engineers, 2000, p. 273.

[10] N. Jenkins, J. B. Ekanayake, and G. Strbac, *Distributed Generation* (Renewable Energy Series). London, United Kingdom: The Institution of Engineering and Technology, 2010, p. 278.

[11] T. Ackermann, G. Andersson, and L. Söder, "Distributed generation: a definition," *Electric Power System Research,* vol. 57, pp. 195-204, 2001.

[12] CIGRE, "Impact of increasing contribution of dispersed generation on the power system; CIGRE Study Committee on 37, Final Report," Septmber 1998.

[13] P. Jorgenden, A. Gruelund Sorensen, J. Falck Christensen, and P. Herager, "Dispersed CHP Units in the Danish Power System," presented at the CIGRE Symposium on *Impact of demand side management, integrated resource planning and distributed generation* Neptun, Romania, 17-19 September 1997.

[14] CIRED, "Dispersed Generation; Preliminary Report of CIRED," presented at the CIRED Working Group WG04, Brussels, Belgium, June 1999.

[15] *2050 Path Way Analysis*.DECC, 2013

[16] A. J. Petrella, "Issues, impacts and strategies for distributed generation challenged power systems," presented at the CIGRE Symposium on Impact of demand sde management, integrated resource planning and distributed generation, Neptun, Romania, 17-19 Septmeber 1997.

[17] B. Buchholz and C. Boese, "The impact of dispersed power generation in distribution systems," in *Quality and Security of Electric Power Delivery Systems, 2003. CIGRE/PES 2003. CIGRE/IEEE PES International Symposium*, 2003, pp. 198-203: IEEE.

[18] G. Pepermans, J. Driesen, D. Haeseldonckx, R. Belmans, and W. D'haeseleer, "Distributed generation: definition, benefits and issues," *Energy policy,* vol. 33, no. 6, pp. 787-798, 2005.
[19] M. Vukobratovic, Z. Hederic, and M. Hadziselimovic, "Optimal Distributed Generation placement in distribution network," in *Energy Conference (ENERGYCON), 2014 IEEE International*, 2014, pp. 1176-1183.
[20] A. Smith, "Electricity Safety, Quality and Continuity Regulations 2002," *Lighting Journal,* vol. 68, no. 2, pp. 35-36, 2003.
[21] N. P. Grid, "Voltage Control Policy: Proposals for a voltage control policy from CLNR learning," ed: Northern Power Grid, 2014.
[22] C. Masters, "Voltage rise: the big issue when connecting embedded generation to long 11 kV overhead lines," *Power engineering journal,* vol. 16, no. 1, pp. 5-12, 2002.
[23] T. Senjyu, Y. Miyazato, A. Yona, N. Urasaki, and T. Funabashi, "Optimal Distribution Voltage Control and Coordination With Distributed Generation," *IEEE Transactions on Power Delivery,* vol. 23, no. 2, pp. 1236-1242, 2008.
[24] M. F. AlHajri and M. E. El-Hawary, "Improving the voltage profiles of Distribution Networks using multiple Distribution Generation Sources," in *Power Engineering, 2007 Large Engineering Systems Conference on*, 2007, pp. 295-299.
[25] M. Ahmad and H. Qin, "Deliverable 5: Evaluation of Representative Substation and Distribution Network Scenarios," WPD, 2014.
[26] N. K. Choudhary, S. R. Mohanty, and R. K. Singh, "Protection coordination of over current relays in distribution system with DG and superconducting fault current limiter," presented at the 2*014 Eighteenth National Power Systems Conference (NPSC)*, Guwahati, 2014.
[27] P. Sudhakar, S. Malaji, and B. Sarvesh, "Impact of UPQC on Protection of Distributed Generation integrated distribution system," presented at the *2016 International Conference on Electrical, Electronics, and Optimization Techniques (ICEEOT)*, Chennai, 2016.
[28] R. C. Dugan, M. F. McGranaghan, and H. W. Beaty, "Electrical power systems quality," *New York, NY: McGraw-Hill,| c1996,* vol. 1, 1996.
[29] "Digest of UK Energy Statistics ", Department for Business, Energy & Industrial Strategy, 2016.
[30] S.-K. Chung and Y. Song, "Design of power conversion system for Stirling engine Micro-CHP integrated into DC power distribution network," in *2011 IEEE 33rd International Telecommunications Energy Conference (INTELEC)*, 2011, pp. 1-8: IEEE.
[31] J. Hindmarsh, *Electrical machines & their applications*. Elsevier, 2014.
[32] W. Colella, "Design options for achieving a rapidly variable heat-to-power ratio in a combined heat and power (CHP) fuel cell system (FCS)," *Journal of Power Sources,* vol. 106, no. 1, pp. 388-396, 2002.
[33] S. Massucco, A. Pitto, and F. Silvestro, "A gas turbine model for studies on distributed generation penetration into distribution networks," *IEEE Transactions on Power Systems,* vol. 26, no. 3, pp. 992-999, 2011.

[34] P. N. Ashitha, "Fuzzy hysteresis based power sharing controller for grid tied operation of a fuel cell," in *2016 IEEE 6th International Conference on Power Systems (ICPS)*, 2016, pp. 1-5.
[35] G. Boyle, *Renewable Energy: Power for a Sustainable Future,* Oxford University Press, USA, 1996.
[36] C. Allan, "Water-turbine-driven induction generators," *Proceedings of the IEE-Part A: Power Engineering,* vol. 107, no. 36, pp. 529-543, 1960.
[37] J. Tong, N. Zheng, X. Wang, J. Hai, and H. S. Ding, "Mini-hydro power," *JOHN WILEY & SONS, BAFFINS LANE, CHICHESTER, WEST SUSSEX PO 19 1 UD(UK).,* 1996.
[38] A. Harvey, *Micro-Hydro Design Manual: a guide to small-scale water power schemes* (no. 621.24/H341). Intermediate Technology Publications, 1993.
[39] S. N. Liew and G. Strbac, "Maximising penetration of wind generation in existing distribution networks," *IEE Proceedings - Generation, Transmission and Distribution,* vol. 149, no. 3, pp. 256-262, 2002.
[40] J. F. Manwell, J. G. McGowan, and A. L. Rogers, *Wind energy explained: theory, design and application*. John Wiley & Sons, 2010.
[41] F. M. M. Bassiouny, "Dynamic performance of isolated asynchronous generators under different loading conditions using Matlab Simulink," in *Power Systems Conference, 2006. MEPCON 2006. Eleventh International Middle East*, 2006, vol. 2, pp. 653-657.
[42] O. Anaya-Lara, N. Jenkins, J. Ekanayake, P. Cartwright, and M. Hughes, *Wind energy generation: modelling and control*. John Wiley & Sons, 2011.
[43] D. A. Spera, *Wind turbine technology : fundamental concepts of wind turbine engineering*. New York New York : ASME Press, 1994.
[44] M. A. Green, "Solar cells: operating principles, technology, and system applications," 1982.
[45] R. VanOverstraeten and R. Mertens, "Physics, technology and use of photovoltaics," 1986.
[46] T. Markvart, *Solar electricity*. John Wiley & Sons, 2000.
[47] *The Contribution to Distribution Network Fault Levels From the Connection of Distributed Generation*., 2005
[48] W. Hoffmann, "PV solar electricity industry: Market growth and perspective," *Solar energy materials and solar cells,* vol. 90, no. 18, pp. 3285-3311, 2006.
[49] K. Zheng, J. h. Zhang, and W. x. Liu, "Distribution network reliability considering complementary distribution generation with wind and photovoltaic powers," in *Critical Infrastructure (CRIS), 2010 5th International Conference on*, 2010, pp. 1-5.
[50] J. M. Bloemink and T. C. Green, "Increasing photovoltaic penetration with local energy storage and soft normally-open points," in *2011 IEEE Power and Energy Society General Meeting*, 2011, pp. 1-8.
[51] S. Sumathi L, A. Kumar, and P. Surekha, *Solar PV and Wind Energy Conversion Systems*. Switzerland Springer, Cham, 2015.
[52] "Power Management & G59," ADE. Ltd,
[53] *Engineering Recommendations G59*.

[54] G. H. Narain and G. Laszlo, "Static Shunt Compensators: SVC and STATCOM," in *Understanding FACTS:Concepts and Technology of Flexible AC Transmission Systems*: Wiley-IEEE Press, 2000, pp. 135-207.
[55] *IEEE Guide for the Functional Specification of Medium Voltage (1 kV-35 kV) Electronic Shunt Devices for Dynamic Voltage Compensation*, 2005.
[56] J. C. Das, "Application of Shunt Capacitor Banks," in *Power System Harmonics and Passive Filter Designs*: Wiley-IEEE Press, 2015, p. 872.
[57] D. P. Ladumor, I. N. Trivedi, R. H. Bhesdadiya, and P. Jangir, "Optimal Power Flow problems solution with SVC using meta-heuristic algorithm," presented at the *2017 Third International Conference on Advances in Electrical, Electronics, Information, Communication and Bio-Informatics (AEEICB)*, Chennai, 2017.
[58] Z. Xu and H. Chen, "Review and Applications of VSC HVDC," *High Voltage Engineering,* vol. 30, no. 1, pp. 1-10, 2007.
[59] N. Flourentzou, V. G. Agelidis, and G. D. Demetriades, "VSC-based HVDC power transmission systems: An overview," *IEEE Transactions on Power Electronics,* vol. 24, no. 3, pp. 592-602, 2009.
[60] R. Adapa, "High-wire act," *IEEE power and energy magazine,* vol. 10, no. 6, p. 18, 2012.
[61] A. M. Abbas and P. W. Lehn, "PWM based VSC-HVDC systems — A review," in *2009 IEEE Power & Energy Society General Meeting*, 2009, pp. 1-9.
[62] E. Mircea, L. Chen-Ching, and E. Abdel-Aty, "Static VAr Compensator (SVC)," in *Advanced Solutions in Power Systems:HVDC, FACTS, and Artificial Intelligence*: Wiley-IEEE Press, 2016, p. 1072.
[63] A. Boström, R. Grunbaum, M. Dahlblom, and H. V. Oheim, "SVC for reliability improvement in the NSTAR 115 kV cape cod transmission system," presented at the *2013 IEEE Power & Energy Society General Meeting*, Vancouver, BC, 2013.
[64] E. Mircea, L. Chen-Ching, and E. Abdel-Aty, "Static Synchronous Compensator-Statcom," in *Advanced Solutions in Power Systems:HVDC, FACTS, and Artificial Intelligence*: Wiley-IEEE Press, 2016, p. 1072.
[65] P. Maibach, "STATCOM Utility-connected power electronic compensator," presented at the *2007 European Conference on Power Electronics and Applications*, Aalborg, *2007*.
[66] G. H. Narain and G. Laszlo, "Static Series Compensators: GCSC, TSSC, TCSC and SSSC," in *Understanding FACTS:Concepts and Technology of Flexible AC Transmission Systems*: Wiley-IEEE Press, 2000, pp. 209-265.
[67] H. XIE and T. LI, "Transformer-less static synchronous series compensator and protection method thereof," ed: Google Patents, 2017.
[68] E. Mircea, L. Chen-Ching, and E. Abdel-Aty, "Static Synchronous Series Compensator (SSSC)," in *Advanced Solutions in Power Systems:HVDC, FACTS, and Artificial Intelligence*: Wiley-IEEE Press, 2016, p. 1072.
[69] J. M. Bloemink and T. C. Green, "Benefits of Distribution-Level Power Electronics for Supporting Distributed Generation Growth," *IEEE Transactions on Power Delivery,* vol. 28, no. 2, pp. 911-919, 2013.
[70] A. Gonzalo, L. Jesús, R. Miguel, M. Luis, and I. Grzegorz, "Back-to-Back Power Electronic Converter," in *Doubly Fed Induction Machine: Modeling and Control for Wind Energy Generation Applications*: Wiley-IEEE Press, 2011, pp. 87-154.

[71] D. Kidd, B. Mehraban, B. Ekehov, J. Ulleryd, and A. Edris, "Eagle pass back to back VSC installation and operation," presented at the *2003 IEEE Power Engineering Society General Meeting*, 2003.
[72] A. Tyagi and K. R. Padiyar, "Dynamic analysis and simulation of a VSC based Back-to-Back HVDC link," presented at the *2006 India International Conference on Power Electronics*, Chennai, 2006.
[73] H. Qin, R. Wu, A. M. Abd-el-Motaleb, L. Ran, X. Deng, and P. Sensarma, "Utilisation of back-to-back VSC in a distribution network with DG," presented at the *2016 IEEE International Conference on the Science of Electrical Engineering (ICSEE)*, Eilat, 2016.
[74] A. S. Corporation, "FAULT-CURRENT LIMITERS (FCL)," ed. Brockenborough, 1996.
[75] S. Eckroad, "Survey of fault current limiter (FCL) technologies," *Electric power research institut,* vol. 1010760, 2005.
[76] K. Jin-Geun *et al.*, "HTS Power Cable Model Component Development for PSCAD/EMTDC Considering Conducting and Shield Layers," *Applied Superconductivity, IEEE Transactions on,* vol. 19, no. 3, pp. 1785-1788, 2009.
[77] Z. Cuixia *et al.*, "Transient Simulation and Analysis for Saturated Core High Temperature Superconducting Fault Current Limiter," in *Electromagnetic Field Computation, 2006 12th Biennial IEEE Conference on*, 2006, pp. 503-503.
[78] M. M. R. Ahmed, G. Putrus, L. Ran, and R. Penlington "Development of a prototype solid-state fault-current limiting and interrupting device for low-voltage distribution networks," *IEEE Transactions on Power Delivery,* vol. 21, no. 4, pp. 1997-2005, 2006.
[79] S. Eckroad, "Survey of Fault Current Limiter (FCL) Technologies Update," *Electric power research institut,* vol. 1016389, 2008.
[80] J. Bock *et al.*, "HTS Fault Current Limiters: First Commercial Devices for Distribution Level Grids in Europe," *IEEE Transactions on Applied Superconductivity,* vol. 21, no. 3, pp. 1202-1205, 2011.
[81] S. M. Blair, C. D. Booth, and G. M. Burt, "Current-Time Characteristics of Resistive Superconducting Fault Current Limiters," *Applied Superconductivity, IEEE Transactions on,* vol. 22, no. 2, pp. 5600205-5600205, 2012.
[82] P. A. Commins and J. W. Moscrop, "Three phase saturated core fault current limiter performance with a floating neutral," in *Electrical Power and Energy Conference (EPEC), 2012 IEEE*, 2012, pp. 249-254.
[83] J. Das, *Power system analysis: short-circuit load flow and harmonics*. CRC press, 2016.
[84] I. E. Commission, "IEC 60909 Short-Circuit Current Calculation in Three-Phase AC Systems," ed: IEC Publication 909, 1988.
[85] I. E. Commission, "IEC 60909-0 (2001-07),'Short-circuit currents in three-phase ac systems-Part 0: Calculation of currents'," *Web site 'www. iec. ch,* 2001.
[86] D. Sweeting, "Applying IEC 60909, Fault Current Calculations," *Industry Applications, IEEE Transactions on,* vol. 48, no. 2, pp. 575-580, 2012.
[87] *Engineering Recommendation G74*, 1992.

[88] M. G. Dwek, "The development of Engineering Recommendation G74," in *Fault Level Assessment - Guessing with Greater Precision?, IEE Colloquium on*, 1996, pp. 1/1-1/5.
[89] N. C. Hicks, "G74 Script," v305: Western Power Distribution, 2013.
[90] Z. Maljkovic, M. Cettolo, and M. Pavlica, "Induction motor's contribution to short circuit current," in *Electric Machines and Drives, 1999. International Conference IEMD '99*, 1999, pp. 354-356.
[91] Z. Maljkovic, M. Cettolo, and M. Pavlica, "The impact of the induction motor on short-circuit current," *Industry Applications Magazine, IEEE,* vol. 7, no. 4, pp. 11-17, 2001.
[92] P. C. Sen, *PRINCIPLES OF ELECTRIC MACHINES AND POWER ELECTRONICS*. Canada: John Wiley 7 Sons, 1989, p. 603.
[93] S. J. Chapman, *Electric Machinery Fundamentals*, Fourth Edition, International Edition, McGrawHill, 2005.
[94] P. Krause, O. Wasynczuk, and S. Sudhoff, *Analysis of electric machinery and drive systems*. Wiley-IEEE Press, 2002
[95] D. Stojanovic, M. Veselinovic, N. Mitrovic, and L. Korunovic, "Calculations and analysis of induction motors impact on short-circuit current," in *Electrotechnical Conference, 2000. MELECON 2000. 10th Mediterranean*, 2000, vol. 3, pp. 1076-1079 vol.3.
[96] J. V. Milanovic, K. Yamashita, S. Martinez Villanueva, S. Z. Djokic, and L. M. Korunovic, "International Industry Practice on Power System Load Modeling," *Power Systems, IEEE Transactions on,* vol. 28, no. 3, pp. 3038-3046, 2013.
[97] L. G. Meegahapola, D. Robinson, A. P. Agalgaonkar, S. Perera, and P. Ciufo, "Microgrids of Commercial Buildings: Strategies to Manage Mode Transfer From Grid Connected to Islanded Mode," *IEEE Transactions on Sustainable Energy,* vol. 5, no. 4, pp. 1337-1347, 2014.
[98] O. H. Abdalla, M. E. Bahgat, A. M. Serag, and M. A. El-Sharkawi, "Dynamic load modelling and aggregation in power system simulation studies," in *Power System Conference, 2008. MEPCON 2008. 12th International Middle-East*, 2008, pp. 270-276.
[99] A. A. Rahim, M. F. Hashim, and M. F. M. Siam, "Dynamic load modelling based on power quality recorder data," in *Power Engineering and Optimization Conference (PEOCO), 2013 IEEE 7th International*, 2013, pp. 119-123.
[100] B. Khodabakhchian and G. T. Vuong, "Modeling a mixed residential-commercial load for simulations involving large disturbances," *Power Systems, IEEE Transactions on,* vol. 12, no. 2, pp. 791-796, 1997.
[101] A. Bokhari *et al.*, "Experimental Determination of the ZIP Coefficients for Modern Residential, Commercial, and Industrial Loads," *Power Delivery, IEEE Transactions on,* vol. 29, no. 3, pp. 1372-1381, 2014.
[102] H. L. Willis, *Power distribution planning reference book*, 2nd ed. London: Taylor & Francis, 2004.
[103] C. R. Bayliss, *Transmission and distribution electrical engineering*, 4th ed. Oxford: Newnes, 2011.
[104] B. Chalmers and A. Williamson, *A.C. Machines: Electromagnetics and Design*. England: Research Studies Press Ltd, 1991.

[105] B. Truslove.. *Cooling towers: Eyesores or sights for sore eyes?*, 2015, Available: http://www.bbc.co.uk/news/uk-england-nottinghamshire-34861835, accessed on 12/01/2016
[106] R. Quinn, "Future Energy Scenarios 2015,": NationalGrid, July 2015.
[107] *UK Future Energy Scenarios: UK gas and electricity transmission*., July 2014
[108] S. Kawachi, H. Hagiwara, J. Baba, K. Furukawa, E. Shimoda, and S. Numata, "Modeling and simulation of heat pump air conditioning unit intending energy capacity reduction of energy storage system in microgrid," in *Power Electronics and Applications (EPE 2011), Proceedings of the 2011-14th European Conference on*, 2011, pp. 1-9.
[109] C. John, "Running Costs of Conventional Electric Space Heating System," Advanced Control Partnerships Limited, 2014.
[110] S. Hansen.. *Heat Pump Consumer Price Guide*. Available: http://www.heatpumppriceguides.com/#sizes, accessed on 14 March, 2015,
[111] G. E. Mahadeo, S. Bahadoorsingh, and C. Sharma, "Analysis of the impact of battery electric vehicles on the low voltage network of a Caribbean island," presented at the *2017 IEEE Transportation Electrification Conference and Expo (ITEC)*, Chicago, IL, 2017.
[112] I. Subotic, E. Levi, M. Jones, and D. Graovac, "Multiphase integrated on-board battery chargers for electrical vehicles," in *Power Electronics and Applications (EPE), 2013 15th European Conference on*, 2013, pp. 1-10.
[113] Z. Duan, F. Zhao, W. Cong, Y. Wang, D. Zhang, and X. Wen, "Analysis of charging torque in a three-phase integrated charger of electrical vehicle," in *Transportation Electrification Asia-Pacific (ITEC Asia-Pacific), 2014 IEEE Conference and Expo*, 2014, pp. 1-5.
[114] A. L. P. de Oliveira, C. E. Tibùrcio, M. N. Lemes, and D. Retzmann, "Prospects of Voltage-Sourced Converters (VSC) applications in power transmission systems," presented at the *2010 IEEE ANDESCON*, Bogota, 2010.
[115] S. Meier, "Losses in Power Electronic Converters.", 2010
[116] T. Masood, "Improvement of Voltage and Power Flow Control in the GCC Power Grid by using Coordinated FACTS Devices," University of Bath, 2012.
[117] H. Ergun and D. Van Hertem, "Comparison of HVAC and HVDC technologies," *HVDC Grids: For Offshore and Supergrid of the Future,* vol. 51, p. 79, 2016.
[118] X. Tang, J. Zhang, and J. Li, "A practical on-line condition monitoring and fault location system for overhead power lines distribution networks," presented at the *2014 IEEE PES T&D Conference and Exposition*, Chicago, IL, USA, *2014*.
[119] R. M. Del Vecchio, B. Poulin, P. T. Feghali, and D. M. Shah Rajendra Ahuja, *Transformer Design Principles: With Applications to Core-Form Power Transformers*, Second Edition ed. CRC Press, 2010.
[120] *IEEE Standard Test Specification for Thyristor Diode Surge Protective Devices*, 1997.
[121] W. Bin and N. Mehdi, "High???Power Semiconductor Devices," in *High-Power Converters and AC Drives*: Wiley-IEEE Press, 2017, p. 480.
[122] G. C. James, "Frequency Domain Temperature Model - A New Method in On-line Temperature Estimation for Power Modules in Drives Applications "

Engineering Doctorate in Power Electronics,Machines and Drives, School of Electrical, Electronic and Computer Engineering, Newcastle University, 2010.
[123] H. A. Mantooth and A. R. Hefner, "Electrothermal simulation of an IGBT PWM inverter," *IEEE Transactions on Power Electronics,* vol. 12, no. 3, pp. 474-484, 1997.
[124] A. Ammous *et al*, "Electrothermal modeling of IGBTs: application to short-circuit conditions," *IEEE Transactions on Power Electronics,* vol. 15, no. 4, pp. 778-790, 2000.
[125] T. Bechtold, E. B. Rudnyi, and J. G. Korvink, "Dynamic Electrothermal Simulationof Microsystems - A Review," *Journal of Micromechanics and Microengineering,* pp. 17 - 31, 2005.
[126] M. Geethanjali and S. Devi, "Optimal location and sizing of Thyristor Controlled Series Capacitor in radial distribution systems using particle swarm optimization and differential evolution techniques," presented at the *International Conference on Power, Energy and Control (ICPEC)*, Sri Rangalatchum Dindigul, 2013.
[127] ABB, "Surge currents for phase controlthyristors," 2014.
[128] R. H. Park, "Two-reaction theory of synchronous machines generalized method of analysis-part I," *American Institute of Electrical Engineers, Transactions of the,* vol. 48, no. 3, pp. 716-727, 1929.
[129] G. Kron, *Equivalent circuits of electric machinery*. J. Wiley & Sons, 1951.
[130] P. C. Krause and C. H. Thomas, "Simulation of Symmetrical Induction Machinery," *IEEE Transactions on Power Apparatus and Systems,* vol. 84, no. 11, pp. 1038-1053, 1965.
[131] P. C. Krause, F. Nozari, T. L. Skvarenina, and D. W. Olive, "The Theory of Neglecting Stator Transients," *IEEE Transactions on Power Apparatus and Systems,* vol. PAS-98, no. 1, pp. 141-148, 1979.
[132] C. Se-Kyo, "A phase tracking system for three phase utility interface inverters," *IEEE Transactions on Power Electronics,* vol. 15, no. 3, pp. 431-438, 2000.
[133] L. Harnefors and H. P. Nee, "Model-based current control of AC machines using the internal model control method," *IEEE Transactions on Industry Applications,* vol. 34, no. 1, pp. 133-141, 1998.
[134] "Losses," in *Transformer Design Principles*: CRC Press, 2010, pp. 447-506.
[135] E. Della Torre, *Magnetic hysteresis*. Wiley, 2000.
[136] J. M. D. Coey, *Magnetism and Magnetic Materials*. Cambridge: Cambridge University Press, 2010.
[137] J. R. Rumble, *CRC Handbook of Chemistry and Physics*, 98th ed. CRC, 2017.
[138] J. C. Aracil, J. Lopez-Roldan, J. C. Coetzee, F. Darmann, and T. Tee, "Saturated core high-temperature superconducting fault current limiters as an alternative to conventional series reactors in a distribution grid," in *AC and DC Power Transmission (ACDC 2012), 10th IET International Conference on*, 2012, pp. 1-6.
[139] S. M. Blair, C. D. Booth, N. K. Singh, G. M. Burt, and C. G. Bright, "Analysis of Energy Dissipation in Resistive Superconducting Fault-Current Limiters for Optimal Power System Performance," *Applied Superconductivity, IEEE Transactions on,* vol. 21, no. 4, pp. 3452-3457, 2011.

[140] B. W. Lee, J. Sim, K. B. Park, and I. S. Oh, "Practical Application Issues of Superconducting Fault Current Limiters for Electric Power Systems," *Applied Superconductivity, IEEE Transactions on,* vol. 18, no. 2, pp. 620-623, 2008.

Appendix I The Electricity System in the UK in 2014

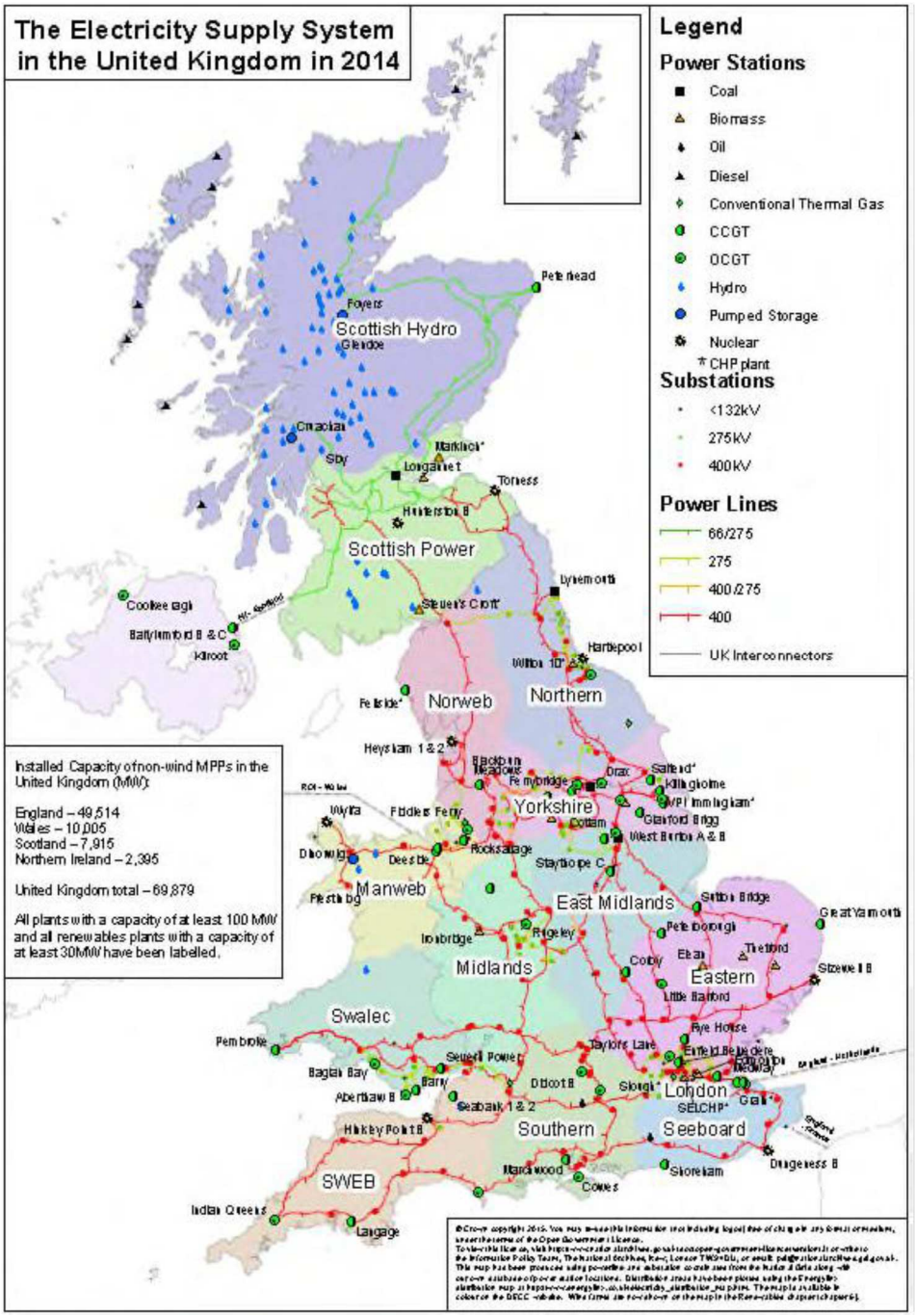

Figure A-I UK Electricity System (2014)

Appendix II 11kV Primary Substation List in Birmingham Area and the Network Diagram

Table A-II 11kV primary Substation List

Substation Name	Busbar No.	Busbar Code	Group No.
A	2728	A1	Group 1
	2736	A2	
	20001	A3	
	20002	A4	
B	2692	B1	
	2696	B2	
	2700	B3	
C	2712	C1	
	2804	C2	
	20501	C3	
D	7056	D1	Group 2
	7060	D2	
G	6540	E1	
	6548	E2	
	6544	E3	
	6552	E4	
F	6688	F1	
	6692	F2	
	6696	F3	
	6700	F4	
G	6724	G1	
	6728	G2	
	6600	G3	
	6596	G4	
H	7100	H1	Group 3
	7096	H2	
	6640	H3	
	7088	H4	
	7092	H5	

Substation Name	Busbar No.	Busbar Code	Group No.
I	7292	I1	
	7296	I2	
	7724	I3	
	7300	I4	
	7304	I5	
	7728	I6	
J	6960	J1	
	6964	J2	
	7568	J3	Group 4
	7564	J4	
K	7500	K1	
	7496	K2	
	7492	K3	
	7488	K4	
L	7416	L1	
	7412	L2	
	7408	L3	
M	7660	M1	
	7664	M2	
	7648	M3	
	7652	M4	
	7640	M5	
	7644	M6	
N	7476	N1	
	7480	N2	
	7484	N3	
	7472	N4	
O	7428	O1	
	21002	O2	
	7436	O3	
	7432	O4	
	7444	O5	

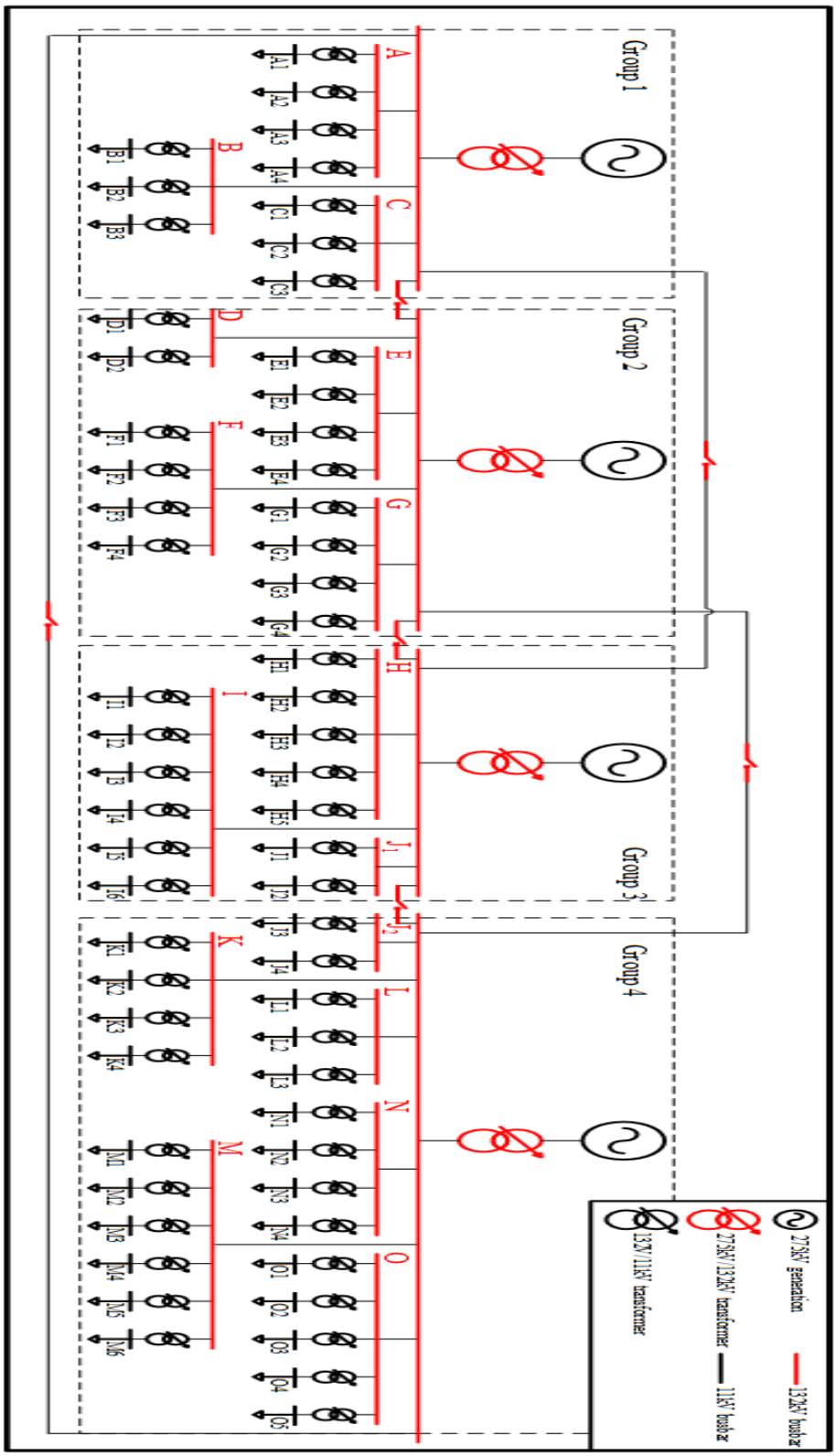

Figure A-II Birmingham Network Diagram

Appendix III List of Publications

1. Wei Lai, Minyou Chen, Li Ran, Shengyou Xu, Han Qin, Olayiwola Alatise, Phil A. Mawby, “Study on the lifetime characteristics of power modules under power cycling conditions,” *IET Power Electronics, vol. 9, no. 5, pp. 1045-1052, 2016.*

2. Han Qin, Ruizhu Wu, Ahmed M. Abd-el-Motaleb, Li Ran, Xiaochuan Deng, Partha Sensarma, “Utilisation of Back-to-Back VSC in a Distribution Network with DG”, *in ICSEE 2016, 2016.*

3. Erfan Bashar, Han Qin, Ruizhu Wu, Li Ran, Olayiwola Alatise, "Analysis of DC Offset in Fault Current Caused by Machines in a Medium Voltage Distribution Network," 9th IET International Conference on Power Electronics, Machines and Drives (PEMD 2018), Liverpool, 2018, pp. 1-19. (Under Revision)

Appendix IV Datasheets for Synchronous Machines, Cables and Thyristors Used in the Thesis

Synchronous Machines

Stamford Power Generation, “HCI 434E/444E - Technical Data Sheet,”
Stamford Power Generation, “PI734B - Technical Data Sheet,”
Stamford Power Generation, “HCI634H - Technical Data Sheet,”
Stamford Power Generation, “LV 804 R WDG 12 - Technical Data Sheet,”
Stamford Power Generation, “PI044D - Winding 311 Technical Data Sheet,”
FKI Energy Technology, “Data Sheets Three Phase Synchronous Generator”

Cables

ELSEWEDY CABLES, “Three Core Cable with Copper Conductors, XLPE Insulated, Copper Tape Screened, Galvanized Steel Wire Armoured and PVC Sheathed 6.35/11 kV cable”

BATT Cables, “TABLE BEC 107. (Continued) Current ratings for 6350/11000 volts grade PILC/SWA/PVC cable to BS6480/69”

Thyristors

ABB, 30H1801 Phase Control Thyristor
ABB, 34T1600 Phase Control Thyristor
ABB, 34T1601 Phase Control Thyristor
ABB, 42L1800 Phase Control Thyristor
ABB, 50Q1801 Phase Control Thyristor
Semikron, SKET800 Phase Control Thyristor

Appendix V Short-circuit Test Equipment

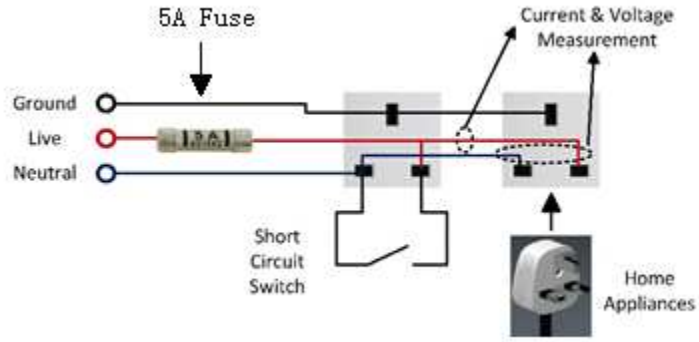

Test circuit

Current Meter

Protection